# Exploring Structural, Electronic, and Switching Properties of Functionalized Platform and Fe(III) Spin-Crossover Molecules with a Scanning Tunneling Microscope

Dissertation

zur Erlangung des Doktorgrades
der Mathematisch-Naturwissenschaftlichen Fakultät
der Christian-Albrechts-Universität zu Kiel

vorgelegt von

Torben Jasper-Tönnies

Kiel, 2021

Erster Gutachter: Prof. Dr. Richard Berndt

Zweiter Gutachter: Prof. Dr. Olaf Magnussen

Dritter Gutachter: Prof. Dr. Jörg Kröger

Tag der mündlichen Prüfung: 28.10.2021

# Eidesstattliche Erklärung

Hiermit bestätige ich, diese Arbeit selbstständig unter der Beratung meiner wissenschaftlichen Mentoren angefertigt und keine weiteren Hilfsmittel, außer den im Text angegebenen sowie den bekannten Nachschlagewerken der Naturwissenschaften, verwendet zu haben. Diese Arbeit wurde weder ganz noch in Teilen an anderer Stelle im Rahmen eines Prüfungsverfahrens vorgelegt und demnach auch nicht in solch einem Rahmen veröffentlicht oder zur Veröffentlichung eingereicht. Frühere Promotionsversuche wurden von mir nicht vorgenommen. Es wurde mir bisher auch kein akademischer Grad entzogen und es ist auch kein Verfahren dazu im Gange. Die Arbeit ist unter Einhaltung der Regeln guter wissenschafticher Praxis der Deutschen Forschungsgemeinschaft entstanden.

Die Kapitel 5-11 der Arbeit basieren auf Publikationen in Fachzeitschriften:

- Torben Jasper-Toennies, Aran Garcia-Lekue, Thomas Frederiksen, Sandra Ulrich, Rainer Herges, and Richard Berndt.

  *Conductance of a Freestanding Conjugated Molecular Wire*

  Phys. Rev. Lett. **119**, 066801 (2017), *Editors' Suggestion*

- Torben Jasper-Tönnies, Aran Garcia-Lekue, Thomas Frederiksen, Sandra Ulrich, Rainer Herges, and Richard Berndt.

  *High-conductance contacts to functionalized molecular platforms physisorbed on Au(111)*

  J. Phys.: Condens. Matter **31**, 18LT01 (2019)

- Torben Jasper-Tönnies, Manuel Gruber, Sven Johannsen, Thomas Frederiksen, Aran Garcia-Lekue, Torben Jäkel, Fynn Röhricht, Rainer Herges, and Richard Berndt.

  *Rotation of Ethoxy and Ethyl Moieties on a Molecular Platform on Au(111)*

  ACS Nano **14**, 3907 (2020)

- Torben Jasper-Tönnies, Manuel Gruber, Sandra Ulrich, Rainer Herges, and Richard Berndt.

  *Coverage-Controlled Superstructures of $C_3$ Symmetric Molecules: Honeycomb versus Hexagonal Tiling*

  Angew. Chem. Int. Ed. **59**, 7008 (2020), *Frontispiece of issue 18*

- Torben Jasper-Tönnies, Igor Poltavsky, Sandra Ulrich, Tobias Moje, Alexandre Tkatchenko, Rainer Herges, and Richard Bernd

  *Stability of functionalized platform molecules on Au(111)*

  J. Chem. Phys. **149**, 244705 (2018), *Editor's Pick*
- Torben Jasper-Tönnies, Manuel Gruber, Sujoy Karan, Hanne Jacob, Felix Tuczek, and Richard Bernd.

  *Deposition of a Cationic Fe$^{III}$ Spin-Crossover Complex on Au(111): Impact of the Counter Ion*

  J. Phys. Chem. Lett. **8**, 1569 (2017)
- Torben Jasper-Toennies, Manuel Gruber, Sujoy Karan, Hanne Jacob, Felix Tuczek, and Richard Berndt

  *Robust and Selective Switching of an Fe$^{III}$Spin-Crossover Compound on $Cu_2N/Cu(100)$ with Memristance Behavior*

  Nano Lett. **17**, 6613 (2017)

Torben Jasper-Tönnies

# Abstract

In this thesis, molecules on metal surfaces are explored using low-temperature scanning tunneling microscopy in ultra-high vacuum. Several organic molecules and an organometallic complex are addressed on the single-molecule scale and results are presented concerning (i) electron transport through metal-molecule contacts, (ii) switching of molecules in response to external stimuli, (iii) self-assembly, (iv) stability of molecules on metal substrates and (v) the deposition of molecules on substrates.

First, flat organic platforms, namely trioxatriangulenium (TOTA) molecules, are used to place functional moieties in a freestanding and upright position on metal substrates. In contrast to most previously studied anchor molecules, the contact to substrates is mediated by an extended $\pi$ system and the binding to metal surfaces takes place through physisorption. Being physisorbed the platforms retain important gas-phase properties of the attached moieties.

After deposition of such platforms on an atomically flat Au(111) substrate, their electric conductance is probed with the tip of a scanning tunneling microscope (STM) to maximize the control of the junction geometry. *Inert* hydrogen, methyl, and *reactive* propynyl subunits that stand in an upright position on the platforms are contacted. Despite the simplicity of these single-molecule junctions the conductances vary in an intriguing manner with the electrode separation. It is shown that the platform molecule is suitable as high-conductance anchor and the current flow is not directly correlated with the chemical interaction between the electrode and the molecule. Because of the high control and characterization of the junctions' geometries, the experiments allow close comparison with theory and help to achieve a high-level understanding of electron transport in molecular junctions. Atomistic density functional theory (DFT) and Green's functions calculations for the propynyl and methyl case indeed reproduce the respective conductance evolution and reveal the role of the junction geometry, forces, orbital symmetries, and formation of chemical bonds at the tip-molecule interface.

Next, two closely-related three-states rotors, namely ethoxy and ethyl moieties, mounted on the TOTA platform on Au(111) were addressed individually with an STM tip. In contrast to other anchors, the platforms retain important gas-phase properties of the rotor. This simplifies a detailed analysis, and permits, *e. g.*, the identification of the vibrational modes involved in the rotation process with the help of action spectroscopy and gas-phase

DFT calculations. The symmetry provided by the platform enables active control of the rotation direction through electrostatic interactions with the tip and charged neighboring adsorbates. This investigation may turn out useful for designing platforms that provide directional rotation and for transferring more sophisticated molecular machines from the gas-phase to surfaces.

Another chapter of the thesis addresses the self-assembly of molecules on substrates. A competition between honeycomb and hexagonal self-assembly of molecules can lead to large honeycomb superstructures on surfaces. Such honeycomb superstructures are presented for the $C_3$ symmetric platform methyl-TOTA on Au(111) and Ag(111) surfaces. The superstructures cover nearly mesoscopic areas with unit cells containing up to 3000 molecules, more than an order of magnitude larger than previously reported. The unit cell size can be controlled via the coverage. A fairly general model is developed that describes the energetics of honeycomb superstructures built from $C_3$ symmetric units. Based on three parameters that characterize two competing bonding arrangements, the model is consistent with the present experimental results and also reproduces various published results. The model identifies the relevant driving force, mostly related to geometric aspects, of the pattern formation. In turn, the model may be employed to guide the design of molecules for building mesoscopic superstructures.

Next, the stability of TOTA derivatives sublimated onto Au(111) substrates were studied. STM data reveal that $> 99\%$ of ethyl–TOTA and methyl–TOTA remain intact whereas 60% of H–TOTA and $> 99\%$ of propynyl–TOTA and ethynyl–TOTA decompose. The observed tendency towards fragmentation on Au(111) is opposite to the sequence of gas-phase stabilities of the molecules. Although Au(111) is the noblest of all metal surfaces, the binding energies of the possible decomposition products to Au(111) destabilize the bond between the platform and the above mentioned functional groups by 2 to 3.9 eV (190–370 kJ/mol) and even render some of the molecules unstable on Au(111) as revealed by DFT calculations.

Finally, an organometallic complex was studied. STM data reveal the first successful deposition of a *charged* $Fe^{III}$ spin-crossover complex, $[\mathrm{Fe(pap)_2}]^+$ (pap=N-2-pyridylmethylidene-2-hydroxyphenylaminato), on Au(111). Furthermore, the bulk form of the molecules is stabilized by a perchlorate counter ion, which depending on the deposition technique, may affect the quality of the deposition and the measurements.

The switching between two spin states in response to external stimuli makes spin-crossover molecules on surfaces attractive for potential applications. The final part reports on $[\mathrm{Fe(pap)_2}]^+$ molecules on a $\mathrm{Cu_2N}$/Cu(100) surface. The adsorbed compound is controllably switched between three different states, each of them exhibiting a characteristic tunneling conductance. The conductance is therefore employed to readily read the state of the molecules. A comparison of the experimental data with the results of gas-phase DFT calculations suggests that all $\mathrm{Fe(pap)_2}$ molecules are initially in their high-spin state. The two other states are compatible with the low-spin state of the molecule but differ with respect to their coupling to the substrate. As a proof of concept, the reversible and selective nature of the switching is used to build a two-molecule memory.

# Kurzzusammenfassung

In dieser Arbeit werden Moleküle auf Metalloberflächen mit Tieftemperatur-Rastertunnelmikroskopie im Ultrahochvakuum untersucht. Es werden verschiedene organische Moleküle und ein organometallischer Komplex auf der Einzelmolekül-Skala betrachtet und Ergebnisse zu folgenden Themen präsentiert: (i) Elektronentransport durch Metall-Molekül-Kontakte, (ii) Schalten von Molekülen als Reaktion auf externe Stimuli, (iii) Selbstorganisation sowie (iv) Stabilität von Molekülen auf Metallsubstraten und (v) Aufbringen von Molekülen auf Oberflächen.

Im ersten Teil der Arbeit wird eine flache organische Plattform, nämlich das Trioxatriangulenium (TOTA) Molekül, genutzt, um verschiedene funktionale Moleküle in einer freistehenden, aufrechten Position auf Metallsubstrate aufzubringen. Im Gegensatz zu den meisten, in früheren Forschungsarbeiten untersuchten Ankermolekülen, wird der Kontakt zum Substrat durch ein ausgedehntes $\pi$-System hergestellt und die Metall-Molekül-Bindung erfolgt durch Physisorption. Dadurch konserviert die Plattform wichtige Gasphaseneigenschaften der angehängten Molekülgruppe.

Nach dem Aufbringen solcher Plattformen auf eine atomar ebene Au(111)-Oberfläche wird der elektrische Leitwert der Plattform mit der Spitze eines Rastertunnelmikroskops (RTM) gemessen, wodurch eine möglichst große Kontrolle der Kontaktgeometrie erreicht wird. *Inerte* Wasserstoff- und Methyl-Einheiten sowie *reaktive* Propinyl-Gruppen, die sich jeweils in einer aufrechten Position auf der Plattform befinden, werden mit der Spitze kontaktiert. Trotz der Einfachheit dieser Einzelmolekülübergänge variieren die Leitwerte in faszinierend komplexer Weise mit dem Abstand der Elektroden, also von Spitze und Au(111)-Substrat. Es wird gezeigt, dass das Plattformmolekül als hochleitender Anker geeignet ist und der Stromfluss nicht direkt mit der chemischen Wechselwirkung zwischen der Elektrode und dem Molekül korreliert ist. Aufgrund der hohen Kontrolle und Charakterisierung der Geometrien der Molekül-Metall-Übergänge erlauben die Experimente einen engen Vergleich mit der Theorie und tragen zu einem detaillierten Verständnis des Elektronentransports in molekularen Übergängen bei. Atomistische Berechnungen mittels Dichtefunktionaltheorie und Greenschen Funktionen für den Propinyl- und den Methyl-Fall reproduzieren in der Tat die jeweilige Leitwertentwicklung und klären die Rolle der Geometrie, Kräfte, orbitale Symmetrien und Bildung chemischer Bindungen an dem Übergang zwischen Metallspitze und Molekül.

Als Nächstes wurden zwei eng verwandte Rotoren, nämlich Ethoxy- und Ethyl-Gruppen, die auf der TOTA-Plattform auf Au(111) montiert sind und drei Zustände einnehmen können, einzeln mit einer RTM-Spitze untersucht. Im Gegensatz zu anderen Ankermolekülen bleiben durch die Plattform wichtige Gasphaseneigenschaften der Rotoren erhalten. Dies vereinfacht eine detaillierte Analyse und erlaubt z. B., die am Rotationsprozess beteiligten Schwingungsmoden mit Hilfe von Wirkungsspektroskopie (*action spectroscopy*) und Gasphasen-DFT-Berechnungen zu identifizieren. Zudem ermöglicht die von der Plattform gebotene Symmetrie eine aktive Kontrolle der Drehrichtung durch elektrostatische Wechselwirkungen mit der RTM-Spitze sowie geladenen benachbarten Adsorbaten. Diese Untersuchung kann sich als nützlich erweisen, um Plattformen zu entwerfen, die eine gerichtete Rotation ermöglichen, und um anspruchsvollere molekulare Maschinen aus der Gasphase auf Oberflächen zu transferieren.

Ein weiteres Kapitel der Arbeit befasst sich mit der Selbstanordnung von Molekülen auf Substraten. Die Konkurrenz zwischen honigwabenartiger und hexagonaler Selbstanordnung von Molekülen kann zu großen honigwabenförmigen Suprastrukturen auf Oberflächen führen. Solche wabenförmigen Überstrukturen werden für die symmetrische $C_3$-Plattform Methyl-TOTA auf Au(111)- und Ag(111)-Oberflächen vorgestellt. Die Einheitszellen der Überstrukturen decken nahezu mesoskopische Bereiche ab, die bis zu 3000 Moleküle enthalten, mehr als eine Größenordnung größer als zuvor berichtet. Die Größe der Einheitszellen kann über die Bedeckung gesteuert werden. Es wird ein relativ allgemeines Modell entwickelt, das die Energetik dieser Überstrukturen beschreibt, die aus $C_3$ symmetrischen Einheiten aufgebaut sind. Basierend auf drei Parametern, die zwei konkurrierende Bindungsanordnungen charakterisieren, ist das Modell mit den vorliegenden experimentellen Ergebnissen konsistent und reproduziert auch verschiedene zuvor veröffentlichte Ergebnisse. Das Modell identifiziert die relevante Antriebskraft der Musterbildung, die hauptsächlich mit geometrischen Aspekten zusammenhängt. Im Gegenzug kann das Modell beim Design von Molekülen zur Herstellung mesoskopischer Einheitszellen helfen.

Anschließend wird die Stabilität von TOTA-Derivaten, die auf Au(111) Substraten sublimiert wurden, untersucht. Aus den STM Daten geht hervor, dass > 99% der Ethyl–TOTA und Methyl–TOTA Moleküle intakt bleiben, während 60% der H–TOTA und > 99% der Propinyl–TOTA and Ethinyl–TOTA Moleküle zerfallen. Die beobachtete Tendenz zur Fragmentierung auf Au(111) ist entgegengesetzt zur Sequenz der Gasphasenstabilitäten der Moleküle. Obwohl Au(111) die edelste aller Metalloberflächen ist, destabilisieren nach DFT-Rechnungen die Bindungsenergien der möglichen Zerfallsprodukte die Bindung zwischen der Plattform und den oben genannten funktionalen Gruppen um 2 bis 3.9 eV (190–370 kJ/mol) und führen bei einigen Molekülen sogar zur Instabilität.

Schließlich wird im zweiten Teil der Arbeit ein organometallischer Komplex untersucht. STM-Daten zeigen das erste erfolgreiche Aufbringen eines *geladenen* $Fe^{III}$ Spin-Crossover-Komplexes, $[Fe(pap)_2]^+$ (pap=N-2-pyridylmethyliden-2-hydroxyphenylaminato), auf Au(111). Darüber hinaus wird die Festform der Moleküle durch ein Perchlorat-Gegenion stabilisiert, welches je nach Depositionstechnik die Qualität der Probe und Messung beeinflussen kann.

Das Schalten zwischen zwei Spin-Zuständen als Reaktion auf externe Reize macht Spin-Crossover-Moleküle auf Oberflächen attraktiv für potenzielle Anwendungen z. B. in der Elektronik und Spintronik. Der letzte Teil behandelt $[Fe(pap)_2]^+$ Moleküle auf einer $Cu_2N$/Cu(100)-Oberfläche. Das adsorbierte Molekül wird kontrollierbar zwischen drei verschiedenen Zuständen geschaltet, die jeweils einen charakteristischen Tunnelleitwert aufweisen. Der Leitwert ermöglicht somit eine einfache Identifizierung des Molekülzustands. Ein Vergleich der experimentellen Daten mit den Ergebnissen von Gasphasen-DFT-Berechnungen legt nahe, dass sich alle Fe(pap)$_2$-Moleküle zunächst in ihrem Zustand mit hoher Multiplizität (*High Spin*) befinden. Die beiden anderen Zustände sind mit dem Zustand geringer Multiplizität (*Low Spin*) des Moleküls kompatibel, unterscheiden sich jedoch in Bezug auf ihre Ankopplung an das Substrat. Schlussendlich wird die reversible und selektive Natur des Schaltenprozesses genutzt, um als konzeptionellen Beweis einen Zwei-Molekül-Speicher aufzubauen.

# Acknowledgements

Many thanks to

- Prof. Dr. Richard Berndt, for giving me the opportunity to work in his group, for providing good equipment and conditions, for giving the freedom to pursue experimental ideas, for invaluable suggestions and discussions, and for improving my English,
- the team of the 4 K laboratory, especially Dr. Alexander Weismann, Dr. Johannes Schöneberg and Dr. Andreas Burtzlaff with whom I spent a lot of time to improve or repair the laboratory and had many fruitful discussions,
- Prof. Dr. Rainer Herges, for giving insights into chemistry, advice, and for suggestions of molecules based on my ideas,
- Prof. Dr. Felix Tuczeck, for the collaboration in scientific matters and in matters of the Integrated Research Training Group of the Collaborative Research Center (CRC 677), which was coordinated by me for some time,
- Jun.-Prof. Dr. Manuel Gruber, for helping me to publish my scientific results, for many fruitful discussions, for our successful collaborations, and for proofreading parts of this thesis,
- Dr. Alexander Weismann, for valuable discussions, for sharing his extensive knowledge, for helping to troubleshoot problems in the labs, and for proofreading parts of this thesis,
- Dr. Sujoy Karan, for discussions and the joint research project,
- Dr. Thomas Jürgens, for technical advice,
- Dr. Aran Garcia-Lekue and Prof. Dr. Thomas Frederiksen from San Sebastian, for their nice and uncomplicated collaboration and detailed calculations, which allowed for a better understanding of my experimental results,
- Dr. Igor Poltavsky and Prof. Dr. Alexandrê Tkatchenko from Luxembourg, for the successful collaboration,
- Sven Johannsen for performing auxiliary experiments and proofreading parts of this thesis,

- all other collaborators,
- Prof. Dr. Pehlke, Prof. Dr. Carmen Hermann, and Dr. Lynn Gross, for discussions,
- Monika Seeger and Claudia Läufer, for helping me out when a bureaucratic task appeared,
- the administrative and non-scientific staff of CAU for making several necessary things available,
- the Deutsche Forschungsgemeinschaft, for funding via SFB 677,
- the state Germany, for providing the framework for my education and for supporting me via BAföG.

I would especially like to thank my family and friends.

It will be interesting to observe which parts of this thesis will stay longest and brightest in my memory ;-).

There are people in this world who live in poverty,[I,1] have no or only limited access to education,[2] health care,[2] and/or clean drinking water.[3] I thank all those people who are aware of this situation and take appropriate actions.

I was *extremely fortunate* to be able to work in science.

---

[I] Extreme poverty was defined as less than US$ 1.9 a day in 2020 by the United Nations.

# Contents

# I Experimental and Theoretical Techniques and Fundamentals

# III Switching, Self-assembly, and Stability of Functionalized Platform Molecules

# IV Deposition and Switching of a Fe(III) Spin-Crossover Complex

# 1

# Introduction

Molecules exhibit a vast diversity of physical and chemical properties.[4] By placing them on a substrate they may be exploited to modify the substrate's properties.[5] Such *functionalized* surfaces may be important for future medical, commercial and industrial applications. Surfaces coated with molecules can, for example, inhibit bacterial adhesion and may prevent infections.[6] Moreover, molecule-induced properties may respond to or be controlled via external stimuli such as temperature, light, and electric current. For instance, the wettability of a surface can be switched by light and temperature by covering it with switchable molecules.[7] Analogously the chemical reactivity of material surfaces can be modified and/or switched by molecules.[8]

In addition to the development of surfaces that can execute defined functions, placing molecules on a substrate may be an essential step in the development of future *single-molecule applications*. The interaction of molecules with a substrate can be utilized to immobilize them – a prerequisite for exploring and addressing molecules *individually*. Although the development of single-molecule applications still appears to be a long-term goal, there are several proof-of-principle studies. *Artificial molecular machines*, in which a molecular component is capable of quasi-mechanical movements in response to specific energy stimuli, have, *e. g.*, been successful operated at the single-molecule level.[9–11]

In particular, the concept of using single or few molecules as *electronic components* has attracted huge research efforts in recent years.[12–19] Such miniaturization is the ultimate goal for shrinking electrical circuits and devices, as single molecules (and atoms) constitute the smallest stable structures possible. In addition, there are possible applications of single molecules in the field of *spintronics* (spin transport electronics),[20–22] which exploits –in addition to charges– *spin* as further degree of freedom to store, transport, and compute data. In this context, spin-crossover molecules are particularly interesting since they provide a spin-switching functionality that can be addressed by external stimuli.[23]

The main motivations to go beyond conventional electronics[13–19] and spintronics[24–35] are new properties emerging at the metal/molecule interfaces and functions such as switching that are incorporated within the molecules themselves. The integration of molecular circuits into conventional electrical circuits will require techniques that establish *metal-molecule contacts* that are reliable, stable in time, and enable nondestructive control and operation of the circuit –at least under ideal conditions such as cryogenic temperatures and ultra-high vacuum. Such techniques appear to be still a long sought-after goal.[19]

A major difficulty for functional molecules on surfaces is the lack of stability of molecular properties and functionalities against adsorption to substrates. The molecule-substrate and/or on-surface molecule-molecule interactions often degrade or even disable the desired molecular functionality or property. This situation can have various reasons such as *surface-induced* (i) fragmentation and other chemical reactions, (ii) structural deformation, (iii) immobilization of important molecular subunits , and (iv) changes of the electronic structure of the molecule. Similarly, the on-surface molecule-molecule interaction can have an undesired impact by, *e. g.*, packing molecules into clusters that sterically hinder a molecular function.

To solve the above-mentioned problems a *special design* of molecules (for a given substrate) is required. Chemical anchor groups comprising a molecular subunit or a single atom attached to the molecule of interest have been used to achieve well-defined molecule-substrate interfaces.[14–17,36–39] Of special interest are platform-like anchor groups because they enable *geometric decoupling* of a target molecule from a substrate and from neighboring molecules.[40,41] This decoupling is achieved by placing the target molecule in a freestanding and upright (or inclined) position on the substrate. In addition, the minimal lateral spacing between adjacent molecules is set by (i) the extended lateral size of the platform anchors and (ii) the on-surface interaction of the anchors. Using such platforms, molecular motors, rotors, and switches have been successfully placed and operated on flat substrates.[41] Usually, the platforms are fixed to a substrate via reactive atoms that form chemical bonds to the substrate. However, bond formation tends to induce significant electronic changes of the sample-molecule complex and may render difficult the desired preservation of the functionalities and properties of the attached molecule.[16,17,38–43]

In this thesis, a class of molecules is explored that rely on a *different* anchoring scheme. It is designed to leave the properties of the functional molecular subunit almost unaffected upon adsorption by avoiding strong hybridization of the molecular states with those of the substrate. This is achieved by using the planar trioxatriangulenium (TOTA) platform molecule that binds to metal substrates via *physisorption.* In contrast to the similar triazatriangulenium (TATA) platform that also binds via physisorption,[42,44,45] TOTA derivatives may be sublimated intact, and thus enables systematic investigations in ultrahigh vacuum (UHV). In this study the conductance, switching, self-assembly, and stability of TOTA derivatives were investigated, as detailed in the next Chapters.

Another approach to retain molecular properties and functionalities is to modify the substrate's properties and by this change the molecule-substrate interactions. Because of their possible application in molecular electronics and other fields of science, metal substrates are of particular interest. However, the attachment of molecules to metals without drastically changing the molecule's properties is challenging, as the coupling of the molecule to the metal's electron gas tends to considerably affect the molecule's electronic structure. To prevent such an undesired effect the metal can be covered by a thin insulating film.[46–50] Such a film reduces the electronic coupling of the molecule to the metal. The success of this approach was, *e. g.*, demonstrated by imaging molecular orbitals similar to those of the gas-phase molecule.[47] In this work single-layer nitrogen islands on Cu(001), known as $Cu_2N/Cu(001)$, are exploited as decoupling film to efficiently switch a $Fe^{III}$ spin-crossover (SCO) complex, namely $[Fe(pap)_2]^+$ (pap=N-2-pyridylmethylidene-2-hydroxyphenylaminato).

# 2

# Overview

A scanning tunneling microscope (STM) operated in ultrahigh vacuum at 4.6 K was used to explore molecules on conducting substrates. The aim of this work is to contribute to the fundamental understanding of functionalities and properties of such hybrid systems.

The following summarizes the contents of the chapters in chronological order and highlights some aspects of the work.

Sections 2.1–2.3 gives an overview regarding applications of STM in molecular science and the molecules studied in this thesis.

**Part I** introduces the experimental techniques and fundamentals helpful for understanding the presented results. In addition, the experimental setup is described and information about tip preparation and molecule deposition is given. To achieve a high level of understanding, experimental results were partly reproduced with the help of density functional theory (DFT), nonequilibrium Green's function (NEGF), and/or force field calculations. The second Chapter of Part I briefly describes these techniques and introduces important terms of the so-called scattering picture of electron transport.

**Part II** reports the electric conductance of single functionalized trioxatriangulenium (TOTA) platform molecules. To measure the electrical conductance of a molecule two contacts are required. In an STM a metal sample and the tip of the microscope serve as electrodes and are used to electrically contact a molecule. In contrast to simple molecules the TOTA platform enables placing functional molecules in a freestanding and upright position on a metal as verified by STM imaging. Because of the characterization of junction geometries and picometer control of the electrodes, little statistics are required to obtain high quality conductance data. This is a significant advantage over other methods such as the break-junction technique, in which a characterization of the junction geometries is usually not possible or missing.[51–53] Moreover, the characterization of the junction geometry simplifies a very detailed analysis of the data. Thus, this thesis includes "prime example[s]" of experiments designed for close comparison with theory to achieve a high-level understanding of electron transport in molecular junctions, as it was highlighted in a review article.[54]

Chapter 5 reports on the conductance of one of the shortest possible molecule wires, namely a propynyl moiety, attached to the TOTA platform. Despite this reductionist approach, conductance data of propynyl–TOTA turned out to be complex. Calculations show that an interplay of geometrical changes, orbital symmetries, and bond formation in the electrode-molecule-electrode junction control the conductance.

Chapter 6 is devoted to electric contacts that are purely mechanical, *i. e.* no reactive atom is contacted and consequently no chemical bond between the molecule and the electrodes is formed. To keep this approach as simple as possible the smallest possible inert and rigid moieties, namely a hydrogen atom and a methyl group, were used to passivate the reactive center of the TOTA platform. The unusual anchoring via an extended *physisorbed* platform is designed to leave the properties of the functional molecular subunit almost unaffected upon adsorption. Therefore, this anchoring scheme may simplify the design of a molecule that will deliver specific electron transport properties. The conductance evolutions of the inert molecules turn out to exhibit features similar to those related to chemical bond formation in other systems. Hence, mechanical contacts may be misinterpreted as contacts with bond formation, if solely the conductance data is considered. Moreover, the study shows that TOTA is a high-conductance anchor group due to the electrical coupling of its *extended* $\pi$-system with the metal.

**Part III** covers switching, self-assembly, and stability of functionalized TOTA platforms on gold or silver substrates.

Chapter 7 reports on two closely related molecular stepper motors that were designed to work on a metal substrate under excitation with tunneling electrons. The motors are comprised of the TOTA platform as a stator and ethoxy and ethyl moieties as rotors. Current-induced rotation of the moieties is demonstrated and traced back to single-electron processes involving excitation of vibrational modes by measurement of microscopic switching rates and yields. The STM tip was used to generate directionality of the motion, modification of the directionality by adjacent charged adsorbates was revealed, microscopic reaction yields were determined, and single-electron processes induced via excitation of vibrational modes were evidenced. By means of DFT calculations for the two related molecules, the results show how the energies and displacement patterns of the vibrational modes, along with the energy barriers towards rotation, can lead to several orders of magnitude variation of the reaction yield. This investigation may turn out useful for designing platforms that provide directional rotation and for transferring more sophisticated molecular machines from the gas-phase to surfaces.

Chapter 8 sheds light into the self-assembly of methyl-TOTA molecules on silver. Honeycomb superstructures with unusual large unit cells comprising almost 3000 molecules were obtained by increasing the molecular coverage. A fairly general model was developed that describes the energetics of honeycomb superstructures built from $C_3$ symmetric units. Based on three parameters that characterize two competing bonding arrangements, the model is consistent with the presented experimental data and also reproduces various published results. The model identifies the relevant driving force, mostly related to geometric aspects, of the pattern formation. In turn, the model may be employed to guide the design of molecules for building mesoscopic superstructures.

Chapter 9 deals with the stability of TOTA derivatives on gold. Depending on the functional groups attached to the TOTA molecules, varying degrees of fragmentation were observed. Intriguingly, the observed tendency towards fragmentation is opposite to the sequence of gas-phase stabilities of the molecules used. Calculations show that the binding energies of the decomposition products to the Au surface destabilize the bond between the functional moieties and the platform by several electronvolts and essentially determine the molecular stability. Hence, the Au(111) surface is not inert enough for the stability of some of the platform molecules.

**Part IV** presents results regarding a charged spin-crossover (SCO) complex, namely $[\mathrm{Fe(pap)_2}]^+$ (pap=N-2-pyridylmethylidene-2-hydroxyphenylaminato).

In Chapter 10 a successful deposition of a charged $\mathrm{Fe^{III}}$ SCO complex on a gold substrate is evidenced. The bulk form of the molecules is stabilized by a perchlorate counter ion, which depending on the deposition technique, may affect the quality of the deposition and the measurements. Moreover, the results show for the first time that it is possible to sublimate *charged* SCO complexes (as highlighted in a review article).[55]

Finally, in Chapter 11 the switching of $[\mathrm{Fe(pap)_2}]^+$ is studied. Interaction with a substrate tends to fragment SCO complexes or disable their switching function. Accordingly, on a gold substrate efficient switching was not observed. Motivated by previous SCO experiments, the molecule was placed on an insulating single-layer island on copper. On this substrate, the $\mathrm{Fe(pap)_2}$ complex could be efficiently switched with a rather high rate. As a proof of concept, the reversible and selective nature of the switching is used to build a two-molecule memory. Moreover, the deposited $\mathrm{Fe^{III}}$ spin-crossover compound is switched between *three* different states rather than the expected two spin states. With the help of gas-phase DFT calculations it is inferred that the molecule is not only switched between different spin states but also between different couplings to the substrate. This represents the first report of combined intrinsic (spin transition) and extrinsic (different coupling to the substrate) switching of a SCO compound on a surface.

This thesis is based on **publications in peer-reviewed journals** as indicated in each chapter. A summary is given here:

- Torben Jasper-Toennies, Aran Garcia-Lekue, Thomas Frederiksen, Sandra Ulrich, Rainer Herges, and Richard Berndt.

  *Conductance of a Freestanding Conjugated Molecular Wire*

  Phys. Rev. Lett. **119**, 066801 (2017), *Editors' Suggestion*

- Torben Jasper-Tönnies, Aran Garcia-Lekue, Thomas Frederiksen, Sandra Ulrich, Rainer Herges, and Richard Berndt.

  *High-conductance contacts to functionalized molecular platforms physisorbed on Au(111)*

  J. Phys.: Condens. Matter **31**, 18LT01 (2019)

- Torben Jasper-Tönnies, Manuel Gruber, Sven Johannsen, Thomas Frederiksen, Aran Garcia-Lekue, Torben Jäkel, Fynn Röhricht, Rainer Herges, and Richard Berndt.

  *Rotation of Ethoxy and Ethyl Moieties on a Molecular Platform on Au(111)*

  ACS Nano **14**, 3907 (2020)

- Torben Jasper-Tönnies, Manuel Gruber, Sandra Ulrich, Rainer Herges, and Richard Berndt.

  *Coverage-Controlled Superstructures of $C_3$ Symmetric Molecules: Honeycomb versus Hexagonal Tiling*

  Angew. Chem. Int. Ed. **59**, 7008 (2020), *Frontispiece of issue 18*

- Torben Jasper-Tönnies, Igor Poltavsky, Sandra Ulrich, Tobias Moje, Alexandre Tkatchenko, Rainer Herges, and Richard Bernd

  *Stability of functionalized platform molecules on Au(111)*

  J. Chem. Phys. **149**, 244705 (2018), *Editor's Pick*

- Torben Jasper-Tönnies, Manuel Gruber, Sujoy Karan, Hanne Jacob, Felix Tuczek, and Richard Bernd.

  *Deposition of a Cationic $Fe^{III}$ Spin-Crossover Complex on Au(111): Impact of the Counter Ion*

  J. Phys. Chem. Lett. **8**, 1569 (2017)

- Torben Jasper-Toennies, Manuel Gruber, Sujoy Karan, Hanne Jacob, Felix Tuczek, and Richard Berndt

  *Robust and Selective Switching of an $Fe^{III}$Spin-Crossover Compound on $Cu_2N$/Cu(100) with Memristance Behavior*

  Nano Lett. **17**, 6613 (2017)

## 2.1. Scanning tunneling microscopy and molecules

The scanning tunneling microscope (STM) is one of the most important tools in surface-based nanoscience.[56,II] It enables the exploration of molecules at the *single-molecule* level.[58] The molecules of interest have to be *adsorbed* on a conducting substrate. The atomically sharp metal tip of an STM is *scanned* over a substrate, while simultaneously measuring the *tunneling* current between the tip and the sample. This procedure enables to image molecules and surfaces at an extremely small scale – down to individual atoms. A more detailed description of the working principle of an STM is given in Chapter 3.

Nowadays, the STM enables various applications in the field of molecular science:

- **Adsorption geometry and molecular assembly**.[5,59,60] The ability to image samples with atomic resolution makes it possible to identify adsorption geometries (Parts II–IV). Additionally, molecular self-assembly and related on-surface intermolecular interactions can be explored (Chap. 8).
- **Electronic structure**. STM is particularly suited to probe electronic properties of individual molecules at the sub-molecular level. Spectroscopic measurements are used to determine the energies of occupied and unoccupied molecular orbitals (Chap. 9). Furthermore, iso-densities of molecular orbitals can be inferred from

---

[II] This Section is based on a Section of Reference 57.

particular topographic measurements.[47,61] With a recently developed setup, quantum motion of molecules can even be probed at the femtosecond-scale.[50]

- **Conductance**.[62–64] By contacting single molecules with an STM tip, metal-molecule-metal junctions can be prepared and their conductance measured. Atomic-scale imaging prior and after recording the conductance data allows to control the junction geometry and renders the quality of data superior to those obtained with other methods (Part II).
- **Magnetic properties**.[65–67] The spin state of individual molecules can be inferred by taking advantage of the Kondo effect[68–73] or spin excitations[46,74] or from spin-polarized STM (SP-STM).[75] Moreover, the utilization of magnetic tips in SP-STM allows spin-resolved imaging.
- **Manipulation**.
  - **Nanopatterning**.[60,76,77] STM is capable of manipulating objects, like single atoms and molecules. To obtain artificial nanostructures tip-induced manipulation can be used to modify local arrangements of adsorbed molecules in a controlled manner.
  - **Switching**.[78] Conformational changes can be induced by an STM tip. As a proof-of concept single molecular multi-state switches (Chap. 11) and artificial molecular machines such as rotors (Chap. 7) were successfully operated with an STM tip.
  - **Chemical reactions**.[79,80] By using an STM tip, it has become possible to perform elementary chemical reaction steps, such as dissociation, diffusion, and bond-formation processes (Chap. 5).
- **Vibrational structure**.[81,82] Spectroscopic measurements are used to determine the energies of vibrational modes and to identify their involvement in manipulation processes (Chap. 7).

STM may be used in combination with atomic force microscopy (AFM)[83,84] which allows to obtain additional information about molecular properties via force measurements.

## 2.2. Functionalized platform molecules

Following a reductionist approach, small functional moieties were attached to the trioxatriangulenium (TOTA) platform and explored in this thesis (Fig. 2.1).[III] The bare TOTA platform is an aromatic cation in the gas phase and all its electrons are paired (Fig. 2.1a). TOTA is planar and evolves to a bowl shape when a functional unit is binding to its central carbon atom (Fig. 2.1b–g). The TOTA platform and the related compound tri-

---

[III] Functionalized molecules do not have to provide a functionality such as switching. In chemistry, an organic compounds is *functionalized* by adding a *functional group* to it.[85] A functional group is the part of a molecule that gives its particular reactivity. In other words, simple molecules that contain the same functional group in their structures can be expected to *react* in similar ways. In fact, names of organic molecules are a systematic reference to the functional groups within the molecules, and can thus be used to identify these.

azatriangulenium (TATA)[IV] are very versatile and an attached functional unit may be exchanged for other moieties of interest. This has been demonstrated for porphyrins, diazocine, norbornadiene, imine, and azobenzene derivatives.[42,86–92] In contrast to the TATA platform,[42,44,45] TOTA may be sublimated intact, and thus enables systematic investigations in ultrahigh vacuum (UHV). As a consequence, TOTA derivatives were solely studied in this work (Fig. 2.1).

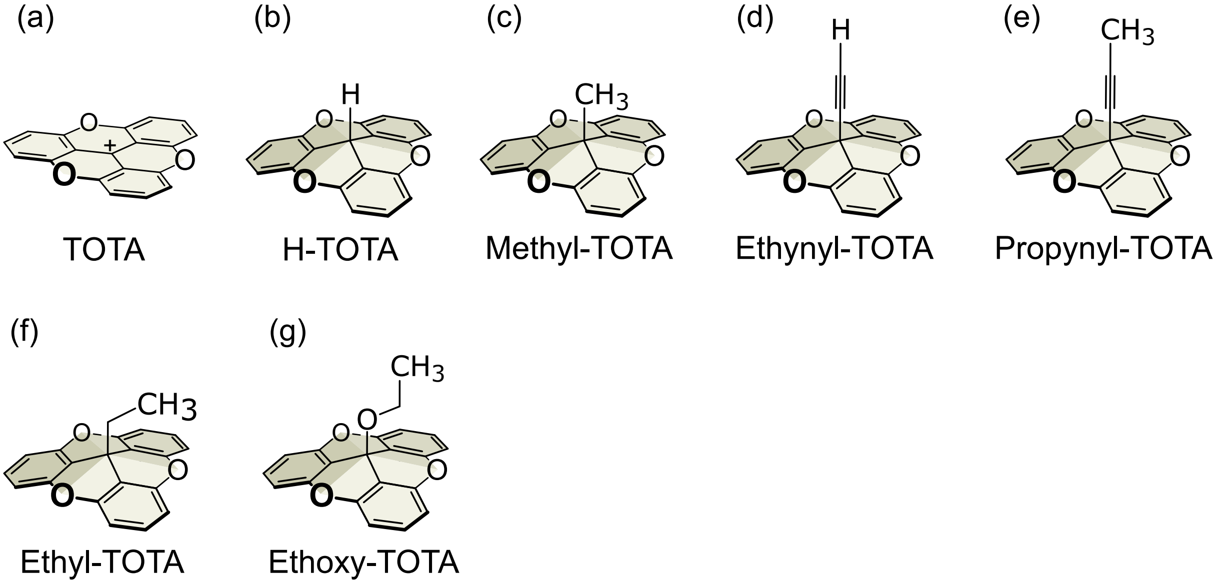

Figure 2.1.: (a–g) Lewis structures of trioxatriangulenium (TOTA), H–TOTA, methyl–TOTA, ethynyl–TOTA, propynyl–TOTA, ethyl-TOTA, and ethoxy-TOTA, respectively.

### 2.2.1. Related results

Prior and parallel to this work, functionalized TATA platforms have been explored with STM and other methods at *ambient conditions* in *air* or *electrochemical environments*.[42,86–102] Molecules were deposited from solution to samples such as gold and quartz. As intended by the involved research groups from Kiel, these studies cover chemical and physical conditions (air or solution and ambient temperature) distinct to those exploited in this work (cryogenic temperatures and UHV). For TATA derivatives on gold in air or solution and at ambient temperature various studies were published.[42,86–102] For instance, the formation of ordered monolayers[87] and their control via side chains attached to the platform,[97] a drastic acceleration of the thermochemical *cis* to *trans* isomerization of azobenzene derivatives,[92] and a design to place molecular switches and altitudinal rotors in a parallel position onto a substrate[91] were reported.

In addition to TOTA and TATA platforms, a few other (often multidentate) platform molecules were used to place functional molecules on substrates in a defined position.[40,41] For a review the reader is referred to the literature.[40,41]

---

[IV] TOTA is transformed to TATA by replacing its oxygen atoms with nitrogen atoms (cf. Fig. 2.1a).

## 2.3. Spin-crossover molecules

Spin-crossover (SCO) is a switching phenomenon between two molecular states that are characterized by a high-spin (HS) or a low-spin (LS) electronic configuration.[V] In principle, it can occur in a transition metal center of a coordination compound under the influence of external perturbation such as a change in temperature, optical excitation, change of electric field, current, and/or change of pressure.[103] For a given coordination symmetry of the metal ion, this occurrence is controlled by the relationship between the strength of the ligand (the electrostatic field acting at the central metal ion) and the mean spin-pairing energy. The ion may be either in HS or LS state, depending on whether the ligand field strength is weaker or stronger, respectively, than the spin pairing energy.

The change of spin state is accompanied by a drastic change of the properties of the substance. Most noticeable is the reversible change of magnetic behavior and color.[23] The spin-switching, which occurs for some compounds at or around ambient temperature, makes SCO complexes promising candidates for the realization of molecule-based electronic and spintronic components such as switching or memory elements.[23,104]

In this thesis, charged $\mathrm{Fe^{III}}$ SCO molecules were investigated (Fig. 2.2a). The spin states of such a compound are described in the following. Figure 2.2b is a simplified illustration of the $d$ orbital configuration of an $\mathrm{Fe^{III}}$ ion in the presence of an octahedral ligand field. The octahedral symmetry breaks the degeneracy of the metal ion's $d$ orbitals and splits them into two subsets with an energy difference $\Delta_{\mathrm{HS}}$. If $\Delta_{\mathrm{HS}}$ is smaller than the spin pairing energy, the $d$ states are filled according to Hund's rules, resulting in five unpaired electrons and a HS state with $S = 5/2$ (Fig. 2.2b). Otherwise, the electrons fill the lower energy orbitals completely leading to the LS state with $S = 1/2$.

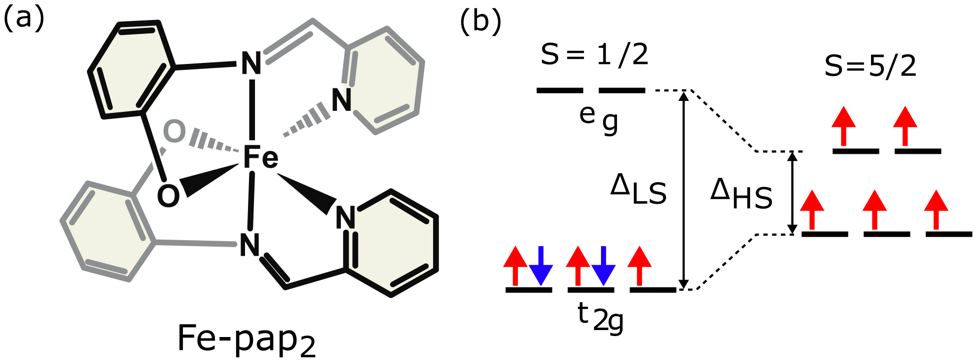

Figure 2.2.: (a) Lewis structures of a spin-crossover (SCO) complex with an octahedral ligand coordination of an $\mathrm{Fe^{III}}$ ion. The shown $[\mathrm{Fe(pap)_2}]^+$ (pap=N-2-pyridylmethylidene-2-hydroxyphenylaminato) molecule[105] is positively charged. Results regarding this molecule are reported in Part IV. (b) Simplified electronic configuration of the five $d$ electrons of an $\mathrm{Fe^{III}}$ ion in an octahedral ligand field. In the LS (HS) state, the electrons occupy the $t_{2g}$ ($t_{2g}$ and $e_g$) $d$ orbitals leading to a total spin $S = 1/2$ ($S = 5/2$).[VI]

A transition between HS to LS goes hand in hand with a geometry change of a SCO complex. During a HS to LS (LS to HS) transition, the metal-to-ligand bond distances

---

[V] The rudimentary introduction of SCO given here essentially follows that given in Reference 57.

[VI] The labels, $t_{2g}$ and $e_g$, indicate orbital symmetries.[106] The energy levels of the $d$ orbitals split in an octahedral ligand field depending on the oribtal's symmetry, as indicated in Figure 2.2b.

are decreased (increased) and the molecule's volume is reduced (increased). The change of the bond length is usually in the range 0.1 – 0.2 Å.[103] As expected from the smaller metal-to-ligand bond distances, the LS state is usually the ground state of the gas-phase molecule.

In contrast to the study of SCO in bulk or in solution, the investigation of SCO complexes on surfaces at the single-molecule level is a rather new field of science.[23] Unfortunately, the interaction with a surface acts on the metastable balance of the spin states and often results in a quenching of the SCO transition. Hence, an important milestone is the reversible switching of single SCO molecules on a molecular monolayer[107] and in direct contact to an insulating film[108] on a metal by an STM. The spin state of the molecules could be determined by structural and electronic changes.[107,108]

# Part I.

# Experimental and Theoretical Techniques and Fundamentals

# 3

# Scanning Tunneling Microscopy and Setup

The scanning tunneling microscope (STM) was developed in 1981 by Binnig and Rohrer,[109,110] who received the Nobel prize in physics for its invention five years later. An STM allows to image and measure electronic structures of (semi-)conducting solid surfaces at the *atomic* level in air, liquid or vacuum environment.[VII] In this thesis, single molecules on metal substrates were explored with an STM operated in ultra-high vacuum and at a cryogenic temperature of 4.7 K. (Below an operation in vacuum is assumed.)

The measurement principle of STM is based on the quantum-mechanical tunneling effect. This effect allows electrons to pass a potential barrier –such as a vacuum gap between two electrodes– although their energy is (classically) not sufficient to overcome it. To probe a sample surface, an atomically sharp metal tip is brought at a few-angstrom distance, making electrons to tunnel across the gap owing to an overlap of tip and sample electronic wave functions. Applying a voltage between the tip and the sample, *i. e.* across the tunnel contact, results in a net *tunneling current.* This tunneling current is extremely sensitive to the tip-sample distance. It decreases exponentially with increasing tip-sample distance. Because of the exponential relation, STM can reach picometer resolution.

Control over the tip position is reached with the help of a $xyz$ piezoelectric scanner (Fig. 3.1a). A topograph of a sample is recorded by *scanning* with the tip a predefined grid on the sample in a line-by-line way and simultaneously probing the *tunneling current.* There are two imaging modes that are briefly described below.

## 3.1. Constant-height and constant-current topographs

In *constant-height* mode a current map is recorded, while the $z$ position of the tip is kept constant, *i. e.* the feedback of the $z$-piezo is off (Fig. 3.1a). In this mode the roughness of the sample must be known to avoid crashing the tip into the sample. There are two main factors that lead to high currents, (i) a short tip-sample distance and (ii) a higher amount of electronic states that are involved in the transport of electrons through the junction.

---

[VII] This chapter gives a rudimentary description of STM imaging and differential-conductance spectroscopy and may help to understand this work. A more comprehensive description of the topic can be found in text books.[111,112]

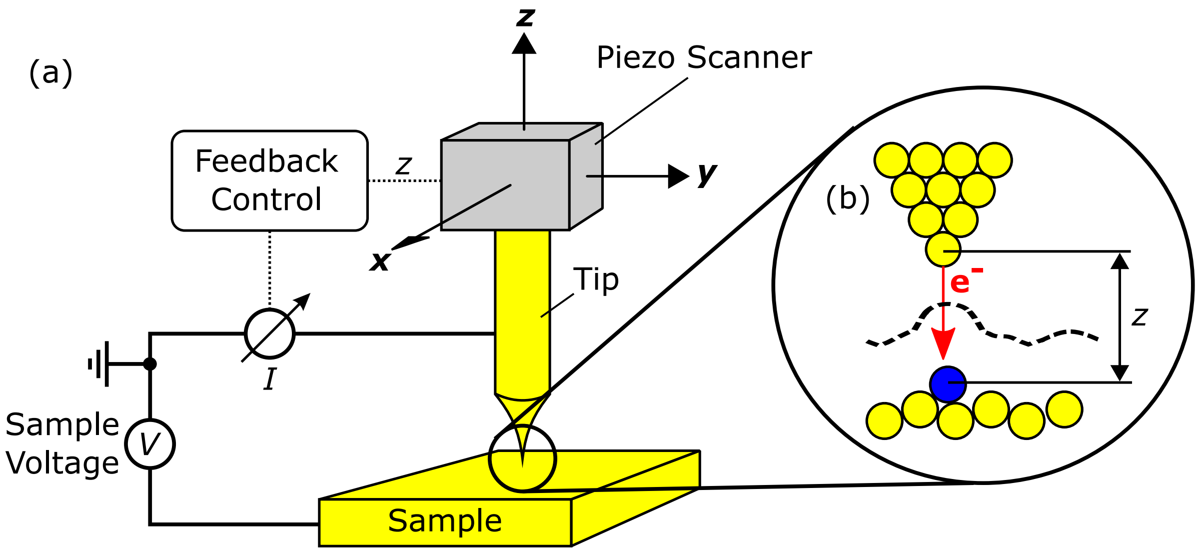

Figure 3.1.: (a) Sketch of the working principle of a scanning tunneling microscope (STM). The tip is scanned in the $x$-$y$ plane above the surface, while a sample voltage $V$ is applied between the tip and the surface. There are two scanning modes. In constant-height mode the $z$ position of the tip is kept constant (feedback off) and the current $I$ between the tip and the sample is recorded. In constant-current mode the feedback is on and regulates the $z$-piezo to keep the current $I$ constant. (b) Sketch of an apparent height profile (dashed line) recorded in the constant-current mode. A positive sample voltage is applied, *i. e.* electrons are injected into the sample (red arrow). The atoms of the tip and surface are indicated as yellow circles. The apparent height profile (dashed line) corresponds to the $\Delta z$ displacements of the tip to keep the current constant. The small corrugation above the bare substrate indicates atomic resolution of the substrate. An adsorbate atom (blue circle) is imaged as a high protrusion in the profile.

Constant-height topographs are highly valuable to investigate parts of the sample that fulfill these conditions.

In constant-current mode a feedback controller regulates the $z$-piezo to keep the current $I$ constant at a value predefined by the experimentalist (Fig. 3.1a). While the sample is scanned in the $x$-$y$ plane above the surface, the $\Delta z$ displacements of the tip are recorded (Fig. 3.1b). The resulting constant-current topograph $\Delta z(x, y)$ shows *apparent heights* and *apparent lateral sizes* of surface structures and usually resolve single adatoms and submolecular details of adsorbed molecules (Fig. 3.1b). Typical tunneling currents are in the pico-ampere to micro-ampere range. Almost all STM topographs presented in this work were acquired in this mode.

### 3.1.1. Apparent height and apparent lateral size

The *apparent* heights $\Delta z(x, y)$ and lateral sizes of patterns in an STM topograph can deviate from the related sample geometry because they are measured via tunneling *currents*. In fact, they map the current-carrying part of the *electronic* structure of the surface and the tip. Thus, they are controlled by the surface geometry and/or *electronic effects*. Therefore, the interpretation of STM images can be challenging.

The apparent height and lateral size are related to the overlap of the sample's electronic states with those of the tip. As a consequence, an STM pattern usually appears *laterally larger* than the related geometric structure. Because of the exponential relation between the tip-sample distance and tunneling current, electrons mainly flow through the apex atom of the tip (cf. Fig. 3.1b).[111,112] Motivated by this fact and using the Bardeen approach to tunneling, Tersoff and Hamann[113,114] developed a model providing a description of STM topographs for low sample voltages. A rudimentary description of the model is given below.

#### 3.1.1.1. Bardeen approach and Tersoff-Hamann model

Depending on the applied sample voltage $V$, and the temperature $T$, the Bardeen approach[115] estimates for the tunneling current[111,116]

$$I \propto \int_{-\infty}^{\infty} [f_{FD}(E-eV,T) - f_{FD}(E,T)]\; D_t(E-eV)\; D_s(E)\; |M(E-eV,E)|^2\, dE, \tag{3.1}$$

where $f_{FD}$ is the Fermi-Dirac distribution[VIII], $e$ is the elementary charge, $D_t$ and $D_s$ are the *densities of states* (DOS) of tip and sample, respectively. $M$ in Equation 3.1 is the Bardeen tunneling matrix element,[111,115] which describes the overlap of the tip wave functions with the sample wave functions. The dependence of the tunnel current on the tip-sample distance is inherent in $M$. As seen from Equation 3.1, the tunneling current additionally depends on the tip and surface DOS.

In the Tersoff-Hamann model the electronic structure of the STM tip is locally approximated by a spherical $s$-like orbital wave function centered at the tip apex at position $\vec{r}_t$. Using this approximation, the Bardeen tunneling matrix element $M$ can be evaluated and equation 3.1 simplifies to

$$I \propto \int_{-\infty}^{\infty} [f_{FD}(E-eV,T) - f_{FD}(E,T)]\; D_t(E-eV,T)\; \rho_s(\vec{r}_t,E)\, dE, \tag{3.2}$$

where

$$\rho_s(\vec{r}_t,E) = \sum_{\nu} |\psi_{s,\nu}(\vec{r}_t)|^2\, \delta(E_{s,\nu} - E), \tag{3.3}$$

denotes the *local density of states* (LDOS) of the sample at the position $r_t$.[IX] Thus, the model predicts that the tunneling current essentially probes the LDOS $\rho_s$ of the sample at the position $\vec{r}_t$ of the tip apex. At sample voltages $V$ and temperatures $T$ close to zero Equation 3.2 approximately reads

$$I \propto \rho_S(\vec{r}_t,0)\; V, \tag{3.4}$$

where $\rho_S(\vec{r}_t,0)$ corresponds to the sample LDOS at the Fermi energy ($E_F$) at location $\vec{r}_t$.[X] Thus, the Tersoff-Hamann approximation gives a simple picture of the apparent heights in

---

[VIII] The factor $[f_{FD}(E-eV,T) - f_{FD}(E,T)]$ takes the temperature broading into account. If $k_BT$ is much smaller than the energy resolution required in the measurement, then $f_{FD}$ can be approximated by a step function, *i. e.* $I(V,T) \propto \int_0^{eV} D_t(E-eV)\; D_s(E)\; |M|^2\, dE$.

[IX] The sum in Equation 3.3 extends over all electronic state of the sample system. $\psi_{s,\nu}$ is the wave function and $E_{s,\nu}$ the energy of the sample state $\nu$.

[X] (i) Zero sample voltage corresponds to the Fermi energy of the tip-sample system. (ii) The above-a constant-current topograph. The tip follows a *contour of constant sample LDOS* taken at the position $\vec{r}_t$ of the tip apex.

It is worth mentioning that the Tersoff-Hamann model can be extended to apex atoms whose electronic structure considerably deviates from $s$-like shape via a generalization to arbitrary orbital symmetries.[117,118]

The Tersoff-Hamann approximation can give *qualitatively* correct apparent height differences and is therefore useful for the interpretation of topographs.[119] For instance, patterns of adsorbate structures induced by oxygen adsorption on Ti(0001) facets on Si(111) were observed to change from protrusions to depressions depending on the applied sample voltage.[120] This bias dependence can be interpreted in terms of local increase (imaged as protrusion) or decrease (recorded as depression) of the integrated LDOS of the sample (cf. Eq. 3.2).

In this thesis, more than 50 % lower apparent heights than those naively expected from geometric heights were recorded for trioxatriangulenium (TOTA) derivatives on Au(111). For instance, propynyl-TOTA molecules on Au(111) exhibit at tunneling current of 30 pA and a sample voltage of 100 mV a maximum apparent height of only ≈ 3.2 Å (Figs. 3.2a and b), although the molecular structure and expected adsorption height gives a geometric height of ≈ 8.6 Å (Fig. 3.2d).

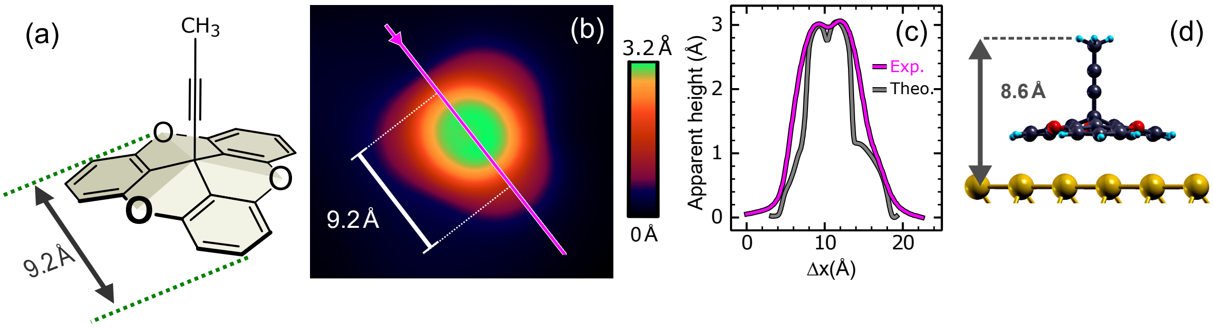

Figure 3.2.: (a) Molecular structure of propynyl-trioxatriangulenium (P-TOTA) (b) Constant-current topograph of P-TOTA (100 mV, 30 pA). The bare Au surface appears dark ($\Delta z = 0$ Å). The TOTA platform is recorded as a low triangular protrusion ($\Delta z \lesssim 1.6$ Å), while the propynyl moiety is imaged as a central, circular protrusion ($\Delta z \approx 3.2$ Å). The lateral distance $d(O,\ H)$ of the outer O and H atoms along the molecule's symmetry plane (projected on a plane perpendicular to the propynyl wire) is 9.2 Å [see scale in (a)]. In (b), a scale of 9.2 Å is inserted. As expected and discussed in the text, it is smaller than the apparent size. (c) Experimental apparent height profile along the magenta line indicated in (b) and the corresponding theoretical profile scaled by an arbitrary factor of 0.5. The theoretical profile was calculated with the help of the Tersoff-Hamann approximation and density functional theory (Details in Chap. 5). It reveals that the shallow minimum at the molecular center is due to the topmost H atoms of the propynyl moiety [see (d)]. (d) Side view of the adsorption geometry of P-TOTA on Au(111) calculated with density functional theory (Details in Chap. 5). Yellow, black, red, and blue spheres correspond to Au, C, O, and H atoms, respectively.

Using the Tersoff-Hamann approximation and density functional theory (DFT) calculations the molecule's STM pattern can be qualitatively reproduced (cf. Fig. 3.2c). This

---

mentioned exponential relation between the tip-sample distance and tunneling current is obtained from the exponential decay of the sample LDOS $\rho_s$ into the tunneling gap.[111,112]

qualitative agreement suggests that the apparent height of the molecule is, as expected, related to the LDOS change of the sample induced by the molecule. The adsorbed molecule drastically increases the vacuum LDOS of the sample, which results in a ≈ 3.2 Å higher apparent height at the molecule's center.[XI] Nonetheless, this apparent height is lower than naively expected from the reduction of the tip-sample gap caused by the molecule (Fig. 3.2d). Thus, the maximum apparent heights of TOTA derivatives are dominated by electronic effects.

Owing to approximations the accuracy of the Tersoff-Hamann model is limited. For instance, it cannot explain experimental observations that are due to inelastic tunneling or a significantly varying tip LDOS.

## 3.2. Differential conductance spectroscopy

In addition to topographs an STM allows to spectroscopically study a sample at the atomic scale.[111,112] For constant-height differential conductance or scanning tunneling spectroscopy (STS) a voltage ramp is applied to the tip-sample junction, while the tip position is kept constant and the current is measured for each voltage. The $dI/dV$ signal is obtained by lock-in technique to improve the signal-to-noise ratio. For elastically tunneling electrons the $dI/dV(V)$ data is related to the sample and tip LDOS (cf. Eq. 3.1).[111,112,121] In this thesis, $dI/dV$ spectra are used to identify electronic states of adsorbed molecules.

In addition to elastic processes, the $dI/dV$ signal is sensitive to inelastic processes, *i. e.* it can detect excitations such as spin excitations[46] or vibrational excitations.[81,82]

The features in the $dI/dV(V)$ data are broadened due to temperature and the lock-in modulation amplitude.[122,123] This broadening can be neglected for $dI/dV$ features that are neither narrow nor small (as those presented in this work).

The constant-height $dI/dV$ signal at fixed voltage can be mapped over a surface while scanning. In other words, a $dI/dV$ map can be recorded. The map provides atomic scale information on the spatial distribution of $dI/dV$ features (at constant height) and a specific energy (given by the sample voltage) (cf. Fig. 6.6b, Sec. 6.7.1).[47,124,125]

It is worth mentioning, that the spatial mapping of a $dI/dV$ signal was recently expanded to iso-$dI/dV$ maps.[61] This imaging technique consists in scanning the tip across the surface while keeping the $dI/dV$ signal constant (instead of the current) and recording changes of the tip-sample distance. It enables direct visualization of density of states (DOS) *isosurfaces*, independently of the corrugation of the sample. Thus, this technique may be especially useful for the investigation of non-planar, three-dimensional molecules on substrates.

---

[XI] At fixed tip position centered above the molecule the tunneling current would reduce by a factor of ≈ $10^{2.9}$ ≈ 900 when the molecule would be removed and electrons directly tunnel into the bare substrate.

## 3.3. Action spectroscopy

Tunneling electrons from the tip of an STM can be used as an atomic-scale source for electronic[126] and vibrational[127–129] excitations and to manipulate individual atoms and molecules on substrates in a controlled manner. In this work molecules were controllably switched by electron injection at suitable parameters and positions (Chaps. 7 and 11). A detailed analysis of switching with respect of tunneling current, sample voltage, and injection point can reveal a microscopic insight into the underlying switching *process* (Chap. 7).

For a given single-adsorbate reaction and a fixed tip position, the reaction *rate* $R(I)$, *i. e.* the number of reaction events per time, as function of tunneling current $I$ can be measured. These measurements reveal the reaction order, *i. e.* how many electrons are required to induce a single reaction event.[127,130,131,XII]

As tunneling electrons at a sample voltage $V$ exhibit an energy equal to or lower than $eV$, a single electron can only excite processes that require energies $\leq eV$. The reaction *yield* $Y = R/(I/e)$ [$e$: elementary charge], *i. e.* number of reaction events per tunneling electron, characterizes the probability per tunneling electron to induce a reaction. The yield $Y(V)$ (for constant tunneling current) measured as function of the sample voltage $V$ is called *action spectroscopy.*[XIII] It may reveal energy thresholds for inducing a given reaction. These thresholds may allow to identify vibrational and/or electronic states responsible for inducing the reaction of interest. Further details regarding the expected action spectrum of vibrational induced reactions[130,131] are given in Chapter 7.

## 3.4. Conductance curves

### 3.4.1. Measurement

To measure the electric conductance of a single molecule or atom two contacts are required. In an STM a metal sample and the tip serve this purpose. To establish a contact between the tip and the adsorbate the following steps are carried out: (i) the tip is positioned above the adsorbate, (ii) the tip-sample distance is fixed by opening the feedback loop of the microscope at a given current and sample voltage, and (iii) the tip is approached towards the surface at a given speed at constant sample voltage $V$ and the current is simultaneously acquired. Using current vs. tip displacement data $[I(\Delta z)]$ the *conductance curve* of the tip-adsorbate-surface junction is obtained via $G(\Delta z) = I(\Delta z)/V$.[XIV]

---

[XII] If $R \propto I^N$ with $N \in \mathbb{N}$ , the reaction order is $N$.

[XIII] The term *action spectroscopy* originates[132] from a technique in the fields of unimolecular reactions,[133] electrochemistry and biology. In these fields the reaction rate is measured as a function of the wavelength of irradiated light for identifying the specific orbital or molecule that is active in the reaction induced by photons.

[XIV] (i) Conductance should not be confused with conductivity, a material constant. (ii) In fact, the conductance in this thesis was obtained via $G(\Delta z) = I(\Delta z)/(V - I(\Delta z)\, R_{\mathrm{STM}})$, where $V$ is the applied sample voltage and the term $I(\Delta z)\, R_{\mathrm{STM}}$ is a correction term. It reflects the voltage drop over the resistance $R_{\mathrm{STM}}$ given by the cables and transimpedance amplifier in the tunneling current circuit of the STM. This part of the voltage is not applied to the tunneling junction. The correction may be relevant for high currents and low voltages. For the instrument used in this thesis (Sec. 3.5.1), applied

### 3.4.2. Contact regimes

Depending on the tip-adsorbate separation conductance curves may be characterized by two or three regimes of contact,[64] namely (I) tunneling contact, (II) mechanical contact, and possibly (III) contact with chemical bond between tip and adsorbate (Fig. 3.3I–III).

In the tunneling contact regime (I), the tip-sample separation is large and the conductance increases exponentially with decreasing separation, as discussed in the Sections before. Moreover, the geometries of the tip and the adsorbate-substrate system are hardly affected by their spatial proximity (Fig. 3.3I).

To characterize the exponential relation in the tunneling regime (I) the *apparent barrier height* $\Phi$ is defined via[111]

$$G(z + \Delta z) = G(z)\ \exp\left[ - \left( \frac{8\,m_e}{\hbar^2}\ \Phi \right)^{0.5}\ \Delta z \right], \tag{3.5}$$

where $z$ is the initial tip position and $\Delta z$ the tip excursion with a negative (positive) value for movements towards (away from) the sample ($\hbar$: reduced Planck constant, $m_e$: electron mass). $\Phi$ generally depends on the sample voltage.[134] At small sample voltages $\Phi$ is related to the average work function of the tip and the adsorbate-substrate system,[111, 135, 136] if no other effects[137, 138] are dominant. Accordingly, $\Phi$ is usually in the range of several electronvolts. For bare Au(111) and a Au tip $\phi$ is, *e. g.*, ≈ 4 eV at ≈ 100 meV.[64, 139–141]

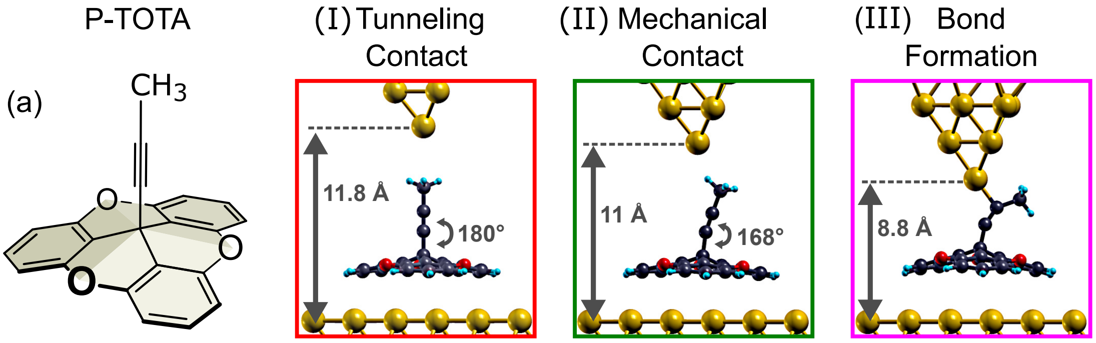

Figure 3.3.: (a) Molecular structure of propynyl-trioxatriangulenium (P-TOTA). (I–III) Side views of a junction in the (I) tunneling, (II) mechanical, and (III) bond-formation regime of contact. The junction is comprised of a Au tip, P-TOTA molecule [cf. (a)], and Au(111). The geometries were calculated with density functional theory (Chap. 5). The related experimental $G(z)$ curve is shown in Figure 3.4 and discussed in detail in Chapter 5). Yellow, black, red, and blue spheres correspond to Au, C, O, and H atoms, respectively. From (I) to (II) the tip is 0.8 Å moved towards Au(111) and from (II) to (III) 2 Å. [The tip is elongated by 0.2 Å in (III).]

In the mechanical contact regime (II) the tip and the adsorbate-surface system are close enough to mechanically couple, *i. e.* noticeable forces act between the tip and the adsorbate-surface system (Fig. 3.3II). Long-range interaction via van der Waals and electrostatic forces and/or short range forces such as Pauli repulsion cause considerable geometric modifications of the tip and/or adsorbate-substrate system. For instance, in the

---

sample voltage of 100 mV, and presented conductances the correction is negligible (relative error below 2 %).

junction with P-TOTA (Figs. 3.3II) the propynyl moiety bends to the side because of repulsion between the tip apex atom and the topmost methyl group (Chap. 5).

At mechanical contact the tip displacement $\Delta z$ may no longer corresponds to the actual modifications of the distance of the tip and the adsorbate-substrate system, as relaxations take place. As a consequence, deviations of the exponential relation between $G$ and $\Delta z$ may occur. Vice versa, a deviation from the exponential behavior (Eq. 3.5) at smaller $\Delta z$, *i. e.* further movement of the tip towards the sample, *indicates* mechanical contact or other effects.

Depending on the reactivity of the tip and adsorbate, a chemical bond may be formed at small tip-sample distances (cf. Fig. 3.3III). Bond formation usually leads to considerable relaxations of the tip and the adsorbate-surface system. Moreover, it drastically affects the electronic structure of the junction. The bond induced change of the electronic structure may support or hinder electron transmission through the junction, *i. e.* increase or decrease $G$.[XV] As a chemical bond is usually very sensitive to the distance of the reactants, bond formation usually depends on a rather small tip movement. Thus, abrupt (and drastic) changes of $G$ are expected, when a chemical bond is formed (Chaps. 5 and 6).[64]

Mechanical contacts can also induce drastic and abrupt changes of the junction geometry and thus the conductance. This case is demonstrated in detail in this thesis (Chap. 6) Hence, mechanical contacts can be misinterpreted as contacts with bond formation, if solely the conductance data is considered. This misinterpretation may be especially relevant when little is known about the contact geometries as in break junction experiments (see description of the break junction method in Sec. 3.4.4).

### 3.4.3. Tip preparation, scatter and absolute tip position

In an STM the structure of the surface electrode and an adsorbate can be imaged with atomic precision prior to and after taking a conductance curve. Moreover, the adsorbate can be contacted at a specific lateral position. This control over the junction geometry drastically reduces scatter of conductance data.[63,64] However, the exact geometry and therefore also the exact electronic structure of the tip is usually unknown.[XVI] In this thesis, prior to conductance measurements effort and time was expended to prepare atomically sharp *metal* tips with specific properties. Au tips were sharpened by softly and *repeatedly* contacting a Au(111) substrate (Sec. 3.5.2.1) until a tip-substrate bond was formed and the following four properties were given:

(i) After formation of a bond the conductance $G$ is approximately equal to $\mathrm{G}_0 \doteq 2e^2/h$ ($\mathrm{G}_0$: quantum of conductance, $e$: elementary charge, $h$: Planck constant)

(ii) During each contact only a *single* Au atom, at most, is deposited on Au(111).

(iii) Bond formation occurs at a characteristic tip position ($\Delta z \approx -5.4 \pm 0.3\,\text{Å}$, $\Delta z = 0\,\text{Å}$ correspond to tunneling at 100 mV and 30 pA).

(iv) Single Au adatoms are imaged as *circular* protrusion with a diameter less than 700 pm.

---

[XV] I am not aware of a reported bond formation that reduces $G$. Nonetheless, it may be possible.

[XVI] A notable exception are $C_{60}$ functionalized tips.[142–145] For these tips the exact orientation of the apex $C_{60}$ molecule can be experimentally determined via imaging of single adatoms.

Properties (i-ii) indicate that the tip apex is comprised of a single Au atom (See Chap. 4, Sec. 4.3.2). As a result, the contacted molecules are essentially probed by an s-orbital (cf. Sec. 3.1.1). Properties (ii) and (iv) suggest a symmetric tip apex. (iii) indicates a similar elasticity of the tips, as the bond formation involves an elastic elongation of the Au tip (Chap. 6).

For a given molecule and tip, the $G(z)$ data hardly scattered, as shown by the resulting line widths of the data after multiple measurements (cf. Fig. 3.4 and Chap. 6). For different molecules and different tips, the $G$ values at contact with chemical bond between the tip and molecule scattered by $\lesssim 2 \times 10^{X}$ $\mathrm{G_0}$ around the average value, where $X$ is the order of magnitude of the average value in units of $\mathrm{G_0}$.[XVII] $G$ curves presented in this thesis are examples that are representative, *i. e.* close to average curves.

The position, at which a tip-substrate bond is formed, allows to define an absolute scale $z$ for the tip position (Chap. 6). Such an absolute scale was also established for $C_{60}$ functionalized tips on Cu(111).[143,145] Neglecting possible relaxations an absolute scale allows to estimate the tip-adsorbate separations.

## 3.4.4. Conductance curve vs. histogram

In STM measurements a conductance curve for a molecule, *i. e.* $G$ as function of the electrode separation $z$, is measured. In break junction measurements,[14,51] a molecular bridge between two contacts may be obtained by exposing a metallic junction to molecules that contain two reactive anchor groups and pulling the junction apart. With a certain probability, the desired geometry may occur in repeated experiments. This technique has been successfully used for several molecules but usually leads to scatter of the data because there is little control of the geometries of the investigated junctions.[146] Owing to the procedure, a huge amount of $G$ data is easily obtained.[53] However, only a fraction of the data may correspond to the desired junction geometry (a single molecule bonded via its reactive anchor groups to two metal electrodes). To extract this fraction, histograms that show the counts of $G$ values vs. the $G$ value were often used.[52] The desired junction geometry and thus its conductance may correspond to the most frequent value. (Thus, only single $G$ values based on histograms without electrode separation data rather than conductance curves were reported.[52]) In the following, data from an STM junction is used to demonstrate interpretational problems that may arise from the use of such histograms.

Figure 3.4 shows a $G(z)$ curve and the corresponding histogram. The curve is discussed and explained in detail in Chapter 5. $G$ values are displayed in a logarithmic scale. Accordingly, an exponential variation of $G$ with respect to the electrode separation $z$ corresponds to a straight line in Figure 3.4a. The variation of $G$ as a function of the electrode separation $z$ (Fig. 3.4a) is rather complex with local minimum and maximum at $z = 6.6$ and $5.8\,\text{Å}$ and an abrupt increase at $z = 4.7\,\text{Å}$. The conversion of the $G$ curve into a histogram (Fig. 3.4b) leads to peaks at $G$ values that corresponds to *small* or *zero slope* of $G(z)$ (Fig. 3.4a). The two peaks at $8.5 \times 10^{-5}$ and $1.6 \times 10^{-4}\,\mathrm{G_0}$ correspond to the local extrema in the *mechanical* contact regime (Chap. 5). They are not due to bond formation. The third peak at $3.3 \times 10^{-3}\,\mathrm{G_0}$ is indeed related to bond formation between

---

[XVII] For example, the $G$ values of the bare TOTA platform directly after bond formation scatter in the range of $3,5 \pm 1 \times 10^{-1}$ $\mathrm{G_0}$ (Chap. 6).

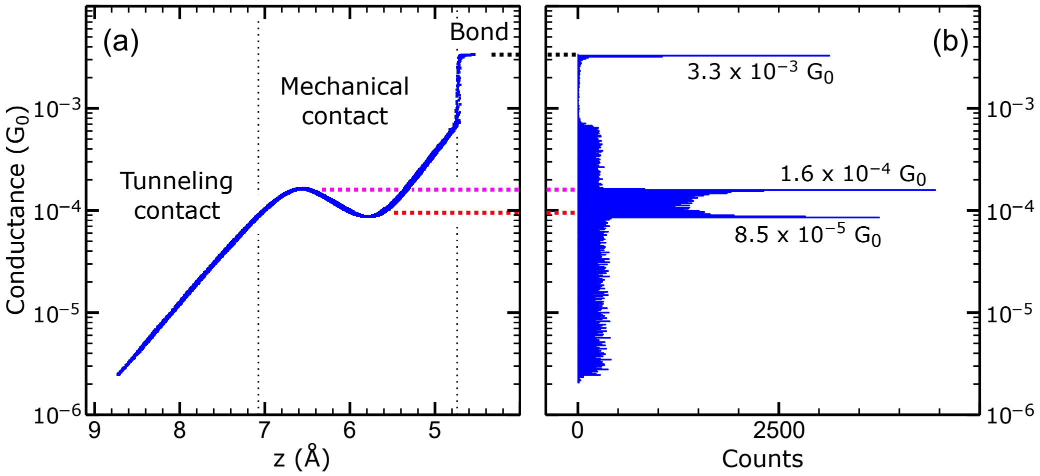

Figure 3.4.: (a) Experimental conductance curve $G(z)$ of propynyl-TOTA. The conductance curve consists of 40 forward and 40 backward traces. Thus, the reproducibility of the experimental result is indicated by the resulting line thickness. The curve is discussed and explained in detail in Chapter 5. Zero tip position is defined as contact of the Au tip to a fcc area of the Au(111) substrate (Sec. 3.5.2.1). Different contact regimes are indicated. (b) Histogram of the $G(z)$ data shown in (a).

the studied molecule and the electrode (tip). Thus, bond formation may lead to a peak in a histogram because of weak varying $G(z)$.[XVIII] However, peaks in histograms are generally *not* related to the most frequent junction geometry but to zero or small slope of $G(z)$. Consequently, the interpretation of histograms is challenging. To circumvent this challenge, plots can be used that show the frequency of $G$ as function of two parameters, namely the conductance value $G$ *and* the electrode separation $z$.[53,147] These data are equivalent to STM conductance curves, when the scatter of the data is sufficiently small.

In fact, many examples show that $G$ crucially depends on the electrode separation and details of the contact geometries (Chaps. 5 and 6). Hence, $G$ is a property of the whole junction comprised of electrodes and molecule and not an intrinsic property of the molecule (cf. Chap. 4, Sec. 4.3.2, Chaps. 5 and 6). Nonetheless, the extraction of conductance values that relate to specific situations such as bond formation may be possible.

## 3.5. Setup

### 3.5.1. Apparatus

The instrument used in most measurements presented in this thesis is a custom-built cryogenic ultra-high vacuum (UHV) STM described in detail in Reference 148. In this work, it was operated at 4.5 K and at a base pressure of $10^{-9}$ Pa. It is comprised of a load-lock, preparation, and an STM chamber. In the preparation chamber (base pressure $10^{-9}$ Pa) samples and STM tips are cleaned and molecules are deposited at ambient

---

[XVIII] The assumption of a weak varying $G(z)$ may be an alternative justification of using a histogram to identify the conductance related to bond formation.

temperature. Prepared samples or tips are inserted into the STM without breaking the UHV.

Weismann, Schöneberg, Burtzlaff, and I worked as a team to improve the apparatus by changing many important details that, *e. g.*, increased the signal-to-noise ratio by a factor of ≈ 5 [XIX], enhanced the thermal coupling of samples, and made the operation of the apparatus easier. In addition, the cabling of the instrument was replaced to allow for shot noise measurements.[149]

## 3.5.2. Substrates

### 3.5.2.1. Au(111) and Ag(111)

Atomically flat Au(111) and Ag(111) single crystals were used in this thesis as substrates for molecules because of their *a priori* expected low reactivity and quick and easy preparation. Gold *and* silver exhibit a face-centered cubic (fcc) structure with a lattice constant of 4.08 Å.

Ag(111) neither exhibits a surface reconstruction nor a significant surface relaxation.[150] Consequently, Ag(111) terraces are imaged as flat background in STM images. However, scattering of electrons may lead to standing wave patterns, *i. e.* corrugations.

Au(111) terraces appear in a parallel zig-zag pattern with a periodicity of 6.3 nm (Fig. 3.5) The pattern are comprised of areas with surface atoms in fcc and hcp packing that are separated with ridges that are resolved in STM images. An uniaxial compression of the topmost atomic layer along one of the three $\langle 1\bar{1}0 \rangle$ directions leads to this $(22 \times \sqrt{3})$ superstructure, called *herringbone reconstruction*.[151–153] Long-range elastic interactions have been reported to cause it.[152,153]

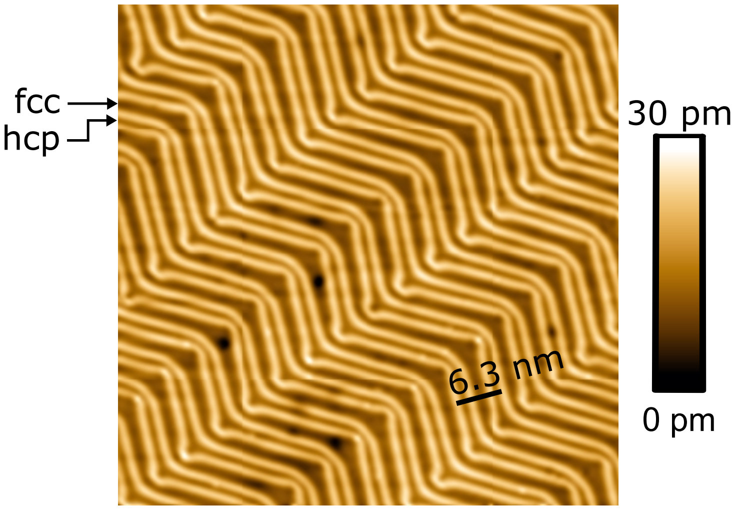

Figure 3.5.: Constant-current topograph of Au(111) (100 mV, 40 pA). While hcp and fcc domains appear low, the domain walls are imaged as protrusions. Dark circular spots corresponds to defects.

---

[XIX] Apparent height fluctuations at constant current were reduced by this value.

### 3.5.2.2. $Cu_2N$/Cu(100)

Various ultrathin insulating films are used to reduce the electronic coupling of adsorbates to the electron bath of a metal.[46,47,49,50] For instance, adsorbates on insulating films may experience reduced hybridization, allowing direct imaging of molecular orbitals similar to those of the gas-phase molecule[47,50] and spin-flip spectroscopy of single atoms.[46,49,74] In this thesis nitrogen islands on Cu(100), known as $Cu_2N$/Cu(100), were used to decouple a spin-crossover molecule (Chap. 11).

The structure of $Cu_2N$/Cu(100) was debated in the literature and finally identified by Choi *et al.* with the help of careful calibrated STM images.[154,155] The nitrogen atoms are approximately located at hollow sites of Cu(100) in a c(2 × 2) lattice (Fig. 3.6a). However, the $Cu_2N$ lattice is incommensurate to Cu(100). The reported lattice parameter of $a_N = 3.72 \pm 0.01\,\text{Å}$ is $\approx 3\,\%$ larger than the value for a commensurate structure ($2 \times a_{Cu} = 3.61\,\text{Å}$).[154] This incommensurability is reflected in the growth of the nitrogen islands. Island of a square shape with a size of approximately 500 Å×500 Å do not continue to grow.[155] This limit may be caused by a too large mismatch between the nitrogen lattice and Cu(100), as this mismatch may render further addition of nitrogen atoms unfavorable.

In contrast to bare Cu(100), $Cu_2N$/Cu(100) exhibits a band gap of ≈ 4 eV centered at the Fermi energy ($E_F$).[156] Accordingly (cf. Sec. 3.1.1), $Cu_2N$ islands show a lower apparent height than the bare Cu(100), although the nitrogen atoms are above the Cu atoms (Fig. 3.6b). Moreover, there is a sample-voltage dependent contrast inversion.[154] While at positive (negative) sample voltages the nitrogen atoms are imaged as depressions (protrusions), close to $E_F$ all hollow sites appear as protrusion (Fig. 3.6b). The atomic resolution of the nitrogen atoms can be exploited to identify adsorption sites of an adsorbate on $Cu_2N$ (See, *e. g.*, Chap. 11, Sec. 11.6.2).

Unfortunately, molecules deposited at ambient temperature usually bind to the more

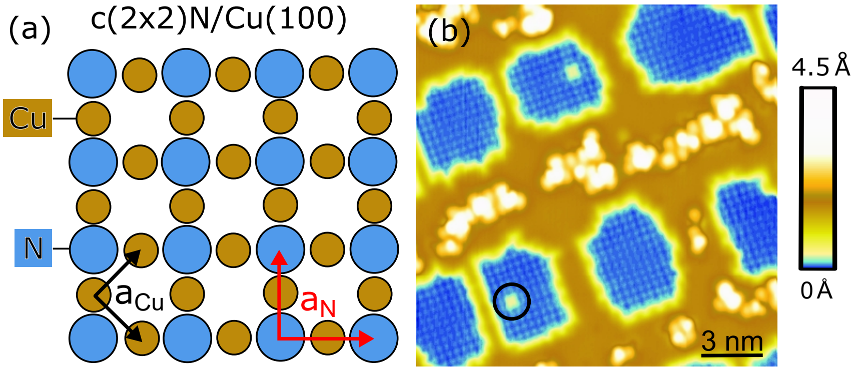

Figure 3.6.: (a) Sketch of a c(2 × 2) adlayer of nitrogen atoms (large blue circles) on the surface atoms of Cu(001) (small yellow circles). (b) Constant-current topograph of $Cu_2N$/Cu(100) with molecular adsorbates or fragments on bare Cu(100) areas (70 pA, 40 mV). At 40 mV the bare Cu(100) appears 1.4 Å higher (yellow) than the approximately rectangular nitrogen islands (blue). The molecular adsorbates or fragments are imaged as protrusions on Cu(100) (white). Although the hollow sites are either empty or occupied with a nitrogen atom within the islands [see (a)], they are both imaged as protrusions at low sample voltage, while the Cu atoms appear dark. Bright spots on $Cu_2N$ (an example is black encircled) corresponds to defects.[154]

reactive Cu(100) areas rather than to $Cu_2N$ islands (cf. Fig. 3.6b). In this work this problem was solved by (i) increasing the size of the $Cu_2N$ islands until only thin Cu trenches between islands were present and (ii) adjusting the molecular coverage until almost all Cu trenches were saturated by molecules and few molecules began to adsorb onto $Cu_2N$ islands. Such a sample is almost void of bare Cu. As a consequence, tip preparation by contacting the sample is challenging.

To prepare atomically sharp Cu tips the following recipe was developed. Double tips or tips covered with molecules or fragments of those were placed at the center of a bare $Cu_2N$ island and the sample voltage was increased above 5 V for a minute. After this procedure a tip exhibited a single apex, was clean, and rather blunt as indicated by STM images of individual atoms or molecules and contacts to bare $Cu_2N$ islands. Soft contacts to small parts of Cu trenches free of molecules usually resulted in dropping Cu clusters or single atoms from the tip and were therefore used to sharpen the tip.

## 3.5.3. Deposition of molecules

### 3.5.3.1. Sublimation

Molecules were sublimated onto substrates at ambient temperature from a heated Ta crucible at pressures of $10^{-8}$ Pa. To avoid decomposition of fragile molecules the heating power of the crucibles was (close to the expected sublimation temperature) increased only by 5-10 % per step. For 10 to 20 minutes two parameters, namely the frequency of a quartz balance and the pressure, were monitored to decide whether molecules start to sublimate. The pressure was measured by an ionization gauge (cold-cathode).[XX] A constant decrease of the frequency and/or a *slow* increase of the pressure per time interval indicated stable molecular sublimation and allowed to calibrate the molecular deposition. This calibration was done with the help of STM images of samples on which molecules were deposited for an arbitrary time (usually $\lesssim 1$ min).

For the deposition of the functionalized platform molecules studied in this thesis, the calibration via the pressure signal proves successful (sublimation at $\approx 70$ °C for $< 10^{-7}$ Pa).[XXI] The quartz balance did not show useful signals because it seemed to be quickly saturated with the molecules. Indeed, sublimation of an amount of molecules sufficient for many monolayers resulted in a sample that was only covered by a single monolayer rather than several. Only occasionally a second-monolayer molecule was found. These observations indicate that the studied platform molecules do not stably adsorb to the first monolayer at ambient temperature and could explain the rapid saturation of the quartz balance.

---

[XX] A pressure gauge that was close to a turbomolecular pump and could be reached by sublimated molecules only after many reflections in the vacuum chamber did not show any signal at the onset of the sublimation temperature. In fact, the crucible ($\approx 6$ mg of molecule powder) could be completely emptied without signal.

[XXI] In the particular setup a pressure increase of $\approx 10^{-9}$ Pa per several minutes was a good indication of (i) their sublimation and (ii) a rather stable sublimation rate. A decrease of the pressure was interpreted as degassing and the heating power was increased.

#### 3.5.3.2. Electrospray ionization

Electrospray ionization (ESI) is a common nondestructive technique to ionize (large) molecules and introduce them into the gas phase from a liquid environment.[157] In the present work the technique was used by Karan to deposit a charged spin-crossover compound onto Au(111). A detailed description of the used instrument and ESI technique can be found in References 158 and 159.

I sublimated the same molecule onto Au(111) (Chap. 10). Comparison with Karan's results suggests intact molecules on Au(111) in addition to fragments. To the best of my knowledge there are up to now[55] no other reports of a successful deposition of a charged spin-crossover complex via sublimation. Deposition of intact complexes may be related to careful use of the initial sublimation temperature. The initial sublimation temperature was determined by using sufficiently small temperature increases (see previous Section).

# 4
# Theory

## 4.1. Force field calculations

Force fields allow *efficient* calculations of large molecular systems with the help of molecular mechanics and molecular dynamics simulations.[160] They present an inductive method, seeking a common analytical representation to a set of observable phenomena. In contrast to quantum mechanical methods, electrons are not treated explicitly but together with the nuclei as *effective* atoms.[161] Single molecules are treated as mechanically connected systems of atoms. A given force field method contains a number of different potential energy functions describing different types of strain possible in a molecule such as bond stretching, angle bending, and torsional bending. The mathematical form of these functions is usually rather simple and based on effective elastic (harmonic) forces.[160] Additionally, long-range van der Waals and electrostatic interactions as well as hydrogen bonds are usually taken into account and allow intermolecular interactions to be modeled in addition to intramolecular interactions.[XXII,161,162] Via comparison with experimental and/or theoretical data the energy expressions and their parameters are chosen such that *specific systems* are well described at typical bond distances.[163] A variety of force fields has been developed and is available.

A main advantage of force field methods is their efficiency. Systems containing tens of thousands or even millions of atoms may be modeled with force fields.[164] However, the application of force fields is normally limited to the observables, for which they were developed. Moreover, their accuracy depends on the quality of their parametrization.[XXIII] In particular, force field calculations cannot provide any information about the explicit electronic structure.[160] Moreover properties depending explicitly on the electronic structure are difficult or impossible to represent with force fields.[160]

In this thesis, force field calculations were performed with *Avogadro*, an open-source

---

[XXII] To model these interactions partial charges are usually assigned to the effective atoms as a function of their bond geometry.

[XXIII] For, *e. g.*, the relevant platform molecules, calculations of the adsorption energy on a Au(111) slab give almost no binding ($\approx 20\,\mathrm{meV}$) with the force field UFF,[165] while density functional theory calculations, *i. e.* an explicit inclusion of the quantum mechanic electron charge density, predict strong binding ($\approx 2\,\mathrm{eV}$). This result indicates that UFF is, as expected from its design,[165] not suited to calculate adsorption energies of physisorbed extended $\pi$ systems.

molecular builder and visualization tool (Version 1.2.0).[166] The Generalized Amber Force Field (GAFF)[167] was used to calculate interaction geometries and energies of platform molecules (Chap. 8). GAFF is suitable because it was designed for simulations of organic molecules that are composed of H, C, N, O, S, P and halogens. The robustness of the results with respect to the chosen force field was checked via calculations with two other (suitable) force fields, namely UFF[165] and MMFF94.[168] As desired, no significant differences occurred.

## 4.2. Density functional theory

Density functional theory (DFT) was developed to compute the *ground state structure* and *energy* of quantum mechanical many-body systems such as solids and molecules.[169–172] It uses the Born-Oppenheimer approximation,[173] *i. e.* the assumption that electrons are at all times in adiabatic equilibrium and in the ground state regarding to the current positions of atomic nuclei.[XXIV] The potential surface set by the electrons of the system is used to iteratively relax the position of the nuclei towards a local energy minimum. For this relaxation, *e. g.*, a damped Newton algorithm can be used.

For the electrons, the nuclei are considered stationary, creating a static external potential. The solution of the related Schrödinger equation are many-electron wave functions and energies. However, only the ground state energy of the electrons is important for the relaxation of the nuclei. Hohenberg and Kohn showed that the ground state energy of an arbitrary nuclei's potential can be derived by minimizing an energy *functional* $E[n(\vec{r})]$ regarding many-electron densities $n(\vec{r})$ ($\vec{r}$: position in space). Actually, the density $n_0(\vec{r})$, which minimize $E[n(\vec{r})]$, is a ground-state density and allows to calculate further ground state properties. Thus, the quintessence of DFT is using a density functional and densities rather than solving the Schrödinger equation to obtain the electronic ground state energy and density.

Although its existence has been proven, the concrete form of the functional is up to now unknown. Moreover, good approximations of the functional directly using electron densities are hard to find and unfortunately not available so far. Kohn and Sham[174] circumvented this problem by introducing a *fictitious* system of non-interacting electrons, whose single-electron wavefunctions, the so-called Kohn-Sham orbitals, generate the same density as the many-electron system of interest. With the help of these *auxiliary* orbitals the minimization problem of the energy functional $E[n(\vec{r})]$ can be reformulated. There is still a term, the so-called exchange-correlation functional, that is unknown. However, useful approximations for it can be constructed and are available.

Although introduced as *auxiliary* functions, the Kohn-Sham orbitals are used to describe the electronic structure of many-electron systems such as solids, surfaces and molecules. This use is motivated by many successful descriptions that lead to a detailed understanding of various systems (*e. g.*, Chaps. 5 and 6). However, the justification of

---

[XXIV] This approximation is justified due to the large difference between the electron mass and the masses of atomic nuclei, and correspondingly the huge differences of the time scales of electron and nuclei motions.

this use of Kohn-Sham orbitals is subject of ongoing research[175–177] and to the best of my knowledge still unclear.

The result of a DFT calculation crucially depends on the initial geometry used as starting point because the initial structure is usually relaxed to a close local minimum, which is not necessarily the global one.[172] Therefore, STM images that verify the calculated adsorption geometry of the molecules of interest are valuable to find a (global) ground state. As discussed in Section 3.4.3, contacts of the STM tip to the bare surface were used to define an absolute $z$ scale for the tip height above the substrate. I used this scale along with STM images to suggest that the propynyl moiety of a propynyl-TOTA molecule bends to the side when contacted, as otherwise tip and wire would come too close (Chap. 5). This hint was helpful for the calculations performed by Garcia-Lekue and Frederiksen. Analogous data led to my suggestion that methyl-TOTA reversibly changes its adsorption place during contact, which could be also supported by calculations (Chap. 6).

As aforementioned, only approximated Kohn-Sham functionals are available. Consequently, the calculated ground state energies and structures may drastically deviate from the exact solution. For example, long-range electron correlations such as van der Waals (vdW) dispersion interactions are difficult to integrate into the functional.[178] However, vdW interactions are crucial for the adsorption of the studied platform molecules (see, *e. g.*, Chap. 9). In the calculations of the platform molecules, dispersion interactions were taken into account by using two different methods. While the theoreticians Potalsky and Tkatchenko used the PBE-vdW$^{\mathrm{surf}}$ method[179–181] (Chap. 9), the theoreticians Garcia-Lekue and Frederiksen calculated with the optB88-vdW functional[182] (Chaps 5 and 6). The calculated minimum-energy adsorption geometry and energy are similar. For instance, the calculated adsorption energies of methyl-TOTA with the two functionals differ by only $\approx 15\,\%$.

DFT gas-phase structures and Kohn-Sham orbitals of an Fe$^{\mathrm{III}}$ spin-crossover complex were calculated by the author along with Gruber using the program GAUSSIAN (Chap. 11). The calculated structures were utilized to assign STM patterns to specific states of the complex. Electronic structures of iron complexes such as that of Fe$^{\mathrm{II}}$-phthalocyanine[183,184] are difficult to map with Kohn-Sham orbitals, as they may depend on the used functional. To avoid misinterpretations caused by such an effect, the robustness of the results with respect to changes of the functional and basis set[XXV] was verified for the Fe$^{\mathrm{III}}$ spin-crossover complex (Sec. 11.5).

---

[XXV] Basis sets are used to expand DFT orbitals. As these are, due to practical reasons, limited, they span only a part of the Hilbert space and may affect the result. Therefore, basis set errors are possible and have to be avoided.

## 4.3. Quantum ballistic transport and the scattering picture

### 4.3.1. Ballistic transport

For macroscopic metallic conductors Ohm's law is valid. The conductance $G$ of a given sample is directly proportional to its transverse area $A$ and inversely proportional to its length $L$, *i. e.* $G = \sigma\ A/L$, where $\sigma$ is the conductivity. Although the conductance remains a key quantity, for atomic sized contacts concepts such as the Ohm's law are not anymore valid and a conductivity is not defined. If the dimensions of the contact are smaller than the mean free path of electrons, they will pass ballistically through it, *i. e.* the electron momentum can be assumed to be constant and only limited by scattering at boundaries of the atomic-sized conductor.[185,186]

### 4.3.2. Scattering picture

The *scattering picture*, which was first introduced by Landauer,[187,188] is a model commonly used to describe ballistic transport through nanostructures. As it was also used to understand conductance curves presented in this thesis, important terms of the scattering state picture such as *quantum of conductance* and *transport channel* are introduced below in a *heuristic* manner following References 186 and 149.

An atomic-sized constriction such as a single atom or molecule can be seen as a barrier or scattering region for electron transport. This scattering region is assumed to be connected to two electrodes that act as ideal electron reservoirs in thermal equilibrium. In contrast to the electrodes, the scattering region may be out of equilibrium. Furthermore, it is assumed that inelastic processes may only take place in the reservoirs.

In an STM, the electrodes are the tip and the substrate. An exhaustive calculation of the electronic transport through this system would require the solution of the time dependent many-body Schrödinger equation of the nonequilibrium system and a thermodynamic treatment of its coupling to the reservoirs. Unfortunately, this calculation is challenging, if feasible at all. To simplify the calculation, many body states are replaced by a set of *single-electron states* in a so-called single-electron picture. This simplification neglects many body effects such as charge screening. Nevertheless, the single-electron states are able to describe the behavior of discrete electrons and relate the conductance with the transmission and reflection probabilities for electrons incident on the atomic-sized constriction.

Henceforth, the two electrodes that contact the ballistic transport region will be referred to as a left ($L$) and a right ($R$) one, without loss of generality.

#### 4.3.2.1. Conductance of a perfect one-dimensional conductor

In the most simple case, the scattering region is comprised of a perfect one-dimensional conductor with a single occupied electronic state. Moreover, the density of states of the electrodes is assumed to be constant close to the average Fermi level of both electrodes.

When a voltage difference $V$ is applied between the electrodes, a net current flows because for a given energy, states are occupied in the left electrode and empty in the right one. The populations of the left and right electrodes are characterized by the Fermi-Dirac distribution $f_L$ and $f_R$. However, for the electron transport between the electrodes only the spin-degenerate states $k \in \left\{ n \frac{\pi}{l} \,|\, n \in \mathrm{N} \right\}$ with energy $\varepsilon_k = \hbar^2 k^2/(2 m_e)$ ($\hbar = h/(2\pi)$: reduced Planck constant, $m_e$: electron mass) of the one-dimensional conductor of length $l$ are available. The resulting net current then reads:[186]

$$\begin{aligned} I &= \frac{2e}{l} \sum_k v_k \left[ f_L(\varepsilon_k) - f_R(\varepsilon_k) \right] \\ &\approx \frac{2e}{l} \int_0^\infty v_k \left[ f_L(\varepsilon_k) - f_R(\varepsilon_k) \right] \frac{l}{2\pi} \, dk, \quad \text{for sufficiently large } l \\ &= \frac{e}{\hbar \pi} \int_0^\infty \left[ f_L(\varepsilon_k) - f_R(\varepsilon_k) \right] d\varepsilon \end{aligned} \tag{4.1}$$

where the factor 2 in the first line is due to the spin degeneracy and $v_k = \hbar k/m_e$ is the group velocity of an electron in state $k$. In the second line the quasi-continuity of the states $k$ ($dN = l/(2\pi)\, dk$: number of states in the interval $[k, k + dk]$) is exploited, and in the third line $dk = d\varepsilon/(\hbar v_k)$ is used. At zero temperature, $f_L(\varepsilon)$ and $f_R(\varepsilon)$ are step functions, equal to 1 below $E_F + eV/2$ and $E_F - eV/2$, respectively, and 0 above this energy ($E_F$: average Fermi level of both electrodes). Thus, the integral in expression 4.1 is equal to $eV$ at zero temperature and the current reads $I = \mathrm{G}_0 V$, where

$$\mathrm{G}_0 = \frac{2e^2}{h} \approx 77.5\,\mu\mathrm{S} \tag{4.2}$$

is the *quantum of conductance.* In other words, a perfect single mode conductor leads to a *finite* resistance $R = 1/\mathrm{G}_0 \approx 12.9\,\mathrm{k}\Omega$ (at zero temperature). This result is drastically different to a macroscopic connection between electrodes that exhibits *zero* resistance for the perfectly conducting case. Owing to the *ballistic* electron transport the conductance in Equation 4.2 does not depend on the concrete length $l$ of the conductor. A conductance $G \approx 1\,\mathrm{G}_0$ is indeed experimentally measured, *e. g.*, for single Au atoms contacted with Au electrodes or a Co atom on Cu(100) contacted with a Cu tip.[64,189]

As discussed below, a scattering region gives rise to the resistance by reducing the electron transmission probability. However, this intuitive picture does not answer the question where the energy related to the finite resistances of atomic-sized connections is dissipated. An intuitive interpretation is that the finite resistance is caused by resistance arising at the *interfaces* between the atomic-sized connection and the electrodes.[186,190,191] For a detailed discussion and interpretation of the finite resistance as well as the related heat dissipation the reader is referred to the literature.[185,190,191]

#### 4.3.2.2. Transport channels and transmissions

In the general case of a atomic-sized scattering region, the incoming wavefunctions from the left and right electrodes, $\left|\psi_k^{L,\,IN}\right\rangle$ and $\left|\psi_k^{R,\,IN}\right\rangle$ with energy $\varepsilon$ are related to the outgoing wavefunctions with energy $\varepsilon$ in the electrodes, $\left|\psi_k^{L,\,OUT}\right\rangle$ and $\left|\psi_k^{R,\,OUT}\right\rangle$ via an energy dependent scattering matrix **S**:

$$\begin{pmatrix} \left|\psi_k^{L,\,OUT}\right\rangle \\ \\ \left|\psi_k^{R,\,OUT}\right\rangle \end{pmatrix} = \mathbf{S} \begin{pmatrix} \left|\psi_k^{L,\,IN}\right\rangle \\ \\ \left|\psi_k^{R,\,IN}\right\rangle \end{pmatrix} = \begin{pmatrix} \mathbf{r} & \mathbf{t}^\dagger \\ \\ \mathbf{t} & \mathbf{r}^\dagger \end{pmatrix} \begin{pmatrix} \left|\psi_k^{L,\,IN}\right\rangle \\ \\ \left|\psi_k^{R,\,IN}\right\rangle \end{pmatrix}. \tag{4.3}$$

The scattering matrix is comprised of the transmission matrix $\mathbf{t}$, the reflection matrix $\mathbf{r}$, and their conjugates $\mathbf{t}^\dagger$ and $\mathbf{r}^\dagger$.[XXVI] For a net current caused by a population imbalance between incoming and outgoing states, the matrix $\mathbf{t}\,\mathbf{t}^\dagger$ turns out to be crucial.[186] $\mathbf{t}\,\mathbf{t}^\dagger$ is Hermitian with eigenvalues $\tau_i \in [0,1]$. Its eigenstates form independent means for electrons to traverse the contact from one electrode to the other. Therefore they are called transport *(eigen)channels* or eigenchannel scattering states. In contrast to a perfect one-dimensional conductor, which can be seen as fully open transport channel ($\tau = 1$), the contribution of a transport channel $i$ to the total conductance is reduced by the eigenvalue $\tau_i \in [0,1]$. Therefore, $\tau_i$ is also referred to as *channel transmission.* Since the transmission channels are independent, the conductances of the transport channels add up to the total conductance of the atomic sized connection between the electrodes:

$$G = \left(\sum_i \tau_i\right) \mathrm{G}_0, \tag{4.4}$$

where $\mathrm{G}_0$ is the quantum of conductance. It is worth mentioning that in Equation 4.4 spin-degenerate channels are assumed, as otherwise $\mathrm{G}_0$ has to be divided by 2.

The number of eigenchannels relevant for the conductance ($\tau_i \neq 0$) is usually limited to few modes ($\lesssim 5$) by the scattering region.[186] Thus, the strength of the scattering approach is to break up the electron transmission into few non-mixing channels and to give an intuitive picture of electron transport (Chaps. 5 and 6).

Different quantities are used for analyzing conductance data of molecular junctions in this thesis (Chaps. 5 and 6). Energy dependent *transmission functions* $T(E)$[192,193] are obtained with the help of eigenchannels via

$$T(E) = \sum_i \tau_i(E). \tag{4.5}$$

They are linked to the conductance at $E_F$ (zero voltage) via $G = T(0)\,\mathrm{G}_0$. Moreover, plotting *isosurfaces* of the eigenchannels may give a spatially resolved picture of the orbitals involved in the transport and helps to identify bottlenecks of the electron transmission.[194]

To get a more detailed picture of the electron transport in the scattering picture, so-called molecular projected self-consistent Hamiltonian (MPSH) states[193,195] can be calculated by diagonalizing only the part of the junction Hamiltonian that corresponds to the molecule.[XXVII] The electrodes only act as an external potential on the molecular states.

---

[XXVI] The matrices $\mathbf{t}$, $\mathbf{r}$, and their conjugates connect the states of the left and right electrodes. Analogously defined scattering matrices are also used to characterize the reflection and transmission of quantum particles at given potential barriers.

[XXVII] Technically, the junction Hamiltonian is projected onto the molecular states, *i. e.* onto a subspace of the junction Hilbert space. The eigenvectors of the resulting Hamiltonian are calculated and transformed

The MPSH states are suited to calculate transmission functions projected on a specific molecular state. This procedure enables to identify the contribution of each molecular orbital to the total conductance. In addition, a MPSH state that strongly (hardly) differs from the corresponding gas-phase orbital of the molecule indicates a drastic (negligible) impact of the electrodes on the electronic structure of the molecule.

#### 4.3.2.3. Eigenchannels from nonequilibrium Green's functions and DFT

The scattering picture does not give any clues on how to obtain the scattering matrix **S** (Eq. 4.3) for a given system. For this task the nonequilibrium Green's Function (NEGF) method combined with DFT can be used.[192–194] NEGF calculations presented in this thesis were performed by Garcia-Lekue and Frederiksen.

Geometries and Kohn-Sham electronic structures of tip-molecule-surface junctions are calculated by DFT (Sec. 4.2). The NEGF formalism takes into account the *nonequilibrium* electronic structure of the junction, that develops when a net current flows.[192–194] In the NEGF calculations the Kohn-Sham electronic structure rather than the exact ground-state electronic structure enters as an input. Thus, possible problems of the Kohn-Sham electronic structure also translate to the NEGF results.

#### 4.3.2.4. Eigenchannels probed with shot noise

From the measurement of the conductance alone (Eq. 4.4), it is not possible to obtain information about the number of channels involved and their transmissions $\tau_i$. However, the shot noise of the current depends on $\tau_i$ and may be used to probe such information.[149,186,196,197] Burtzlaff *et al.* directly measured shot noise from single-atom contacts with an STM.[197] To the best of my knowledge, this was the first report of a direct shot noise measurement *with* an STM. Motivated by results presented in this thesis (Chap. 6), Mohr along with me *et al.* expanded the STM shot noise measurements to a single molecule.[198] For a bare TOTA platform on Au(111) the transport turned out to be dominated by a fully open ($\tau \approx 1$) spin-degenerate channel. This result was reproduced by DFT-NEGF calculations.

---

via rotations to orthogonal states, the MPSH states. For further details the reader is referred to the literature.[193,195]

# Part II.

# Electrical Contacts to Single Functionalized Molecular Platforms

# 5

# Conductance of a Freestanding Conjugated Molecular Wire

This chapter is based on a manuscript published in *Physical Review Letters*. It is reprinted with permission from

Torben Jasper-Toennies, Aran Garcia-Lekue, Thomas Frederiksen, Sandra Ulrich, Rainer Herges, and Richard Berndt, Phys. Rev. Lett. **119**, 066801 (2017), *Editors' Suggestion*, Copyright (2017) by the American Physical Society.

## 5.1. Abstract

A free-standing molecular wire is placed vertically on Au(111) using a platform molecule and contacted by a scanning tunneling microscope. Despite the simplicity of the single-molecule junction its conductance $G$ reproducibly varies in a complex manner with the electrode separation. Transport calculations show that $G$ is controlled by a deformation of the molecule, a symmetry mismatch between the tip and molecule orbitals, and the breaking of a C≡C triple in favor of a Au–C–C bond. This tip-controlled reversible bond formation/rupture alters the electronic spectrum of the junction and the states accessible for transport, resulting in an order of magnitude variation of the conductance.

## 5.2. Introduction

To measure the electrical conductance of a molecule two contacts are required. In a scanning tunneling microscope (STM) a metal sample and the tip of the microscope serve this purpose. However, preparing a single, freestanding molecule on a metal surface is difficult because simple molecules tend to increase their adsorption energy by lying flat on the substrate. Recent experiments succeeded in contacting oligomers at one of their ends, retracting the tip, and forming a partially freestanding wire.[199–205] Changes of the conductance during the pulling process have been attributed to the breaking of bonds to the substrate. Owing to the complexity of the investigated structure, significant variations occurred in repeated experiments. Related results along with the observation of a Kondo effect and molecular switching were reported for single perylene-tetracarboxylicacid-dianhydride or diarylethene molecules pulled off from a Ag or Au substrate.[206–208] A molecular bridge between two contacts may also be obtained by exposing a metallic junction to molecules that contain two reactive anchor groups and pulling the junction apart. With a certain probability, the desired geometry may occur in repeated experiments. This technique has been successfully used for several molecules but usually leads to scatter of the data because there is little control of the geometries of the investigated junctions.[14, 51]

We have solved the above-mentioned problems using a chemical approach and verified its success via STM imaging. We synthesized a molecule that is composed of a short propynyl moiety and an extended platform that lies flat on the substrate.[42] The propynyl wire is attached perpendicularly to the platform and stands upright on the surface. Related platform approaches involving different chemistry have been used to arrange molecular subunits parallel to a substrate or as an inclined cantilever (see, *e.g.*, Refs. 209, 210). Moreover, rather than studying the rupture of a preformed contact, a contact is controllably made by moving the tip closer to the wire, starting from a nm distance until contact occurs. This process is fully reproducible, exhibits no hysteresis, and little scatter between different experimental runs on different molecules.

Despite the simplicity of our setup, we observe the conductance to vary in a complex manner. Using atomistic transport calculations we find that the tip initially causes the propynyl wire to bend. This hardly affects the electronic states of the molecule, but the match between the symmetries of the current-carrying states of the molecule and the tip worsens, and the conductance consequently is reduced. Upon further approach, the Au atom at the tip apex breaks the triple bond of propynyl and binds to the adjacent C atoms. This leads to new tip-molecule states accessible for transport, because unoccupied molecular orbitals strongly hybridize with tip states. As a result the conductance is enhanced and dominated by unoccupied instead of occupied molecular states.

## 5.3. Results and discussion

Measurements were performed with a STM operated at 4.5 K and in ultrahigh vacuum (base pressure $10^{-9}$ Pa). Au(111) surfaces and chemically etched W tips were cleaned by repeated $Ar^+$ bombardment and annealing. After mounting into the STM the tips were repeatedly indented into the substrate. Finally, to ensure atomically sharp tips the sample was softly contacted until single Au atoms were deposited and the contacts were stable at conductance of $G \approx G_0 \doteq 2e^2/h$ (Chap. 4, Sec. 4.3.2; $G_0$: quantum of conductance, $e$: elementary charge, $h$: Planck constant). This indicates that the tip apex is comprised of a single Au atom (Chap. 3, Sec. 3.4.3). As a result, the contacted molecules are essentially probed by an $s$-wave. We verified that tips were not modified during measurements on molecules by contacting the Au(111) again after each set of measurements. Propynyl-trioxatriangulenium (P-TOTA) molecules were mixed with 40% ethyl-TOTA [XXVIII] and deposited onto Au(111) at ambient temperature from a heated Ta crucible (Chap. 3, Sec. 3.5.3). Here, we exclusively report the results for P-TOTA. The synthesis of P-TOTA is described in Section 5.5.1 of the Supporting Information (SI). Submonolayer coverages were prepared to enable tip preparation on clean Au.

---

[XXVIII] The mixture was used to perform two experiments in parallel on the same sample.

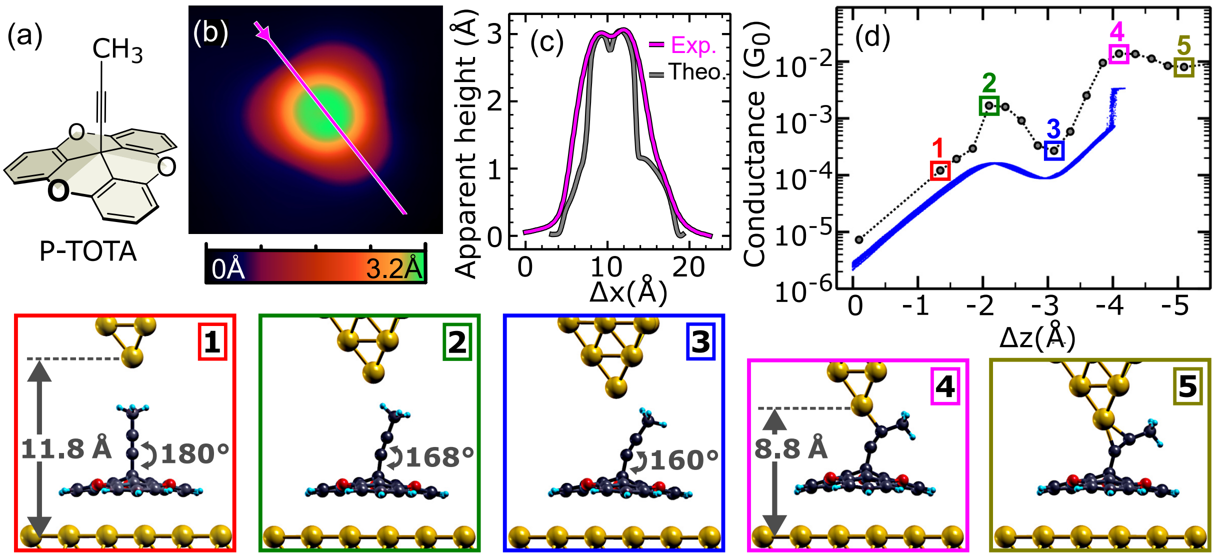

Figure 5.1.: (a) Lewis structure of propynyl-trioxatriangulenium (P-TOTA) (b) Constant-current STM topograph of a single P-TOTA ($V$ = 100 mV, $I$ = 30 pA) (c) Experimental apparent height profile along the line indicated in (b) and the corresponding theoretical profile scaled by an arbitrary factor of 0.5 (SI, Sec. 5.5.3). (d) Experimental and theoretical conductance curves $G(\Delta z)$ of P-TOTA. The experimental conductance curve consists of 40 forward and 40 backward traces. Zero tip displacement is defined for the experimental curve by feedback loop parameters of 19 pA and 100 mV, whereas for the theoretical data points it corresponds to a distance $z$ of 13.1 Å between apex atom and Au surface. Contact to a bare *fcc* area of Au(111) with the same tip corresponds in the experiments to $\Delta z \approx -9$ Å (Chap. 6). (**1** – **5**) Calculated junction geometries corresponding to $\Delta z$ = −1.3, −2.1, −3.1, −4.1, −5.1 Å as indicated in panel (d).

P-TOTA (Fig. 5.1a) was designed to ensure an upright and freestanding position of the propynyl group on a metal surface. The coupling between P-TOTA and Au is expected to be mediated by the TOTA platform and its conjugated $\pi$ system. Indeed, constant current STM images of a single P-TOTA (Fig. 5.1b) reveal an upright orientation of the propynyl group. The TOTA platform appears as a low triangular protrusion ($\lesssim$ 1.6 Å), whereas the propynyl-group is imaged as a central, circular protrusion with a maximum apparent height of ≈ 3.2 Å. Cross-sectional profiles through the protrusion reveal a shallow minimum at the center (Fig. 5.1c). The qualitative agreement of the experimental and the theoretical cross-sectional profiles (Fig. 5.1c) indicates that the ring of maximum apparent height is caused by the topmost H atoms of the propynyl group.

Next, the conductance $G$ was measured, while the tip was brought closer to the center of P-TOTA at a speed of 16.5 Å/$s$. The measurements were conducted on molecules in clusters to prevent lateral movements (SI, Sec. 5.5.2). Figure 5.1d displays the measured conductance $G(\Delta z)$ of P-TOTA (blue curve) vs. the tip excursion $\Delta z$ towards the molecule. Zero displacement corresponds to the position of the tip before opening the feedback loop of the STM. The exponential increase of $G$ in the tunneling region corresponds to an apparent barrier height of 4 eV, similar to that of clean Au(111) measured with a Au tip. Starting at ≈ $10^{-4}$ $G_0$, the slope decreases drastically indicating a mechanical contact between the tip and the molecule. Counterintuitively, the conductance decreases by a factor of ≈ 2, although the tip is moved closer to the molecule by 1 Å. At a conductance of ≈ $10^{-3}$ $G_0$, surprisingly, a sudden jump by almost 1 order of magnitude in the conductance occurs. This remarkable conductance variation exhibits no hysteresis and is highly reproducible. STM imaging before and after the conductance measurements revealed no change of the P-TOTA and its environment.

The transport properties of P-TOTA in a STM junction were calculated using density functional theory (DFT, see Chap. 4, Sec. 4.2) combined with nonequilibrium Green's function (NEGF) methods (SI, Sec. 5.5.3 and Chap. 4, Sec. 4.3). The supercell contained a single P-TOTA molecule adsorbed on a 10-layer Au(111) slab with $6 \times 6$ periodicity, and a Au(111) 10-atom tetrahedron mounted on the reverse side, representing the STM tip. The electronic structure and geometries were obtained with the Siesta code[211] on a $2 \times 2 \times 1$ $k$-mesh while the elastic transmission was computed with TranSiesta[192,193] on a finer $21 \times 21$ $k$-mesh. Dispersion interactions were taken into account by the non-local optB88-vdW functional.[182]

Figure 5.1d also displays the calculated zero-bias conductance (black dots) versus electrode separation. These results closely follow the experimental ones, both in the tunneling and the contact regimes. As shown in the lower panels of Fig. 5.1, P-TOTA is strongly distorted as the tip is approaching. For large electrode separations ($\Delta z \geq -3.5$ Å, configurations **1** – **3**), the bond angle between the propynyl-group and the platform decreases drastically by $\approx 20°$, whereas the corresponding deformation energy is below $\approx 100$ meV (SI, Sec. 5.5.4). Hence, the bond between the propynyl-group and the $sp^3$ C atom of the TOTA platform is highly flexible.[45] The abrupt jump at conformation **4**, however, suggests a different origin.

Figure 5.2a presents transmission functions (Chap. 4, Sec. 4.3.2.2) computed for electrode separations **2** – **4** in Fig. 5.1. At large separation (**2**) the electron transport around $E_F$ is dominated by the nearly degenerate highest occupied molecular orbitals (HOMOs) at $\approx -1.1$ eV, while the nearly degenerate lowest unoccupied molecular orbitals (LUMOs) at $\approx 2.3$ eV are essentially unimportant. This is shown by a projection of the transmission onto the nearly degenerate HOMOs and LUMOs of the molecular projected self-consistent Hamiltonian (MPSH)[193,195] (SI, Sec. 5.5.5, Figs. 5.7–5.9). Accordingly, the projection onto the dominant HOMO hardly changes the transmission close to $E_F$ (green dashed line in Fig. 5.2a).

The counter-intuitive conductance reduction from **2** to **3** can be understood from the calculations as a result of a reduced coupling between the states of the tip and the molecule. As revealed by the eigenchannel scattering states[194,212,213] (Chap. 4, Sec. 4.3.2.2), the tip $s$-wave shifts from entering a molecular lobe at **2** (Fig. 5.2b) closer to a nodal plane of the functional group in **3** (Fig. 5.2c). As a result the amplitude of the scattering states on the molecular TOTA platform, and consequently the transmission, is suppressed. The importance of orbital symmetry matching for the conductance has recently also been pointed out for a CO-terminated tip tunneling to a acetylene molecule in the Supplementary Online Material to Ref. 214.

The above transport scenario is changed as the tip moves even closer and breaks the C≡C triple bond as in **4** (Fig. 5.2). The energy spectrum of this tip-molecule structure is new and different (black arrow in Fig. 5.2a) as one of the LUMOs strongly hybridize with tip states, while the HOMOs remain largely unaffected. The projection of the transmission onto MPSH eigenstates now reveals that a broad LUMO resonance dominates transport near $E_F$ (magenta dashed line in Fig. 5.2a and SI, Sec. 5.5.5, Fig. 5.9). Along with a reduced electrode separation, the tip-LUMO hybridization augments the transmission by

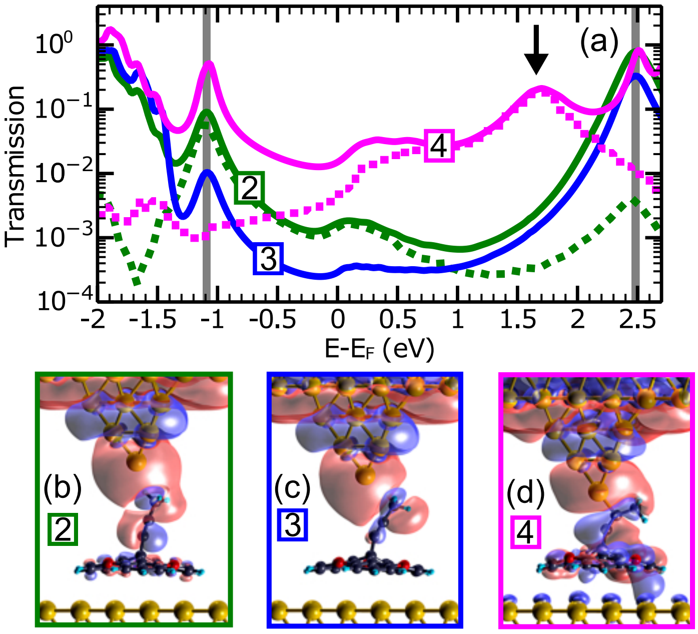

Figure 5.2.: (a) Calculated transmission functions vs. energy for configurations **2** – **4** (solid lines). Vertical gray bars indicate resonances related to the HOMO and LUMO states of an isolated P-TOTA. For **2** and **4** the transmission functions were also calculated by projection onto MPSH eigenstates (SI, Sec. 5.5.5, Figs. 5.7 and 5.8 and Chap. 4, Sec. 4.3.2.2), that dominate at $E_F$, namely the HOMO for **2** and LUMO for **4** (dashed lines).[193] (b-d) Isosurface plots of the real part of the most transmitting eigenchannel scattering states (Chap. 4, Sec. 4.3.2.2) of **2** – **4** at $E_F$. Electron waves are incoming from the tip electrode at the $\bar{\Gamma}$ point.[194,212,213]

about two orders of magnitude over a wide energy range. This is also reflected in the transmitting eigenchannel scattering state at $E_F$ (Fig. 5.2d) where the delocalization over the molecular junction is evident and the bottleneck of transmission is restricted to the platform-to-substrate interface.

To understand the tip-induced chemistry in more detail we analyzed the energetics and electronic structure of the tip and molecule subsystems to single out the interplay between them without the influence of the platform-substrate interface [XXIX]. The energy of tip and molecule varies as a function of $\Delta z$ as shown in Fig. 5.3a. For small separations ($\Delta z \leq -3.5$ Å), between **3** and **4**, we find a drastic energy decrease by ≈ 600 meV over a range of only 0.5 Å. This value mainly results from an energy gain of ≈ 1 eV due to increased interaction of the tip and the molecule [XXX] and an energy of ≈ 450 meV required to further deform the propynyl moiety itself (SI, Sec. 5.5.4). Together with the small distance of 2.2 Å between the apex atom and the molecule, this further corroborates the breaking of a C≡C bond and the formation of a new covalent bond to the apex Au atom as illustrated in Fig. 5.1. For even smaller electrode separations ($\Delta z < -3.5$ Å), we find an

---

[XXIX] Technically the substrate atoms were removed without modifying the molecule-tip atom positions. We checked that basis set superposition errors amount to less than 10 % in the binding energy and thus do not qualitatively affect the reported results.

[XXX] For $\Delta z = -3.6$, $-4.1$ and $-5.1$ Å the interaction energies of the tip and the molecule are $-0.22$, $-1.22$ and $-1.50$ eV. Here, the interaction energy is defined as the energy of the entire tip-molecule subsystem minus the energies of the isolated molecule and tip, both calculated at the same geometries as in the entire tip-molecule subsystem.

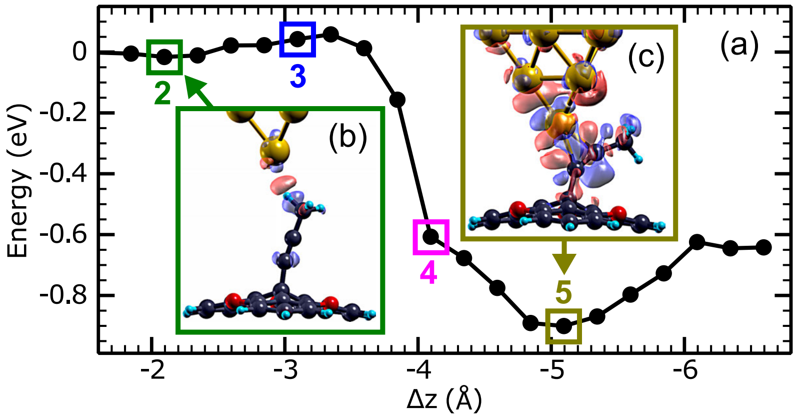

Figure 5.3.: (a) Energy change of the tip-molecule subsystem versus tip displacement $\Delta z$ with data highlighted corresponding to configurations **2** – **5** from Fig. 5.1. (b-c) Electron density redistributions for the tip and the molecule as a result of the tip-molecule interaction before and after bond formation. Blue (red) colored isosurfaces correspond to depletion (accumulation) of electron density.

energy minimum in **5**. Here the tip apex atom has almost identical distances ($\approx 2.25$ Å) from two C atoms of the propynyl-group, which were originally triple bonded (Fig. 5.1). Such a bonding scheme of gold clusters or cationic gold atoms to triple-bonded C atoms (Au–C–C bond) is well studied, because it represents the highly important activation step of C≡C triple bonds towards nucleophiles in a catalytic cycle (SI, Sec. 5.5.6).[215–217] Electron density is withdrawn from the bonding orbitals by the Au which makes the carbon atoms susceptible to nucleophilic attack.[218]

To analyze the electron density change due to the bond formation, we define the electron density redistribution as difference of the density of the entire junction and the densities of its two components, namely the molecule and the tip+surface, both with frozen geometries like in the entire junction. For **2** there is only very little charge redistribution (Fig. 5.3b) which can be understood by electrostatic interaction of the tip and the molecule. By contrast, there is a large and complex charge redistribution in **5** within tip and molecule (Fig. 5.3c) due to the formation of a Au−C−C bond. Moreover, Fig. 5.3c confirms a density reduction at the originally triple bonded C atoms at the opposite side of the Au−C−C bond. A withdrawal of electrons actually is a necessary condition for the activation of a C≡C triple bond.[218]

Remarkably, in all configurations from **4** to **5** the Au tip apex atom binds to at least one of the originally triple bonded C atoms. These novel bond configurations are mechanically constrained and all show a withdrawal of electronic charge similar to **5** (SI, Sec. 5.5.6).

Although the calculated conductance values follow closely the experimental data, they do not exhibit a jump during bond formation as observed in the experiment (Fig. 5.1). We attribute this difference to the elasticity of the tip shaft and a corresponding elongation of the tip during the bond formation as proposed in Refs. 219 and 144, which is not included in the atomistic calculations. For this reason, the experimentally observed conductance right after the sudden jump in the conductance cannot be unambiguously assigned to a specific configuration between **4** and **5**. Furthermore, $G$ is systematically overestimated in the model which we ascribe to the tendency of DFT to underestimate HOMO-LUMO gaps.[220]

Conductance data measured with different tips and molecules are remarkably similar. For most electrode separations $\Delta z$, they vary by less than a factor of $\approx 1.4$. However, in the range $\Delta z \in [-3.5\ \text{Å}, -1.8\ \text{Å}]$ the scatter is more obvious (factor of $\approx 3$) (SI, Sec. 5.5.2). Our tip preparation ensures an atomically sharp tip apex. Thus, the remaining differences may be attributed to the *mesoscopic* tip shape, which affects long range dispersion and electrostatic forces. In the range between **2** and **3**, where repulsion between the apex atom and methyl prevails, the long-range forces apparently exert a larger influence on the geometry than at closer distances, where a strong covalent bond is forming. These results suggest that combining an anchoring unit for covalent bonding, a C≡C triple bond in the present case, and a degree of flexibility within a molecule helps to achieve reproducible bonding geometries and conductances.[XXXI]

## 5.4. Summary

We have presented two effects that oppositely affect the conductance of P-TOTA during contact formation. At large electrode separation, the flexibility of P-TOTA causes a symmetry mismatch of the tip and molecule orbitals and reduces the conductance. At closer distances, a covalent bond between the Au tip and a C≡C triple bond reversibly forms under mechanical control. This bond induces new delocalized states near $E_F$ that increase the conductance by more than one order of magnitude.

Moreover, the results demonstrate that TOTA is a useful platform for geometrical decoupling of a molecular subunit from a metal substrate and neighboring molecules. Interestingly Au–C–C bonds play an important role in the activation of C≡C triple bonds. Thus our results hint that it may be possible to design a mechanically controlled single molecule catalyst.

---

[XXXI] Usually $G$ critically depends on the atomic geometry. A notable exception has been reported for the amine–Au bond.[221]

## 5.5. Supporting information

### 5.5.1. Synthesis of 12c-propynyl-4,8,12-trioxatriangulene (P-TOTA)

4,8,12-trioxatriangulenium tetrafluorborate (150 mg, 403 $\mu$mol) suspended in 200 ml anhydrous tetrahydrofuran (THF) was mixed with propynyl magnesium bromide (20 mL, 10 mmol, 0.5 M in THF) under nitrogen. The reaction mixture was heated under reflux for 7 h and the solvent was removed under reduced pressure. The residue was purified by chromatography over Florisil (cyclohexane/diethyl ether 1:1). The product was obtained as a colorless solid (31.2 mg, 96.2 $\mu$mol). The compound was identified by the following nuclear magnetic resonance (NMR) and mass spectra (MS) signatures:

1H NMR (500 MHz, THF−d8): $\delta$ = 7.29 (t, J=8.2 Hz, 3H, H−5), 6.97 (d, J=8.2 Hz, 6H, H−4), 1.59 (s, 3H, H−8) ppm.
13C NMR (125.8 MHz, THF−d8): $\delta$ = 153.03 (q, C−3), 129.56 (t, C−5), 112.18 (t, C−4), 111.78 (q, C−2), 81.62 (q, C−6), 80.86 (t, C−7), 22.23 (q, C−1), 3.05 (p, C−8) ppm.
MS (EI): m/z (%) = 324 (31), 285 (100).
MS (CI): m/z (%) = 325 (100), 285 (81).

### 5.5.2. Conductance measurements of P-TOTA

The conductance of P-TOTA was measured on molecules in clusters, where P-TOTA is adjacent to one or two ethyl-TOTA molecules (Fig. 5.4a).[XXXII] This was sufficient

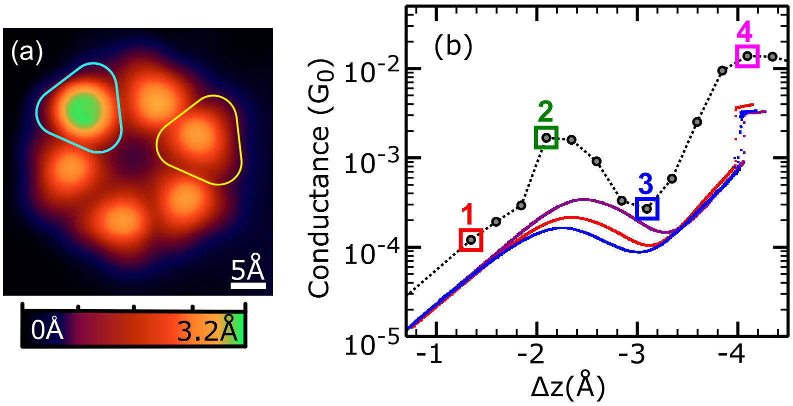

Figure 5.4.: (a) Constant-current STM topograph of a cluster comprising of one P-TOTA and five ethyl-TOTA molecules (100 mV, 30 pA). A single P-TOTA (ethyl-TOTA) is marked by a turquoise (yellow) border. (b) Experimental conductance curves G($\Delta z$) of P-TOTA measured with different tips and calculated conductance. Zero tip displacement $\Delta z$ is defined by feedback loop parameters of 19 pA and 100 mV in the experiment. In the calculation, this corresponds to a distance $z$ = 13.1 Å between the tip apex atom and the Au surface layer. Contact to bare *fcc* areas of Au(111) corresponds in the experiments to $\Delta z \approx -9$ Å. Configurations **1** – **4** are indicated.

---

[XXXII] A mixture of P-TOTA and ethyl-TOTA molecules was evaporated onto the Au(111) surface to acquire comparable data with the same tips. Here, we focus on P-TOTA.

to prevent rotational and lateral movements of P-TOTA during the contact formation. Conductances measured with different tips and from different molecules along with calculated results are displayed in Fig. 5.4b. The experimental and theoretical conductances are remarkably similar. However, there are also differences which are discussed in in Section 5.3.

### 5.5.3. Computational methods

SIESTA calculations[211] were done using a basis set consisting of split-valence double-zeta plus polarization DZP orbitals with 0.02 eV energy shift for the C, H and O atoms, as well as for the Au tip atoms and the surface Au atoms below the tip and the molecule. For bulk Au atoms, single-zeta plus polarization SZP orbitals with 0.02 Ry energy shift were used. Atomic coordinates of the molecule, tip, and surface gold atoms were relaxed until forces were smaller than 0.04 eV/Å. A cutoff of 400 Ry was used for the real-space grid integrations. During geometry optimization and for the TRANSIESTA calculations[192,193] a Monkhorst-Pack mesh with $2 \times 2 \times 1$ $k$-point sampling of the three-dimensional Brillouin zone was used. The transmission functions were sampled over $21 \times 21$ $k$-points. To obtain the theoretical apparent height profile for P-TOTA on Au(111) a constant current image was simulated within the Tersoff-Hamann approximation at 100 meV. Eigenchannel scattering states were computed with INELASTICA.[194,212,213]

### 5.5.4. Deformation energy of P-TOTA

P-TOTA is strongly distorted as the tip is approaching. The corresponding deformation energies of P-TOTA in the gas phase (Fig. 5.5) reveal a high flexibility of the bond angle between the propynyl-group and TOTA (configurations **1** – **3**). Furthermore, the more complex deformation of P-TOTA from configuration **3** to **4** significantly increases the energy. This deformation is caused by the Au–C–C bond formation between the tip and the molecule.

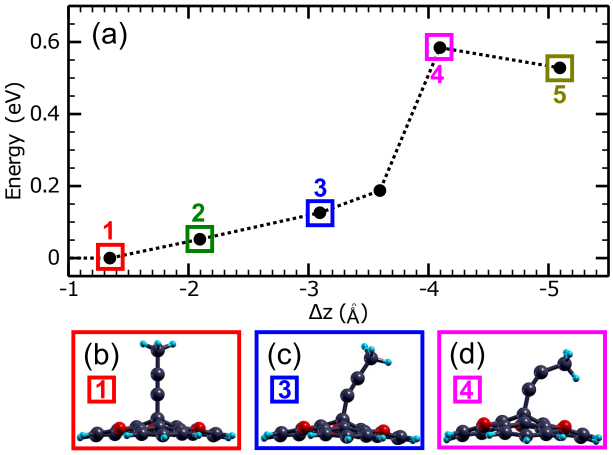

Figure 5.5.: (a) Deformation energy of isolated P-TOTA for various tip displacements $\Delta z$ and corresponding geometries. Configurations **1** – **5** are indicated. (b–d) Geometry of P-TOTA in configurations **1**, **3**, and **4**.

### 5.5.5. Molecular orbitals and MPSH states

The degenerate HOMOs and nearly degenerate LUMOs of isolated P-TOTA are shown in Fig. 5.6. The upper and lower panels correspond to the pristine configuration **1** and the tilted configuration **3**. Figure 5.6 shows that these orbitals are hardly affected by the tilting of the molecule. With respect to the conductance, the most important difference between the intermediate configuration **2** and **3** is a change of the local symmetry match between the tip and molecule orbitals as described in Section 5.3.

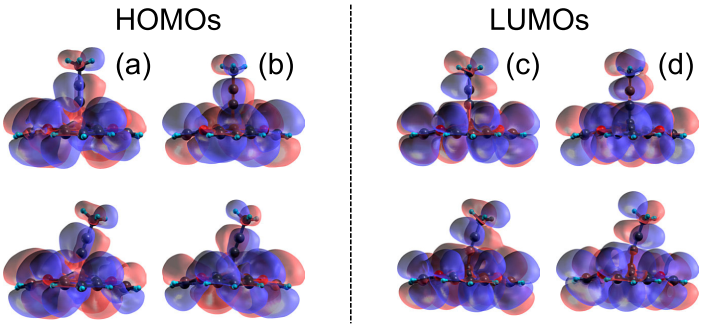

Figure 5.6.: Molecular orbitals of isolated P-TOTA in its undistorted form (upper row) and tilted as in **3** (lower row). (a–b) degenerate HOMOs, (c-d) nearly degenerate LUMOs. The HOMO-LUMO gap is in both configurations 3.6 eV.

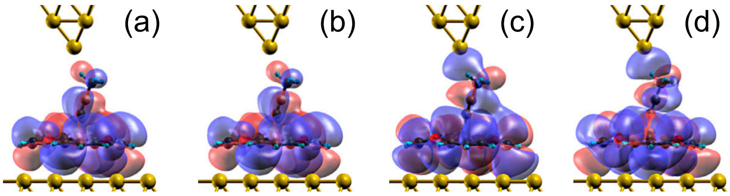

Figure 5.7.: HOMO-1, HOMO, LUMO, and LUMO+1 of the MPSH Hamiltonian for configuration **2** with eigenenergies $E - E_F = -1.22$, $-1.17$, $2.35$, and $2.38$ eV (left to right) used for the transmission projections presented in Figs. 5.2a and 5.9.

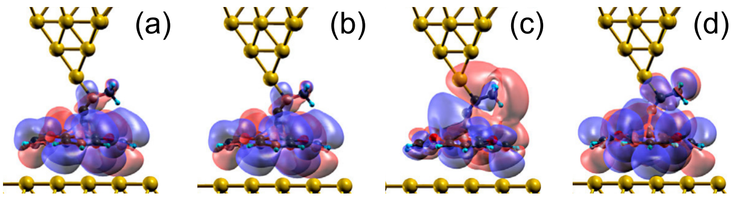

Figure 5.8.: HOMO-1, HOMO, LUMO, and LUMO+1 of the MPSH Hamiltonian for configuration **4** with eigenenergies $E - E_F = -1.19$, $-1.14$, $1.18$, and $2.41$ eV (left to right) used for the transmission projections presented in Figs. 5.2a and 5.9.

To disentangle the roles of the different P-TOTA molecular states for electron transport across the junction we have performed an analysis based on the molecular projected self-consistent Hamiltonian (MPSH)[193,195] corresponding to the subspace of P-TOTA (Chap. 4, Sec. 4.3.2.2). [XXXIII] We have computed the electron transmission projected

---

[XXXIII] For configuration **4**, where the electrode distance is quite short, we had to reduce the extension of the basis orbitals on the Au apex atom to allow folding of the electrode self-energies fully on the molecular part. In practice, we used the same, more short-ranged SZP basis as used for the bulk Au atoms.

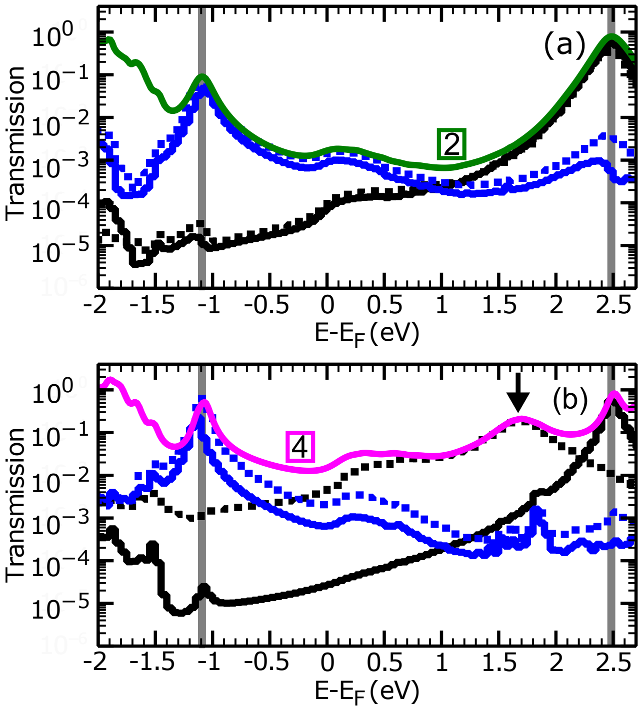

Figure 5.9.: Electron transmission projected onto HOMO-1 (blue solid), HOMO (blue dashed), LUMO (black dashed), and LUMO+1 (black solid line) of the MPSH Hamiltonian (Figs. 5.7 and 5.8) for the configurations **2** (a) and **4** (b) along with the full transmissions (green and magenta solid lines).

onto HOMO-1, HOMO, LUMO, and LUMO+1 for the configurations **2** and **4** (states shown in Figs. 5.7 and 5.8) following the scheme presented in Ref. 193.

As observed in Fig. 5.9, for configuration **2** the transmission near $E_F$ is dominated by the HOMO states, while for configuration **4** it changes to the strongly hybridized LUMO state (black arrow).

### 5.5.6. Au–C–C bond geometry and charge redistribution

Below, we compare our calculated Au–C–C bond geometry of configuration **5** with recent results for an ethyne molecule on a cluster of 18 Au atoms (Table 5.1). Both geometries are remarkably similar confirming that the mechanical approach of the Au apex atom leads to the formation of a Au–C–C bond.

Remarkably, for all configurations from **4** to **5** and smaller electrode separations the Au tip apex atom binds to at least one of the originally triple bonded C atoms. For example in **4** ($\Delta z = -4.1$ Å) the Au tip apex atom binds mainly to the carbon atom labeled C2 in Fig. 5.10a. These novel bond configurations are mechanically constrained. They all show a withdrawal of electronic charge similar to the minimum energy bond geometry **5** (Fig. 5.11). Interestingly, the electron density redistribution due to the Au–C–C bond hardly involves the TOTA platform. Consequently, the Au substrate has negligible effect on the charge redistribution of the propynyl moiety.

| P-TOTA and Au-tip | | Ethyne and $Au_{18}$ cluster[217] | |
|---|---|---|---|
| $d$(Au,C1) | 2.28 Å | $d$(Au,C1) | 2.32 Å |
| $d$(Au,C2) | 2.20 Å | $d$(Au,C2) | 2.32 Å |
| ∠(Au,C1,C2) | 69.9° | ∠(Au,C1,C2) | 74.6° |
| ∠(Au,C2,C1) | 77.2° | ∠(Au,C2,C1) | 74.6° |
| ∠(Au,C2,C3) | 121.6° | ∠(Au,C2,H3) | 118.5° |
| ∠(C1,C2,C3) | 161.1° | ∠(C1,C2,C3) | 166.9° |

Table 5.1.: Calculated Au–C–C bond geometry of configuration **5** vs. calculated bond geometry of an ethyne molecule on a Au cluster.[217] $d$(Au,X) is the distance between the Au apex atom and atom X and ∠(X,Y,Z) the bond angle between atom X, Y and Z. The atom labels are defined in Fig. 5.10.

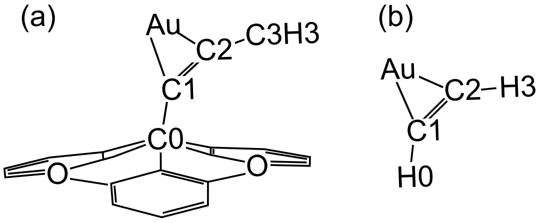

Figure 5.10.: (a, b) Labels of the atoms involved in the Au–C–C bond between the Au apex atom of the STM tip and P-TOTA or the apex atom of a Au cluster and an ethyne molecule.

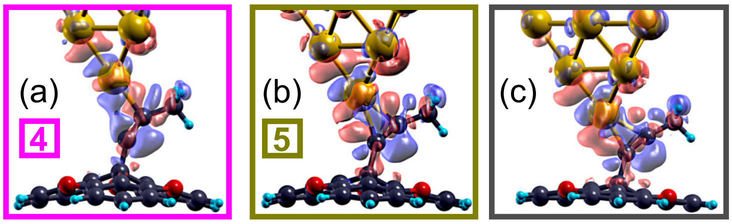

Figure 5.11.: (a–c) Electron density redistributions of the tip and the molecule caused by the tip-molecule interaction. Configurations are shown for $\Delta z = -4.1, -5.1$ and $-6.1$ Å. Blue (red) isosurfaces indicate depletion (accumulation) of electron density.

## 5.6. Acknowledgments

We thank Lynn Gross, Carmen Herrmann, Igor Poltavskyi and Alexandre Tkatchenko for discussions and the Deutsche Forschungsgemeinschaft (SFB 677) and the Gobierno Vasco (PI-2016-1-0027) for financial support.

## 5.7. Contributions

I proposed to study the molecule. Sandra Ulrich and Rainer Herges synthesized it. I measured and analyzed the experimental data. Aran Garcia-Lekue and Thomas Frederiksen performed the DFT-NEGF calculations. I wrote the first draft of the manuscript.[140] Richard Berndt supervised the project. All authors discussed the results and improved and commented on the manuscript.

# 6

# High-conductance Contacts to Functionalized Molecular Platforms Physisorbed on Au(111)

This chapter is based on a manuscript published in *Journal of Physics: Condensed Matter*. It is reproduced in whole or in part from that manuscript, with the permission of *IOP Publishing Ltd.*

Torben Jasper-Tönnies, Aran Garcia-Lekue, Thomas Frederiksen, Sandra Ulrich, Rainer Herges, and Richard Berndt, J. Phys.: Condens. Matter **31**, 18LT01 (2019), Copyright 2019 IOP Publishing Ltd.

## 6.1. Abstract

The conductances of molecules physisorbed to Au(111) via an extended $\pi$ system are probed with the tip of a low-temperature scanning tunneling microscope to maximize the control of the junction geometry. Inert hydrogen, methyl, and reactive propynyl subunits were attached to the platform and stand upright. Because of their different reactivities, either non-bonding (hydrogen and methyl) or bonding (propynyl) tip-molecule contacts are formed. The conductances exhibit little scatter between different experimental runs on different molecules, display distinct evolutions with the tip-subunit distance, and reach contact values of 0.003–0.05 $G_0$. For equal tip-platform distances the contact conductance of the inert methyl is close to that of the reactive propynyl. Under further compression, the inert species, hydrogen and methyl, are found to be better conductors. This shows that the current flow is not directly correlated with the chemical interaction. Atomistic calculations for the methyl case reproduce the conductance evolution and reveal the role of the junction geometry, forces and orbital symmetries at the tip-molecule interface. The current flow is controlled by orbital symmetries at the electrode interfaces rather than by the energy alignment of the molecular orbitals and electrode states. Functionalized molecular platforms thus open new ways to control and engineer electron conduction through metal-molecule interfaces at the atomic level.

## 6.2. Introduction

The transport of electrons through molecule-metal junctions is relevant for processes in many branches of science and crucial for potential applications in electric engineering.[13–18] However, understanding and tailoring the charge transport through a molecule-metal junctions is a major challenge, because it drastically depends on geometric and electronic details of the molecule-metal interfaces.[13–17,36,37,145,222–227] Chemical anchor groups comprising a molecular subunit or a single atom attached to the molecule of interest have been used to achieve well-defined interfaces.[XXXIV] In particular, reactive anchor groups that chemisorb to metal electrodes have been a focus of interest, because they are expected to provide strong forces that stabilize a desired molecule-electrode geometry.[16,17,37–39] However, bond formation tends to induce significant electronic changes of the electrode-molecule complex and renders difficult the design of a molecule that will deliver specific transport properties.[14,15,36,37,39,223]

Here, we explore the transport properties of a class of molecules that rely on a different anchoring scheme. It is designed to leave the properties of the functional molecular subunit almost unaffected by avoiding strong hybridization of the molecular states with those of the electrode. This is achieved by using a platform that binds to metal substrates via physisorption. Functional subunits are attached to its center and stand upright. Like other platform molecules it can be used to achieve decoupling from neighbor molecules.[41] In contrast to the triazatriangulenium (TATA) platform,[42,44,45] the trioxatriangulenium (TOTA) we use here may be sublimated intact, and thus enables systematic investigations in ultrahigh vacuum. The extended $\pi$ system of the platform provides a high-conductance contact to the substrate,[140] as expected (see, *e. g.*, Refs. 17, 225 and 228). To the best of our knowledge, the only *physisorbed* multidentate molecular anchors that enabled stable contacts to metal electrodes so far are fullerenes, pyrene and benzene.[17,38,225,229,230]

We investigated the conductance of platform-based molecules by controllably contacting them with the atomically sharp tip of a scanning tunneling microscope (STM). The geometries before contact formation were monitored by STM imaging. Contacts to inert and rigid functional units, methyl and hydrogen, turned out to exhibit similar conductances as a reactive propynyl wire that covalently binds to the STM tip.[XXXV,231] Atomistic transport calculations, however, show that different orbitals carry the current in these cases. Orbital symmetries are shown to affect the conductance as previously reported for small molecules (see, *e. g.*, Refs. 118 and 214). In addition, the forces acting across the tip-molecule-surface junction affect the geometry and the conductance-vs.-distance data.

---

[XXXIV] See, *e. g.*, Refs. 14–17, 36–39.

[XXXV] We use the term bond or bonded according the AIM (atoms in molecules) definition.[231] This definition implies that there is significant electron density between two atoms that are bonded to each other.

## 6.3. Experimental results

### 6.3.1. Metal-molecule junctions

TOTA (Fig. 6.1a) was used as a platform. The bare platform and TOTA functionalized with hydrogen, methyl and propynyl (H-TOTA, Me-TOTA and P-TOTA, Figs. 6.1b–d) were sublimated onto Au(111) surfaces at ambient temperature (Chap. 3, Sec. 3.5.3) and studied with STM at 4.6 K. Details of the syntheses can be found in References 140 and 232–234. Single molecules appear as triangular protrusions in STM images (Figs. 6.1e–h). The attached methyl and propynyl moieties are imaged as circular protrusions at the center of the platforms (Figs. 6.1 g and h). The H atom in H-TOTA (Fig. 6.1f) is not resolved, as expected (see, *e. g.*, Refs. 235 and 236). The molecules were contacted at their center with Au tips, whose apex orbital, close to the Fermi level, may be modelled as an *s* orbital (Chap. 3, Sec. 3.4.3). We verified that tips were not modified during measurements on molecules via STM imaging. The measurements were conducted at molecules in small clusters to reduce lateral movements. Results from the reactive P-TOTA molecules have been discussed in detail (Chap. 5) and are used here for comparison.

A related platform, triazatriangulenium (TATA), was previously investigated in an electrochemical environment.[44] Those experiments did not allow for the degree of control available in the present work. Nonetheless, conductances similar to those of thiols were found for junctions comprising one or a few ten molecules. In contrast to TATA, we found TOTA derivatives to be robust towards sublimation.

### 6.3.2. Conductances vs. electrode position

Figure 6.1i displays the conductances $G$ measured while the electrode, *i. e.* STM tip, was moved closer to the center of a molecule from the initial tunneling conditions ($V = 100$ mV, $I = 30$ pA). The position $z$ of the tip is referenced to the point of contact that was observed with the same tip on a bare fcc area of the Au(111) substrate (yellow curve). Before contact ($z > 0$ Å), the Au contact curve (yellow) exhibits an exponential variation (apparent tunneling barrier height: ≈ 4 eV) that reflects the size of vacuum tunneling gap. At $z = 0$ Å it abruptly rises to 1 $G_0$. This effect reflects (i) the formation of a bond to the Au(111) surface and (ii) a related elastic elongation of the Au tip.[144,219,237] After bond formation ($z < 0$ Å), the conductance varies only weakly.

The conductance curve of the bare TOTA platform (black curve, Fig. 6.1i ) serves as a reference. In the tunneling regime ($z < 2.2$ Å), the bare platform conducts by ≈ 2 orders of magnitude better than a corresponding vacuum gap (cf. black and yellow curves). At $z = 2.4$ Å, the conductance (black) abruptly rises. Since the Au apex atom is approaching the reactive center of the platform, a similar mechanism like for the pure Au contact may be expected and we attribute the abrupt rise to the formation of a Au–C bond between the tip and the molecule. The related conductance after contact formation (black dashed horizontal line), $\approx 3.5 \times 10^{-1}$ $G_0$, is high compared to other molecules connected to Au electrodes[238–240] and close to that of a pure Au point contact (≈ 1 $G_0$). However, a bond to a functional group may drastically change the electronic structure of the platform and may reduce the conductance.

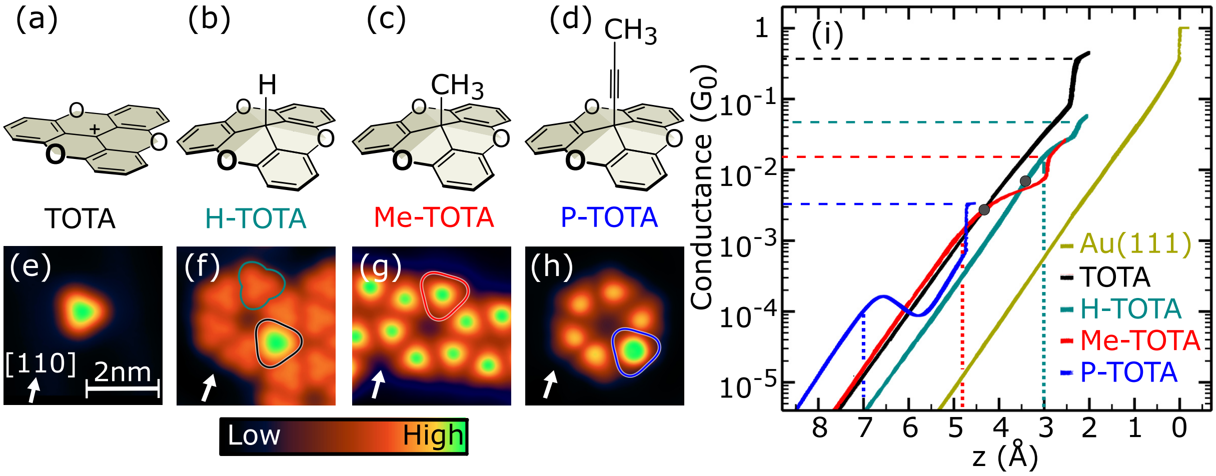

Figure 6.1.: (a–d) Lewis structures of trioxatriangulenium (TOTA), H-TOTA, Me-TOTA, and P-TOTA. The lengths of the functional groups measured from the central C atom of the platform to the topmost H atoms are 1.1, 2.0, and 4.5 Å (from left to right). (e–h) Constant-current STM topographs of (e) a single TOTA, (f) a cluster of H-TOTA (turquoise) along with a single TOTA (black), (g) a cluster of Me-TOTA (red) and (h) a single P-TOTA (dark blue) embedded in a cluster of 5 ethyl-TOTA molecules ($V$ = 100 mV, $I$ = 30 pA). The apparent heights of the molecules (a–d) in these images are 2.2, 1.6, 2.3, and 3.2 Å, respectively. White arrows indicate a ⟨111⟩ direction of the Au lattice. (i) Experimental conductance curves $G(z)$ of TOTA (black), H-TOTA (turquoise), Me-TOTA (red) and P-TOTA (dark blue) in units of the quantum of conductance $G_0 \doteq 2e^2/h$ ($e$: elementary charge, $h$: Planck constant). Zero tip position is defined as contact of the Au tip to a fcc area of the Au(111) substrate (yellow). The conductance curves of the molecules consists of at least 10 forward and 10 backward traces.

For a given $z$, the moieties attached to the TOTA platform (Figs. 6.1a–d) reduce the distance between the tip and the molecules. Naively a corresponding conductance increase would be expected in the tunneling regime. However, the conductance of H-TOTA (turquoise curve) at large separations ($z$ > 5 Å) is ≈ 4 times lower than that of the bare platform (black, Fig. 6.1i). In addition, the conductance of Me-TOTA (red curve) is about as large as that of TOTA (black). This effect is caused by substantial electronic differences between TOTA and the functionalized platforms. TOTA on Au(111) has its lowest unoccupied molecular orbital (LUMO) at ≈ $E_F + 0.6$ eV, while states of the functionalized platforms that protrude towards the tip are located at energies below $E_F - 1.5$ eV, much farther away from $E_F$ (SI, Sec. 6.7.1). As a result, these states contribute less to the current than the LUMO of the bare platform.

For $G \lesssim 10^{-4}$ $G_0$, the sequence of the conductances of the functionalized platforms reflects the lengths of the attached moieties. Surprisingly all molecules studied here exhibit a similar apparent tunneling barrier height of ≈ 4 eV.

At smaller separations, intriguing deviations from an exponential conductance evolution occur (Fig. 6.1i, dotted vertical lines) suggesting that forces between the molecule and the tip are involved. The slope of the conductance of Me-TOTA (red) begins to reduce at $z$ ≈ 4.8 Å ($G \approx 1.5 \times 10^{-3}$ $G_0$) indicating that mechanical contact occurs (red dotted vertical line). Mechanical contact to H-TOTA (turquoise) sets in at $z$ = 3 Å (turquoise dotted vertical line), *i. e.* 1.8 Å closer to the surface compared to Me-TOTA. This value may be caused by (i) the position of the topmost H atom (0.9 Å lower in H-TOTA) and

(ii) a smaller tip-induced force acting on the H atom than on a methyl moiety. In the case of P-TOTA (dark blue curve), the change of slope begins at $z \approx 7$ Å (dark blue dotted vertical line) and $G \approx 10^{-4}$ $G_0$. Taking into account that P-TOTA has an extra ethynyl spacer compared to Me-TOTA (length ≈ 2.5 Å), we find that mechanical interaction starts at similar tip-methyl distances (distance of the dark blue and the red dotted vertical line ≈ 2.2 Å).

The conductances of Me-TOTA (red) and P-TOTA (dark blue, Fig. 6.1i) at the onset of mechanical contact differ by one order of magnitude. Compared to Me-TOTA, the current path through P-TOTA is longer by ≈ 2.5 Å. In vacuum, this increase of the path length would reduce the conductance by a factor of ≈ 100. Hence, the ethynyl unit is one order of magnitude more conductive than a vacuum gap of the same size.

As discussed in Chapter 5, the complex conductance variation of P-TOTA results from short range repulsion between the topmost methyl moiety (Fig. 6.1d) and the tip apex. The propynyl wire bends while the tip-molecule and the molecule-substrate separations remain almost constant. The deformation induces a symmetry mismatch of the current-carrying orbitals at the tip-molecule interface that drastically reduces the conductance. As a result, at $z \approx 5.8$ Å, P-TOTA (dark blue) is ≈ 2.5 less conductive than Me-TOTA (red). In the range $z \approx 5.8$ to ≈ 4.8 Å the conductance G rises exponentially because the distance of the tip apex atom and the C atoms of the propynyl moiety, that are originally triple bonded (Fig. 1d), is reduced. The steep rise of G at ≈ 4.8 Å is due to bond formation between these C atoms and the apex atom.[140] Such bonding of Au clusters or cationic Au atoms to triple-bonded C atoms (Au–C–C bond) is well studied,[215–217] partially because it represents the highly important activation step of C≡C triple bonds towards nucleophiles in a catalytic cycle. The related strong hybridization of a LUMO of P-TOTA leads to new tip-molecule states close to $E_F$ that dominate the current flow.

During contact formation to Me-TOTA and H-TOTA the formation of a chemical bond is *not* expected, because the reactive center of TOTA is passivated by inert and rigid functional groups like a H atom or a methyl moiety.[XXXVI] Nevertheless, we observe abrupt increases of the conductance at positions $z = 2.3$ Å and 3 Å for H-TOTA (turquoise) and Me-TOTA (red curve), respectively. The corresponding conductances of $\approx 1 - 5 \times 10^{-2}$ $G_0$ are relatively high. For example, non-bonding Xe-Xe and CO-$C_2H_2$ contacts were reported to exhibit conductances that are an order of magnitude lower.[214,241] Considering the approximate sizes of H (1.1 Å) and methyl (2.0 Å) and the fact that bond formation to the bare platform occurs at $z = 2.5$ Å, drastic changes of the conductance are *expected* to occur at $z$ values that are much larger (gray circles in Fig. 6.1i). The surprisingly low $z$ values of the abrupt increases suggest that significant geometric changes of the junctions are involved. In order to understand the intriguing variations of the conductance of H-TOTA and Me-TOTA, we henceforth focus on the Me-TOTA junction. Most likely, the results are transferable to the H-TOTA junction.

---

[XXXVI] We use the term bond or bonded according the AIM (atoms in molecules) definition.[231] This definition implies that there is significant electron density between two atoms that are bonded to each other.

## 6.4. Theoretical results

### 6.4.1. Conductance and tip-induced geometry changes

The transport properties of Me-TOTA in a STM junction were calculated using density functional theory (DFT) combined with nonequilibrium Green's function (NEGF) methods (see Sec. 6.6). Figure 6.2a displays the calculated zero-bias conductance (black and grey) along with the experimental data (red) versus electrode separation $z$.

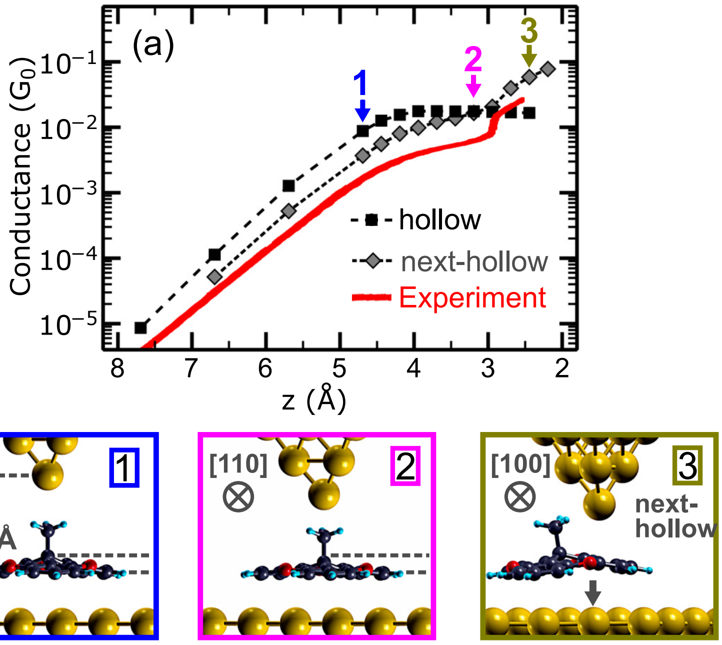

Figure 6.2.: (a) Theoretical and experimental conductance curves $G(z)$ of Me-TOTA. In the experiment (red), the tip was centered above the molecule before bringing it closer. Calculated conductances for the molecule located at a hollow (an adjacent hollow site) with the tip centered above the hollow site are shown by black squares (gray diamonds). The value $z = 0$ Å refers to the distance where a jump to contact is observed (see yellow curve in Fig. 6.1i). It corresponds to a distance of 4.3 Å between the bare surface and the apex of a frozen tip. (**1**–**3**) Calculated junction geometries corresponding to $z = 4.7$, 3.2 and 2.4 Å as indicated in panel (a). In configurations **1** and **2** (configuration **3**) the molecule is placed at the hollow (next-hollow) site. **1** and **2** are shown as side views in a ⟨110⟩ direction. **3** is viewed from a ⟨100⟩ direction. The arrow in **3** indicates the position of the hollow site.

For large tip-molecule separations the DFT calculations favor a Me-TOTA position at a hollow site of the substrate (SI, Sec. 6.7.2). The tip is centered above the molecule as in configuration **1** of Fig. 6.2. When the electrode separation is smaller than in configuration **1**, repulsive interaction between the methyl moiety and the tip occurs. At $z = 3.2$ and 3.0 Å the adjacent hollow sites (next-hollow) are already 0.35 eV and 0.50 eV more favorable than the initial hollow site (SI, Sec. 6.7.2). Consequently, instead of adopting configuration **2**, Me-TOTA shifts to an adjacent hollow site to relax strain. Configuration **3** displays the resulting geometry at small electrode separation ($z = 2.4$ Å).

The conductance calculated for the molecule and the tip centered on a hollow site (configurations **1** and **2**) is shown by black squares. It reproduces the experimental trend (neglecting an overestimation by a factor of ≈ 4, which is typical of DFT+NEGF results because DFT tends to underestimate HOMO–LUMO gaps[220]) but saturates for $z \lesssim 4$ Å in contrast to the experimental observations. The conductance for an adjacent hollow position of the molecule with the tip still centered over the original hollow site (configuration **3**) is displayed by gray diamonds. It exhibits a further rise of $G$ as observed in the experiments. We therefore attribute the $G(z)$ data and, in particular, the rapid rise at $z \approx 3$ Å to a reversible lateral shift of the molecule from its original hollow position to an adjacent hollow site. The experimentally probed molecules are embedded into molecular clusters. These clusters are too large to model them on the level of calculation we used. In our simplified model with only a single molecule, for large tip-molecule separations, neighboring adsorption sites have approximately the same energy (cf. SI, Sec. 6.7.2, Fig. 6.7). The displacement of single molecules is therefore not expected to be reversible and a hysteresis may occur. However, in the experiments intermolecular forces within a cluster usually prevent hysteresis (cf. Fig. 6.1i). The interpretation that Me-TOTA reversibly laterally shifts is also consistent with the observation that irreversible changes of the conductance only occurred for $z \lesssim 3$ Å and changed the arrangement of Me-TOTA in clusters. A related scenario of reversible hopping between adjacent hollow sites was previously reported for single Co and Ag atoms on Cu(111) and Ag(111), respectively.[242,243] In that case, local heating and attractive forces of the tip lead to bistability. Here, we emphasize that the abrupt conductance variation of Me-TOTA does not involve chemical bond formation.

### 6.4.2. Mechanical coupling at the metal-molecule interface

To analyze the mechanical properties of the junctions we determined the energy of the tip-molecule subsystem (Fig. 6.3a, black squares), which we define as the total energy of a junction from which all substrate atoms are removed while keeping the positions of the remaining atoms fixed. This energy is not affected by changes of the molecule-substrate interface. For Me-TOTA and different electrode separations with the tip centered above the molecule a shallow minimum of −140 meV (Fig. 6.3a, black squares) occurs close to configuration **1** of Fig. 6.2 confirming that no covalent or other chemical bond (binding energy $\gtrsim 0.5$ eV) between the tip and the molecule is formed. The absence of a chemical bond is also obvious from only marginal redistribution of electron charge within the molecule and the tip (SI, Sec. 6.7.3). In the repulsive regime ($z \lesssim 4$ Å), the tip-molecule energy (black squares) drastically increases as expected. Moreover, the repulsion of the tip and the methyl moiety induces a rapid increase of the strain energies of the molecule (gray circles) and the tip (yellow diamonds).

Although the tip presses on the molecule, the distance $d_1$ between the platform and the surface hardly changes ($< 0.2$ Å) when the tip is moved 1.8 Å towards the molecule (Figs. 6.3b and c). The platform is, however, flattened as indicated by the decreasing height of the central C atom of the platform ($d_2$ of Figs. 6.3b and c). Moreover, the tip is compressed ($d_4$ in Fig. 6.3c). These deformations prevent the tip apex from approaching the methyl group ($d_3$ in Figs. 6.3b and c). Consequently, the geometry of the tip-molecule and molecule-surface interfaces change only little compared to that of the molecule and the tip. Thus, both interfaces turn out to be more rigid than the molecule (Fig. 6.3a, gray circles) and the tip (Fig. 6.3a, yellow diamonds). This comes as a surprise, because the molecule is physisorbed.

To quantify the stiffness of the interfaces we calculated the energy change of the

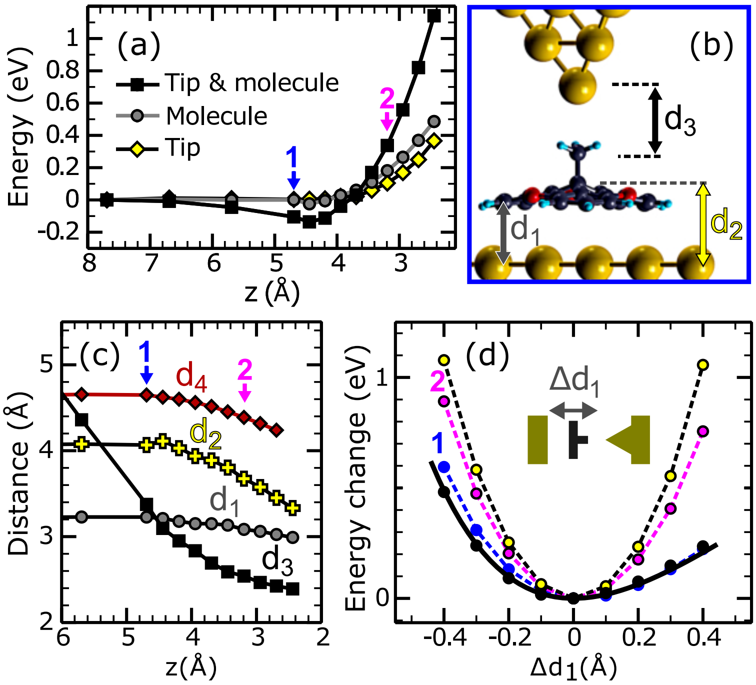

Figure 6.3.: Calculated results for Me-TOTA at a hollow site with the tip centered above the molecule. (a) Energy change of the subsystems tip-molecule (black squares), molecule (grey circles), and tip (yellow diamonds) versus $z$. The energy of each subsystem was calculated as the total energy of a junction from which all atoms that are not part of the subsystem are removed while keeping all other atomic positions fixed. Arrows indicate results for configurations **1** and **2** from Fig. 6.2. (b) Definition of distances. $d_1$: from outer C atoms of the platform to surface. $d_2$: from central C atom of the platform to surface. $d_3$: from apex atom to C atom of the methyl moiety. (c) Geometry changes of the metal-molecule interfaces vs. $z$. Results for distances $d_1 - d_3$ are indicated by black squares, grey circles, and yellow crosses, respectively. In the calculations a tetrahedral tip comprised of 3 Au(111) layers was used. Its length $d_4$ is defined as the distance of the apex atom to a reference plane at the base of the tip. (d) Energy change vs. rigid displacement $\Delta d_1$ (cf. pictogram) for junction configurations corresponding to $z = 7.7$ (black), 4.7 (dark blue), 3.2 (magenta) and 2.4 Å (yellow). $\Delta d_1 > 0$ indicates displacements of Me-TOTA towards the tip. A Morse potential fit to the black data points is shown by a black solid line.

junction upon a rigid vertical displacement of the molecule (Fig. 6.3d). When the influence of the tip is negligible (black and blue circles), the molecule-surface interaction can be modeled by an effective Morse potential (black curve). For the fit (black curve) the potential depth was set to the calculated adsorption energy of 1.8 eV. A force constant of 7 nN/Å is extracted from the fit. This value is comparable to those reported for covalent S–Au bonds (S–Au(111): 7–10 nN/Å[244] or S–Au$^+$: 17 nN/Å[245]) and also matches results for $C_{60}$ on Au electrodes.[246] The binding energies of a S atom (up to 1.8 eV[51,247]) and the TOTA platform are similar as well. These results show that physisorption of an extended $\pi$ system to a metal provides stable adsorption heights and thus is an attractive alternative to other bonding schemes.

Deeper in the repulsive regime ($z \lesssim 3.5$ Å, magenta and yellow circles in Fig. 6.3d) the energies for lifting and lowering the molecule become similar. The symmetry of the parabolas shows that the molecule is much deformed and thus rigidly couples the tip and the substrate.

The electrode-molecule interfaces may be viewed as hard springs (Fig. 6.3d), while the molecule itself and the STM tip are more compliant (gray circles and yellow diamonds of Fig. 6.3a). In a lateral direction, however, the stability of the position of the platform is low. Strain is therefore relaxed by the aforementioned lateral shift.

### 6.4.3. Impact of the electrodes on the molecular orbitals

As molecular orbitals lead to resonances of the electron transmission through the junctions, changes of the molecular orbitals may control the conductance during contact formation. Therefore, we calculated the influence of the tip-molecule and surface-molecule interactions on the molecular orbitals via the molecular projected self-consistent Hamiltonian (MPSH).[193,195] For a molecule at a hollow position (Figs. 6.4a–f) the spatial shapes of the MPSH states are hardly affected by the tip position and correspond to the molecular states of the gas-phase molecule. Surface-molecule and tip-molecule interactions are fairly unimportant in this case. For a molecule at an adjacent hollow position and at small electrode separation (Figs. 6.4g–i) the interaction with the tip leads to a slight increase of the MPSH density between the tip and the molecule. We attribute this effect to the electrostatic interaction of the tip and the molecule, which does not crucially affect the transmission through the states (see SI, Sec. 6.7.4). In addition to the orbitals' shapes, the energy separations of the orbitals close to $E_F$ are hardly affected by the interaction

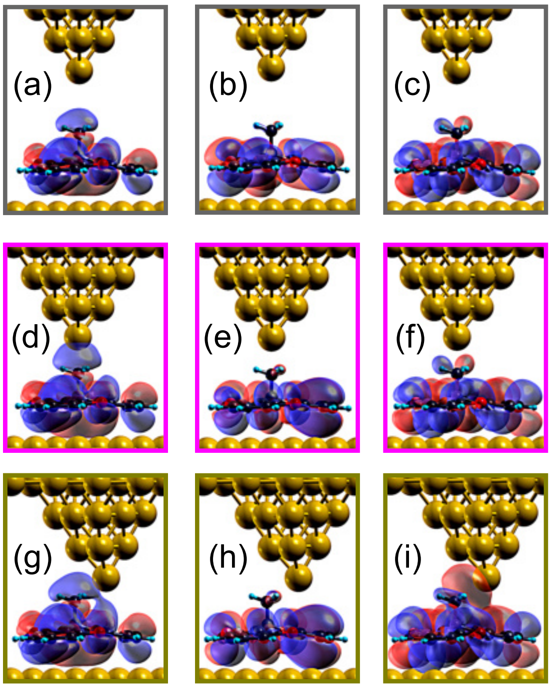

Figure 6.4.: (a–i) Isosurfaces of the HOMO−1, HOMO, and LUMO (left to right) of the MPSH Hamiltonian for different configurations. Blue and red colors indicate the sign of the wave functions. The HOMO and LUMO are both degenerate or nearly degenerate. As the shapes of the degenerate states are similar, only one of them is shown. (a–c) $z = 5.7$ Å with eigenenergies at $E - E_F = -1.56$, $-1.14$, and 2.54 eV (left to right), (d–f) $z = 3.2$ Å (configuration **2**) with eigenenergies at −1.83, −1.43, and 2.20 eV, (g–i) $z = 2.7$ Å (close to configuration **3**) with eigenenergies at −1.72, −1.33, and 2.35 eV.

with the surface and the tip (Figs. 6.4a–i and SI, Sec. 6.7.4). For example, the resulting gaps between the HOMO (highest occupied molecular orbital) and LUMO of Me-TOTA for configurations **2** (3.63 eV) and **3** (3.67 eV) from Fig. 6.2 are almost identical to the calculated gas-phase value (3.73 eV). Accordingly the conductance is *not* controlled by significant changes of the current-carrying orbitals. Instead, it is closely related to the geometry of the tip-molecule-surface junction.

### 6.4.4. Electron transport mechanisms

At electrode separations larger than in configuration **1** of Fig. 6.2, the vacuum gap represents the bottleneck for electron transmission. In configuration **1**, however, the bottleneck has shifted to the molecule-substrate interface as revealed by the calculated eigenchannel (Fig. 6.5a). As seen, the scattering state on the molecule reflects the HOMO−1 (cf. Fig. 6.5e), which dominates the transmission at $E_F$ (see SI, Sec. 6.7.4). The HOMO (Fig. 6.5f) is $\approx 0.5$ eV closer to $E_F$ than the HOMO−1 (Fig. 6.5e) but hardly contributes to the conductance because of its orbital symmetry. The local symmetry of the HOMO−1 at the methyl group is $s$-like, matches the tip $s$ wave (Fig. 6.5a), and provides large overlap and good electrical contact. By contrast, the HOMO exhibits a $p$-like shape at the methyl moiety. Its nodal plane reduces the overlap with the tip and leads to a bad electrical contact. The LUMO is farther away from $E_F$ and only has a weak impact on the conductance.

A projection of the transmission onto either all occupied or all empty states of the MPSH Hamiltonian (SI, Sec. 6.7.4) reveals that transport pathways through the empty states of Me-TOTA near $E_F$ *interfere destructively* with those through the occupied states.[XXXVII] For P-TOTA we find the opposite effect, *i. e.* the occupied and empty states interfere *constructively* (SI, Sec. 6.7.4). This shows that a functional group can change the interference properties of a molecular bridge, as previously reported, *e. g.*, for anthracene and anthraquinone based molecular wires.[248]

Between configurations **1** and **2** the conductance varies weakly (Fig. 6.2). While the molecule-substrate distance and the molecular states (see above) hardly change, the distance between the tip and the molecule shrinks despite the tip-induced deformation of the molecule. The lack of a corresponding increase of the conductance indicates that the coupling of the tip and the methyl group is almost saturated in configuration **1**. This is confirmed by the scattering states that hardly change from configuration **1** to **2** (Figs. 6.5a and b).

As shown above, to relax the repulsive forces across the junction, Me-TOTA shifts to an adjacent hollow position like in configuration **3** of Fig. 6.2. The shift affects the current in two ways (Fig. 6.5c). First, the coupling of the tip $s$ wave and the methyl moiety changes, because the nodal plane of the HOMO is no longer located at the tip position. Second, the vacuum-tunneling gap between the tip and the platform itself closes for small tip-molecule distances. As a result, the scattering state of configuration

---

[XXXVII] In contrast to eigenchannels and their transmissions (Chap. 4, Sec. 4.3.2.2) the transmission through MPSH states do not have to add independently. Therefore, the sum of different electronic pathways related to different molecular orbitals can add to a lower transmission than that of a single pathway.

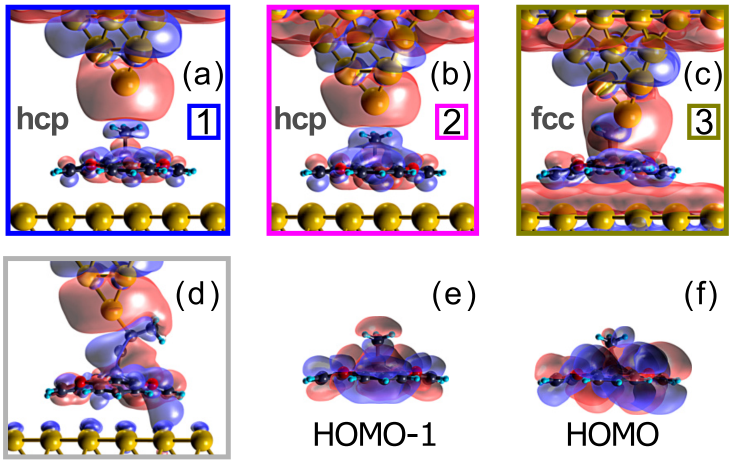

Figure 6.5.: (a–c) Isosurface plots of the real part of the most transmitting eigenchannels of configurations **1**–**3** of Me-TOTA (side views in the [110] direction). Electron waves coming in from the tip electrode at the $\bar{\Gamma}$ point. (d) Isosurface plot for P-TOTA at $z$ = 4.8 Å. The tip position is as in configuration **1** for Me-TOTA. (e–f) Isosurface plots of the HOMO-1 and the HOMO of Me-TOTA in the gas phase.

**3** exhibits no localized transmission bottleneck and the conductance increases but still remains < 0.1 $G_0$.

Remarkably, the geometries of the current paths through Me-TOTA and P-TOTA, namely a single C atom protruding from the platform, are similar around $z$ = 4.8 Å (cf. Figs. 6.5a and d). In the case of Me-TOTA, a soft mechanical contact with weak attractive interaction is formed, whereas P-TOTA covalently binds to the tip. Despite this difference the conductances differ only by a factor of 2. At further reduced electrode separations ($z \approx 3.8$ Å) the mechanical contact actually conducts better (≈ 35 %) and is still slightly attractive (Fig. 6.3a).

Chemical bonding changes the electronic structure of the electrodes-molecule junction and in particular the electronic structure of the molecule. Avoiding this complexity, *i. e.* preserving the electronic structure of the molecule despite attachment to an electrode, may simplify the design of a molecule with specific transport properties.[14,15,36,37,39,223]

## 6.5. Conclusions

We synthesized molecules that physisorb on a metal substrate with a wide platform and make a functional unit stand vertically. Conductance data from low-temperature STM contacts exhibit little scatter and show that the $\pi$ system of the platform provides a good electrical and mechanical contact to the substrate. This makes possible a detailed comparison between functional groups that are inert (methyl, H) or bind (propynyl, bare TOTA platform) to the tip. The lengths of the functional groups are reflected by the range of tip-molecule distances where deviations from an exponential conductance variation occur. All molecules exhibit a rapid conductance rise at small separations. The reasons under lying the rise in the cases of inert and binding subunits, however, are widely different, namely lateral motion vs. bond formation. The conductance of methyl TOTA at contact formation is only twice that of propynyl TOTA, which differs from methyl by an ethynyl spacer. Yet, similar conductances arise because the spacer is circumvented by the tip and because different orbitals carry the current. The results show that the platform anchor group and pm-control of the electrode position lead to reproducible contacts and large conductance without requiring chemisorption. Despite the simplicity of the functional groups used the conductance evolutions have multifaceted origins.

## 6.6. Computational methods

Simulations were performed with SIESTA[211] and TRANSIESTA[193,249] taking into account dispersion interactions.[182] The supercell contains a single Me-TOTA molecule adsorbed on a 10-layer Au(111) slab with $6 \times 6$ periodicity. A 10-atom Au(111) tetrahedron, mounted on the reverse side of the slab, represents the STM tip apex. We used a double-$\zeta$ plus polarization basis set with 0.02 eV energy shift for C, H, and O, as well as for the Au tip and surface layer atoms. For the bulk Au atoms, we used a single-$\zeta$ plus polarization basis with 0.02 Ry (0.272 eV) energy shift. Atomic coordinates of molecule, tip, and surface layer were relaxed until forces were smaller than 0.04 eV/Å. A cutoff of 400 Ry was used for the real-space grid integrations. The electronic structure was computed on a $2 \times 2 \times 1$ Monkhorst-Pack $k$-mesh. The transmission functions were sampled over $21 \times 21$ $k$-points. Projection of transmissions onto MPHS states were performed as described in Ref. 193. Eigenchannel scattering states were computed with INELASTICA.[194,212,213]

## 6.7. Supporting information

### 6.7.1. $dI/dV$ spectra

Differential conductance ($dI/dV$) spectra of TOTA, Me-TOTA, and P-TOTA molecules (Fig. 6.6a) reveal a broad LUMO peak at $\approx 0.6$ eV for the bare TOTA platform that is not present at the other molecules. A constant-height $dI/dV$ map of the bare platform (Fig. 6.6b) at of the energy of the LUMO ($E_F + 0.6$ eV) reveals that the LUMO is mainly located at the platform's reactive center. Passivating the reactive center by attaching a functional moiety may therefore drastically affect the electronic structure of the platform close to $E_F$. In fact, all investigated functionalized platforms do not exhibit any prominent state in the range $|E - E_F| \lesssim 1.5$ eV (cf. Fig. 6.6a). For Me-TOTA and P-TOTA the onset of an occupied molecular state is visible at $< E_F - 1.5$ eV.

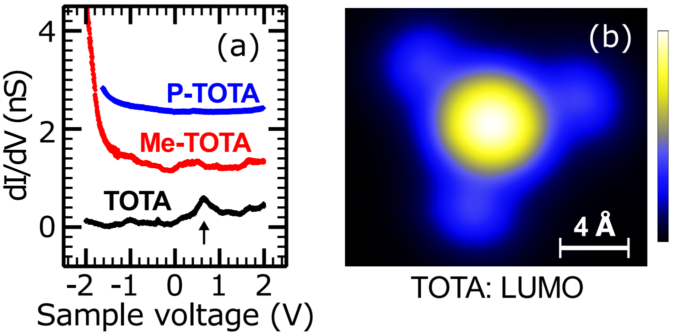

Figure 6.6.: (a) Differential conductance ($dI/dV$) spectra of TOTA (black), Me-TOTA (red), and P-TOTA (blue). A black arrow indicates the position of the LUMO peak of the bare platform. For clarity the $dI/dV$ spectrum of Me-TOTA (P-TOTA) is vertically shifted by +1 nS (+2 nS). Zero voltage corresponds to $E_F$. The feedback loop was opened at 0.5 nA and 2 V. (b) Constant-height $dI/dV$ map of the LUMO of a single TOTA molecule ($V = 0.6$ V). The feedback loop was opened over the molecule's center at 0.9 nA and 0.6 V.

### 6.7.2. Energy of the Me-TOTA junction

Figure 6.7 displays the energy change of Me-TOTA junctions with the height $z$ of the tip, which is centered above the hcp-hollow site. Data are shown for the molecule initially located at a hcp-hollow site (hollow, black squares) and at a fcc-hollow site (next-hollow), either fixed at this position (yellow circles) or allowing for lateral relaxation (blue diamonds).

At large tip-molecule separations ($z \gtrsim 4.8$ Å), the energy change is negligible in all cases because the tip does not affect the adsorption energy of the molecule. Our DFT calculations favor hcp-hollow and fcc-hollow sites on Au(111) (adsorption energy $\approx 1.8$ eV). Other sites like the on-top position are less favorable by more than 100 meV.

For electrode separations $z \lesssim 4.5$ Å the tip begins to modify the junction energy. The different positions of the molecule with respect to the tip therefore evolve differently.

When the tip is centered over the molecule (black squares), the energy increases first slightly and then more drastically at smaller $z$. The slight increase at $z \approx 4.5$ Å is

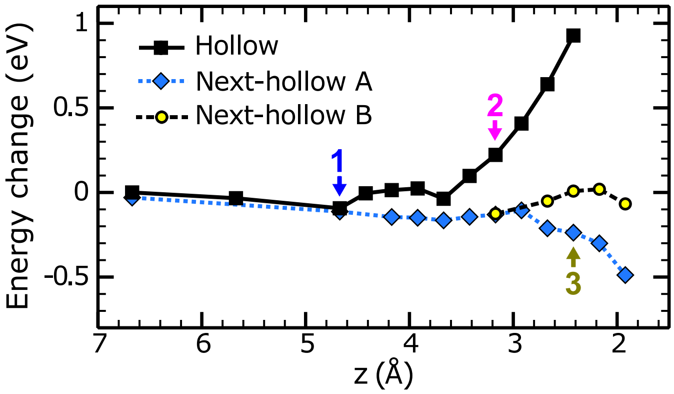

Figure 6.7.: Calculated energy change for Me-TOTA at a hcp-hollow site (black squares), at an adjacent fcc-hollow site (blue diamonds), and at an adjacent fcc-hollow site with laterally frozen adsorption position (yellow circles) versus tip position $z$. The tip is centered above the hcp-hollow site. The minor energy difference (< 30 meV) of the hcp-hollow and fcc-hollow positions at large tip-molecule distance ($z \gtrsim 4.8$ Å) is below the expected accuracy of the DFT calculations.

dominated by tip-induced changes of the adsorption geometry (Fig. 6.3c), *i. e.* changes of the substrate-molecule interaction. The more steep increase at $z \lesssim 3.5$ Å is mainly caused by repulsive tip-molecule interaction (black squares in Fig. 6.3a) as discussed in in Section 5.3.

When the tip and the molecule are not vertically aligned (molecule placed at an adjacent hollow site, blue diamonds and yellow circles in Fig. 6.7) the distance between the methyl moiety and the tip is larger. Consequently the adsorption geometry is not much affected for $z > 3.4$ Å and the energy change of the junction is controlled by a weak attractive tip-molecule interaction. As a result, the adjacent fcc-hollow sites become more favorable than the hcp-hollow site for electrode separations smaller than in configuration **1**.

For $z < 3.4$ Å the interaction between the tip and the methyl moiety is repulsive and the energy first increases (blue diamonds). However, to relax strain the molecule shifts laterally (by 0.7 Å at $z = 2.4$ Å). As coupling of the tip to the molecular $\pi$ system increases at $z < 3.0$ Å, the junction energy is considerably reduced. When the molecule is laterally frozen at the adjacent fcc-hollow site (yellow circles), the junction energy slightly increases due to the strain within the junction and hardly changes compared to a configuration without tip. Moreover, the tip deforms in such a way that the geometry of the tip-molecule interface is hardly different to the case where the molecule is not fixed at the adjacent hollow site. As a result, the conductances of with a frozen and a relaxed lateral position of the molecule are very similar.

When the tip is lowered further ($z = 1.9$ Å) in any of the geometries of Fig. 6.7, it does not remain stable, the apex atom detaches, and is deposited on the surface.

### 6.7.3. Electron density redistributions

To highlight differences between tip-molecule contacts with (P-TOTA) and without (Me-TOTA) chemical bond,[XXXVIII,231] we analyze the electron density change induced by the tip-molecule interaction. The electron density redistribution is calculated by subtracting the densities of two components of the junction, namely, the molecule and the tip + surface, both with frozen geometries like in the entire junction, from the density of the entire junction. The charge redistribution for Me-TOTA at $z = 4.2$ Å (Fig. 6.8a) is only marginal despite maximal tip-molecule attraction. This is not compatible with a formation of a chemical bond between the tip and the molecule. It can be understood from electrostatic interaction of the tip and the molecule.

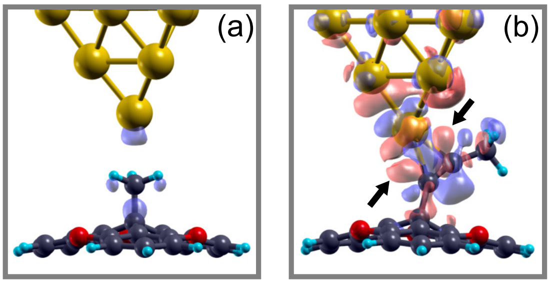

Figure 6.8.: Calculated electron density redistribution induced by the tip-molecule interaction. (a) Me-TOTA at $z = 4.2$ Å (hcp-hollow), (b) P-TOTA at $z = 3.7$ Å. Blue (red) colored isosurfaces correspond to depletion (accumulation) of electron density. In both configurations the attraction between tip and molecule is almost maximal (cf. Fig. 6.3a for Me-TOTA and Fig. 5.3a for P-TOTA). The arrows in (b) indicate areas of accumulation of electron density between the tip apex and the originally triple bonded C atoms.

For P-TOTA, there is a large and complex charge redistribution in the tip and the molecule (Fig. 6.8b), in contrast to the Me-TOTA case. The reduced electron density (blue) around the originally triple bonded C atoms in the propynyl moiety is caused by the formation of a Au–C–C bond,[140,215–217] as the tip apex breaks the triple bond in favor of a double bond and binds to the adjacent C atoms. Accordingly, the two areas of accumulation of electron density between the tip and the molecule (red balloons indicated by arrows in Fig. 6.8b) reflect the two bonds between the apex Au atom and the originally triple bonded C atoms.

### 6.7.4. Electron transmission functions, MPSH states, and interference effects

Figure 6.9 presents transmission functions of a Me-TOTA molecule located at a hcp-hollow site and the tip above at its center (cf. black squares in Fig. 6.2a). Data for three electrode separations are displayed. The current around $E_F$ is dominated by the HOMO–1 resonance at $\approx -1.5$ eV, whereas the nearly degenerate HOMOs at $\approx -1.1$ eV do not cause prominent transmission resonances. The resonance related to the nearly degenerate LUMOs at energies $\gtrsim 2.2$ eV dominate the transmission only up to $\approx +1$ eV.

---

[XXXVIII] We use the term bond or bonded according the AIM (atoms in molecules) definition.[231] This definition implies that there is significant electron density between two atoms that are bonded to each other.

Consequently, the HOMOs and LUMOs are rather unimportant for the transmission at $E_F$. A broad resonance at ≈ 0.2 eV contributes to the calculated current and is related to states of the tetrahedral tip.

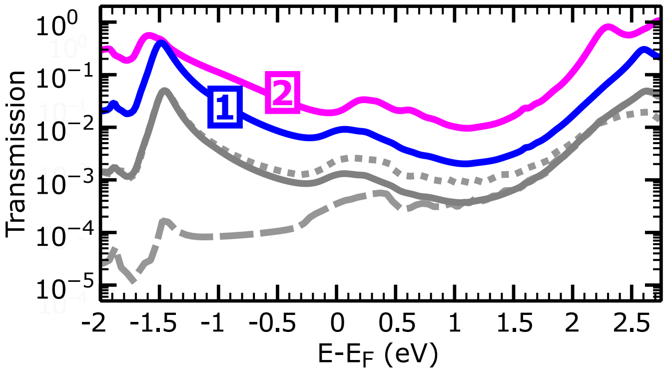

Figure 6.9.: Electron transmission vs. energy for Me-TOTA at the hcp-hollow position for different electrode separations $z$ = 5.7 (gray), 4.7 (blue, configuration **1**) and 3.2 Å (magenta, configuration **2**). The tip is centered above the molecule. Dotted (dashed) gray curves show projected transmissions onto the occupied (empty) MPSH states for $z$ = 5.7 Å.

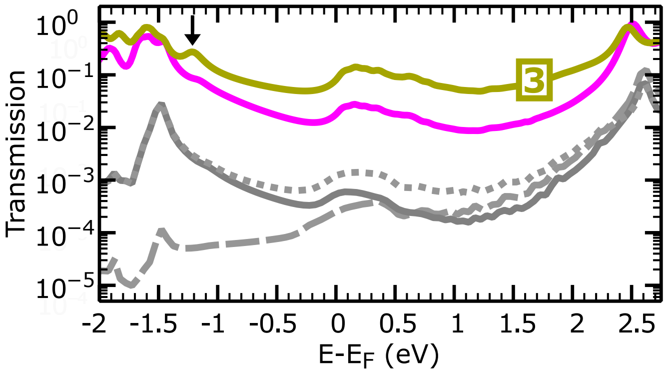

Figure 6.10.: Electron transmission vs. energy for Me-TOTA shifted to an adjacent fcc-hollow position for different electrode separations $z$ = 5.7 (gray), 3.2 (magenta) and 2.4 Å (yellow, configuration **3**). The lateral tip position is unchanged with respect to the surface, hence these geometries correspond to an off-center tip position over the shifted molecule. Dotted (dashed) gray curves show projected transmissions onto the occupied (empty) MPSH states for $z$ = 5.7 Å.

The above simple picture of transport through one predominant orbital only holds approximately as interference effects arise between pathways associated with the individual states of the molecular bridge. Transmission functions in Figs. 6.9 and 6.10 projected onto either all occupied (dotted gray line) or all empty states (dashed gray line) of the MPSH Hamiltonian reveal that near $E_F$ the transmission is decreased (increased) in the absence of the occupied (empty) states. Thus, the empty states such as the LUMOs interfere *destructively* with the occupied states that dominate via the HOMO–1 the overall transport through Me-TOTA.

For comparison, we show in Fig. 6.11 the corresponding transmission projections on occupied and empty states for P-TOTA. As explained in Ref. 140, for P-TOTA the HOMO resonance dominates until a Au-C bond is formed and a new LUMO-resonance (cf. arrow in Fig. 6.11b) comes into play. Further, from Fig. 6.11 we also conclude that the occupied and empty states interfere *constructively* for transport through P-TOTA. The two functional groups thus display different interference effects.

Whereas the positions of the resonances hardly change for electrode separations larger than in configuration **1** (cf. gray and blue curves in Fig. 6.9), they are shifted by ≈ 0.3 eV in configuration **2** (magenta). In fact, the separation of the resonances related to the HOMO–1 and LUMOs is reduced by 5% from 4.08 eV to 3.88 eV. This change between configuration **1** and **2** is due to a deformation of the molecule (namely flattening) that is induced by the STM tip. Gas-phase calculations for a molecule frozen in the distorted geometry reproduce the change. As a consequence, the conductance is mainly controlled by the geometry of the junction rather than changes of its orbitals.

The transmission of a molecule at an fcc-hollow position with the tip still centered over an hcp-hollow site (cf. gray diamonds in Fig. 2a) is displayed in Fig. 6.10. For large electrode separation (blue) the transmission is mediated by the same molecular states as for the hcp-hollow configuration. In addition, the molecule is less deformed when the tip-molecule distance is reduced and the molecular states are hardly affected. For small electrode separation (yellow) a new resonance appears at ≈ −1.1 eV (arrow in Fig. 6.10b). It is related to the nearly degenerate HOMOs. As discussed in the main text, this is caused by a change of the orbital symmetries at the tip-molecule interface.

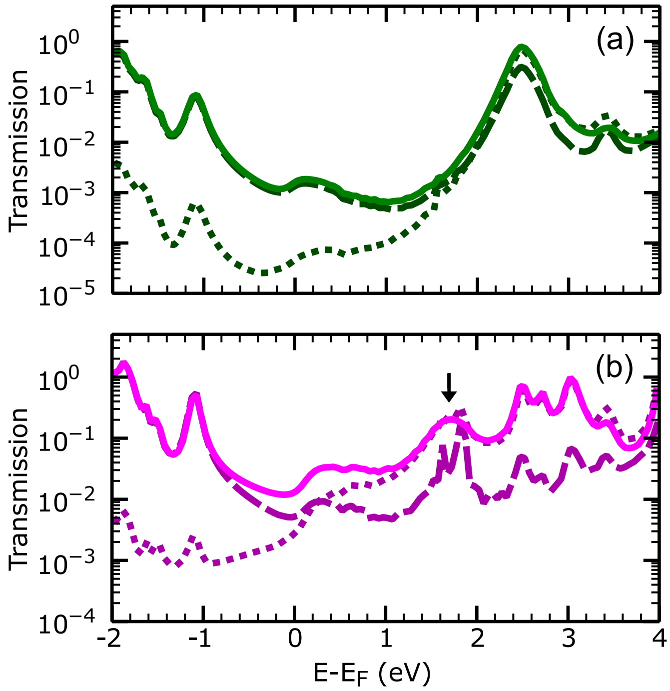

Figure 6.11.: Electron transmission vs. energy for P-TOTA at the hcp-hollow position for different electrode separations. (a) configuration **2** and (b) configuration **4** from Ref. 140. The tip was centered above the molecule. Dashed (dotted) curves show projected transmissions onto the occupied (empty) MPSH states. *Close* to $E_F$, the transmissions projected onto all occupied and all empty states essentially add up to the total transmission, indicating that occupied and empty states do not interfere destructively.

## 6.8. Acknowledgement

We thank the Deutsche Forschungsgemeinschaft (SFB 677), and the Spanish MINECO (Grants No. MAT2016-78293-C6-4-R and FIS2017-83780-P) for financial support.

## 6.9. Contributions

Sandra Ulrich and Rainer Herges synthesized the molecules. I measured and analyzed the experimental data. Aran Garcia-Lekue and Thomas Frederiksen performed the DFT-NEGF calculations. I wrote the first draft of the manuscript.[141] Richard Berndt supervised the project. All authors discussed the results and improved and commented on the manuscript.

# Part III.

# Switching, Self-assembly, and Stability of Functionalized Platform Molecules

7

# Directional Rotation of Ethoxy and Ethyl Moieties on a Molecular Platform on Au(111)

This chapter is based on a manuscript published in *ACS Nano*. The publication is reprinted (adapted) with permission from

Torben Jasper-Tönnies, Manuel Gruber, Sven Johannsen, Thomas Frederiksen, Aran Garcia-Lekue, Torben Jäkel, Fynn Röhricht, Rainer Herges, and Richard Berndt, ACS Nano **14**, 3907 (2020). Copyright 2020 American Chemical Society.

## 7.1. Abstract

Molecular rotors have attracted considerable interest for their prospects in nanotechnology. However, their adsorption on supporting substrates, where they may be addressed individually, usually modifies their properties. Here, we investigate the switching of two closely-related three-states rotors mounted on platforms on Au(111) using low-temperature scanning tunneling microscopy and density functional theory calculations. Being physisorbed the platforms retain important gas-phase properties of the rotor. This simplifies a detailed analysis, and permits, for instance, the identification of the vibrational modes involved in the rotation process. The symmetry provided by the platform enables active control of the rotation direction through electrostatic interactions with the tip and charged neighboring adsorbates. The present investigation of two model systems may turn out useful for designing platforms that provide directional rotation and for transferring more sophisticated molecular machines from the gas-phase to surfaces.

## 7.2. Introduction

Switches and motors are essential engineering components in our macroscopic world as well as at the molecular level.[250,251] Considerable effort is made to synthesize artificial motors that mimic biological examples or offer prospects in nanotechnology.[10] Rotor molecules deposited on surfaces may be investigated at a sub-molecular scale using scanning tunneling microscopy (STM).[9,11] The compounds thus studied fall into two classes.

Either molecular adsorbates serve as a rotor and the substrate is used as a stator[252–267] or the stator and the rotor are subunits of the same molecule.[268–272] Besides rotors there are also rotary switches that alternate between two rotation angles[91,127,236,273,274] and consequently do not enable studies on the directionality of the motion, which is essential for using a rotor in a motor.[9,10]

The adsorption of molecules on surfaces often modifies their gas-phase properties. While these modifications may be beneficial, *e. g.*, by inducing an asymmetry,[275] which is essential for the directionality of the rotation,[272,276,277] they render predictions of the on-surface properties of a molecule difficult.

Here, we investigate two closely related three-state stepper motors using STM and density functional theory (DFT) calculations. In contrast to previous studies, we employ a rigid and planar molecular platform, namely trioxatriangulenium (TOTA),[232] as anchor rather than using single atoms like, *e. g.*, sulfur[269–271] or flexible molecular subunits.[272] The platform serves as stator, separates the rotor from the substrate[42,140,141] and provides an electronic decoupling because it binds to Au surfaces *via* physisorption[140,141] in contrast to most chemically bonded platforms.[41] We show that this approach preserves important gas-phase properties of the molecules, such as the rotational energy barriers and the vibrational modes involved in rotation. Inelastic electron tunneling excites the relevant vibrations, which in turn switch the orientation of the rotors. Although the molecules are achiral, directionality of the rotational steps is induced and controlled through the interaction with the STM tip or neighboring adsorbates. The electronic decoupling provided by the platform effectively increases the switching yield of the rotor, and may lead to longer lifetime of electronic excited states of the rotor, which would be useful to control the rotation by light.[278–280]

## 7.3. Results and discussion

### 7.3.1. Three-state rotors

Ethoxy-TOTA and ethyl-TOTA molecules (Figs. 7.1a and b) were designed to serve as three-state rotors with the versatile TOTA platform adsorbed to the substrate as stator and the central moiety as rotor. Although the platform physisorbs, its adsorption energy on a metal surface is close to that of a chemical bond owing to the lateral extension of the molecule, *i. e.* in the order of 1 eV (100 kJ/mol).[140,141] The ethoxy and ethyl moieties are freestanding and inclined with respect to the metal substrate,[140,141] and are located in one of the three mirror planes of the $C_{3v}$ symmetric platform (see topviews in Figs. 7.1a and b). Two hydrogen atoms of the moieties bind via a CH···O hydrogen bond to one of the three oxygen atoms of the platform. In addition, ethyl-TOTA has two further CH···O bonds to the remaining two oxygen atoms of the platform. Switching between the three symmetry-equivalent positions corresponds to a rotation of the moiety, *i. e.* a change of its torsion angle. As the molecules exhibit a $C_{3v}$ symmetry, no directional rotation is expected.

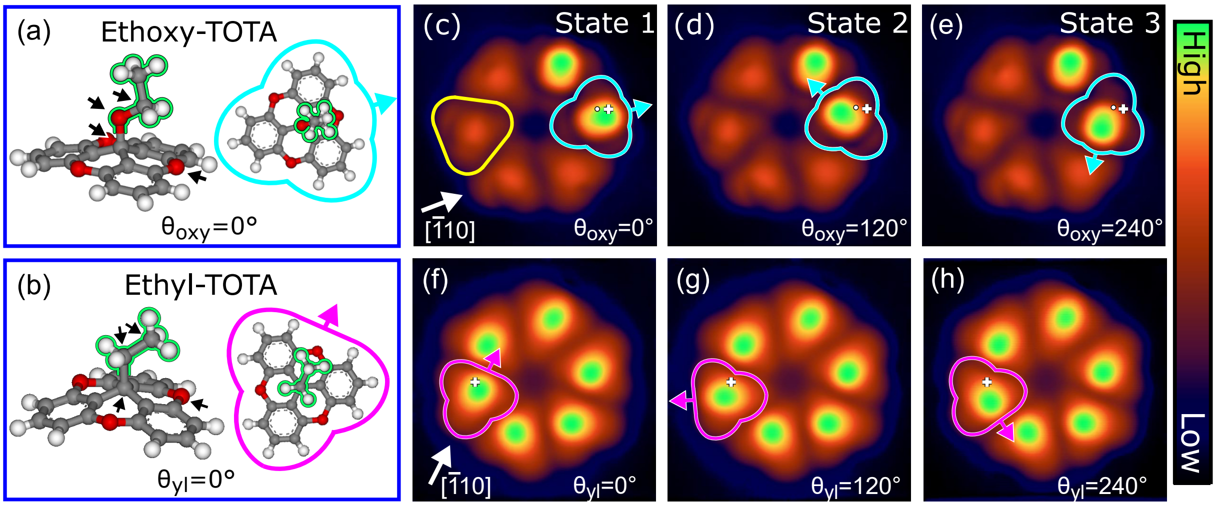

Figure 7.1.: (a–b) Gas-phase molecular structure of ethoxy-trioxatriangulenium (ethoxy-TOTA) and ethyl-TOTA. Gray, red and white spheres indicate carbon, oxygen and hydrogen atoms. The torsion angles $\theta_{\mathrm{oxy}}$ and $\theta_{\mathrm{yl}}$ of the ethoxy and ethyl moieties (encircled in green) are defined by the four atoms that are highlighted by black arrows in (a) and (b). (c–e) STM topographs showing current-induced switching (image size $(3.9\,\mathrm{nm})^2$, current $I = 30\,\mathrm{pA}$, sample voltage $V = 100\,\mathrm{mV}$). An ethoxy-TOTA molecule (turquoise border) in a hexagonal cluster of two ethoxy-TOTA and four OH-TOTA molecules (example marked with yellow border) is switched by injecting current at the position of the white cross. A turquoise-colored arrow shows the orientation of the ethoxy group. Starting from $\theta_{\mathrm{oxy}} = 0$ in (c), 120° and 240° are obtained in (d) and (e). (f–h) Analogous data from a cluster comprising of six ethyl-TOTA molecules. From (f) to (h) the direction of the $CH_2{-}CH_3$ bond of the ethyl moiety within the marked molecule is switched into three configurations with $\theta_{\mathrm{yl}} = 0, 120$ and 240°. The STM images were processed by merging the raw data with a smoothed and inverted Laplace-filtered image to enhance the contrast. In the raw images the maximum apparent heights of OH-TOTA, ethyl-TOTA, and ethoxy-TOTA molecules are 0.21, 0.26 and 0.31 nm, respectively.

## 7.3.2. Adsorption geometry

In two separate experiments, ethoxy-TOTA mixed with OH-TOTA molecules[XXXIX] and ethyl-TOTA molecules (Figs. 7.1a and b) were sublimated onto Au(111) at ambient temperature and studied with STM at 4.6 K (Sec. 7.5 and Chap. 3, Sec. 3.5.3). At low coverages, the intact TOTA molecules self-assemble into clusters composed of 6 molecules. Single molecules (Figs. 7.1c and f, ethoxy-TOTA: turquoise bordered, OH-TOTA: yellow bordered, ethyl-TOTA: magenta bordered) are imaged as triangular protrusions in accordance with the symmetry of the platform.

The orientation of the moiety of ethoxy-TOTA is discernible by its off-centre position and the elliptic shape of the highest areas of the image (green colored area, Fig. 7.1c). For example, the configuration of the ethoxy-TOTA in Fig. 7.1c (turquoise) is equal to that in the model in Fig. 7.1a. Analogous data from ethyl-TOTA are shown in Fig. 7.1f (magenta).

The three possible orientations of the moieties translate into three torsion angles

---

[XXXIX] The mixture was used to perform two experiments in parallel on the same sample. Here, we focus on ethoxy-TOTA.

$\theta_{oxy}$ and $\theta_{yl}$ that are defined via the four atoms marked in Figs. 7.1a and 7.1b. STM topographs (Figs. 7.1c and f) reveal that the stable orientations $\theta_{oxy}$ ($\theta_{yl}$) of the ethoxy (ethyl) moiety, namely 0, 120 and 240°, are identical to those of the gas-phase molecules. $\theta_{oxy} = 0°$ ($\theta_{yl} = 0°$) is defined as the torsion angle for which the mirror plane of the molecule is approximately parallel to the $[\bar{1}10]$ direction of Au(111) (cf. Figs. 7.1c and f).

### 7.3.3. Tunneling induced moiety rotation

The torsion angle can be changed by injecting current through the molecules at suitable sample voltages and positions. For example, in Figs. 7.1c–e the ethoxy-TOTA molecule (turquoise) was switched from $\theta_{oxy} = 0°$ to 120° and then to 240°. Analogous data for ethyl-TOTA (magenta) are displayed in Figs. 7.1f–h. The switching is molecule-selective and does not affect any neighbors as long as mild parameters ($V < 400$ mV, $I < 500$ pA) are used.

To efficiently read out the torsion state of a molecule, the STM tip was positioned over it at a specific position indicated by a white cross in Figs. 7.1c–e and f–h. This position breaks the molecular symmetry and leads to characteristic currents (feedback off) or heights (feedback on).[XL] After moving the tip to such a position, the sample voltage was increased until abrupt changes of the current were observed (feedback off). Figure 7.2 shows a typical time series of the tunneling current from an ethoxy-TOTA molecule at $V = 185$ mV. Three distinct levels 1–3 are discernible with average currents of 115 pA, 75 pA (–35 %) and 33 pA (–71 %) colored in blue, black and red, respectively. Using additional topographs, we verified that the levels reflect states $\theta_{oxy} = 0$, 120 and 240°, respectively. Ethoxy-TOTA and ethyl-TOTA can actually be set to a desired state (0, 120 and 240°) by rapidly reducing the sample voltage once the corresponding target current is reached. The switching does not show any sign of fatigue, even after tens of thousands of events.

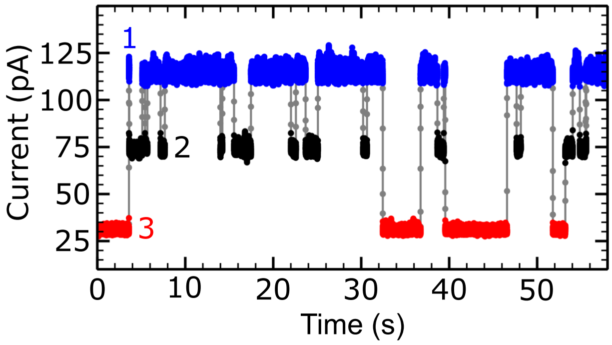

Figure 7.2.: (a) Time series of the tunneling current measured with the tip positioned over an ethoxy-TOTA molecule. The corresponding lateral tip position is indicated by a white cross in Figures 7.1c–e. A sample voltage $V = 185$ mV was applied and the current feedback was opened at a current $I = 27$ pA. The current levels 1–3 correspond to states **1**–**3** (cf. Figs. 7.1c–e). Intermediate current values (gray points) are measured because the band-width limited signal from the transimpedance amplifier was oversampled.

---

[XL] This detection scheme has previously been used for, *e. g.*, oxygen molecules on Pt(111)[253] and thioether on Au(111).[254]

The switching rate $R$, defined as the number of detected switching events per time interval, depends crucially on the tunneling current $I$. At a given voltage and for $I <$ 500 pA, we find $R \propto I^N$ with $N \approx 1$ (not shown). The reaction order of one indicates that, while a large fraction of the electrons elastically tunnels without affecting the state of the investigated molecule, the switching is induced by single-electron tunneling. In that respect, the energy transfer from a single tunneling electron is sufficient to change the state of the adsorbate. At smaller tip-molecule distances, *i. e.* higher currents, mechanical contact may play a role, too (Chap. 6). Here, we focus on results obtained at large separations.

## 7.3.4. Action spectroscopy

Action spectra, *i. e.* the switching yields $Y = R/(I/e)$ ($e$ : elementary charge) per electron as function of the sample voltage (Chap. 3, Sec. 3.3),[129–131] were measured for both molecules (Fig. 7.3). As the switching rate $R$ is proportional to the current $I$, the yield $Y$ is approximately constant at fixed $V$. The action spectra of ethoxy-TOTA and ethyl-TOTA are drastically different (Fig. 7.3). In particular, while the minimal voltage to efficiently switch ethoxy-TOTA ($Y \gtrsim 10^{-11}$) is $\approx$ 160 mV, this voltage has to be more than doubled ($\approx$ 360 mV) for ethyl-TOTA. This difference is rather surprising because the binding of the TOTA stator molecules to Au(111) is virtually identical (see below) and both moieties are attached via $sp^3$ $\sigma$ bonds (cf. Figs. 7.1a and b).

The evolutions of $Y(V)$ in Fig. 7.3 are typical of switching events that are induced by single-electron tunneling via vibrational excitation of the molecules.[129,130] For this scenario an analytic expression for $Y(V)$ was derived in Ref. 131 (see also Equation 7.4 and 7.5 in SI, Sec. 7.7.1) that we used to fit the data (gray and green lines in Fig. 7.3). The fits reveal two vibrational modes at $180 \pm 2$ and $367 \pm 3$ meV for ethoxy-TOTA and one mode at $371 \pm 1$ meV for ethyl-TOTA (see arrows in Fig. 7.3). It should be noted that a similar quality of the fits can be achieved by using several modes whose energies differ by less than $\approx 10$ meV from the aforementioned values. The experimental data consequently do not enable the identification of a *single* vibrational mode. For ethoxy-TOTA, only the onset of the second drastic yield increase at $|V| \gtrsim 360$ mV could be measured because the switching became too rapid to be resolved with our STM at pA currents.

The onsets of abrupt increases are essentially dictated by the energies and the spectral form of the vibrational modes involved in the process (SI, Sec. 7.7.1 and Ref. 131). The increases at $|V| > 200$ and $< 350$ mV for ethoxy-TOTA and $|V| > 390$ mV for ethyl-TOTA can be modeled with the expression (SI, Sec. 7.7.1):

$$Y(|V|) = K\left(1 - \frac{\hbar\Omega}{|eV|}\right)\theta(|eV| - \hbar\Omega), \tag{7.1}$$

where $K$ is a dimensionless prefactor, $\hbar\Omega$ the vibrational mode energy, and $\theta$ is the step function, which extends the definition of Equation 7.1 to voltages $|eV| < \hbar\omega$. The energies of the tunneling electrons range from 0 to $|eV|$. Assuming a constant density of states, the factor $(1 - \hbar\Omega/|eV|)$ corresponds to the fraction of the current for which the electron energies exceed $\hbar\Omega$, *i. e.* it describes the fraction of tunneling electrons that can excite the vibrational mode.

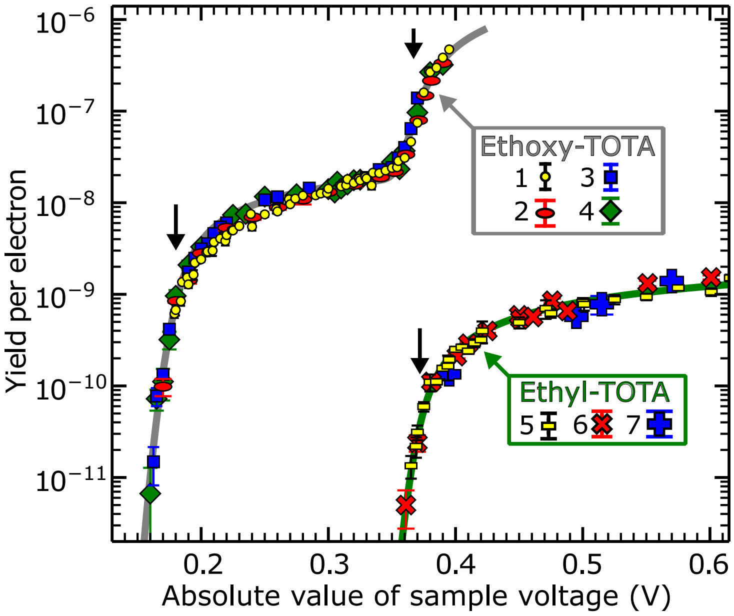

Figure 7.3.: (a) Yield (switching probability per electron) vs. $|V|$ for ethoxy-TOTA (symbols 1–4) and ethyl-TOTA (symbols 5–7). Current was injected into ethoxy-TOTA (ethyl-TOTA) at the position of the white cross in Fig. 7.1(c–e) [Fig. 7.1(f–h)]. Data sets 2 and 6 were recorded at negative $V$. Bars indicate the standard deviation $\sigma$ expected from a Poisson process. Fits using Equations 7.4 and 7.5 (gray and green line) reveal that vibrational modes at energies of $180 \pm 2$ and $367 \pm 2$ meV for ethoxy-TOTA and $371 \pm 3$ meV for ethyl-TOTA (black arrows) are involved in the switching processes . Data sets 3 and 4 were acquired on a molecule adjacent to a 6-molecule cluster, *i. e.* with a single neighbor. The best agreements are obtained with widths of the vibrational density of states (vDOS) $\sigma_G \lesssim 10$ meV (Eq. 7.6, SI, Sec. 7.7.1).

At first glance, $K$ may seem to be closely related to the probability of vibrational excitation by tunneling electrons, which is typically of the order of 0.01 to 0.1.[281–283] However, to lowest order in the electron-vibration coupling, the inelastic cross section approximately cancels out from $K$ because the competing electron-hole pair creation rate of the vibrational mode varies in a similar manner (see SI, Sec. 7.7.1 and Refs. 131 and 129). Therefore, the prefactor $K$ is mainly determined by the (anharmonic) decay rate $\gamma_{RC}$ of the excited vibrational mode into the rotation coordinate. In the case of ethoxy-TOTA $K \approx 3.4 \times 10^{-8}$ is more than one order of magnitude larger than for ethyl-TOTA ($\approx 3.2 \times 10^{-9}$). The second rise of the yield for ethoxy-TOTA further increases this ratio to more than three orders at $\approx$ 400 mV. This drastic increase suggests that ethoxy-TOTA transfers energy from the excited vibrational modes to the reaction coordinate more efficiently despite the fact that relevant vibrational mode energies are almost identical ($\approx$ 370 meV). We would like to stress that in the off-resonant regime, the prefactor $K$, and henceforth the yield at a given voltage, is proportional to $1/\Gamma^2$, where $\Gamma$ is the related to the electronic coupling of the adsorbate to the substrate (SI, Sec. 7.7.1). Therefore, electronic decoupling, provided for instance by the platform itself or by employing a thin insulating layer, may significantly increase the yield of a rotor.

### 7.3.5. Vibrational modes involved in the rotation

Ethoxy-TOTA and ethyl-TOTA both physisorb to Au(111) in a typical configuration for functionalized TOTA platforms, namely on *hcp* or *fcc* sites with an orientation consistent to that revealed by STM topographs (Figs. 7.1c and f).[141,284] To understand the different action spectra in Fig. 7.3 it is sufficient to consider density functional theory (DFT) calculations for the isolated molecules (see Sec. 7.6). The calculated energy barriers for the rotation of the attached moieties are quite different, namely 140 meV for ethoxy-TOTA and 195 meV for ethyl-TOTA. The geometries of the CH···O bonds between the attached moieties and the platform that fix the orientation are hardly different (calculated H···O distances of 0.29 to 0.30 nm). Moreover, the geometries of the transition states are similar. Therefore, we attribute the higher energy barrier for ethyl-TOTA mainly to the two additional CH···O bonds of the $CH_2$ unit of the ethyl-moiety that is directly attached to the central C atom of the platform (H···O distance of 0.30 nm, Figs. 7.1a and b).

In contrast to the energy barriers for the rotation, the computed vibrational spectra of ethoxy-TOTA and ethyl-TOTA are found to be very similar, and reveal a gap between $\approx 200$ (C–H bending) and 350 meV (C–H stretch) (Fig. 7.4). The calculated vibrational density of states (vDOS) are consistent with infrared spectra of powder samples (not shown). The rotation is assumed to be due to an over-barrier process (in contrast to tunneling processes) because no switching was observed with voltages lower than the energy barrier of the investigated rotor, even after days of measurements. Therefore, all vibrational modes with an energy lower than 140 meV (dashed turquoise line in Fig. 7.4a) and 195 mV (dashed magenta line in Fig. 7.4a) for respectively ethoxy- and ethyl-TOTA are irrelevant for the rotation.

The fit of the action spectrum of ethyl-TOTA revealed vibrational modes at $\approx 370$ meV (Fig. 7.3, right arrow in Fig. 7.4). In this energy range, we find only C–H stretching modes that are located to the moieties (cf. Fig. 7.4a). Another set of C–H stretch modes around 390 meV involves the outer H atoms of the platform. The absence of an additional increase of the switching yields above 370 mV leads us to conclude that the platform modes do not efficiently couple to the rotation, despite their large energy. Calculated vibrational modes located on the moiety are displayed in the SI (Sec. 7.7.2). Most of modes of the ethyl group with an energy $\approx 370$ meV involve significant displacements of the hydrogen atoms, which mediate hydrogen bonding to the platform. The rotation in ethyl-TOTA is therefore due to one or several C–H stretching vibrational mode(s) located on the moiety, which most likely weakens the hydrogen bonds between the moiety and the platform, and in turn efficiently decays into a rotation. In other words, the combination of the energy barrier, the vibrational energy gap, and the type of vibrational modes (Figs. 7.9 and 7.10) are consistent with the absence of rotation of ethyl-TOTA ($Y < 10^{-12}$) at electron energies below $\approx 350$ meV. The importance of C–H stretching modes has been reported for other electron-induced processes[285] such as: on-surface rotation,[127,258,286] hopping,[287] and synthesis.[288]

Analogous to ethyl-TOTA, the second abrupt increase of the action spectrum of ethoxy-TOTA at $\approx 370$ meV is caused by C–H stretching vibrational modes of the moiety. However, the first abrupt increase in the action spectrum is related to one or several C–H bending vibrational mode(s) of energy $\approx 180$ meV located on the moiety (SI, Sec. 7.7.2 and left arrow in Fig. 7.4).

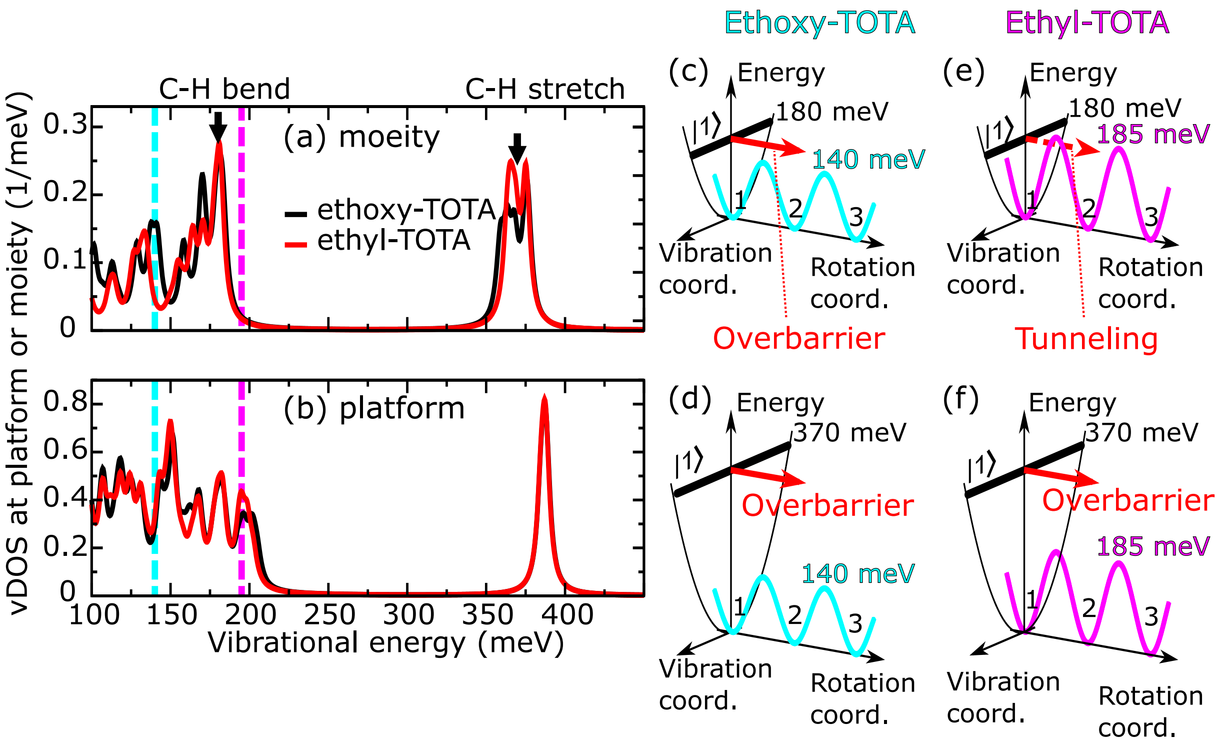

Figure 7.4.: (a) Calculated vibrational density of states (vDOS) projected onto the ethoxy moiety of ethoxy-TOTA (black line) and onto the ethyl group of ethyl-TOTA (red line). The discrete spectra were broadened by 3 meV. Turquoise and magenta dashed vertical lines indicate the computed energy barriers for the rotation reaction for ethoxy-TOTA and ethyl-TOTA, respectively. The arrows indicate the vibrational-mode energies extracted from the fits to the data shown in Figure 7.3. (b) Corresponding vDOS projected onto the TOTA platform for ethoxy-TOTA (black line) and ethyl-TOTA (red line). (c–f) Illustrations of the relevant vibrational modes (C–H stretch and bend) and rotation barriers. The turquoise and magenta curves describe idealized rotational energy potentials with energy barriers of respectively 140 and 195 mV. The indexes **1**, **2** an **3** represent the three stable orientations of the respective rotors. Along the vibration coordinate, only the relevant C–H bending (c,e) and C–H stretching (d,f) modes of the moieties are shown (180 meV and 370 mV). The solid (dashed) red arrow is a representation of energy transfer from the vibration to the rotation coordinate in an over-barrier (tunneling) process.

The barrier for rotation is lower in ethoxy-TOTA (≈ 140 meV), where several vibrational modes below the onset of the gap (≈ 200 meV) are capable of decaying into rotation, and as a result the situation is drastically different. The relevant vibrations are C–H bending modes and therefore directly affect the CH···O bonds that stabilize the orientation of the ethoxy group (SI, Fig. 7.9). The experimental action spectra (Fig. 7.3) suggest that these pure ethoxy modes indeed efficiently induce the rotation, while all other modes below 350 meV do not. In line with this observation, the other calculated modes between 140 and 350 meV are mainly vibrations of the platform (cf. Fig. 7.4b) and are therefore less likely to lead to ethoxy rotation.

The relevant vibrational modes and rotation energy barriers are illustrated in Figures 7.4c–f. Two series of modes with energies of ≈ 180 and ≈ 370 meV, common for the two moieties, may effectively decay into a rotation. For ethyl-TOTA, the calculated rotational energy barrier is 195 meV (magenta curve in Fig. 7.4c). The vibrational modes at 180 meV therefore cannot provide enough energy for the rotation of the moiety (Fig. 7.4e), and only the subsequent relevant vibrational modes at 370 meV may induce a rotation (Fig. 7.4f). In contrast, for ethoxy-TOTA, the energy barrier (140 meV) is low enough such that both relevant series of modes can, in principle, transmit sufficient energy for the rotation (Figs. 7.4c,d). This explains the presence of two abrupt increases in the yield of ethoxy-TOTA (Fig. 7.3).

The energies of the C–H stretching modes are approximately twice as high as those of the C–H bending modes of the ethoxy group (cf. right and left arrows in Fig. 7.3). Time resolved measurements with picosecond light pulses on liquid hydrocarbons showed a highly efficient decay of C–H stretching modes into two C–H bending modes.[289] We speculate that an efficient *simultaneous* excitation of two C–H bending modes via the decay of a C–H stretching mode causes drastically higher (by more than three orders) switching yield of ethoxy-TOTA compared to ethyl-TOTA ($|V| > 350$ meV, Fig. 7.3). This scenario is supported by the fact that an excitation of a single C–H bending mode of the ethoxy moiety is $\approx 10$ times more efficient in inducing rotation than a single C–H stretching mode of the ethyl moiety.

In principle, tunneling electrons could also sequentially excite two vibrational modes (vibrational ladder climbing) without a preceding excitation of a high-energy mode. However, such a multi-electron process would lead to a switching rate proportional to $I^N$ where $N > 1$, in contrast to $N = 1$ experimentally observed (not shown). In principle, tunneling electrons could also simultaneously excite two vibrational modes without a preceding excitation of a high-energy mode.

Separate calculations of ethyl-TOTA on Au(111) (not shown) reveal an additional piece of important information. The energy barriers for moiety rotation and the vibrational modes of interest ($\hbar\omega > 130$ meV) hardly change upon adsorption indicating that the TOTA platform efficiently decouples of the functional moieties from the substrate as intended. Important gas-phase properties of a molecule are preserved.

## 7.3.6. Microscopic yields and directionality of the rotation steps

Next, we experimentally studied microscopic switching events of the three-state rotors, *i. e.* switching from an initial state $\boldsymbol{i}$ to a final state $\boldsymbol{j}$. The microscopic yields $y_{ij}$ (Fig. 7.5b) were obtained from time series of $I$ at various sample voltages (SI, Sec. 7.7.3). The total yield $Y$ is linked to $y_{ij}$ as follows:

$$Y = \sum_i \left( \alpha_i \sum_{j \neq i} y_{ij} \right), \tag{7.2}$$

where $\alpha_i$ is the probability of finding the rotor in an initial state $\boldsymbol{i}$. To verify the consistency of all microscopic yields presented below, we derived the stationary solutions of the three-state master equation with $y_{ij}$ as input (SI, Sec. 7.7.3). Less than 4 % variation is observed between the $\alpha_i$ estimated from the measurements and the $\alpha_i$ resulting from the master equation.

First, data from ethoxy-TOTA (Figs. 7.1a and c–e, with two OH-TOTA neighbors close to ethoxy-TOTA) are discussed. The STM tip was positioned at a location (magenta cross in Fig. 7.5a) equivalent to that indicated by a white cross in Figures 7.1c–e. This

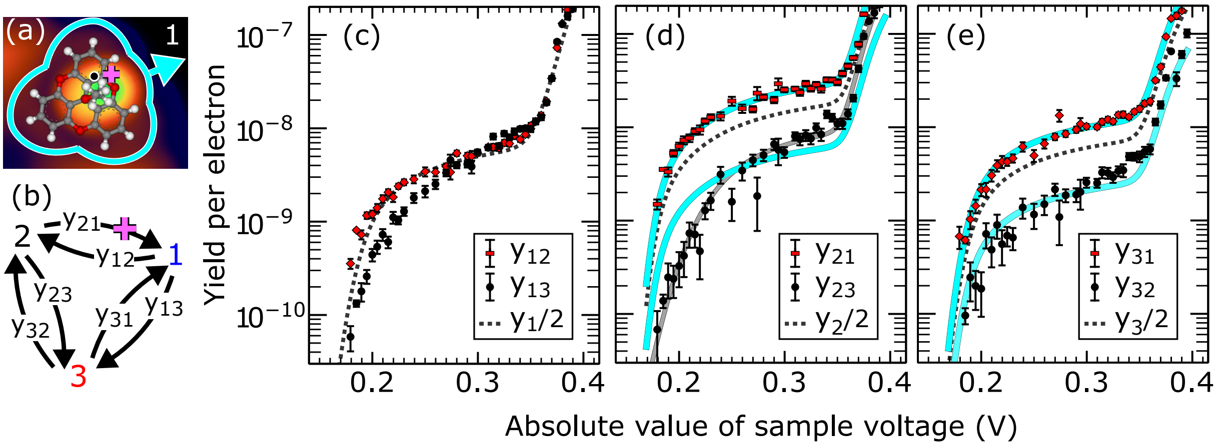

Figure 7.5.: (a) STM topograph of ethoxy-TOTA with a calculated scaled molecular structure overlayed. The magenta cross (black dot) indicates the same positions as the white cross (circle) in Figures 7.1(c–e). Both positions allow to distinguish states **1**-**3** [cf. Fig. 7.1(c–e)] as distinct current levels at constant tip height. (b) Definition of the yields $y_{ij}$ for switching from state $\boldsymbol{i}$ to state $\boldsymbol{j}$. States **1**, **2**, and **3** are defined with respect of the tip position (magenta cross) during switching, *i. e.* they correspond to the highest, middle, and lowest current level, respectively [cf. Figs. 7.2 and 7.1c–e]. (c–d) Measured yields $y_{ij}$ for switching out of state (c) **1**, (d) **2** and (e) **3** with the tip positioned at the magenta cross in (a). While the data points at high yield are based on 20000 switching events, the lowest yield corresponds to 5 events. Bars indicate the standard deviation $\sigma$ expected from a Poisson process. Dashed lines show fits to $y_i/2$ using Equations 7.4 and 7.5 (SI, Sec. 7.7.1), and correspond to the expected yields when switching is not directional. The upper (lower) solid turquoise lines in (d) and (e) represent the fits of $y_i/2$ (dashed lines) multiplied with a factor of 1.65 (0.35). Direct fits to $y_{ij}$ (not shown) and $y_i$ indicate active vibrational modes at 176 to 184 meV and 373 to 400 meV. The fits to $y_{13}$ (not shown) and $y_{23}$ [solid gray line in (d)] are exceptions that suggest vibrational modes at ≈ 206 and 231 meV, respectively.

tip position makes the states **1**–**3** inequivalent, which allows to obtain three distinct current values (feedback off) in time series. $y_{31}$ and $y_{32}$ (Fig. 7.5e, red and black symbols, respectively) are voltage dependent as expected from the overall yield (Fig. 7.3). For $V \lesssim 330\,\mathrm{mV}$, $y_{31}$ is five times larger than $y_{32}$. In other words, switching out of state **3** is directional.

For further analysis, we first fitted the sum $y_3 = y_{31} + y_{32}$, *i. e.* switching events starting in state **3**, using Equations 7.4 and 7.5 (SI, Sec. 7.7.1). Assuming non-directional switching, we obtain the dotted line in Fig. 7.5d with vibrational modes at ≈ 180 and ≈ 375 meV, in agreement with the energies ≈ 180 and ≈ 365 meV extracted from the action spectra (Figure 7.3). The obtained fit is scaled by 1.65/2 and 0.35/2 (turquoise lines in Fig. 7.5d) to match $y_{31}$ and $y_{32}$, respectively. These factors are related to the probability $p_{ij}$ of switching from state $\boldsymbol{i}$ to $\boldsymbol{j}$ where

$$p_{ij} = \frac{y_{ij}}{\sum_{j \neq i} y_{ij}}. \tag{7.3}$$

$p_{31} = 1.65/2 \approx 0.83$ ($p_{32} = 1 - p_{31} \approx 0.17$) for $|V| \lesssim 360\,\mathrm{mV}$. A reduction by 10–20 % occurs when the second vibrational mode at ≈ 370 meV may be excited. The difference between $p_{31}$ and $p_{32}$ is related to the directionality of the rotation, and strongly depends on the tip position (SI, Sec. 7.7.4). The directionality is mostly induced by the tip, and the result of an attractive interaction between the tip and the moiety. Indeed, we observed that the favored final state is the one closest to the tip position (Fig. 7.5 and SI, Sec. 7.7.4). For example, state **1** is preferred as a final state over **2** when the tip is located as indicated in Figures 7.5a and b (magenta cross).

Consequently, switching from state **2** (Fig. 7.5d) also preferably ends in state **1** with $p_{21} \approx 0.83$. $y_{21}$ is higher than any other microscopic yield of ethoxy-TOTA and actually exceeds the total yield $Y$. Note that there is no contradiction in having some of the microscopic yields larger than the total yield because the former ones are weighed by the probability of finding the initial state ($< 1$) to give the total yield (Equation 7.2). $y_2/2$ is fitted using Equations 7.4 and 7.5, and scaled by 1.65 and 0.35 to obtain the lower and higher turquoise lines in Figures 7.5d,e. Clear deviations from the experimental $y_{23}$ data are observed, especially for $|V| < 250\,\mathrm{mV}$, and suggest that the directionality depends on the sample voltage. Indeed, $p_{21}$ evolves from $\approx 95\,\%$ for $V \approx 180\,\mathrm{mV}$ to $\approx 80\,\%$ for $V \approx 250\,\mathrm{mV}$. Because of $y_{23} = y_2 - y_{12}$, the yield $y_{21}$ has similar deviations as $y_{23}$ but of opposite sign. While the variations of $y_{23}$ to the non-voltage dependent directionality case (turquoise line in Fig. 7.5d) are significant, they represent only a small fraction of $y_{21}$ and are therefore barely observable in Figure 7.5d. We speculate that they are due to small tip-height changes with the voltage, which in turn mainly affects $y_{21}$. Indeed, the ethoxy moiety passes below the tip for switching from state **2** to **1**.[XLI]

Finally, we consider switching from state **1** (Fig. 7.5c). For $|V| \gtrsim 270\,\mathrm{mV}$, we hardly observe any directionality. Given that the STM tip is positioned close to the symmetry plane of state **1** (cross in Fig. 7.1c), the final states **2** and **3** are almost equivalent and similar yields $y_{12}$ and $y_{13}$ are expected. However, there are deviations between $y_{12}$ and $y_{13}$ with a clear preference of **2** as final state for $V < 270$ mV. Similar to the yields in Figure 7.5d, these deviations may be linked to the tip that is located above the path of rotation, *i. e.* between configurations **1** and **2**.

## 7.3.7. Tuning the directionality of the rotation

The ethoxy moiety seems to be attracted by the tip, which leads to a directionality of the rotation. The adsorption geometry of the molecule relative to the substrate atoms and neighboring molecules may also influence the energetic landscape of the ethoxy moiety, and in turn affect the directionality. In the following, we discuss the influence of (i) the tip position, (ii) the adsorption geometry and (iii) neighboring molecules on the directionality.

Additional microscopic yield data (SI, Sec. 7.7.4) were recorded, where the tip has been laterally displaced by 0.15 nm (dot in Figs. 7.5a and 7.1c–e). As expected, the total yield $Y$ is hardly affected by the change of tip position. However, the microscopic yields

---

[XLI] A direct fit to the $y_{23}$ data (gray line in Fig. 7.5d) leads to vibrational modes at $\approx$ 230 meV and $\approx$ 373 meV. While the energy of the second mode is consistent with that obtained fitting $y_{21}$, the energy of the second mode is drastically different. Furthermore, the energy of the second mode is inconsistent with DFT calculations, which indicate a vibrational gap between 200 and 350 meV. In addition, the width $\sigma_G$ of the first mode spectral form (Eq. 7.6, SI, Sec. 7.7.1) has to be increased to excessively large values to achieve an acceptable fit.

$y_{ij}$ are drastically modified, and reflect the different symmetry of the tip-molecule system. The new tip position is close to the symmetry plane of state **3**, leaving states **1** and **2** approximately equivalent. In turn, the switching from the initial state **3** shows fairly low directionality ($p_{31} \lesssim 0.6$, $p_{32} \gtrsim 0.4$). Moreover, the switching between **1** and **2** occurs with almost identical yields $y_{12} \approx y_{21}$, in contrast to $y_{21} \approx 5\,y_{12}$ observed with the previous tip position. Therefore, a displacement of the tip as small as 0.15 nm can have a drastic effect on the directionality. For the new position, the favored final state **1** is the one closest to the tip, which is consistent with an attractive force between the ethoxy moiety and the tip.

An important role of the substrate appears to be rather unlikely because the platform decouples the moiety from the surface. Nevertheless, the adsorption geometry of ethoxy-TOTA on Au(111) is chiral as inferred from DFT calculations along with STM data.[141,284] It breaks the symmetry of the substrate and induces a chirality of the molecule-substrate system, while the molecule itself is hardly changed upon adsorption, *i. e.* remains achiral. Indeed, the mirror plane of the molecule is rotated by $\approx -4°$ (enantiomer left) or by $\approx +4°$ (enantiomer right) relative to a close-packed $\langle 110 \rangle$ direction of Au(111). We measured microscopic yields as the ones shown in Figure 7.5 on two different enantiomers but did not observe a significant variation of the directionality. Therefore, within the uncertainty of the measurements, the directionality is not affected by the substrate.

As to factor (iii), adjacent TOTA molecules without substitution at the central carbon atom were observed to strongly affect the directionality of switching whereas neighboring OH-TOTA and ethoxy-TOTA molecules were passive. In particular, when the tip is positioned above ethoxy-TOTA close to an adjacent bare TOTA molecule (Fig. 7.6a), the switching into state **1**, *i. e.* rotation of the moiety towards the adjacent TOTA, is efficiently suppressed. At 300 mV, $y_{21}$ and $y_{31}$ are respectively reduced by factors of $\approx 10$ and $\approx 5$ compared to the case without neighboring TOTA molecule. Most switching events instead occur between states **2** and **3** (Fig. 7.6b). We attribute this striking effect to Coulomb repulsion between the moiety and the TOTA neighbor. Indeed, adsorbed TOTA molecules are positively charged as evidenced by the fact that TOTA in contrast to ethoxy- and ethyl-TOTA molecules do not form clusters on Au(111).[284] The topmost ethyl moiety of ethoxy-TOTA is most probably also positively charged because of the bond with electronegative oxygen. The measurements show that the electrostatic repulsion exceeds the attraction to state **1** caused by the STM tip.

States **2** and **3** are almost symmetric with respect to the adjacent bare platform. Switching between these states is therefore expected to be mainly controlled by the tip position. Indeed, switching from state **3** to state **2**, where the moiety is closer to the tip, is more efficient than the reverse process. The corresponding directionality induced by the tip ($y_{32} \approx 5\,y_{23}$) is similar to the case without a TOTA neighbor (Figs. 7.5d,e where $y_{21} \approx 4.7\,y_{23}$ and $y_{31} \approx 4.7\,y_{32}$). The net result of the various yields is that the molecule with a neighbor prefers state **2** (Fig. 7.6b) instead of state **1**, which exhibits the largest lifetime when no TOTA is present (Fig. 7.2). Modifications of residence times and reaction yields by adsorbates have also been reported for other systems, such as intramolecular hydrogen transfer in a porphycene molecule on Cu(110) and phthalocyanine molecules on Ag(111).[290,291]

We did not observe a significant influence of OH-TOTA or ethoxy-TOTA neighbors on the directionality of switching. This may be expected because OH-TOTA or ethoxy-

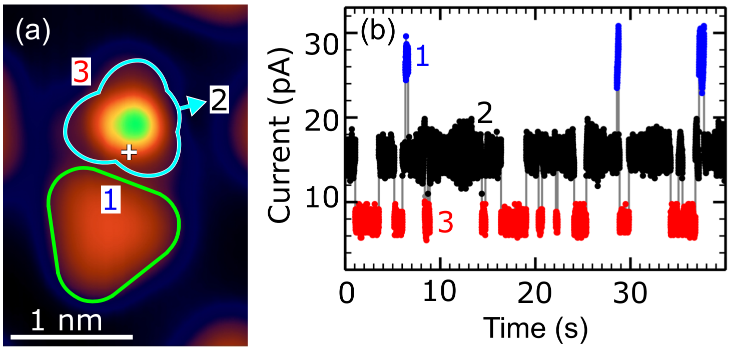

Figure 7.6.: (a) STM topograph showing a single ethoxy-molecule (turquoise) adjacent to a bare TOTA platform (light green). The image was processed by merging the raw data with a smoothed and inverted Laplace-filtered image. Tunnel parameters: 100 mV, 30 pA (b) Time series of the tunneling current measured with the tip positioned over the cross in (a). $V = 300\,\mathrm{mV}$ was applied and the current feedback was opened at $I = 7\,\mathrm{pA}$. The current levels 1–3 correspond to states **1**–**3** (cf. Fig. 7.1c–e). The states are indicated in (a), where the orientation of the ethoxy moiety corresponds to state **2**.

TOTA molecules do not repel each other on Au(111), which indicates that they are significantly less charged than TOTA.[284] In these cases, the tip position determines the directionality.

We also investigated the microscopic yields of the ethyl moiety in ethyl-TOTA (data not shown). The topmost methyl moiety tends to switch into the state that minimizes the separation from the tip. The measured directionalities are rather low ($p_{21,31} = 60 \ldots 70\,\%$), similar to those of ethoxy-TOTA at large voltages, $|V| > 350\,\mathrm{mV}$. The reduced directionality is possibly related to the excitation of the C–H stretching vibrational mode that occurs in this energy range in ethyl-TOTA and ethoxy-TOTA.

We then employed the tip-induced control of the directionality to perform clockwise or anti-clockwise rotation of an ethoxy moiety (Figure 7.7).

At least two different tip positions are necessary to obtain a complete rotation (*e. g.* white and gray crosses in Fig. 7.7a-d). The tip-induced directionality allows realizing a complete rotation without backward steps with a success rate of ≈ $0.90^3 = 0.73$.

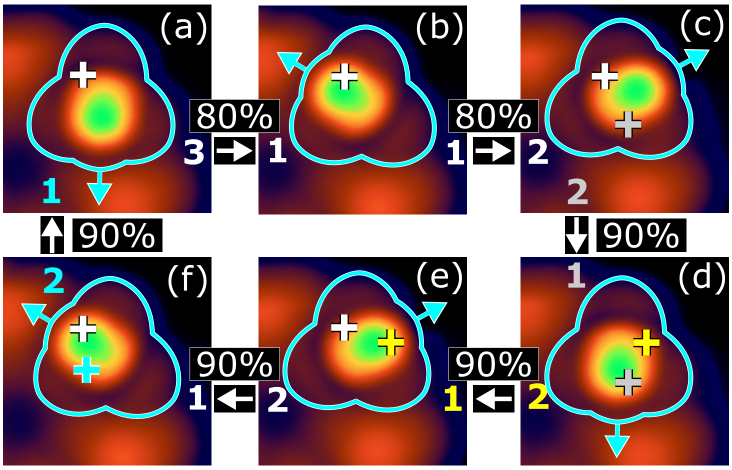

Figure 7.7.: (a–f) STM topographs of the same ethoxy-TOTA molecule (marked with a turquoise border). From (a) to (d) the torsion angle $\theta_{\text{oxy}}$ was switched at 185 mV in a clockwise direction and from (d) to (f) and back to (a) in an anti-clockwise direction. Two crosses in (c–f) indicate the tip positions used for switching into and from the state. For example, in (c) the gray and white crosses indicate the tip positions for current injection between topographs (b) to (c) and between (c) and (d). As the labeling of the states depends on the tip position, the color of the labels (numbers) indicates which tip position is used as a reference.

## 7.4. Summary

We present a model study of two closely related molecular stepper motors that were designed to work on a metal substrate under excitation with tunneling electrons in a STM. The motors are comprised of the TOTA platform as a stator and ethoxy and ethyl moieties as rotors. The platform approach reduces the complex interactions with the metal and thus preserves important properties built into the gas-phase molecules. This simplifies a detailed analysis and also defines three symmetry equivalent positions where the rotor is stabilized via CH···O bonds. Current-induced rotation of the moieties is demonstrated, the STM tip is used to generate directionality of the motion, modification of the directionality by adjacent charged adsorbates is revealed, and microscopic reaction yields are determined. By means of DFT calculations for the two related molecules, we show how the energies and displacement patterns of the vibrational modes, along with the barriers towards rotation, can lead to several orders of magnitude variation of the reaction yield.

## 7.5. Experimental details

### 7.5.1. Synthesis of the molecules

Functional groups were attached to the cationic TOTA platform by polar C–C and C–O bond formation. The synthesis of 12c-ethyl-4,8,12-trioxatriangulene (ethyl-TOTA) and OH-TOTA is described in Refs. 284 and 232, respectively.

The synthesis of 12c-Ethoxy-4,8,12-trioxatriangulene (ethoxy-TOTA) was performed as follows: 390 mg (16.7 mmol) sodium was added to 100 ml ice cooled ethanol and stirred for 1 h. Afterwards 100 mg (269 $\mu$mol) 4,8,12-trioxatriangulenium-tetrafluoroborate was added to the solution. After 20 min ultrasonic treatment the mixture was stirred at room temperature for 17 h. The solution was concentrated to 20 ml, dissolved in 300 ml anhydrous diethyl ether and washed three times with 200 ml ultrapure water. The combined aqueous layers were extracted with 200 ml anhydrous diethyl ether. The combined organic layers were dried over magnesium sulfate and evaporated under reduced pressure. The beige solid was purified by sublimation at $1.2 \times 10^{-2}$ mbar and 170 °C yielding white crystals.

Yield: 42.0 mg (127 $\mu$mol, 47 %).

$^1$H-NMR (600 MHz, aceton-d6, 300 K, TMS): $\delta = 7.51$ (t, $^3J = 8.3$ Hz, 3 H, $H$-2,6,10), 7.13 (d, $^3J = 8.3$ Hz, 6 H, $H$-1,3,5,7,9,11), 3.04 ($q$, $^3J = 7.0$ Hz, C-$H_2$), 0.82 ($t$, $^3J = 7.0$ Hz, 3 H, C-$H_3$) ppm.

$^{13}$C-NMR (151 MHz, aceton-$d_6$, 300 K, TMS): $\delta = 153.8$ ($C$-3a, 4a, 7a, 8a, 11a, 12a), 131.1 ($C$-2, 6 , 10), 112.0 ($C$-1, 3, 5, 7, 9, 11), 109.7 ($C$-7b, 11b, 12b), 57.4 ($C$H$_3$), 55.6 ($C$-12c), 15.4 ($C$-H$_2$) ppm.

MS (EI, 70 eV): m/z (%)= 285.05(100) $[C_{19}H_9O_3]^+$, 330.09 (0.5) $[M]^+$.

MS (EI, 70 eV): m/z (%) ($C_{21}H_{14}O_4$): measured 330.08915; calculated 330.08921.

EA ($C_{21}H_{14}O_4$): measured C: 75.83, H: 4.00, N: 0.00 %; calculated C: 76.36, H: 4.27, N: 0.00 %.

Melting point: 235.3 °C.

FT-IR: $\tilde{\mu} = 2976.35$ (w), 2324.29 (w), 2014.61 (w), 1615.44 (s), 1486.14 (s), 1456.42 (s), 1386.93 (w), 1341.62 (w), 1308.22 (w), 1260.34 (s), 1199.69 (m), 1159.52 (w), 1116.12 (w), 1067.35 (s), 1053.98 (m), 1013.23 (s), 957.27 (m), 943.30 (s), 902.46 (m), 882.00 (m), 785.23 (s), 774.61 (s), 759.51 (s), 737.88 (s), 664.74 (w) cm$^{-1}$.

### 7.5.2. Measurements

Au(111) surfaces and chemically etched W tips were cleaned by repeated Ar$^+$ bombardment and annealing. After mounting into the STM, the tips were repeatedly indented into molecule-free areas of the substrate. To obtain a sharp tip the sample was repeatedly contacted with the tip until the contacts were stable at a conductance $G \approx G_0$ and adatoms were imaged as circular protrusions of < 700 pm diameter. All STM images were acquired using the constant-current mode (4.6 K, $10^{-9}$ Pa).

## 7.6. Theoretical details

The electronic structure and harmonic vibrational modes of free-standing ethoxy-TOTA and ethyl-TOTA were computed from Kohn–Sham DFT as implemented in VASP.[292] A plane-wave basis energy cutoff of 500 eV was used together with the optB88-vdW exchange correlation functional.[182] Forces were relaxed to within 0.02 eV/Å and vibrations were obtained with a finite-difference amplitude of 0.02 Å. The rotation barriers were computed using the nudged elastic band (NEB) method[293] with a single intermediate image between the stable configurations.

# 7.7. Supporting information

## 7.7.1. Action spectroscopy

### 7.7.1.1. Fit function

The action spectra have been fitted using[131]:

$$Y(V) = \sum_{\Omega} Y_{\Omega}(V), \tag{7.4}$$

where the sum is over the vibrational modes of energy $\hbar\Omega$ ($\hbar$: reduced Planck constant) involved in the rotation. In the present cases of ethoxy-TOTA and ethyl-TOTA these are only two modes and one, respectively. For a given vibrational mode with energy $\hbar\Omega$, the reaction yield $Y_{\Omega}$, *i. e.*, the probability to induce a rotation per electron, reads[131]:

$$\begin{aligned} Y_{\Omega}(V) = \; K(\Omega)\Bigg[ & 1 + \frac{|eV| - \hbar\Omega}{|eV|} E_G(|eV| - \hbar\Omega) - \frac{|eV| + \hbar\Omega}{|eV|} E_G(|eV| + \hbar\Omega) \\ & + \frac{\rho_v(|eV|)\sigma_G^2}{|eV|}\Bigg], \quad E_G(X) = \frac{1}{2}\frac{\mathrm{Erf}(X/\sqrt{2}\sigma_G)}{\mathrm{Erf}(\Omega/\sqrt{2}\sigma_G)}, \end{aligned} \tag{7.5}$$

where $K(\Omega)$ is a dimensionless prefactor, $\mathrm{Erf}(X)$ the error function, $V$ the applied sample voltage and $e$ the elementary charge. Equation 7.5 assumes Gaussians with a standard deviation $\sigma_G$ centered at $\pm\hbar\Omega$ for the vibrational density of states (vDOS) of the relevant modes:

$$\rho_v(\omega) = \frac{1}{\sigma_G\sqrt{2\pi}} \frac{1}{\mathrm{Erf}(\Omega/\sqrt{2}\sigma)} \left\{ \exp\left( -\frac{(\hbar\omega - \hbar\Omega)^2}{2\sigma_G^2} \right) - \exp\left( -\frac{(\hbar\omega + \hbar\Omega)^2}{2\sigma_G^2} \right) \right\}, \tag{7.6}$$

which takes into account all broadening effects encountered in practice like, *e. g.*, thermal, noise/instrumental and intrinsic lifetime broadening.[129]

Equation 7.5 depends on three parameters: $\Omega$, $K(\Omega)$ and $\sigma_G$. Therefore, fitting experimental action spectra requires three fit parameters per vibrational mode.

### 7.7.1.2. Interpretation and simplification of the fit function

The width $\sigma_G$ of the vibrational modes is typically on the order of 10 meV in our experiments. The last term in Equation 7.5 can be neglected for $|eV| > \hbar\Omega + 3\,\sigma_G$ because $\rho_\nu(eV)\,\sigma_G$ converges to zero (less than 1.2 % deviation). Moreover, $E_G(|eV| - \hbar\Omega)$ and $E_G(|eV| + \hbar\Omega)$ effectively converge to 1/2 (less than 0.5 % deviation). Equation 7.5 simplifies to:

$$Y_{\Omega}(V) = \; K(\Omega)\, \frac{|eV| - \hbar\Omega}{|eV|}\, \theta(|eV| - \hbar\Omega), \tag{7.7}$$

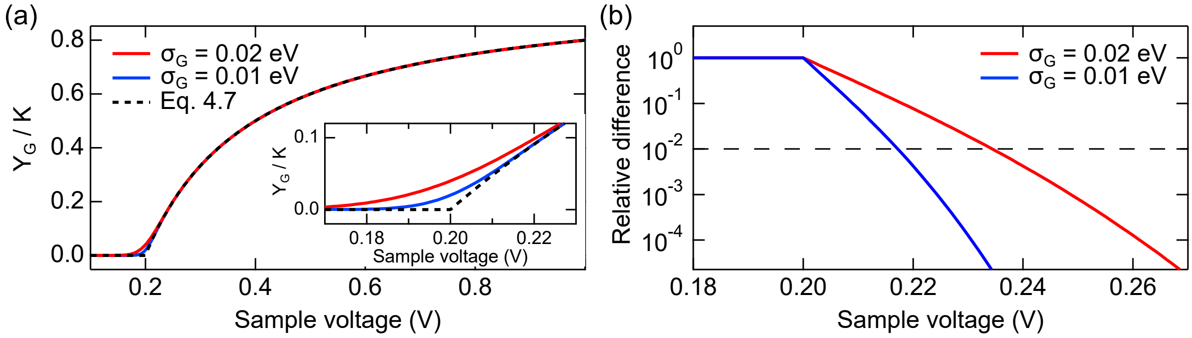

Figure 7.8.: (a) Yields inferred from Equation 7.5 for a vibrational mode at $\hbar\Omega = 0.2$ eV with a Gaussian broadening $\sigma_G = 0.02$ eV (red) and $\sigma_G = 0.01$ eV (blue). The dashed black curve corresponds to the yield given by the simplified Equation 7.7. The inset is a zoom for sample voltages close to the excitation energy of the vibrational mode. (b) Relative difference between the yields given by Equations 7.5 and 7.7.

where $\theta$ is the step function, which allows to extend the definition of Equation 7.7 to voltages $|eV| < \hbar\omega$. Equation 7.7 corresponds to the reaction yield due to single vibrational mode with a vDOS described by a Dirac $\delta$-function.[129] Related expressions have been used to describe the inelastic excitations in solid-state tunneling junctions.[294]

We would like to emphasize that the derivation of Equation 7.5 is done in the wide-band limit, where the densities of states of the tip and adsorbate+surface are assumed to be independent of the energy. Under these conditions, the factor $(|eV| - \hbar\Omega)/|eV|$ gives the proportion of tunneling electrons whose energy is sufficient to excite the vibrational mode of energy $\hbar\Omega$. The prefactor $K(\Omega)$ describes the combined probability of (i) a tunneling electron with sufficient energy to excite the vibrational mode of interest and (ii) the mode to decay into the reaction of interest, *e.g.*, a rotation.

Figure 7.8 illustrates that Equation 7.7 is a very good approximation of the yield, except close to the excitation energy. The deviation between the yields given by Equations 7.5 and 7.7 becomes more pronounced when the broadening of the vibrational mode $\sigma_G$ is increased. However, the relative difference decays rapidly and is on the order of 1 % for sample voltages $|eV| - \hbar\Omega > 2\sigma_G$ (Fig. 7.8b). This rapid decay also occurs when Lorentzians $\rho_L$ are assumed for the vibrational DOS (cf. Eq. 7.6). Considering that yields for $|eV| < \hbar\Omega + 2\sigma_G$ are usually low and may be barely experimentally measurable within a reasonable time, Equation 7.7 is generally well suited to fit experimental action spectra for $|eV| - \hbar\Omega > 2\sigma_G$. It neglects broadening effects and reduces the fit parameters to the energy of the vibrational mode $\hbar\Omega$ and the prefactor.

### 7.7.1.3. Discussion of the prefactor *K*

The probability of an electron with sufficient energy to induce vibrational excitation depends on the electron-phonon coupling. This probability can be on the order of 1 to 10 %.[281–283] Although $K$ is the combined probability of (i) excitation of a given vibrational mode and (ii) decay of this mode into the reaction of interest, we will see that $K$ is effectively independent of the electron-phonon coupling.

The reaction yield may be rewritten as:[129]

$$Y_{\Omega}(V) = \tilde{K}(\Omega)\,\frac{I_{in}(V,\Omega)}{I(V)}, \tag{7.8}$$

where $\tilde{K}(\Omega)$ is a prefactor describing the efficiency of the excited mode with energy $\hbar\Omega$ in inducing the reaction. $I_{in}(V,\Omega)/I(V)$ is the related inelastic proportion of the tunneling current, *i. e.* the fraction of tunneling electrons exciting the vibrational mode $\hbar\Omega$. It may be worth mentioning that a larger electron-phonon coupling increases the ratio $I_{in}(V,\Omega)/I(V)$. The prefactor $\tilde{K}(\Omega)$ is actually included in the factor $K(\Omega)$ in Equations 7.5 and 7.7.

For an over-barrier process, *i.e.*, when enough energy is transferred to the system to overcome the reaction barrier (in contrast to tunneling processes), the prefactor is determined by:[129]

$$\tilde{K}(\Omega) \cong \frac{\gamma_{RC}(\Omega)}{\gamma_{eh}(\Omega)}, \tag{7.9}$$

where $\gamma_{RC}(\Omega)$ is the conversion rate of the vibrational mode $\hbar\Omega$ into decay channels that induce the reaction and $\gamma_{eh}(\Omega)$ is the rate at which the vibrational mode decays into other channels. The predominant decay channel very often is electron-hole pair creation,[129] which is also related to the electron-phonon coupling. Therefore, while a large electron-phonon coupling leads to a larger proportion of electrons exciting the vibrational mode of energy $\hbar\Omega$, it effectively does not affect the yield because $\gamma_{eh}$ increases in the same proportion (cf. Equations 7.8 and 7.9).

Following the derivations in Ref. 129,

$$K(\Omega) = \frac{\gamma_{eh}(\Omega)\,\tilde{K}(\Omega)}{2\Omega\rho_a(E_F)\,\Gamma} \cong \frac{\gamma_{RC}(\Omega)}{2\Omega\rho_a(E_F)\,\Gamma}, \tag{7.10}$$

where $\rho_a(E_F)$ is the DOS of the adsorbate at the Fermi energy $E_F$ and $\Gamma$ is the width of the electronic resonance. Thus, $K$ depends on the conversion rate $\gamma_{RC}$ of the vibrational mode into the reaction and on the system parameters $\rho_a(E_F)$ and $\Gamma$.

In the off-resonant tunneling regime, relevant for the ethoxy-TOTA and ethyl-TOTA molecules, the position of the current-carrying orbital $E_a$ with respect to $E_F$ satisfies the relation $|E_a - E_F| \gg \Gamma/2$, and one has $\rho_a(E_F) \approx \Gamma/(2\pi(E_a - E_F)^2)$. Consequently, the prefactor can be expressed as:

$$K(\Omega) \approx \pi\frac{\gamma_{RC}(\Omega)}{\Omega}\frac{(E_a - E_F)^2}{\Gamma^2}. \tag{7.11}$$

As may be expected, $K$, and hence the reaction yield $Y$, is proportional to the conversion rate $\gamma_{RC}$ relative to the oscillation frequency $\Omega$ as well as to the orbital level position $|E_a - E_F|$ relative to the resonance width $\Gamma$.

From the analysis of the prefactor $K(\Omega)$, we predict that reaction yields on (partially) insulating surfaces should be significantly larger than on metal surfaces because $\Gamma$ would be significantly reduced. Alternatively, the electronic decoupling may be implemented in the molecules themselves. In that respect, for the same functional unit (*e.g.*, rotor), larger yields are expected for physisorbed systems than for chemisorbed systems.

## 7.7.2. Mode analysis

Figures 7.9 and 7.10 illustrate some of the calculated vibrational modes of the moiety for ethoxy- and ethyl-TOTA. The length of the green arrows is associated to the displacement amplitude of the corresponding atoms.

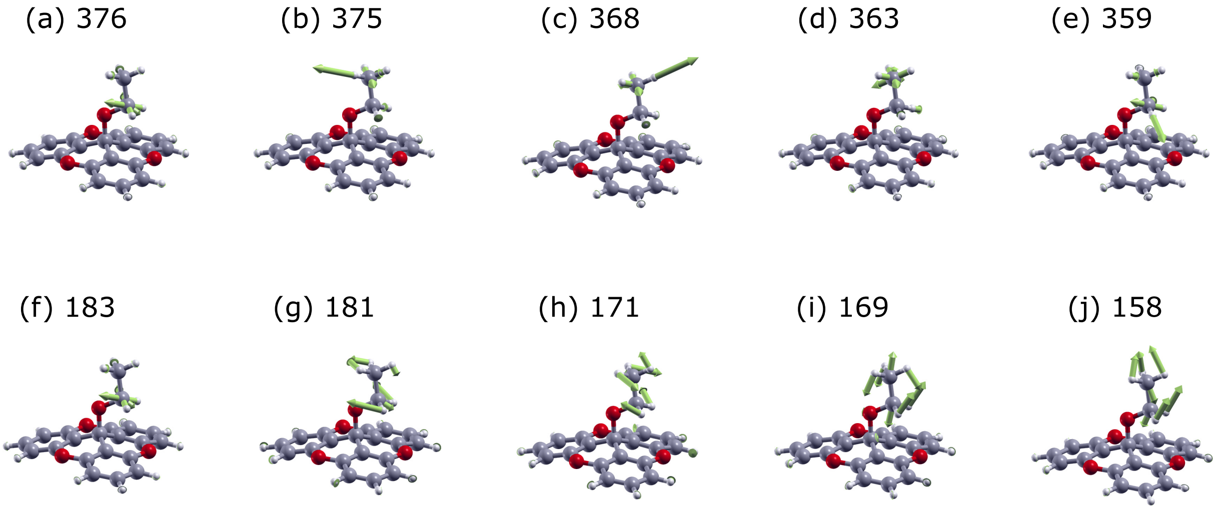
(a) 376
(b) 375
(c) 368
(d) 363
(e) 359
(f) 183
(g) 181
(h) 171
(i) 169
(j) 158

Figure 7.9.: Calculated vibrational modes that are predominantly localized on the moiety of ethoxy-TOTA. Mode energies are given in meV. (a–e) C–H stretching modes. (f–j) C–H bending modes.

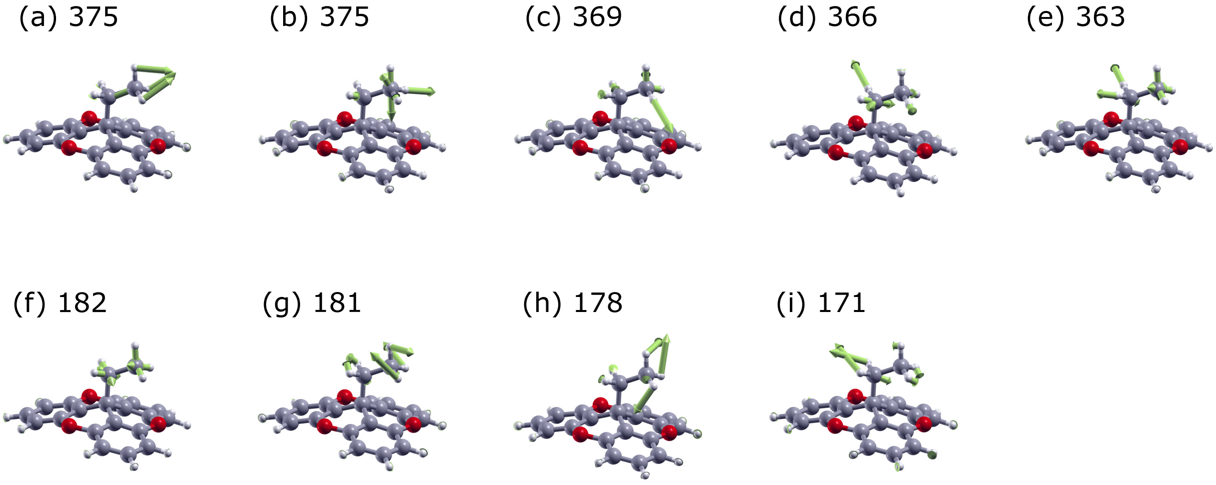
(a) 375
(b) 375
(c) 369
(d) 366
(e) 363
(f) 182
(g) 181
(h) 178
(i) 171

Figure 7.10.: Calculated vibrational modes that are predominantly localized on the moiety of ethyl-TOTA. Mode energies are given in meV. (a–e) C–H stretching modes. (f–i) C–H bending modes.

We recall that the rotors have three stable positions, where two hydrogen atoms of the moieties bind via a CH···O hydrogen bond to one of the three oxygen atoms of the platform. Vibrational modes of the moiety involving a large displacement of the corresponding hydrogen atoms may lead to an effective weakening of the hydrogen bond. In turn, such a vibrational mode may efficiently decay into a rotation of the moiety.

### 7.7.3. Master equation of rates and yields of a three-state rotor

A master equation connects the probability $p_i$ of finding the system in the state $i$ at the time $t$ with the microscopic rates $r_{ij}$ for switching from an initial state $i$ to a final state $j$:

$$\frac{dp_i}{dt} = \sum_{i \neq j} p_j r_{ji} - p_i r_{ij}. \tag{7.12}$$

The studied three-state rotors are switched via single tunneling electrons. Changing the tunneling current affects the switching rates $r_{ij}$ and the probabilities $p_i$, and therefore Equation 7.12 depends on the tunneling current. To circumvent this limitation, the master equation with respect to time (Eq. 7.12) is rewritten to a master equation with respect to the number of tunneling electrons $n$ as a (quasi) continuous parameter. Note that representing $n$ as a continuous parameter is justified by the low yield of the investigated rotor, where one out of every $10^6$ electrons may induce a switching event. The transformation is achieved via the following substitutions:

$$t \implies n \tag{7.13}$$

$$p_i \implies \alpha_i \tag{7.14}$$

$$r_{ij} \implies y_{ij}, \tag{7.15}$$

where $\alpha_i$ is the probability to find state $i$ after $n$ tunneling electrons and $y_{ij}$ is the number of switching events per tunneling electron ( $y_{ij} < 1$). Note that $y_{ij}$ is effectively a yield, but in contrast to the total yield $Y$ (Equation 7.8), it considers a particular transition from state $i$ to state $j$. With these substitutions the master equation reads:

$$\frac{d\vec{\alpha}}{dn} = \begin{pmatrix} -(y_{12}+y_{13}) & y_{21} & y_{31} \\ y_{12} & -(y_{21}+y_{23}) & y_{32} \\ y_{13} & y_{23} & -(y_{31}+y_{32}) \end{pmatrix} \vec{\alpha} \ , \quad \vec{\alpha} := \begin{pmatrix} \alpha_1 \\ \alpha_2 \\ \alpha_3 \end{pmatrix} \tag{7.16}$$

Its stationary solution ($\frac{d\vec{\alpha}}{dn} = 0$) is

$$\begin{pmatrix} \alpha_1 \\ \alpha_2 \\ \alpha_3 \end{pmatrix} = \begin{pmatrix} \dfrac{y_{23}\,y_{31} + y_{32}\,y_{21} + y_{21}\,y_{31}}{y_{12}\,y_{23} + y_{23}\,y_{31} + y_{31}\,y_{12} + y_{32}\,y_{21} + y_{13}\,y_{32} + y_{21}\,y_{13} + y_{12}\,y_{32} + y_{23}\,y_{13} + y_{31}\,y_{21}} \\ \dfrac{y_{32} + (y_{12} - y_{32})\alpha_1}{y_{21} + y_{23} + y_{32}} \\ 1 - \alpha_1 - \alpha_2 \end{pmatrix}. \tag{7.17}$$

Experimentally, time-series of the tunneling current have been acquired (Fig. 7.2 2, Sec. 7.3.3 ) at a given voltage and a given tip-sample distance. $\alpha_i$ and $y_{ij}$ are determined experimentally using:

$$\alpha_i = \frac{n_i}{\sum\limits_{i=1}^{3} n_i} = \frac{t_i I_i/e}{\sum\limits_{i=1}^{3} t_i I_i/e}, \tag{7.18}$$

$$y_{ij} = \frac{N_{ij}}{n_i}, \tag{7.19}$$

where $I_i$ is the current corresponding to state $i$, $t_i$ ($n_i$) the time (number of tunneling electrons) during which the system is in the state $i$, and $N_{ij}$ the number of observed transitions from state $i$ to state $j$. The consistency of the microscopic yields $y_{ij}$ was verified by inserting them into Equation 7.17 and comparing the resulting $\alpha_i$ with those obtained experimentally. The corresponding deviations are systematically below 4 %, which shows that the uncertainties on the experimentally determined microscopic yields are rather limited.

### 7.7.4. Additional microscopic yields of ethoxy-TOTA

In contrast to the total yields, the microscopic yields $y_{ij}$ of ethoxy-TOTA drastically depend on the precise tip position. Lateral displacements of the tip as small as 0.15 nm can significantly change the microscopic yields. For instance, for the data shown in Figures 7.5c–d of Section 7.3.6, the tip was positioned above the white cross displayed in Figure 7.11. Changing the location of the tip to the black dot (Figure 7.11) leads to drastically different microscopic yields as shown in Figure 7.11c–d. For example, the microscopic yield $y_{12}$ ($y_{13}$) is higher (lower) by approximately a factor 5 when the tip is above the black dot compared to the case when the tip is above the white cross.

The modifications of $y_{ij}$ actually reflect the changed symmetry of the tip-molecule system. While the white cross (Figure 7.11a) is close to the symmetry plane of state **1**, the black dot is closer to the symmetry plane passing through state **3**. Therefore, for the tip position depicted by the black dot (white cross), the states **1** and **2** (**2** and

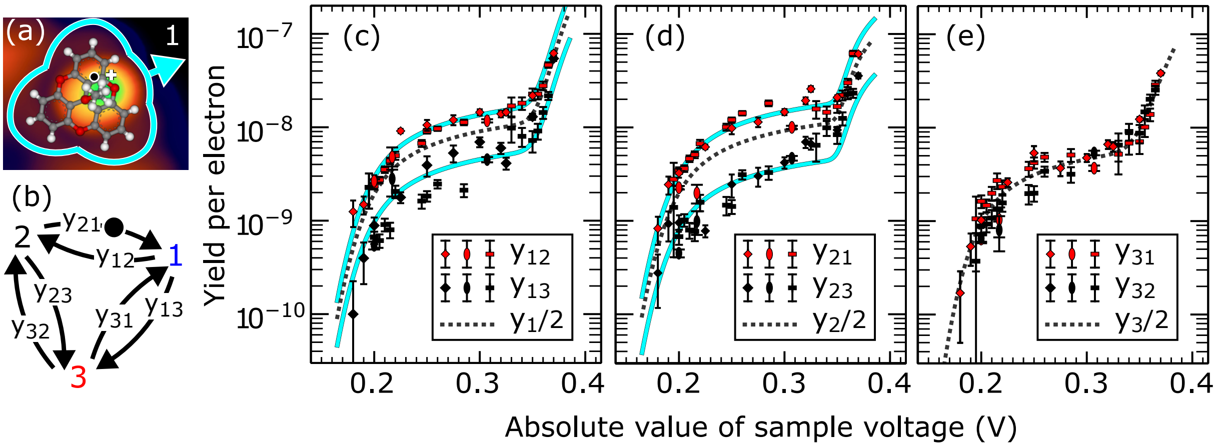

Figure 7.11.: (a) STM topograph of ethoxy-TOTA with an overlayed scaled molecular structure. The black dot (white cross) indicates the same relative positions as the white circle (cross) in Figures 7.1c–e (Sec. 7.3.1). Both positions allow to distinguish states **1-3** (cf. Figs. 7.1c–e) as distinct current levels at constant tip height. (b) Definition of the yields $y_{ij}$ for switching from state $\boldsymbol{i}$ to state $\boldsymbol{j}$. States **1**, **2**, and **3** are defined with respect of the tip position (black dot) during switching, *i. e.* they correspond to the highest, middle, and lowest current level, respectively. (c–d) Measured yields $y_{ij}$ for switching out of state (c) **1**, (d) **2** and (e) **3** with the tip positioned over the black dot in (a). Different symbols correspond to different STM tips and molecules. While the data points at high yields are based on ≈ 500 switching events, the lowest yield corresponds to ≈ 2 events. Bars indicate the standard deviation $\sigma$ expected for a Poisson process. Dashed lines correspond to fits to $y_i/2$ using Equation 7.5, and show the expected yields of non-directional switching. The fits indicate electron-induced vibrational modes between 177 to 185 meV and 355 to 400 meV. The upper (lower) solid turquoise lines in (c) and (d) represent the fits of $y_i/2$ (dashed lines) multiplied by a factor of 1.5 (0.5) and 1.6 (0.4), respectively.

**3**) are approximately equivalent. Indeed, the directionality for switching out of state **3** is relatively low for the tip position marked with a black dot ($p_{31} \lesssim 0.6$, $p_{32} \gtrsim 0.4$, Fig. 7.11e), in contrast to the data obtained at the tip position marked with a white cross (Figure 5e). Switching out of state **1** is directional for the tip position marked with a black dot with $y_{12} \approx 3 \times y_{13}$ for $|V| < 350$ mV (red and black symbols in Fig. 7.11c), whereas no directionality is observed at the white cross for $|V| \gtrsim 270$ meV (red and black symbols in Fig. 5c). Finally, switching from state **2** is directional with both tip positions. It may be worth mentioning that only two levels instead of three are observed when the tip is positioned in a symmetry plane.

At the tip position marked with a black dot, state **1** still corresponds to the smallest distance between the ethoxy moiety and the tip and therefore remains favored as a final state. This suggests that the STM tip induces directionality via an attractive force on the ethoxy moiety, as discussed above.

## 7.8. Acknowledgment

We thank the Deutsche Forschungsgemeinschaft (SFB 677 and SPP 1928-II (COORNETs)) and the Spanish MINECO (Grants No. MAT2016-78293-C6-4-R and FIS2017-83780-P) for financial support.

## 7.9. Contributions

I proposed to study the molecules. Torben Jäkel, Fynn Röhricht, and Rainer Herges synthesized them. I performed the measurements and carried out the detailed analysis of the data. Sven Johannsen performed an auxiliary measurement. Thomas Frederiksen and Aran Garcia-Lekue confirmed my gas-phase DFT calculations (not shown) and performed the calculations of adsorbed molecules. I wrote with support from Manuel Gruber the first draft of the manuscript.[295] Richard Berndt supervised the project. All authors discussed the results and improved and commented on the manuscript.

# 8

# Coverage-Controlled Superstructures of $C_3$ Symmetric Molecules: Honeycomb versus Hexagonal Tiling

This chapter is based on a manuscript published in the *Angewandte Chemie International*. The article is freely available and distributed under the terms of the *Creative Commons CC BY license*:

Torben Jasper-Tönnies, Manuel Gruber, Sandra Ulrich, Rainer Herges, and Richard Berndt, Angew. Chem. Int. Ed. **59**, 7008 (2020), *Frontispiece of issue 18.*

## 8.1. Abstract

The competition between honeycomb and hexagonal tiling of molecular units can lead to large honeycomb superstructures on surfaces. Such superstructures exhibit pores that may be used as two-dimensional templates for functional guest molecules. We present honeycomb superstructures of molecules that comprise a $C_3$ symmetric platform on Au(111) and Ag(111) surfaces. The superstructures cover nearly mesoscopic areas with unit cells containing up to 3000 molecules, more than an order of magnitude larger than previously reported. The unit cell size may be controlled via the coverage. We developed a fairly general model that describes the energetics of honeycomb superstructures built from $C_3$ symmetric units. Based on three parameters that characterize two competing bonding arrangements, the model is consistent with the present experimental results and also reproduces various published results. The model identifies the relevant driving force, mostly related to geometric aspects, of the pattern formation. In turn, the model may be employed to guide the design of molecules for building mesoscopic superstructures.

## 8.2. Introduction

Molecular self-assembly on substrates may be used to fabricate desired molecular nanostructures on surfaces. The assembly process is initiated and controlled by the molecule-substrate and molecule-molecule interactions. The former interaction ideally ensures the stable adsorption of the molecules and their efficient diffusion on the surface at suitable temperatures.[60] The molecule-molecule interactions usually determine the self-assembled molecular patterns. Often weak interactions are used such as hydrogen bonding, dispersion forces, $\pi$-$\pi$ stacking, metal coordination, and electrostatic interactions.[296–299] Local, directional and selective molecule-molecule interactions, *e. g.* hydrogen bonding and metal coordination, are particularly attractive because they enable further control of the patterns via suitable design of molecules (see, *e. g.* Ref. 300).

A vast variety of molecular surface tilings, both periodic and nonperiodic, have been reported.[60,87,97,299,301–309] In particular, a competition between honeycomb and hexagonal arrangements of $C_3$ symmetric molecules can lead to honeycomb superstructures, which have attracted considerable interest for several reasons. These superstructures exhibit cavities that may serve to arrange functional guest molecules or for synthetic molecular recognition.[60,310–316] Furthermore, a variety of periodic patterns exhibiting different pore-to-pore distances have been obtained employing a single compound on a given surface.[317–325] It has been reported that the number of molecules composing the unit cells is affected by the molecular coverage.[320] Although this control via coverage should, in principle, enable superstructures of any size, the largest unit cells reported so far were comprised of some two hundred molecules per unit cell. In addition, honeycomb superstructures may turn out useful to control the density of functional molecules on surfaces. In the context of platform molecules,[5,41,42] where a functional unit is attached to a molecular base,[87,88,91,92,210,326–328] the pattern of the platforms is imposed on the functional units.

Here, we report on coverage-controlled molecular superstructures of a $C_3$ symmetric molecule on Ag(111). While the molecule has lateral dimensions of $\approx 1\,\mathrm{nm}$, the superstructures have lattice parameters exceeding 50 nm, contain up to approximately 3000 molecules per unit cell, and cover nearly mesoscopic surface areas. The present molecular unit is a platform onto which different functional groups can be attached.[140,141,284] Moreover, we developed a model describing the dimension of the honeycomb superstructures of $C_3$ symmetric molecules. According to the model, the geometric properties of the superstructures essentially depend on three parameters related to the two competing molecule-molecule interactions that favor either hexagonal and or honeycomb arrangements. The model explains the large superstructures reported here and also reproduces previously observed superstructures of various $C_3$ molecular units. The parameters of the model can in principle be inferred from force-field calculations with moderate computational effort. Therefore it may be employed to predict geometric properties of new molecules and to guide the design of new $C_3$ molecules to realize particular honeycomb superstructures.

## 8.3. Experiments

### 8.3.1. Preliminary results for methyl-trioxatriangulenium

For the experiments we used the compound methyl-trioxatriangulenium (Me-TOTA, Fig. 8.1d) for a number of reasons. This molecule may be sublimated clean and intact in an ultra-high vacuum environment, which enables convenient control of the surface coverage.[140,141,284]

Its $C_3$ symmetry allows for a range of molecular assemblies. The molecule is mobile on the surface when prepared at suitable temperatures, which is essential for the molecules to be able to explore different superstructures. In addition, the TOTA platform and the related compound triazatriangulenium are very versatile and the methyl moiety may be exchanged for other moieties of interest. This has been demonstrated for small moieties such as hydrogen, ethyl, ethynyl, and propynyl[140,141,284] as well as porphyrins, diazocine, norbornadiene, imine, and azobenzene derivatives.[42,86–92]

Using low-temperature scanning tunneling microscopy (STM) along with density function theory (DFT) calculations[140,141,284] we previously showed that the TOTA platform lies flat on Au(111) substrates with the attached moiety standing vertical (Fig. 8.1d). Me-TOTA binds to Au(111) via *physisorption* with an adsorption energy on the order of $-2\,\mathrm{eV}$, which is comparable to that of a covalent bond. This large binding energy is caused by the extended $\pi$ electron system of the platform The adsorption is strongest when the center of the molecule is located above a hollow site of the Au(111) surface.

Below we first present the patterns formed by Me-TOTA on Au(111). While fairly large superstructures were observed, we suspected that the herringbone reconstruction of this substrate may be a limiting factor for the self-assembly process and therefore extended our study to Ag(111). Indeed, much larger superstructures were achieved as presented below.

## 8.3.2. Experimental results on Au(111) substrates

At low coverages, Me-TOTA forms a honeycomb mesh on Au(111) (Fig. 8.1a).[XLII] A unit cell with two molecules is indicated by a red rhombus whose corners are located at pores of the molecular network. We label the structures by the number $N$ of molecules along the line connecting two adjacent pores. According to this definition, Figure 8.1a shows a $N = 1$ superstructure.

Figure 8.1e displays a model of a pair Me-TOTA molecules that is based on the STM observations. The two molecules are rotated by 60° with respect to each other, which enables the formation of two O···H hydrogen bonds. The sides of the molecules form an angle of 35° with a densely-packed direction of the Au substrate (Fig. 8.1e) rendering the adsorption geometry chiral. For an isolated molecule, DFT calculations predict a very similar value of 36° (Chap. 9, Sec. 9.9.6).

In addition, the pairwise interactions make the honeycomb structures chiral as well. For example, the O atom of the left molecule in Figure 8.1e binds to the H atom located below the O atom of the right molecule. In the other enantiomer the H atom above the O atom of the right molecule is involved in bonding.

The structure of Figure 8.1e involves the occupation of two hollow sites (marked green and yellow for the left and right molecule, respectively) that correspond to *hcp* and *fcc* positions of the Au lattice. The calculated energy difference between these sites ($\lesssim 30$ meV) is within the uncertainty of DFT calculations (Chap. 6, Sec. 6.7.2).

On sample areas with different local coverages other ordered superstructures were observed (SI, Sec. 8.7.1). While they exhibit the same symmetry as the simple honeycomb

---

[XLII] Images were recorded at 4.6 K.

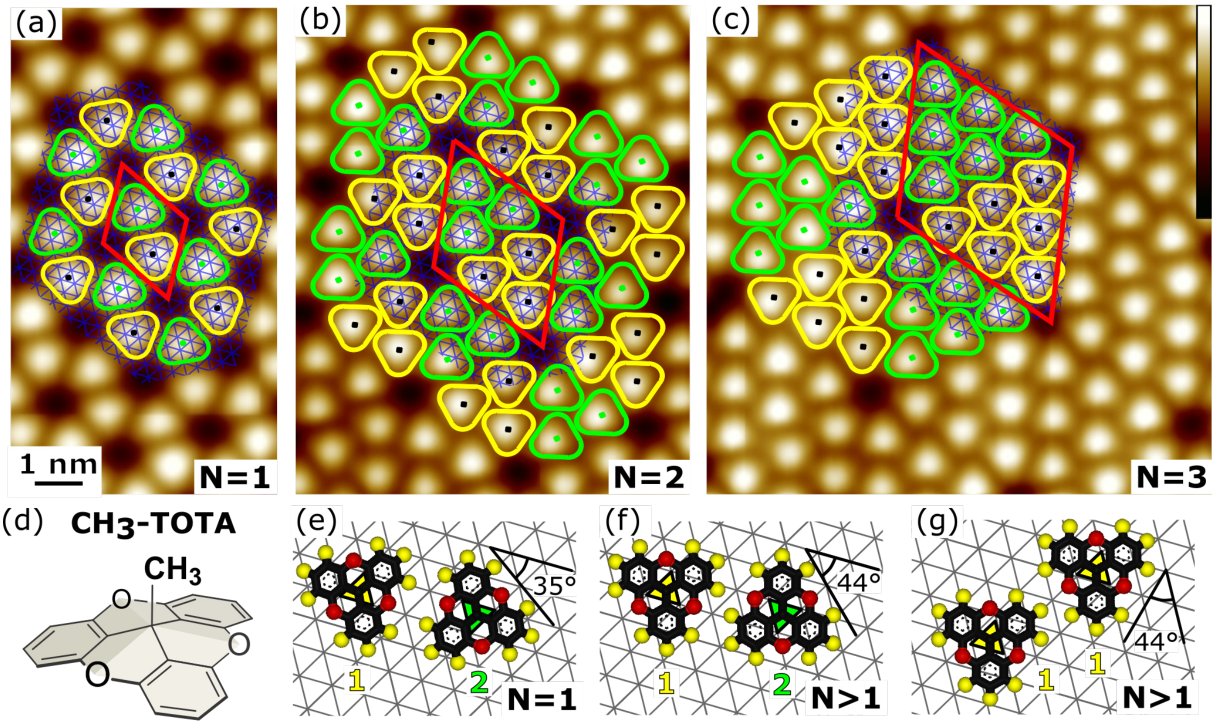

Figure 8.1.: (a–c) Constant-current STM topographs of a series of honeycomb superstructures of Me-TOTA on Au(111) (tunneling parameters: 30 pA, (a) 1 V, (c–b) 100 mV). Some molecules are marked with rounded triangles whose color is representative of the molecular adsorption site — hollow site in *hcp* or *fcc* position of the substrate lattice — and of the orientation of the molecule relative to the substrate (cf. e–g). The vertices of the blue hexagonal meshes indicate the approximate positions of the underlying surface Au atoms neglecting the herringbone reconstruction. Red rhombi show the unit cells of honeycomb superstructures of orders (a) $N = 1$, (b) 2 and (c) 3. The colorscale shown as an inset in panel (c) ranges over 0.23 nm, and is common for the three topographs. (d) Lewis structures of methyl-trioxatriangulenium (Me-TOTA). (e–g) Pairwise configurations commonly observed for Me-TOTA on Au(111). Scaled gas-phase models of Me-TOTA are overlayed on hexagonal meshes indicating the Au(111) surface atoms (nearest neighbor distance $a = 0.288\,\mathrm{nm}$). Hydrogen (oxygen) atoms are depicted by yellow (red) spheres. The center-to-center distances between the molecules are $\sqrt{37/3}\,a = 1.01\,\mathrm{nm}$ for (e) and (f) and $\sqrt{13}\,a = 1.04\,\mathrm{nm}$ for (g).

pattern the sizes of the unit cells are larger. Figures 8.1a–c show examples of $N = 1, 2,$ and 3 superstructures. The number of molecules per unit cell (red rhombi) is $N_N = N(N+1)$, *i. e.* 2, 6, and 12 molecules, respectively. Each unit cell is comprised of two subunits with hexagonal packing of the molecules that corresponds to a $\sqrt{13} \times \sqrt{13}\, R\, 13.9°$ mesh relative to the underlying Au plane. The equivalent matrix notation of the structure reads $\left(\begin{smallmatrix} 3 & 1 \\ -1 & 4 \end{smallmatrix}\right)$.[XLIII] The subunits are different in terms of the molecular orientations (rotated by 60°) and the adsorption sites (*fcc* vs. *hcp*). The molecules are arranged in a corner-to-side manner within the subunits (*e. g.* molecules marked in yellow in Fig. 8.1c), and side-by-side at the subunit boundaries.

---

[XLIII] For completeness, we point out that a more dilute hexagonal packing of Me-TOTA on Au(111) has been reported elsewhere.[86] The difference may be related to deviations in the sample preparation (wet chemistry versus sublimation).

Closer inspection of the side-by-side arrangement (Fig. 8.1f) reveals a subtle difference of the $N > 1$ structures compared to the simple $N = 1$ honeycomb mesh. The angle between a densely-packed direction of the substrate and the side of a molecules is 44° rather than 35°. This small rotation leads to corner-to-side orientation that improves O···H bonding (Fig. 8.1g). Neighbors share one such bond in the subunits whereas two hydrogen bonds occur in the side-by-side configuration at boundaries. Naively one may expect that the molecules will form patterns that maximize the number of double hydrogen bonds. However, as will be shown below, this is not the primary driving force.

We observed Me-TOTA superstructures up to $N \approx 8$ on Au(111). The structures have an epitaxial relation with the underlying surface within the uncertainty of the calibration of the piezo scanner of $< 5\,\%$.[317–325] To the best of our knowledge, such a relation was not reported before for honeycomb superstructures. We therefore hinted that the herringbone reconstruction of Au(111) may prevent the formation of superstructures with larger $N$. To test this hypothesis, we used a Ag(111) substrate. Its lattice parameter is very close to that of Au(111) and its surface is unreconstructed and regular over large terraces.

### 8.3.3. Large honeycomb superstructures on Ag(111)

The deposition of Me-TOTA on Ag(111) at ambient temperature produces very large honeycomb superstructures. Figure 8.2a (Page 98) shows a $N = 43$ mesh. The distance between pores is 44.7 nm and each unit cell comprises ≈ 1900 molecules. Another example of a large honeycomb superstructure with $N = 54$ corresponding to ≈ 3000 molecules per unit cell is shown in Figure 8.2b. Interestingly, the lines separating unit cells exhibit different orientations than those of Figure 8.2a (compare, for instance, the yellow and green triangles in Figs. 8.2a and b, respectively). A more detailed analysis shows that a chirality is induced by adsorption of the molecules on the Ag(111) mesh. The corner-to-side arrangement of the molecules, occurring at the borders of hexagonal domains (*e. g.*, triangles in Figs. 8.2a and b), defines a direction relative to the underlying substrate. The molecules in domains R and S (green an yellow triangles in Figs. 8.2a and b) arrange themselves along axes (green and yellow lines in Fig. 8.2c) that are rotated by $\pm 13.9\,°$ relative to a densely packed atomic row (dashed red line in Fig. 8.2c). In other words, R and S are rotational domains ($27.8\,°$ rotation). The additional numbers 1 and 2 denote areas where the molecules occupy *fcc* and *hcp* adsorption sites.

Comparing Figures 8.1 and 8.3 we find that the honeycomb superstructures observed on Ag(111) are essentially the same as on Au(111). In both cases, the molecules within a domain are arranged with a corner-to-side configuration (*e. g.*, molecules marked by magenta or yellow triangles in Fig. 8.3) and occupy the same type of hollow adsorption site. Molecules belonging to neighboring domains are rotated by 60° relative to each other. The side-by-side configurations at domain boundaries on Ag(111) (Fig. 8.3b) and Au(111) (Fig. 8.1f) are identical.

The large superstructures on Ag(111) are more prone to defects at the unit cell corners. Figure 8.3a shows an example: the domain at the lower right (magenta) is interrupted by a row of molecules with a different orientation (green). These molecules actually occupy bridge sites, a case we did not observe for superstructures of intermediate $N$. In addition, the pores are sometimes occupied by a molecule (molecule marked in grey in Fig. 8.3a).

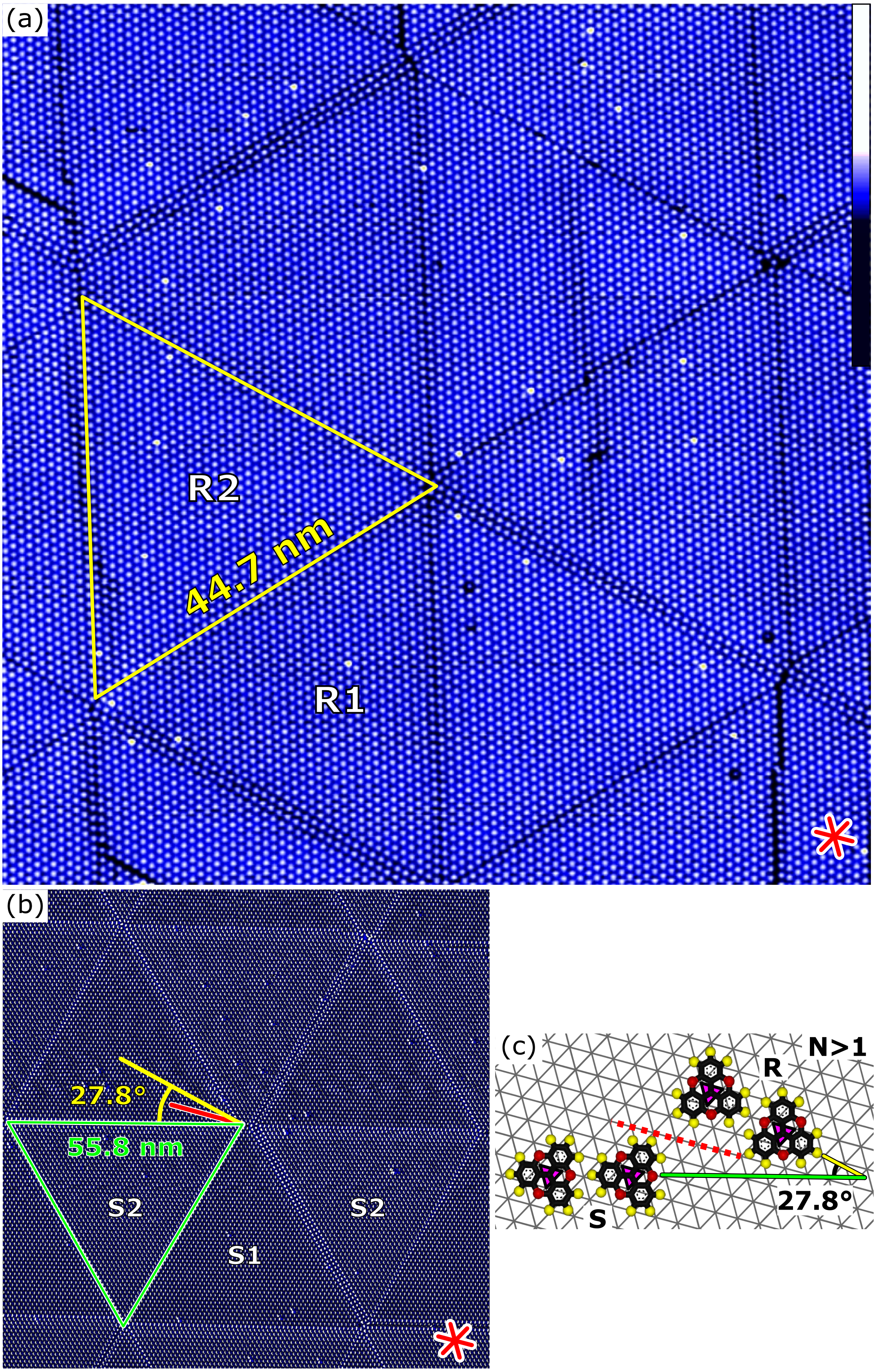

Figure 8.2.: See the next page for the caption.

Figure 8.2.: (Caption) (a) Constant-current STM topograph of a $N = 43$ superstructure of Me-TOTA on Ag(111) (Image width: 97 nm; tunneling parameters: 1 V, 30 pA). Each bright dot corresponds to a single molecule. The brightest spots may be due to ethyl-TOTA impurities (on the per mil level). Triangular areas (example indicated by a yellow triangle) corresponding to half of the superstructure unit cell exhibit edges with 43 molecules (neglecting defects). Red lines (lower-right corner) indicate densely packed directions of the Ag(111) surface. The inset on the right displays the false-color scale. (b) STM image of a $N = 54$ Me-TOTA pattern on Ag(111) with the opposite chirality as reflected by the domain orientations in (a) (yellow) and (b) (green). Each unit cell contains almost 3000 molecules. The data shown are the deviations (±10 %) of the tunneling current from a constant value of 23 pA at 0.8 V. (c) Corner-to-side molecular arrangements relative to the silver-atom mesh (gray) for the enantiomers S and R. The yellow and green lines indicate the orientation defined by the corner-to-side stacking of the molecules in the domain R and S, respectively. The dashed red line is oriented along a densely packed atomic row. The letters in (b) and (c) specify the enantiomers in the corresponding domain, while the numbers indicate adsorption sites (1 and 2 for *fcc* and *hcp* hollow sites).

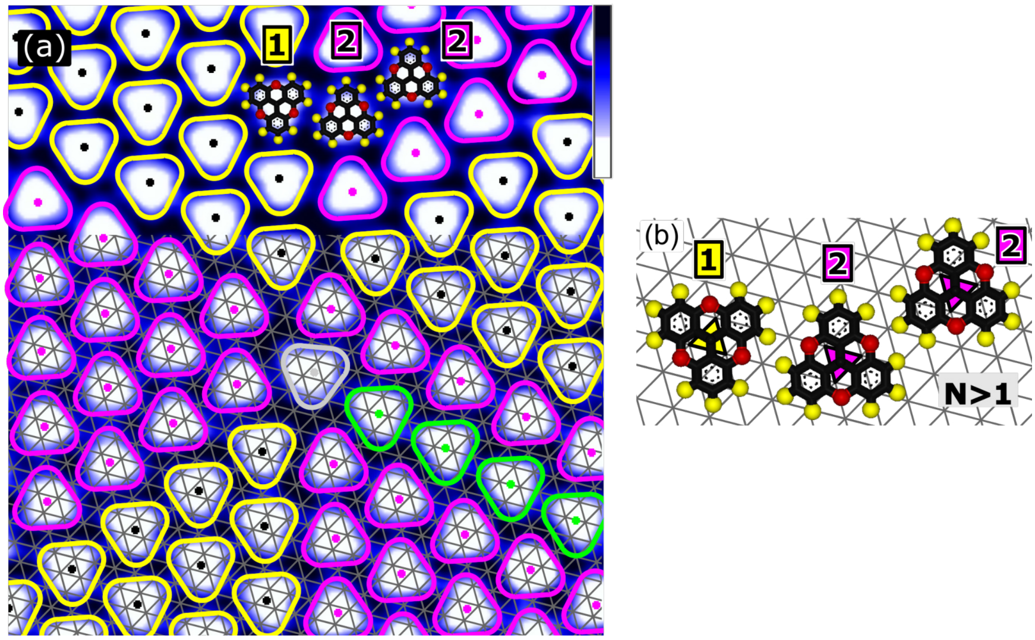

Figure 8.3.: (a) Constant-current STM topograph of Me-TOTA on Ag(111). The image show a a defect-rich area at the vertex of $N = 43$ unit cells, where the pore is occupied by a molecule (grey). A mesh is superimposed onto the lower part of the topograph to indicate the positions of the underlying silver atoms. The molecules marked in magenta and yellow are oriented as expected for the hexagonal domains. They also occupy different hollow adsorption sites. Green triangles point out molecules adsorbed at bridge sites forming a defect raw. Image width: 9.2 nm, tunneling parameters: 1 V, 30 pA. The inset shows the color scale used. (b) Ag lattice with scaled molecular structures illustrating the arrangement of molecules at domain boundaries. The pairwise geometries are identical to those on Au(111) (Figs. 8.1f and g). The numbers identify different adsorption sites (*e. g.*, 1 for *fcc* and 2 for *hcp*).

## 8.4. Model

To interpret the evolution of the unit cells from 2 molecules in the $N = 1$ honeycomb structure to huge cells with $N = 54$ we developed a model that considers $C_3$ symmetric molecules with two interactions that favor either honeycomb or hexagonal patterns. Related models have been previously reported for specific systems. Ye *et al.*[320] assumed that trimesic-acid molecules maximize the density of double hydrogen bonds, which leads to a coverage dependence of $N$. Xiao *et al.*[321] considered the intermolecular interaction energy per surface area as a function of $N$. Both models invoke energy density rather than total energy. However, for a given coverage, one would expect the latter quantity to be minimized in the ground state. Honeycomb structures of trimesic-acid molecules on a hexagonal lattice of sites have also been studied with Monte Carlo simulations.[329] The simulations involved two short-range pairwise interactions and lead to periodic superstructures with $N$ up to 4 (lattice parameter $\approx 4.5$ nm).

Our model aims to describe the ground-state structure of any $C_3$-symmetric molecule exhibiting two dominating pairwise interactions characterized by the energies $\varepsilon_{\mathrm{Hc}}$ and $\varepsilon_{\mathrm{Hex}}$. The obtained ground-state structure is the result of a competition between adsorption and interaction energies, and depends on the coverage $\theta$. We note that a given sample coverage, used as a global quantity, does not necessarily reflect a single (local) molecular density, but may be realized by a combination of areas with different molecular densities.

## 8.4.1. Assumptions

The interaction energy $E_N$ is defined as the average energy reduction of a single molecule due to the interaction with neighboring molecules, while $\varepsilon_{\mathrm{Ads}}$ is the adsorption energy per molecule. $\varepsilon_{\mathrm{Ads}}$ is assumed to be constant for all molecules in all superstructures. Analogously, the two dominating pairwise interactions of the molecules are supposed to be independent of the order $N$ of the superstructure. Adsorption on the second layer is assumed to be unfavorable because no second-layer molecules were reported for the systems considered below.

We mainly focus on the case where the total energy of the molecules is dominated by adsorption rather than interaction energy, *i. e.* $|\varepsilon_{\mathrm{Ads}}| \gg |E_N|$. This case is particularly interesting because (i) predictions of the ground-state superstructure can be made without a precise knowledge of $\varepsilon_{\mathrm{Ads}}$ and (ii) this condition is often fulfilled for largish molecules on metal surfaces. Indeed, interactions mediated by hydrogen bonds and dispersion forces bind with energies on the order of 0.1 eV, while adsorption of molecules is often much stronger, *i. e.* $|\varepsilon_{\mathrm{Ads}}|$ in the order of a few electronvolts per molecule. In the present case of physisorbed Me-TOTA calculations yielded $|\varepsilon_{\mathrm{Ads}}| \approx 2\,\mathrm{eV}$.[141,284]

Finally, kinetic aspects are neglected.

## 8.4.2. Energy considerations

Hereafter, *negative* interaction and adsorption energies indicate *attraction.* For $|\varepsilon_{\mathrm{Ads}}| \gg |E_N|$, every adsorbed molecule reduces the energy of the system (Supporting information (SI), Sec. 8.7.2) and the ground state is obtained by first maximizing the number of adsorbed molecules and then minimizing the intermolecular interaction energy in a second step (SI, Sec. 8.7.2). If not all available molecules can be accommodated in any superstructure of order $N$, the ground state is the superstructure with maximal density $\rho_N$. Otherwise, the ground state is found among those superstructures that can lead to a coverage $\theta$ by minimizing the interaction energy.

In the following, we consider a single phase with a superstructure $N$. Separation into several phases is not expected as discussed in the SI, Section 8.7.3. Below we first derive expressions for the molecular densities and interaction energies that are required for the total energy minimization.

### 8.4.3. Molecular density and interaction energy

Figures 8.4a and 8.4b display schematics of $C_3$ symmetric molecules in honeycomb and hexagonal arrangements. In the honeycomb mesh, every molecule has three nearest neighbors at a center-to-center distance $d_1$ (Fig. 8.4a). The number of nearest neighbors increases to six in the hexagonal arrangement (Fig. 8.4b), with a center-to-center distance $d_\infty$. The angle $\varphi$ takes different stacking directions of the two configurations into account (Fig. 8.4b). With the above definitions, the unit-cell area of a honeycomb superstructure of order $N$ reads (SI, Sec. 8.7.4):

$$A_N = \frac{\sqrt{3}}{2}\left\{3 + c\,(N-1)\left[3\,\cos(\varphi) + \sqrt{3}\,\sin(\varphi)\right] + (N-1)^2\,c^2\right\}d_1^2, \quad (8.1)$$

where $c = d_\infty/d_1$. Since the number of molecules in the unit cell is $N_N = N(N+1)$, the molecular density is given by:

$$\rho_N = \frac{N(N+1)}{A_N}. \quad (8.2)$$

The densities $\rho_1$ and $\rho_\infty$ of honeycomb $N = 1$ and hexagonal structures are:

$$\rho_1 = \frac{4}{3\sqrt{3}\,d_1^2}, \quad \rho_\infty = \frac{2}{\sqrt{3}\,c^2\,d_\infty^2}, \quad (8.3)$$

from which we find:

$$\frac{\rho_\infty}{\rho_1} = \frac{3}{2}\,\frac{1}{c^2}. \quad (8.4)$$

This implies that the molecular densities in the honeycomb $N = 1$ and hexagonal structures are equal for $c = \sqrt{3/2}$. We note that for $c = \sqrt{3/2}$, the largest molecular densities are achieved for $N = 2$ and 3, and in particular $\rho_{2,3} > \rho_1$.

Different evolutions of the superstructures may be expected depending on the pairwise interaction energies. The interaction energies of the configurations depicted in Figures 8.4a and b are $E_1 = 3\,\varepsilon_{\mathrm{Hc}}$ and $E_\infty = 6\,\varepsilon_{\mathrm{Hex}}$, where $\varepsilon_{\mathrm{Hc}}$ and $\varepsilon_{\mathrm{Hex}}$ are the energies of an edge-edge and a corner-edge bond, respectively. These values correspond to the energy reduction of a single Me-TOTA molecule due to the interactions with neighboring molecules in honeycomb $N = 1$ and hexagonal structures, respectively. The interaction energy in honeycomb superstructures of order $N$ depends on the relative position of the molecules. Molecules at the edges of domains, at the corners, and in the hexagonal structure have interaction energies $\varepsilon_{\mathrm{Hc}} + 4\,\varepsilon_{\mathrm{Hex}}$, $2\,\varepsilon_{\mathrm{Hc}} + 2\,\varepsilon_{\mathrm{Hex}}$, and $6\,\varepsilon_{\mathrm{Hex}}$, respectively. In turn, the average interaction energy $E_N$ reads:

$$E_N = 6\,\frac{(N-1)\,\varepsilon_{\mathrm{Hex}} + \varepsilon_{\mathrm{Hc}}}{N+1}, \tag{8.5}$$

where negative values of $E_N$, $\varepsilon_{\mathrm{Hc}}$, and $\varepsilon_{\mathrm{Hex}}$ indicate attraction. The derivative of Equation 8.5,

$$\frac{dE_N}{dN} = \frac{6}{(N+1)^2}\left(2\varepsilon_{\mathrm{Hex}} - \varepsilon_{\mathrm{Hc}}\right), \tag{8.6}$$

reveals that $E_N$ monotonously increases (decreases) with $N$ for $\varepsilon_{\mathrm{Hc}}/\varepsilon_{\mathrm{Hex}} > 2$ ($\varepsilon_{\mathrm{Hc}}/\varepsilon_{\mathrm{Hex}} < 2$).

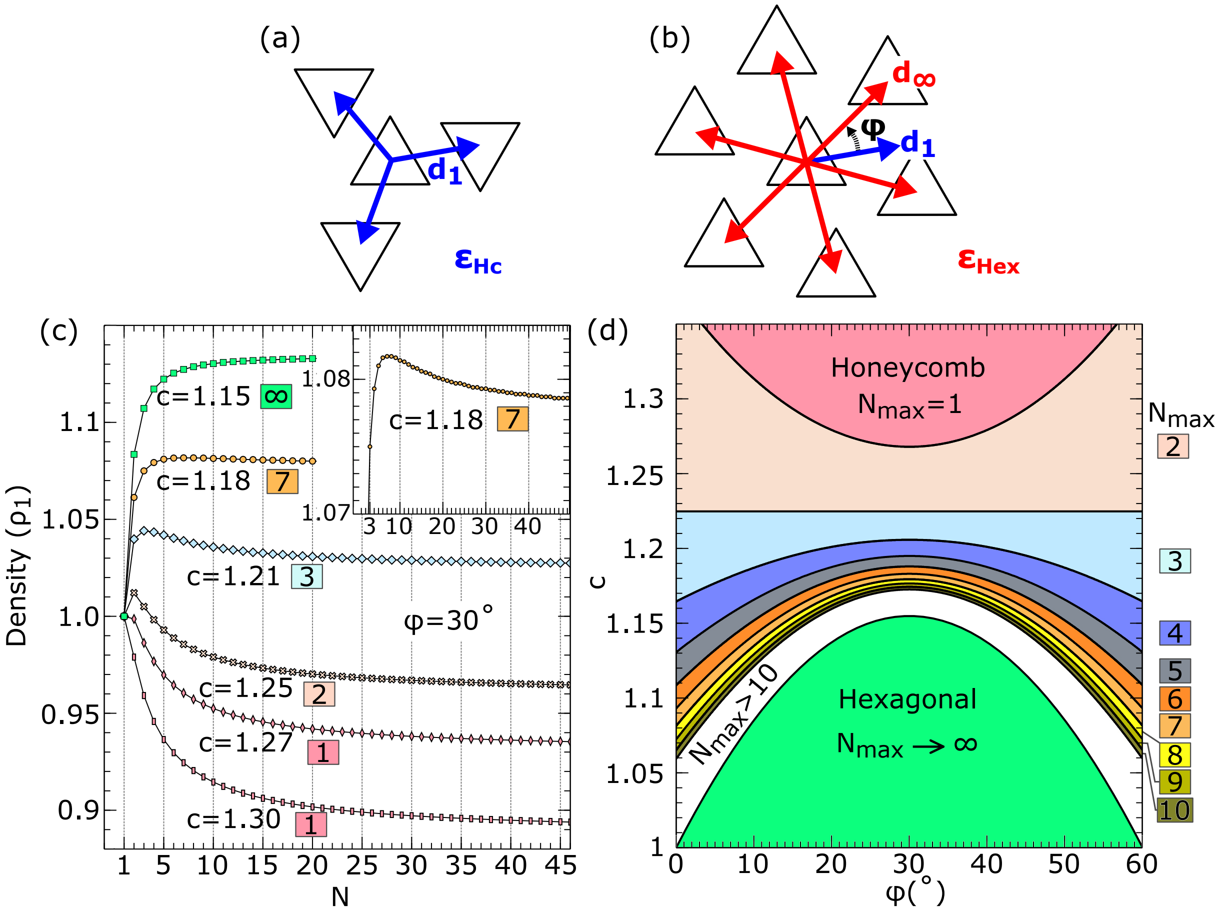

Figure 8.4.: Schematic of (a) honeycomb and (b) hexagonal arrangements of $C_3$ symmetric molecules represented by triangles. $d_1$ ($d_\infty$) denotes the center-to-center distance between neighbor molecules in the honeycomb (hexagonal) stacking. $\varphi$ is the angle between the vectors $d_1$ and $d_\infty$ and can assume values between 0 and 60°. The pairwise interaction energies for the arrangements are (a) $\varepsilon_{\mathrm{Hc}}$ and (b) $\varepsilon_{\mathrm{Hex}}$. (c) Evolution of the density (in units of $\rho_1$) evaluated using Equation 8.2 as a function of the order $N$ of the honeycomb superstructure. Curves were calculated for various $c = d_\infty/d_1$ while keeping $\varphi = 30°$. The numbers in colored boxes indicate the orders $N$ of the superstructures that maximize the density for given $c$ and $\varphi$. The inset is a zoom of the case $c = 1.18$, which exhibits a maximum density for $N = 7$. (d) Order $N_{\mathrm{max}}$ of the superstructures with maximum density versus the distance ratio $c$ and angle $\varphi$. The color code used for $N_{\mathrm{max}}$ is shown on the right. White color is used for $N_{\mathrm{max}} > 10$.[XLIV]

For low densities of Me-TOTA on Au(111) the $N = 1$ honeycomb structure is observed, which implies $E_1 < E_\infty$, and therefore $\varepsilon_{\mathrm{Hc}} < 2\,\varepsilon_{\mathrm{Hex}}$. Under this condition, $E_N$ increases with the order $N$, *i. e.* high orders are unfavorable at low coverage. The discussion below pertains to this case, $\varepsilon_{\mathrm{Hc}}/\varepsilon_{\mathrm{Hex}} > 2$.[XLV]

The evolution of the density $\rho_N$ with the order $N$ of a honeycomb superstructure is shown in Figure 8.4c for $\varphi = 30°$ and various ratios $c$. For $c = 1.30$, the density decreases with $N$ (rectangles in Fig. 8.4c). The $N = 1$ structure consequently maximizes the density and minimizes the interaction energy making $N = 1$ the ground state of the system for any coverage. The situation is different for $c = 1.15$, where the molecular density continuously increases with $N$ (green squares in Fig. 8.4c). The system evolves from a $N = 1$ honeycomb lattice at low coverages into superstructures with larger $N$ to accommodate further molecules at larger coverages. In practice, the maximum size $N$ may be limited by kinetics and surface irregularities such as steps.

A markedly different evolution occurs for $c = 1.25$. The density first increases from $N = 1$ to $N = 2$, and then continuously decreases towards larger $N$ (crosses in Fig. 8.4c). Only superstructure with $N = 1$ and 2 may be expected in this case. Larger $N$ imply a less favorable interaction energy and also a reduced density. When the distance ratio $c$ is changed, the density assumes a maximum at other values $N = N_{\mathrm{max}}$. For instance, $c = 1.18$ leads to a maximum of $N = 7$ (inset to Fig. 8.4c). We have calculated the maximal superstructure order $N_{\mathrm{max}}$ for a range of angles $\varphi$ and distance ratios $c$. The results are displayed in Figure 8.4d with colors representing $N_{\mathrm{max}}$. For any angle $\varphi$, any $N$ may occur if the distance ratio $c$ is in a suitable range.

## 8.4.4. Comparison of the model to experimental data

The model was tested for a variety of superstructures of $C_3$ symmetric molecules. Table 8.1 summarizes the relevant parameters. System B corresponds to this work. Systems C–I, K, and L were previously reported. A and J are fictitious cases with particularly small or large values of $c$.

For systems A–J, we calculated the interaction energies $E_N$ (in units of $|E_{\mathrm{Hc}}|$) and the densities $\rho_N$ (in units of $\rho_1$) for different values of $N$ (Fig. 8.5). The pairwise-interaction energies were either extracted from the corresponding reference or calculated using the Generalized AMBER Force Field[167] (cf. Sec. 4.1, Chap. 4). Owing to the normalization, the $N = 1$ honeycomb structure has a density of 1 and an interaction energy per molecule of $-1$ in all cases. The interaction energy per molecule increases as the order $N$ is increased, *i. e.* structures with higher $N$ are less favorable.

Superstructures of order $N$ can be obtained through control of the surface coverage

---

[XLIV] $N_{\mathrm{max}}$ in Fig. 8.4d was technically derived as follows: (i) The order $N$ was considered a continuous variable and the equation $\frac{d\rho_N}{dN} = 0$ was solved as a necessary condition for a maximum. (ii) Starting at the positive, real solutions of $\frac{d\rho_N}{dN} = 0$, the integer $N_{\mathrm{max}}$ with the highest density was numerically determined as function of $c$ and $\varphi$. At the border between two colored areas in Fig. 8.4d, the highest density was numerically derived at two successive integers. (iii) The limit $N_{\mathrm{max}} \to \infty$ and solutions of $\frac{d\rho_N}{dN} = 0$ give the condition $c = \cos(\varphi) + 1/\sqrt{3}\,\sin(\varphi)$. This condition defines the border between the green and white area in Fig. 8.4d.

[XLV] We recall that both energies are negative.

Table 8.1.: Parameters used in Fig. 8.5 extracted from experimental observations (B–I and K–L) or fictitious (A, J). System B is Me-TOTA.

| System | $c$ | $\varphi(°)$ | $\varepsilon_{\mathrm{Hc}}/\varepsilon_{\mathrm{Hex}}$ | $N_{\mathrm{max}}^{\mathrm{theo}}$ | $N_{\mathrm{max}}^{\mathrm{exp}}$ |
|---|---|---|---|---|---|
| A | 0.60[a] | 30[a] | 2.50[a] | $\infty$ | |
| B | 1.03 | 18.6 | 2.15[b, c] | $\infty$ | 54[e] |
| C[317,318,320] | 0.98 | 30 | 2.33[d] | $\infty$ | 8[e] |
| D[323] | 1.10 | 28.5 | 2.14[b] | $\infty$ | 12[e] |
| E[321] | 1.00 | 15 | 3.06 | $\infty$ | 8 |
| F[322] | 1.17 | 19.5 | 2.27 | 7 | 8 |
| G[330] | 1.17 | 48 | 2.73 | 5 | 5[f] |
| H[331] | 1.50 | 26 | 2.83[b] | 1 | 1[e] |
| I[324] | 1.58 | 22 | 2.75[a] | 2[g] | 2[g] |
| J | 2.00[a] | 22[a] | 2.75[a] | 1 | |
| K[319] | 1.19 | 35 | 1.14 | 5 | 2[e] |
| L[325] | 1.16 | 57 | 1.76[b] | 4 | 4[f] |

[a]Fictitious value. [b]Calculated with the Generalized Amber Force Field.[166,167] [c]Upon substrate-induced modification (SI, Sec. 8.7.5). [d]Extracted from Ref. 332. [e]Hexagonal structure was also observed. [f]Upon annealing the sample. [g]Only $N > 1$ structures are based on the same pairwise interactions.

so long as the density increases with $N$. Our model predicts that this is the case for systems B–E and in the fictitious scenario A. Hexagonal lattices were indeed reported for B–D with the orders of the largest observed structures scattering between 7 and 54. These upper limits may have various reasons including limited control of the coverage, kinetics, and surface inhomogeneities. Systems D–E actually exhibit different superstructures at submonolayer coverages, which may be due to kinetics or a dependence of the adsorption energies on the superstructure. In addition, for the systems B and C, our model predicts a large number of high $N$ superstructures within a small density interval. For instance, a coverage increase of Me-TOTA by 0.6 % would change a $N = 50$ superstructure into a hexagonal lattice. Consequently, small variations in densities between different sample areas lead to superstructures with different $N$ as observed for Me-TOTA and system C. It may be worth mentioning that between $N = 50$ and $N = \infty$, the interaction energy $E_N$ increases by only 0.3 % for Me-TOTA, which may explain the larger number of defects in the $N \approx 50$ structures.

For systems H–J, the honeycomb lattice is preferred at all coverages because it minimizes the interaction energy and provides the most dense packing. Honeycomb superstructures up to $N = 4$ were observed under special circumstances for system I. Motivated by this observation of only low $N$, we considered a fictitious ratio of $\varepsilon_{\mathrm{Hc}}/\varepsilon_{\mathrm{Hex}} = 2.75$ that favors low order structures [XLVI]. System H exhibits both honeycomb and hexagonal lattices at submonolayer coverages suggesting that $\varepsilon_{\mathrm{Hc}} \approx 2\varepsilon_{\mathrm{Hex}}$.

For systems F, G, K, and L, the density initially increases and then decreases with

---

[XLVI] A calculation of the interaction energies for system I is challenging because the intermolecular interaction is mainly mediated by flexible alkoxy chains that are deformed in the $N > 1$ assemblies.

$N$. In these examples the size of the honeycomb superstructures can be controlled up to $N = N_{\max}$. Our model predicts $N_{\max} = 7$, 5, 5, and 4 for systems F, G, K, and L, which is in line with the experimental observations (Table 8.1). Note that for K and L, $\varepsilon_{\mathrm{Hc}}/\varepsilon_{\mathrm{Hex}} < 2$. For such cases, the molecules exhibit a hexagonal packing ($N = \infty$) at low coverage, which can evolve into lower order ($N < \infty$) honeycomb superstructures at larger coverage.

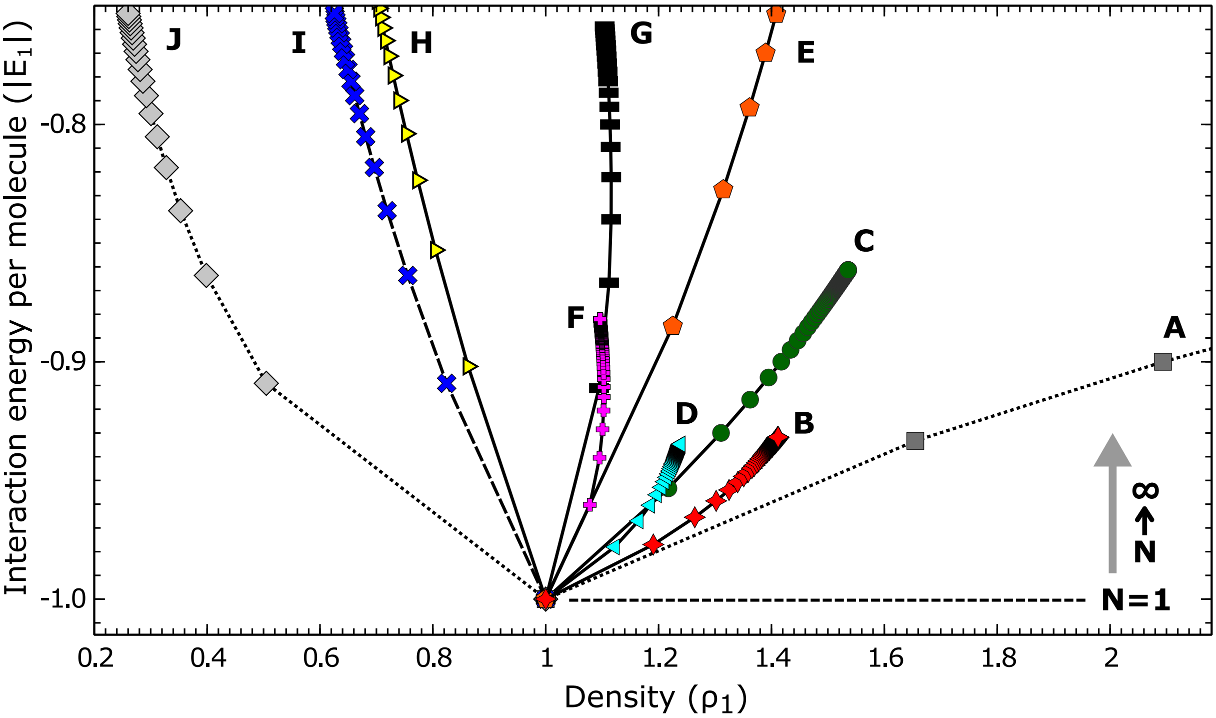

Figure 8.5.: Parametric plot of the interaction energy per molecule (Eq. 8.5) in units of $|E_1|$ versus molecular density (Eq. 8.2) in units of $\rho_1$ for honeycomb superstructures. Letters and symbols indicate different systems from Table 8.1. Lines connect the data points for each system starting from $N = 1$ (point at coordinates (1,−1)) to $N = 2, 3, \ldots$ (see inset on the right indicating the direction of increasing $N$). Upper ends of the curves correspond to $N = \infty$. Negative interaction energies $E_N$ indicate attraction. For the case considered here, $\varepsilon_{\mathrm{Hc}}/\varepsilon_{\mathrm{Hex}} > 2$, $E_N$ increases with $N$.

## 8.4.5. Case of a reservoir of molecules

The above model assumes (i) $|\varepsilon_{\mathrm{Ads}}| \gg |E_N|$ and (ii) a fixed number of available molecules. Condition (i) is violated when the system is coupled to a reservoir of molecules. This may for instance be the case when a concentrated solution of molecules is drop cast to the sample or when the molecular deposition is performed over a relatively long time. In this case the total binding energy for a superstructure $N$ reads (SI, Sec. 8.7.2):

$$E_N^{\mathrm{Tot}} = \rho_N A \left( \varepsilon_{\mathrm{Ads}} + \frac{E_N}{2} \right), \tag{8.7}$$

where $A$ is the surface area. Because both the adsorption $\varepsilon_{\mathrm{Ads}}$ and the interaction $E_N$ energies are assumed negative, it is favorable to accommodate as many molecules in the first layer as the density $\rho_N$ of the superstructure allows, *i. e.* $\theta = \rho_N$. For $|\varepsilon_{\text{Ads}}| \gg |E_N|$, Equation 8.7 simplifies to $E_N^{\text{Tot}} \approx \rho_N A \varepsilon_{\text{Ads}}$, and the ground state of the system is the superstructure that maximizes the density $\rho_N$. In contrast, for $|\varepsilon_{\text{Ads}}| \ll |E_N|$, $E_N^{\text{Tot}} \approx \rho_N A E_N/2$, such that the ground state is the structure that minimizes $\rho_N E_N$. It may be worth mentioning that $\rho_N E_N$ corresponds to the interaction energy density, *i. e.* the quantity minimized by Xiao *et al.*[321]

For $\varepsilon_{\text{Ads}} \approx E_N$ the adsorption and interaction energies compete and the result is not straightforward. Ibenskas and Tornau[329] derived a ground state phase diagram for this regime.

### 8.4.6. Discussion

We recall that our model attempts to determine the ground state. Kinetic limitations may therefore lead to the observation of intermediate superstructures as illustrated by systems G and L (Table 8.1). The initial hexagonal and disordered metastable configurations evolve toward honeycomb superstructures of order $N_{\text{max}}$ upon annealing. Trapping into metastable states may be facilitated when the energies involved are close to the ground state energy. This problem arises at large $N$ where interaction energy differences are small. For instance the interaction energy differences between the $N = 50$ and 51 structures are $\approx 20\,\mu\text{eV}$ for a single Me-TOTA molecule and $\approx 45\,\text{meV}$ for the complete unit cell.

The model drastically simplifies the complexity of interactions and atomic positions at surfaces. It may nevertheless be useful beyond an interpretation of existing structures and provide some guidance for the design of molecules that implement certain superstructures. First, the decision between a honeycomb and a hexagonal lattice at low coverage is determined by the ratio $\varepsilon_{\text{Hc}}/\varepsilon_{\text{Hex}} > 2$ ($\varepsilon_{\text{Hc}}/\varepsilon_{\text{Hex}} < 2$), *i. e.* the respective strengths of the intermolecular attractions. Second, the geometric parameters $c = d_\infty/d_1$ and $\varphi$ may be adjusted to favor a particular lattice in the limit of large coverages (Fig. 8.4d). Finally, a large variation of the density with $N$ (Fig. 8.5) simplifies the control of the superstructure order $N$ via the coverage. It also renders a superstructure more stable with respect to coverage variations.

## 8.5. Conclusions

The triangular molecule Me-TOTA forms honeycomb superstructures on Au(111) and Ag(111). The characteristic scale of the patterns is controlled by the molecular coverage. The largest unit cells observed (≈ 3000 molecules) are significantly larger than previously reported coverage-controlled honeycomb structures.[317–325] We developed a general three-parameter model of the energetics of honeycomb superstructure of $C_3$ symmetric molecules. The ground-state structure is rationalized in terms of energy minimization rather than a surmised energy density optimization. The model reproduces important aspects of the present experimental results as well as several previously reported structures. This demonstrates the versatility of the model, which may in turn be used to guide the design of molecules for honeycomb superstructures.

## 8.6. Experimental details

*Synthesis:* Me-TOTA molecules were synthesized following Ref. 284 (Chap. 9, Sec. 9.9.1).

*Sample preparation:* Clean and flat Au(111) and Ag(111) surfaces were prepared by repeated cycles of Ar sputtering and subsequent annealing. Molecule deposition was performed by sublimation from a Ta crucible under pressures below $10^{-7}$ Pa onto a sample held at ambient temperature (Chap. 3, Sec. 3.5.3). The samples were then inserted into a cryogenic STM without breaking the vacuum.

## 8.7. Supporting information

### 8.7.1. Additional data of Me-TOTA on Au(111)

Figure 8.6 shows an overview topograph of Me-TOTA on Au(111), which exhibits superstructures of different orders. The coexistence of several superstructures, with different molecular densities, suggests that kinetic effects have hindered the convergence to the ground state characterized by a single superstructure.

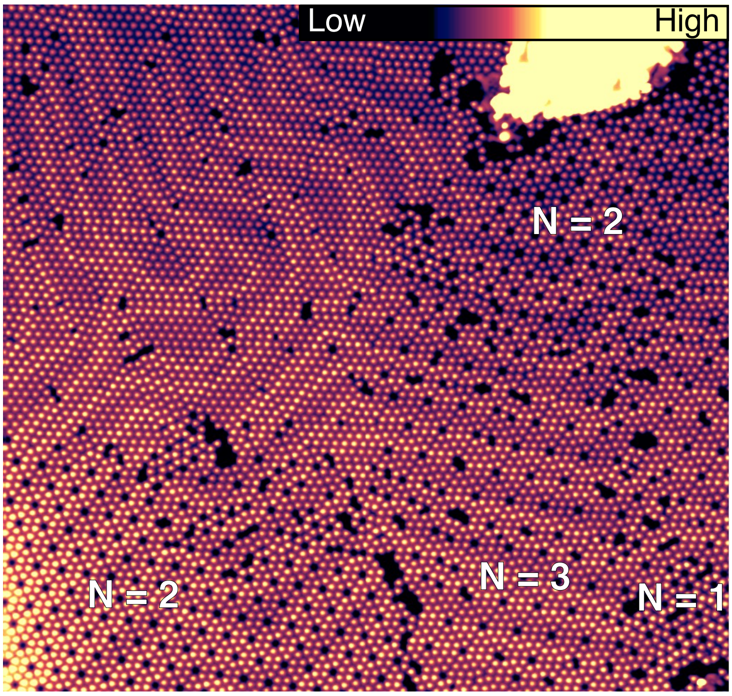

Figure 8.6.: Large-scale constant-current STM topograph (93 nm wide) of Me-TOTA on Au(111). Different areas of the sample are labeled with the order of the corresponding superstructure.

### 8.7.2. Total binding energy

We recall that every superstructure of order $N$ is associated with a molecular density $\rho_N$ and an averaged interaction energy $E_N$. On a sample of surface area $A$ with a molecular coverage $\theta$, $\theta A$ molecules are available. To simplify the discussion, we only consider coverages $\theta$ that match given molecular density $\rho_N$. In this case, the ground state structure can be described with a single superstructure $N$, while intermediate coverages may involve two superstructures.

Every molecule adsorbed within the first layer reduces the total binding energy by $\varepsilon_{\mathrm{Ads}}$ (adsorption) and by $E_N/2$ (interaction with neighboring molecules), while other molecules (in the gas phase or second layer) do not contribute to the binding energy. For a superstructure $N$ with $\rho_N \geq \theta$, *i. e.* a superstructure that can accommodate all available molecules, the total binding energy is:

$$E_N^{\mathrm{Tot}} = \theta A \left( \varepsilon_{\mathrm{Ads}} + \frac{E_N}{2} \right), \tag{8.8}$$

whereby parts of the surface may remain molecule-free. However, if $\rho_N < \theta$, only $\rho_N A$ molecules are in the first layer, while $\theta A - \rho_N A$ molecules are in the second layer or in the gas phase and do not contribute to the binding energy. In that case, the total binding energy reads:

$$E_N^{\mathrm{Tot}} = \rho_N A \left( \varepsilon_{\mathrm{Ads}} + \frac{E_N}{2} \right). \tag{8.9}$$

Thus, the total binding energy of a structure and $\theta\, A$ available molecules can be expressed as:

$$E_N^{\mathrm{Tot}} = \begin{cases} \theta A \left( \varepsilon_{\mathrm{Ads}} + \frac{E_N}{2} \right), & \text{if } \rho_N \geq \theta. \\ \rho_N A \left( \varepsilon_{\mathrm{Ads}} + \frac{E_N}{2} \right), & \text{otherwise.} \end{cases} \tag{8.10}$$

The ground-state superstructure $N$ is the one that minimizes Equation 8.10.

For $\varepsilon_{\mathrm{Ads}} \gg E_N$, the interaction between the molecules may be viewed as a perturbation. In that case, the adsorption energy is minimized first, followed by a minimization of the interaction energy. The first minimization is realized by fulfilling $\rho_N \geq \theta$, as this condition ensures that all available molecules are adsorbed within the first layer. From the subset of superstructures $N$ minimizing the adsorption energy, the ground state is the one that minimizes the interaction energy $E_N$. The resulting superstructure $N$ is the one minimizing the total binding energy.

In the particular case that the system is coupled to a reservoir of molecules, the coverage is not fixed but follows the molecular density $\rho_N$, as every adsorbed molecule reduces the total binding energy, *i. e.* molecule-free areas on the sample are energetically unfavorable. The total binding energy then simplifies to:

$$E_N^{\mathrm{Tot}} = \rho_N A \left( \varepsilon_{\mathrm{Ads}} + \frac{E_N}{2} \right). \tag{8.11}$$

In other word, the ground state for that case is the superstructure minimizing the energy density $E_N^{\mathrm{Tot}}/A$.

## 8.7.3. Single phase *N* vs. phase separation

Below we determine conditions under which a single phase being energetically preferred over several phases. We consider a surface area with coverage $\rho_N$ and superstructure order $N$ that decomposes into two phases of orders $\alpha$ and $\beta$ covering fractions $x_\alpha$ and $x_\beta$ of the area. This implies

$$\rho_N = x_\alpha \rho_\alpha + x_\beta \rho_\beta \text{ and } x_\alpha + x_\beta = 1. \tag{8.12}$$

Using Equations 8.12, the fraction $x_\alpha$ covered with phase $\alpha$ reads:

$$x_\alpha = \frac{\rho_N - \rho_\beta}{\rho_\alpha - \rho_\beta} \tag{8.13}$$

We first consider the case $\varepsilon_{\mathrm{Hc}}/\varepsilon_{\mathrm{Hex}} > 2$. As shown in Section 8.4.3, this condition leads to interaction energies $E_N$ that increase with $N$. We further assume geometric parameters $c$ and $\varphi$ of the pairwise interactions (defined in Figs. 8.4a and b) that lie in the green area of Figure 8.4d (Sec. 8.4.3). This assumption leads to *increasing* densities $\rho_N$ with increasing $N$. The orders $\alpha$ and $\beta$ then are lower and higher, respectively, than $N$ (cf. Eq. 8.12). The relations between the interaction energies and the densities read

$$E_\alpha < E_N < E_\beta \text{ and } \rho_\alpha < \rho_N < \rho_\beta. \tag{8.14}$$

Neglecting energy contributions of phase boundaries and using Equations 8.12 the total interaction energy of the two phases is given by:

$$\frac{N_\alpha E_\alpha + N_\beta E_\beta}{2} = \frac{x_\alpha A \rho_\alpha E_\alpha + (1 - x_\alpha) A \rho_\beta E_\beta}{2}, \tag{8.15}$$

where $N_\alpha$ ($N_\beta$) is the number of molecules that arrange in phase $\alpha$ ($\beta$) and cover the area $x_\alpha A$ ($x_\beta A$). The factor 1/2 avoids double counting.

A single phase is preferred over several phases when [XLVII]:

$$N_\alpha E_\alpha + N_\beta E_\beta > N_A E_N. \tag{8.16}$$

Using Equations 8.12, 8.13, 8.14, and 8.15 the above equation develops to

$$\frac{E_N - E_\beta}{\rho_N - \rho_\beta} > \frac{\rho_\alpha}{\rho_N} \frac{E_\beta - E_\alpha}{\rho_\beta - \rho_\alpha}. \tag{8.17}$$

Since $\rho_\alpha/\rho_N < 1$, a more restrictive condition is

$$\frac{E_N - E_\beta}{\rho_N - \rho_\beta} > \frac{E_\beta - E_\alpha}{\rho_\beta - \rho_\alpha}. \tag{8.18}$$

Figure 8.7 shows the interaction energy $E_N$ as a function of coverage $\rho_N$ for a fictitious system fulfilling Equation 8.14. The left and right terms of Equation 8.18 correspond to the slopes of the red and blue lines in Figure 8.7. Equation 8.18 is fulfilled in this case and generally when

$$d^2 E_N / d\rho_N^2 > 0. \tag{8.19}$$

Systems B–E fall into this class (cf. Fig. 8.5).

A single phase is also expected for all systems that assume a maximal density at a

---

[XLVII] Negative energies indicate binding.

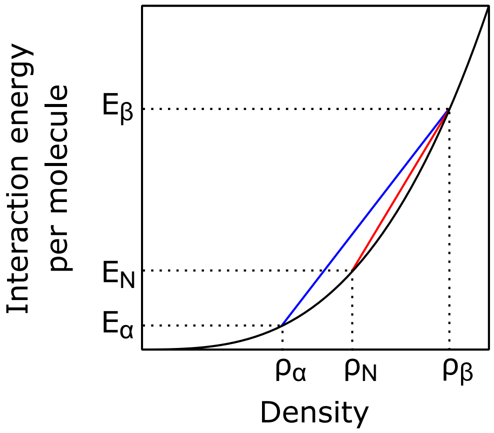

Figure 8.7.: Interaction energy $E_N$ as a function of density $\rho_N$ for a fictitious system satisfying Equation 8.18 . The red and blue lines exhibit slopes $(E_N - E_\beta)/(\rho_N - \rho_\beta)$ and $(E_\beta - E_\alpha)/(\rho_\beta - \rho_\alpha)$.

finite order $N_{max}$ (cf. Fig. 8.4d, Sec. 8.4.3) because their density increases up to this order and higher orders are inaccessible. This is the case of systems F and G.

Equation 8.19 is not satisfied for the fictitious system A. Nonetheless, a single phase is preferred because $\rho_\alpha/\rho_N$ is sufficiently small to fulfill Equation 8.17.

Finally, we address the case $\varepsilon_{\mathrm{Hc}}/\varepsilon_{\mathrm{Hex}} < 2$, *i. e.* systems in which $E_N$ *decreases* with increasing $N$. Additionally we assume that $\rho_N$ *decreases* with $N$, *i. e.* parameters $c$ and $\varphi$ that lie in the red area of Figure 8.4d (Sec. 8.4.3). Arguments analogous to the ones used above apply and lead to the conclusion that a single phase is preferable. Systems K–L belong to this class with minimal density for the hexagonal structure ($N = \infty$) and a maximal density at a finite order $N_{max}$.

In summary, a single-phase ground state is preferred in all cases considered.

It may be worth noting that usually the number of molecules will be no integer multiple of the number of molecules per unit cell, $N(N+1)$. While this has a negligible effect on large terraces, it may become relevant when the molecules are confined to a small area.

### 8.7.4. Unit cell area of honeycomb superstructures

A lattice vector $\vec{a}_{\mathrm{I}}$ of the rhombic unit cell of a superstructure of order $N$ is given by

$$\vec{a}_{\mathrm{I}}(N) = \vec{d}_1 + \underline{R}(60°)\,\vec{d}_1 + (N-1)\,\vec{d}_\infty, \tag{8.20}$$

where $\vec{d}_1$ and $\vec{d}_\infty$ are the lattice vectors of the simple $N = 1$ honeycomb and hexagonal meshes. $\underline{R}(\theta)$ is the matrix for an in-plane rotation by the angle $\theta$. Equation 8.20 is illustrated in Figure 8.8 for $N = 3$.

The second lattice vector $\vec{a}_{\mathrm{II}}$ of the superstructure reads:

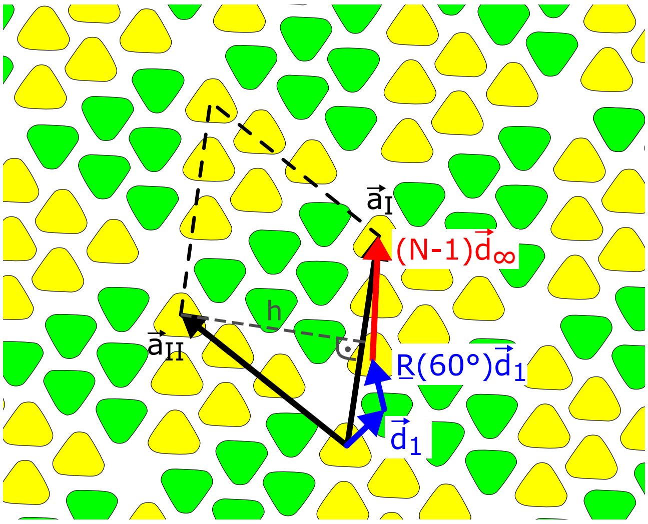

Figure 8.8.: Sketch of a $N = 3$ honeycomb superstructure. A rhombus (dashed black line) shows a unit cell with lattice vectors $\vec{a}_\text{I}$ and $\vec{a}_\text{II}$.

$$\begin{aligned}\vec{a}_\text{II}(N) &= \underline{R}(120°)\,\vec{d}_1 + \underline{R}(60°)\,\vec{d}_1 + (N-1)\,\underline{R}(60°)\,\vec{d}_\infty && (8.21)\\ &= \underline{R}(60°)\,\vec{a}_\text{I}. && (8.22)\end{aligned}$$

The angle between $\vec{a}_\text{I}$ and $\vec{a}_\text{II}$ is therefore 60°, and $|\vec{a}_\text{I}| = |\vec{a}_\text{II}|$. The area $A_N$ of the rhombus is

$$A_N = \frac{\sqrt{3}}{2}\,a_I^2(N). \tag{8.23}$$

Considering the definitions of $\vec{d}_1$ and $\vec{d}_\infty$ (Figs. 4a and b, Sec. 8.4.3), we have:

$$\vec{d}_\infty = c\,\underline{R}(\varphi)\,\vec{d}_1,\; c = \frac{d_\infty}{d_1}. \tag{8.24}$$

Equation 8.1 in Section 8.4.3 is obtained from Equation 8.23 using Equations 8.20 and 8.24.

### 8.7.5. Pairwise interaction energies of Me-TOTA

The interactions energies were estimated from calculations with the generalized AMBER force field[167] using Avogadro, an open-source molecular builder and visualization tool (Version 1.2.0).[166] The structure of the Me-TOTA molecules was fixed to that inferred from DFT calculations upon relaxation on Au(111).[141,284] The pairwise interaction energies $\varepsilon_\text{Hc} = -160\,\text{meV}$ and $\varepsilon_\text{Hex} = -100\,\text{meV}$ (cf. Sec. 4.1, Chap. 4) were obtained by minimization of the total energy of two molecules constrained to a plane.

Previous calculations predicted a charge transfer between the Me-TOTA molecules and the metal substrate.[284] This adds further electrostatic interaction between the molecules.

To estimate its energy, a partial charge $|q| = 0.3$ e (e: electron charge) was assumed to be localized to the center of the Me-TOTA molecule. Image charges in the substrate were also taken into account. This lead to a repulsive pairwise electrostatic interaction of $\approx 50\,\mathrm{meV}$. The total pairwise interaction energies are $\varepsilon_{\mathrm{Hc}} = -110\,\mathrm{meV}$ and $\varepsilon_{\mathrm{Hex}} = -50\,\mathrm{meV}$.

The pairwise interaction may in general be affected by the substrate, *e. g.* through deformation of the molecules. For the model presented in the main text, however, it is only necessary to determine whether $\varepsilon_{\mathrm{Hc}}/\varepsilon_{\mathrm{Hex}} > 2$ or $< 2$, *i. e.* whether the honeycomb or the hexagonal structure is more favorable. This information can be determined experimentally from measurements at submonolayer coverage.

Despite the above caveat, we observed that the ratios $\varepsilon_{\mathrm{Hc}}/\varepsilon_{\mathrm{Hex}}$ estimated from gas phase calculations are nonetheless consistent with the experimental observations for almost all systems in Table 1. The only exception is Me-TOTA, for which we found it necessary to take image charges into account.

## 8.8. Acknowledgment

We thank the Deutsche Forschungsgemeinschaft (SFB 677 and SPP 1928-II (COORNETs)) for financial support.

## 8.9. Contributions

Sandra Ulrich, and Rainer Herges synthesized the molecule. I measured and analyzed the experimental data and developed the model. Together with Manuel Gruber I wrote the first draft of the manuscript.[333] Richard Berndt supervised the project. All authors discussed the results and improved and commented on the manuscript.

# 9

# Stability of Functionalized Platform Molecules on Au(111)

This chapter is based on a publication in *The Journal of Chemical Physics*. It represents the submitted manuscript except for editorial changes. It is reprinted from the article

Torben Jasper-Tönnies, Manuel Gruber, Sujoy Karan, Hanne Jacob, Felix Tuczek, and Richard Bernd, J. Phys. Chem. Lett. **8**, 1569 (2017), *Editor's Pick*,

with the permission of *AIP Publishing*.

## 9.1. Abstract

Trioxatriangulenium (TOTA) platform molecules were functionalized with methyl, ethyl, ethynyl, propynyl and hydrogen and sublimated onto Au(111) surfaces. Low-temperature scanning tunneling microscopy data reveal that $> 99\%$ of ethyl–TOTA and methyl–TOTA remain intact whereas 60% of H–TOTA and $> 99\%$ of propynyl–TOTA and ethynyl–TOTA decompose. The observed tendency towards fragmentation on Au(111) is opposite to the sequence of gas-phase stabilities of the molecules. Although Au(111) is the noblest of all metal surfaces, the binding energies of the decomposition products to Au(111) destabilize the functionalized platforms by 2 to 3.9 eV (190–370 kJ/mol) and even render some of them unstable as revealed by density functional theory calculations. Van der Waals forces are important, as they drive the adsorption of the platform molecules.

## 9.2. Introduction

The properties and functions of molecules adsorbed to metals crucially depend on the adsorption geometry and the electronic coupling to the substrate. Chemical anchor groups consisting of a molecular subunit or just a single atom are used to determine these parameters for a class of molecules.[17,36,37,334–345] Recently platform molecules have been used as anchors to a substrate and to achieve decoupling from neighbor molecules.[41,346] Extended aromatic platforms are particularly interesting because they adhere to a substrate via physisorption instead of chemisorption. With these platforms lying flat on the substrate the functional molecule juts out into vacuum.[42] The electronic coupling at the molecule-surface interface is mediated by an extended $\pi$ system. Accordingly, physisorbed platforms were employed as high-conductance contacts between a metal electrode and molecular wires[44,140] and Zn-porphyrin molecules.[45] To reduce the electronic coupling a spacer may be inserted between the functional molecule and the platform.[41,42,209,347,348] Photochemical cleavage of an axial phenyl acetylene from a platform molecule at the ethanol/Au(111) interface was reported.[349]

While Au(111) is the noblest of all metal surfaces,[350] nm-sized Au structures can be catalytically active.[351–358] Here we show that even on well-ordered Au(111) surfaces some functionalized trioxatriangulenium (TOTA) platform molecules fragment despite the fact that they physisorb.[XLVIII,359] We functionalized TOTA platforms with methyl, ethyl, ethynyl, propynyl and hydrogen. After sublimation onto Au(111) all methyl–TOTA and $> 99\%$ ethyl–TOTA on Au(111) are intact. However, $\approx 60\%$ of the H–TOTA molecules and almost all ($> 99\%$) propynyl–TOTA and ethynyl–TOTA decompose. Intriguingly, this tendency towards fragmentation on Au(111) is opposite to the sequence of gas-phase stabilities of the molecules. Density functional theory (DFT) calculations show that the different on-surface stabilities reflect the binding energies of the products to Au(111). Dispersion interaction binds the platform molecules to Au(111) and affects the positions of the intact molecules and the decomposition products but hardly affects the stability against fragmentation.

## 9.3. Experimental Results

### 9.3.1. Deposition of TOTA functionalized with methyl, H, and ethynyl onto Au(111)

Functionalized platforms **1**–**3** (Fig. 9.1) were sublimated onto Au(111) at mild parameters to make sure that intact molecules were deposited (Sec. 9.7). During sublimation the samples were held at ambient temperature and then investigated using scanning tunneling microscope (STM) at low temperature ($T = 4.6$ K).

Figures 9.1a and b present typical STM topographs recorded after sublimation of methyl–TOTA (**1**) molecules. Pristine Au(111) areas appear low (dark). A single molecule **1** is imaged as a triangular shape with a central circular protrusion (green bordered molecule in Fig. 9.1b). The triangle (height $\lesssim 0.16$ nm) and the central protrusion (0.23 nm) correspond to platform **1** and the attached $CH_3$ moiety, respectively. The platform lies flat on Au(111) with an upright $CH_3$ group as desired. The molecules arrange into hexagonal clusters, preferably on the hcp and fcc areas of the herring-bone reconstructed Au(111) substrate. These clusters are stabilized by CH···O bonds with bond angles of 150 to 170° and H–O distances between 0.27 and 0.32 nm. Although we

---

[XLVIII] For small molecules the binding energy was often used to define physisorption and chemisorption. This approach is not useful for largish molecule where dispersion interaction may be significant. For example, the calculated adsorption energy of 4-mercaptobenzoic acid on Au(111) of 1.75 eV is mainly due to dispersion interaction (1.2 eV).[359]

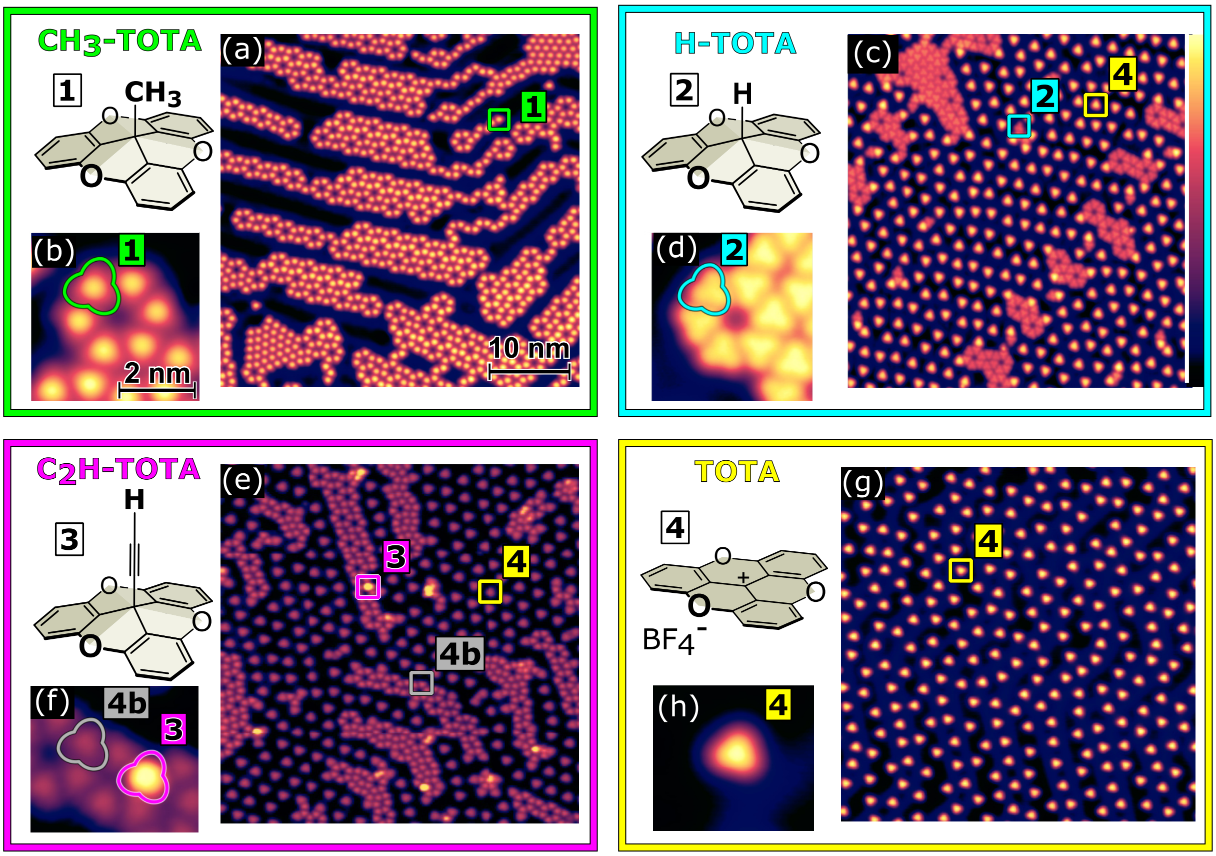

Figure 9.1.: (1–3) Functionalized trioxatriangulenium (TOTA) platform molecules: methyl–TOTA (**1**), H–TOTA (**2**), and ethynyl–TOTA (**3**) molecules. (4) Bare TOTA platform **4** with counterion $BF_4{}^-$. (a, c, e, g) STM topographs of **1**–**4**, respectively, on Au(111). Image width 44 nm. (b, d, f, h) Close-up views, image width 4.4 nm, of **1**–**4**. Green, turquoise, magenta, yellow, and gray symbols highlight single molecules **1**–**4** and **4b**, respectively. The color scale shown in (c) is used throughout but corresponds to different maximum height in each image. **1**–**4** and **4b** exhibit maximum apparent heights of 0.23, 0.16, 0.36, 0.22, and 0.21 nm at 100 mV. (e) was recorded at −1.0 V.

imaged thousands of molecules, we did not find a single fragmented molecule. In other words, methyl–TOTA remains intact on Au(111).

The deposition of H–TOTA (**2**) molecules leads to a different result (Figs. 9.1c and d). Here two patterns with apparent heights of 0.16 and 0.21 nm (turquoise and yellow squares in Figs. 9.1c and d) were found. The higher pattern (yellow) is identical to the pattern found after deposition of the bare platform **4** (Figs. 9.1g and h). Consequently, the higher pattern is attributed to the bare platform **4**. In Figure 9.1c, **4** is a fragment of H–TOTA. Its occurrence indicates that the bond between the central H atom and the platform occasionally dissociates upon deposition. The lower pattern (turquoise in Figs. 9.1c and d) is attributed to the intact H–TOTA molecule. In drastic contrast to the methyl-functionalized molecule **1**, only ≈ 41 % of more than 3000 H–TOTA molecules were intact after deposition. The central H atom of H–TOTA is not individually resolved as expected (see, *e. g.*, Refs. 235 and 236). Despite its similar geometry, the H-TOTA molecule appears ≈ 0.06 nm lower than the bare platform **4**. This difference is caused by an electronic effect as discussed below.

Figures 9.1e and h present topographs recorded after deposition of ethynyl–TOTA (**3**) molecules. Again, the bare platform **4** (yellow square in Fig. 9.1e) is found as a fragment on the sample. In addition, a different pattern denoted **4b** (gray markers in Figs. 9.1e and f) occurs. Pattern **4b** is exclusively found after deposition of ethynyl–TOTA molecules with fractions varying between 5 and 80 % at coverages of 0.05–0.45 molecules per 1 $\mathrm{nm}^2$. As discussed below we attribute pattern **4b** to the bare platform in a different adsorption state than **4**. Intact ethynyl–TOTA molecules (magenta in Figs. 9.1e and f) appear highest (0.36 nm) due to the attached ethynyl group. However, less than 1% of the ethynyl–TOTA molecules are intact on Au, showing that the $C_2H$ moiety makes these molecules marginally stable on Au(111).

### 9.3.2. Intermolecular interactions

The topographs in Figures 9.1c, e, and g provide important additional information. By contrast to the functionalized molecules **1–3** and molecule **4b**, the bare platform **4** does not cluster. The molecules **4** rather prefer to maximize their average nearest-neighbor distance $d$ in fcc and hcp regions of the substrate (Figs. 9.1c, e, and g). The square of the average nearest-neighbor distance, $d^2$, describes (up to a constant factor) the surface area that is occupied by a single molecule. Given a long-range repulsive interaction, $d^2$ is expected to be inversely proportional to the coverage, which determines the area that is available for a single molecule. Fig. 9.2a shows that this proportionality indeed holds. Moreover, it evidences that $d$ is not limited to specific values. This observation excludes the possibility of surface-mediated long-range interactions via Friedel oscillations of surface-state electrons, where $d$ would change with a period of half of the Fermi wavelength, *i. e.* 1.8 nm for Au(111).[360–362]

Long-range interactions between adsorbates can also be mediated by elastic deformation of the substrate.[363–365] The herring-bone reconstruction, which is due to a stressed atomic layer, is sensitive to changes of the surface elastic energy.[152,366] However, we find that the herring-bone reconstruction is unaffected by submonolayer coverages of platform **4**. Moreover, the platform is physisorbed to the Au substrate and consequently the induction of a significant amount of strain is unlikely. Hence, an elastic surface-mediated interaction is improbable.

Next, the nearest-neighbor (NN) pair distribution functions for low coverages were investigated (Figs. 9.2b and c). They show that the NN distances have lower and upper limits, *e. g.* in case of Fig. 9.2b there are no NN distances $< 2$ or $> 3.5$ nm. This effect along with the shape of the distributions indicates long-range Coulomb repulsion between the molecules[366] and suggests a significant charging of the adsorbed platform **4**, consistent with its cationic nature in the gas phase.

Clusters of functionalized platforms **1–3** and the pattern **4b** (Figs. 9.1c, e, and g) exhibit the same hexagonal structure and orientation with respect to the substrate. They are stabilized by CH···O bonds between the platforms (Chap. 8). The formation of H bonds indicates a smaller intermolecular Coulomb repulsion and consequently less charging of the molecules, consistent with their neutral character in the gas phase. In fact, the on-surface interactions of the molecules **1–4** (Fig. 9.1) reflect the molecular tendency to ionize. A related switching of intermolecular interactions by attaching a ligand to a molecule has recently been reported for Fe-tetramethyl-tetraazaannulene on Au(111).[367]

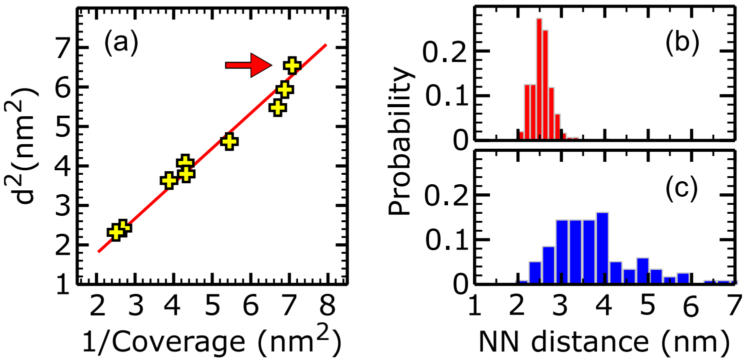

Figure 9.2.: (a) Average nearest-neighbor distance squared ($d^2$) versus inverse coverage evaluated for the bare platform **4**. Each data point is an average over at least 300 molecules from large areas of a newly prepared sample. This average neglects differences in local coverage between hcp and fcc areas that are significant at low densities ($\lesssim$ 7 nm$^2$ per molecule). The line shows a linear fit to the data ($d^2 = a/\gamma$, $\gamma$ being the coverage in molecules per nm$^2$). We find $a = 0.89$, which is close to the value expected for a hexagonal lattice ($\sqrt{3}/2 \approx 0.87$), which the molecules approximately form (cf. molecules **4** in Figs 9.1c and e). (b–c) Nearest-neighbor (NN) pair distribution functions of the bare platform **4** for coverages (b) 0.14 and (c) 0.03 molecules per nm$^2$ (Figs. 9.1g and 9.4a, respectively). The distributions were obtained from > 200 molecules. Steric hindrance limits the smallest distance to ≈ 1 nm. The data point marked by an arrow in (a) corresponds to the data shown in (b).

### 9.3.3. Induced dissociation and electronic states near $E_F$

As presented above, methyl–TOTA (**1**) is stable on Au(111) at ambient temperature, H–TOTA (**2**) fragments, and ethynyl–TOTA (**3**) is marginally stable. Moreover, the occurrence of the bare platform as fragment indicates that the bond between platform and attached moiety dissociates upon deposition. To verify that this bond is weaker than the other bonds of the adsorbed molecules, we investigated the stability of the molecules upon injecting high currents into the molecules. Indeed, injection of several nA current into the functionalized molecules **1–3** at elevated voltages ($\gtrsim$ 2 V) dissociates the attached moieties from the platform, but does not lead to further fragmentation of the platform. An example for such an induced dissociation is shown in Figure 9.3 for a methyl-TOTA molecule (**1**) on Au(111). Initially (Fig. 9.3a), methyl–TOTA molecules arranged in a compact island are observed. After applying a current/voltage pulse to a molecule at the position indicated by a black point, a new state is obtained (Fig. 9.3b) whose characteristics match the bare platform **4**. This kind of dissociation, which was repeatedly observed, is selective, *i. e.* no other molecules are affected. After an induced dissociation, the STM tip was usually contaminated, *i. e.* contacts to the bare Au substrate revealed a non-metallic tip and STM images tended to be fuzzy. We attribute this contamination to the transfer of the functional group or fragments thereof to the tip. After tip preparation by repeated dipping into the Au surface STM images could again be recorded with a clean metal tip. Figure 9.3b was actually recorded with such a re-prepared tip.

Further information about the electronic states of adsorbates can be obtained with the help of differential conductance ($dI/dV$) spectra, which probe the local density of states (LDOS, Chap. 3). $dI/dV$ spectra of methyl–TOTA (**1**) and the bare platform **4** (Fig. 9.3c) reveal a LUMO peak at ≈ 0.6 eV for the platform **4** that is not present at methyl–TOTA (**1**). Actually all investigated functionalized platforms do not exhibit any

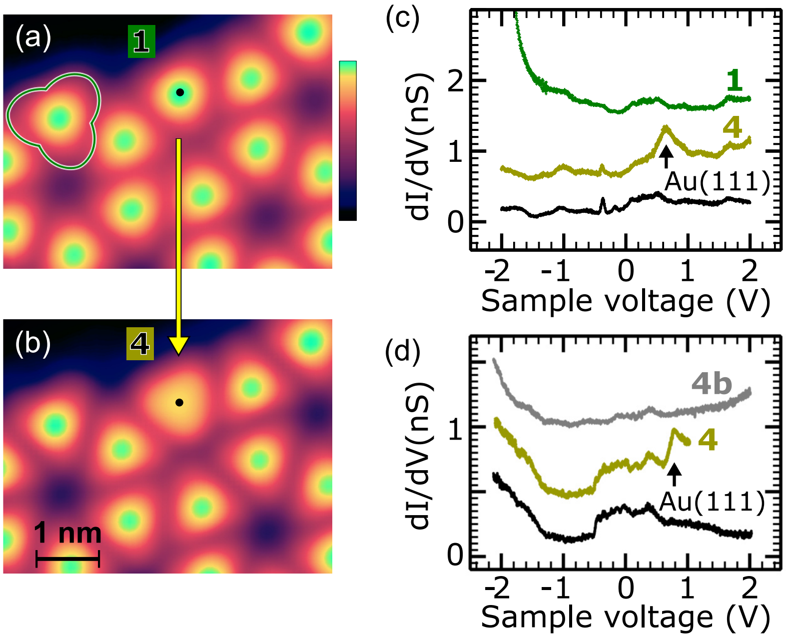

Figure 9.3.: (a–b) STM topographs (a) before and (b) after STM-induced dissociation of the methyl moiety from the single molecule **1** indicated by black points. (c–d) Differential conductance ($dI/dV$) spectra of a methyl–TOTA (**1**), the TOTA platform (**4**), and fragment **4b** along with the respective background spectra of the bare Au(111) substrate. Black arrows indicate the positions of the LUMO peak of **4** when it is (c) isolated or (d) adjacent to **1**. The steep rise of the conductance of **1** at $\approx -1.8$ eV is attributed to the HOMO. The Au(111) spectrum in (d) exhibits a rapid rise at $\approx -0.5$ V that is related to the edge of the surface state. The increase of the $dI/dV$ signal in (d) for sample voltages $\lesssim -1.5$ eV is due to tip states. For clarity some spectra are vertically shifted: (c) **1**: +1.5 nS, **4**: +0.9 nS and (d) **4b**: +0.9 nS, and **4**: +0.3 nS. The feedback loop was opened at 0.5 nA and 2 V (1 V for **4** in (d)).

prominent state in the range $|E - E_F| \lesssim 1.5$ eV. For methyl–TOTA (**1**) a steep increase of the differential conductance is visible for energies below $E - E_F \lesssim -1.5$ eV. This is an onset of a HOMO peak. A complete measurement of this peak at the tunneling parameters of Figure 9.3c would lead to the aforementioned induced dissociation of the molecule. The $dI/dV$ spectra of the bare platform **4** in Figures 9.3c and d reveal a further piece of information. The energy of the LUMO of **4** depends on its environment. Isolated molecules **4** show a LUMO at $\approx 0.6$ eV (Fig. 9.3c). An adjacent functionalized platform shifts the level away from $E_F$ by $\approx 0.2$ eV (Fig. 9.3d). Polarization screening of neighboring molecules may cause this shift as observed for, *e. g.*, perylenetetracarboxylic-dianhydride on Au(111),[368] and tetracene on Ag(111).[369]

Besides the bare platform **4**, also pattern **4b** was identified as a fragment of **3** (Figs. 9.1e and f). The $dI/dV$ spectra of **4** and **4b** (Fig. 9.3d) reveal a marked difference of their electronic structures. Whereas **4** exhibits a LUMO resonance at below 1 eV, fragment **4b** has state for $|E - E_F| \lesssim 2$ eV. The absence of an unoccupied state close to $E_F$ along with the clustering of **4b** (see section 9.3.2) is presumably caused by a different charge state.

### 9.3.4. Decomposition products

As to fragment **4b**, several observations indicate that it is the bare platform in a different adsorption state on Au(111). **4b** is found exclusively after decomposition of ethynyl–TOTA (**3**, Figs. 9.1e and f). Neither the sublimation of the bare platform (**4**, Figs. 9.1g and h) nor the decomposition of H–TOTA (**2**, Figs. 9.1c and d) lead to the presence of **4b**. Thus, its formation is most likely a kinetic effect of the dissociation of ethynyl–TOTA. As an intermediate, molecule **4b** should be energetically less favorable than **4**. Consistent with this, **4b** can be converted to **4** by injecting current into the molecules at elevated voltages ($\gtrsim 2$ V) and the reverse process could not be achieved despite various attempts at different manipulation parameters. Another intriguing observation is that the fraction of **4b** after deposition of ethynyl–TOTA drastically depends on the coverage of the molecules (Figs. 9.4a and b). Low (high) coverages correlate with small (high) fractions of molecule **4b** (*e. g.*, 0.05 (0.45) molecules per 1 $\text{nm}^2$ translates to $\approx 5$ % (80 %) **4b**). When the coverage is increased from 0.29 (Fig. 9.1e) to 0.45 molecules per 1 $\text{nm}^2$ (Fig. 9.4b), the intermolecular distance of the bare platform slightly reduces by $\approx 0.1$ nm. However, the fraction of **4b** increases from 59 % to 80 %, *i. e.* most of the additional molecules disintegrate into molecule **4b**. This coverage dependence indicates that the interaction with other molecules hinders the conversion of **4b** to **4**. Since **4** is significantly charged (Sec. 9.3.2), this hindrance may be linked to the intermolecular Coulomb repulsion of **4** that renders **4**, in contrast to **4b**, energetically less favorable at higher coverages. Analogously, the rather high molecular density within the clusters of molecule **4b** can be explained (Fig. 9.4b). In Chapter 8 it is shown that such high densities may be

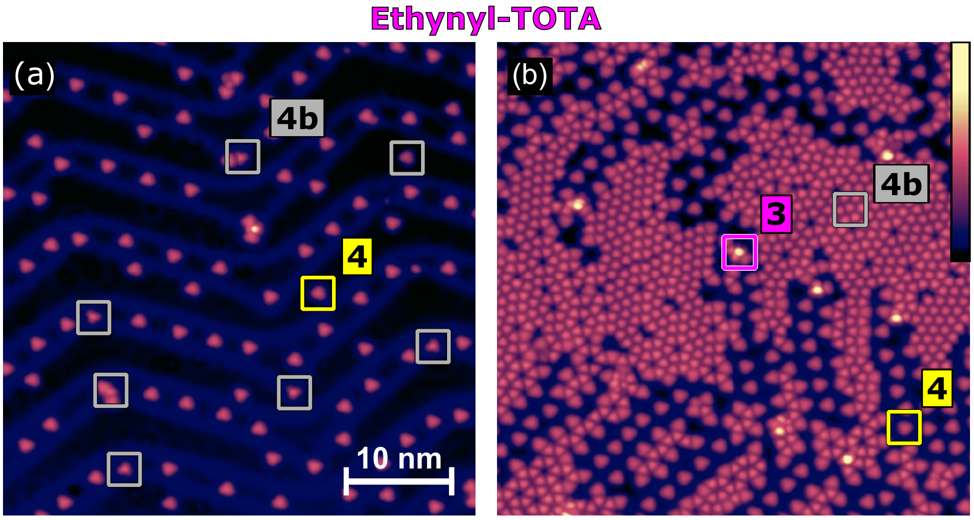

Figure 9.4.: STM topographs after deposition of different coverages of ethynyl–TOTA (**3**) molecules on Au(111): (a) 0.05 and (b) 0.45 molecules per 1 $\text{nm}^2$ (Image width 44 nm). In (a) the fragments **4b** are at the reactive elbows of the herring-bone reconstruction and marked by a gray square, respectively. In (b) the molecules **4b** (gray) cluster to large islands. Bare TOTA molecules (**4**, yellow) do not cluster. The color scale shown in (b) on the right upper side is used and corresponds to an apparent height of 3.7 nm. (b) was recorded at -1 V.

energetically unfavorable for submonolayer coverage.[XLIX] However, on the samples concerned here molecules **4** are co-adsorbed and a higher density of **4b** decreases the density (and therefore the Coulomb repulsion) of **4**. Thus, the Coulomb repulsion of **4** may also render the *compressed* clustering of **4b** favorable.

The aforementioned properties of **4b** are all similar to those of the functionalized platforms and could be explained by an moiety attached to the platform. However, there were, in contrast to the induced dissociations of the functionalized platforms (Sec. 9.3.3), no indications of a detached moiety after conversion of **4b** to **4**. As molecule **4b** is a fragment of $C_2H$–TOTA, the attached moiety should comprise either one or two C atoms. Such moieties are neither chemically intuitive (high gas-phase dissociation energies of the related bonds: (i) $HC_2$–H: 5.8 eV (560 kJ/mol), (ii) HC≡CH: 10 eV (965 kJ/mol))[370] nor consistent with the STM topographs. Hence, fragment **4b** is most likely the bare platform in a metastable adsorption state.

While fragments **4** and **4b** are directly observed upon dissociation of $C_2H$–TOTA (Figs. 9.1e and f) the fate of the $C_2H$ group is less clear. STM topographs reveal fuzzy areas (SI, Sec. 9.9.4) that may represent clusters of $C_2H$. The high reactivity of $C_2H$ may also lead to the formation of gaseous molecules like $HC_2$–$C_2H$ (bond formation energy −6.5 eV (627 kJ/mol) in the gas phase)[371] and their partial desorption at ambient temperature.

The fragmentation of H–TOTA molecules upon adsorption on Au(111) at ambient temperature (Fig. 9.1c) may lead to H atoms on the sample—in addition to the bare platforms **4**. H atoms on Au(111) were reported to desorb at ≈ 110 K via the formation of $H_2$.[372] In agreement with that, we found no indications of their presence on our samples.

## 9.4. Calculated results

The $CH_3$ and $C_2H$-functionalized platforms **1** and **3** are extreme cases with either exclusively intact molecules or > 99% fragments on Au(111). We therefore calculated their dissociation energies with DFT assuming different reaction scenarios (see below). Moreover, we focused on the bare platform **4** as a product because we hint that **4b** may result from a cooperative effect that is difficult to tackle with existing methods (see Sec. 9.9.5 in the SI). In other words, our calculations reflect the case of small coverages where most of the deposited ethynyl-TOTA molecules fragment to **4**. To adequately describe the adsorption geometries, dispersion interactions were taken into account by using the vdW$^{\text{surf}}$ method (Sec. 9.8).[179–181]

### 9.4.1. Dissociation energies

Reaction **I** represents the gas-phase dissociations of molecules methyl–TOTA and ethynyl–TOTA (Fig. 9.5). It turns out (Tab. 9.1) that methyl–TOTA and ethynyl–TOTA are stable with dissociation energies exceeding 2 eV (190 kJ/mol), which is consistent with the observed stability towards sublimation. Moreover, in contrast to the observed instability

---

[XLIX] Analogous to methyl-TOTA, hexagonal arrangements of **4b** are (more frequently) observed at low coverage (cf. Fig. 9.1).

on Au(111), the bond of the functional group is 1 eV stronger in ethynyl–TOTA than in methyl–TOTA. Reaction **I** therefore cannot explain the experimental observations.

Reaction **II** describes the on-surface dissociation assuming that the platform remains on Au and the functional group desorbs (Fig. 9.5). Interestingly, both dissociation energies (**II** in Tab. 9.1) are ≈ 0.45 eV (43 kJ/mol) lower than the gas-phase values. This destabilization is mainly caused by the more favorable adsorption of the flat platform **4** (≈ 0.4 eV) compared to the curved platforms with attached functional group (Fig. 9.5). It is not due to the geometric deformation caused by the adsorption. Since both dissociation energies exceed 1.5 eV (144 kJ/mol) and ethynyl–TOTA is 1 eV (96 kJ/mol) more stable than methyl–TOTA, **II** does not reflect the experimental observations.

Reaction **III** is a on-surface dissociation with both products remaining on Au (Fig. 9.5). Remarkably, **III** reveals that ethynyl–TOTA is *not stable* on Au, while methyl–TOTA is *stable* (Tab. 9.1). The dissociation of ethynyl–TOTA reduces the total energy by ≈ 0.1 eV (9.6 kJ/mol) whereas dissociation of methyl–TOTA requires more than 0.4 eV (38 kJ/mol). In other words, the on-surface dissociation **III** is consistent with the experimental observation of mainly decomposed ethynyl–TOTA and fully intact methyl–TOTA molecules on Au.

| | Dissociation | $CH_3$–TOTA (**1**) | $C_2H_2$–TOTA (**3**) |
|---|---|---|---|
| **I** | R–TOTA → R + TOTA | 2.43 | 3.77 |
| **II** | R–TOTA/Au → R + TOTA/Au | 1.98 | 3.30 |
| **III** | R–TOTA/Au → R/Au + TOTA/Au | 0.46 | −0.10 |

Table 9.1.: Dissociation energies of methyl–TOTA (**1**) and ethynyl–TOTA (**3**) in eV (96 kJ/mol) for calculated reaction pathways **I** –**III**. The dissociation energies were obtained as described in Section 9.8.

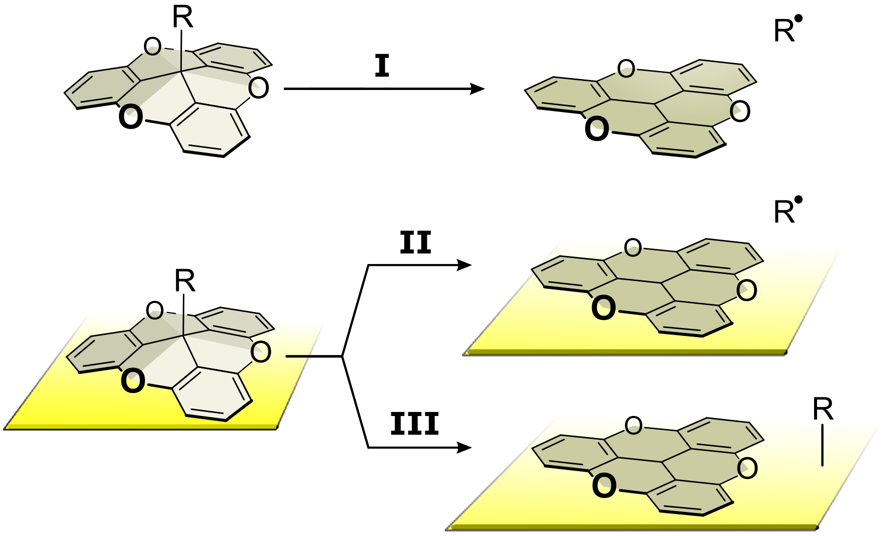

Figure 9.5.: Sketch of gas-phase dissociation **I** and on-surface dissociations **II** and **III** of the substituent R from the platform. In the on-surface dissociations, R either (**II**) desorbs or (**III**) adsorbs to Au(111).

In addition to the dissociation pathways **I**–**III** it is conceivable that the R moieties of two R–TOTA molecules directly react to R–R without the adsorption of the R moieties on the substrate. In other words, the reaction 2 R–TOTA/Au → R–R + 2 TOTA/Au (denoted as **IV** below) might occur *without* reaction **III** as intermediate step. However, the dissociation energies of reaction **IV**, 0.10 and 0.06 eV for R = $C_2H_2$ and $CH_3$, respectively, are almost identical. As a consequence reaction **IV** (without reaction **III** as intermediate step) cannot explain the drastically different stabilities of ethynyl–TOTA (almost all dissociated) and methyl–TOTA (all intact) molecules on Au(111), in contrast to reaction **III**.

## 9.4.2. Adsorption energies and geometries

The key reason for the different stabilities on Au(111) are the adsorption energies of the ethynyl ($C_2H$) and methyl ($CH_3$) radicals (Tab. 9.2). The former is 1.9 eV (180 kJ/mol) more favorable than that of $CH_3$. Along with the lower adsorption energy of the bare platform **4** this energy difference is enough to render ethynyl–TOTA (**3**) unstable whereas methyl–TOTA (**1**) is not. Hence, the Au(111) surface is not inert enough for ethynyl–TOTA to remain stable. Consistent with this interpretation, we observed that ethynyl–TOTA dissociates on the more reactive Ag(111) surface, too (SI, Sec. 9.9.2).

| | $\mathbf{1}^a$ | $\mathbf{3}^b$ | $\mathbf{4}^c$ | $CH_3$ | $C_2H$ |
|---|---|---|---|---|---|
| $E_{ad}$ (PBE+vdW) | –2.17 | –2.15 | –2.62 | –1.5 | –3.4 |
| $E_{ad}$ (PBE) | +0.01 | –0.02 | –0.57 | –1.3 | –3.2 |

${}^a$CH$_3$–TOTA, ${}^b$C$_2$H–TOTA, ${}^c$TOTA

Table 9.2.: Adsorption energy in eV (96 kJ/mol) of the methyl–TOTA (**1**), ethynyl–TOTA (**3**), and TOTA (**4**) molecules and the ethynyl ($CH_3$) and methyl ($C_2H$) radicals on Au(111). The adsorption energies were obtained as described in Section 9.8.

Figure 9.6 shows the optimized geometries of an ethynyl ($C_2H$) and a methyl ($CH_3$) moiety on Au(111). $C_2H$ adsorbs upright at fcc-hollow sites (Figs. 9.6a and b), whereas $CH_3$ is located on top of a surface Au atom (Figs. 9.6c and d). The calculated Au–C distances, 0.221 nm for $C_2H$ and 0.212 nm for $CH_3$, are typical of covalent Au–C bonds.[217] The strong binding of $C_2H$ reflects the fact that $C_2H$ binds to three Au atoms rather than one in the case of $CH_3$. Interestingly, $CH_3$ is marginally stable or unstable at the hollow sites, as indicated by the relaxation to the top site in the DFT calculations. We attribute this effect to the close proximity of the H atoms in $CH_3$ and the Au(111) for the expected C–Au bond distance of 0.21 nm at the hollow sites. Details of the calculated adsorption geometries of the platforms **1**, **3** and **4** are presented in the SI (Sec. 9.9.6).

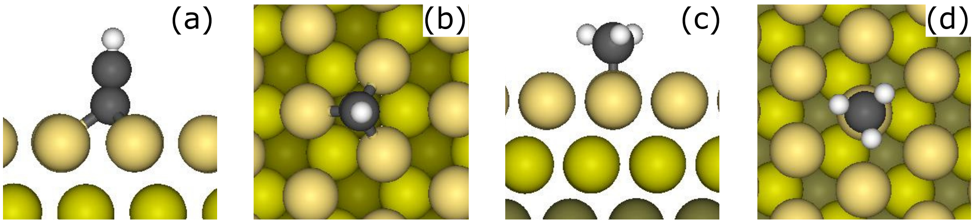

Figure 9.6.: Adsorption geometries of (a–b) an ethynyl ($C_2H$) and (c–d) a methyl ($CH_3$) moiety calculated with PBE+vdW (Sec. 9.8). (a) and (c) show side views, (b) and (d) top views. The ethynyl and methyl moiety are adsorbed in hollow and top sites, respectively. Yellowish: Au atoms of the first three (111) surface layers, gray: carbon, white: hydrogen.

### 9.4.3. Role of dispersion interaction

The decomposition of several molecules and the relative stabilities of intermediates in on-surface reactions on Au have recently been attributed to the strong van der Waals (vdW) interaction.[373–377] We therefore investigated the role of dispersion for dissociation **II** and **III** by calculating the related adsorption energies with and without inclusion of vdW interaction (Tab. 9.2), namely with the PBE+vdW functional (Sec. 9.8) and the pure PBE. The adsorption energies of methyl–TOTA (**1**), ethynyl–TOTA (**3**), and TOTA (**4**) increase by ≈ 2.2 eV with PBE compared to PBE+vdW, reflecting strong dispersion interaction with Au(111) and its crucial role for the adsorption process. The adsorption energies of methyl–TOTA (**1**) and ethynyl–TOTA (**3**) may contribute to overcoming the energy barrier of dissociation process **III**. However, the calculated adsorption energies of **1** and **3** (Tab. 9.2) are almost identical and therefore cannot explain the observed stability difference. Similarly, dispersion interaction has little influence on the dissociation energies when the *correct* adsorption geometries are used. The energy differences relevant for dissociation paths **II** and **III**, namely between the bare platform **4** on one hand and the functionalized platforms **1** and **3** on the other (≈ 0.4 eV) and between $CH_3$ and $C_2H$ (≈ 1.9 eV), are almost unaffected when changing from PBE+vdW to PBE. Hence, the dispersion interaction plays an indirect role in the reactions. It defines the position of the adsorbates on the Au(111) surface, but cancels out from the reaction energies. We emphasize that vdW interactions are crucial, as not taking them into account, *i. e.* only using the pure PBE functional, leads to incorrect adsorption geometries and unreasonable dissociation energies.

## 9.5. Discussion

Experimentally we observed that ethynyl-TOTA molecule fragments with a very high probability. If a reaction barrier is present it obviously can be overcome at ambient temperature. In any event, according to our DFT results dissociation lowers the energy of the system. As to molecule methyl-TOTA, our calculations show that dissociation is energetically unfavorable in agreement with its observed stability. An activation barrier towards dissociation may add to this stability but cannot be evaluated from the available data.

The pathway to dissociation is a multi-step process and it is not realistic to model the complete dissociation with existing *ab initio* methods.[L] Nonetheless, it is interesting to speculate about the mechanisms of fragmentation and molecular assembly. Dissociation **III** may require that the functional group is oriented towards the surface. Disregarding a hypothetical steering effect of the surface during the impact of the molecules, approximately half of the molecules are expected to impinge with the platform oriented toward the surface. The observations for ethynyl-TOTA molecules (**3**, Fig. 9.1e) imply that this orientation during impact is no obstacle to fragmentation. However, the barrier for flipping **3** on a flat area is expected to exceed 1 eV (96 kJ/mol) because of its large adsorption energy (Tab. 9.2). Diffusion of the molecules to step edges may facilitate a reorientation. It is also conceivable that diffusing Au atoms may attack the moiety bond of ethynyl-TOTA.

Our interpretation of the fragmentation data is consistent with results from other functionalized TOTA platforms. We synthesized propynyl–TOTA, which may be viewed as methyl–TOTA with an inserted ethynyl spacer. As expected, we find propynyl–TOTA to be only marginally stable on Au(111) with $< 1$ % molecules remaining intact (SI, Sec. 9.9.3). The stability of ethyl–TOTA is also in line with our model. The gas-phase dissociation energy of ethyl–TOTA and the binding energy of ethyl to Au(111) are expected to be similar to those of methyl. Indeed, in our experiments, we found almost only ($> 99\%$) intact ethyl–TOTA molecules on Au(111) (SI, Sec. 9.9.3).

## 9.6. Conclusion

The interaction of closed-shell platform molecules with the inert Au(111) surface surprisingly renders a rather stable $sp_3$ C bond within a molecule unstable. The stability of the molecules depends drastically on their functional moiety. Modeling shows that the binding energies of the fragments to Au(111) destabilize the $sp_3$ C bond between the functional moieties and the platform by 2 to 3.9 eV (190–370 kJ/mol) and essentially determine the molecular stability. Dispersion interaction plays an important indirect role, as it binds the platforms to the Au(111) surface, but it cancels out from the reaction energies. Moreover, the results show that the thermal energy at ambient temperature and the impact of the molecules are sufficient to overcome kinetic limitations.

## 9.7. Experimental Details

### Synthesis of the molecules

Functional groups were attached to the cationic TOTA platform **4** by polar C–C and C–H bond formation as described in the SI (Sec. 9.9.1). The powders of the functionalized platforms **1–3** were purified by sublimation at ≈ 0.5 Pa and ≈ 100 °C.

---

[L] For example, the unit cell required for reliable adsorption geometries and energies contains 305 atoms (Sec. 9.8). This renders *ab initio* calculations of reaction barriers with any reliable level of accuracy extremely challenging, if not impossible.

### Sample preparation

Submonolayers of $TOTA^+BF_4^-$ salt and the molecules **1–3** were sublimated onto flat and clean Au(111) held at ambient temperature. The sublimation parameters for molecules **1–3** were almost identical ($< 10^{-7}$ Pa and ≈ 70 °C) and milder than during the aforementioned purification by sublimation to make sure that intact molecules were deposited. The time between sublimation (< 2 min) and cool down of the sample to ≈ 10 K for STM measurements did not exceed 25 min.

### STM

STM images were recorded at 4.6 K, $< 10^{-9}$ Pa, low constant currents (20–40 pA), and low positive sample voltages (100–130 mV). All STM topographs were acquired using the constant-current mode.

## 9.8. Theoretical Details

### DFT

Electronic structure calculations were performed by using DFT with non-empirical exchange-correlation functional of Perdew-Burke-Ernzerhof[378] (PBE) and the vdW$^{surf}$ method to model screened van der Waals interactions for atoms and molecules on surfaces[179–181] as implemented in the FHI-aims code[379] denoted PBE+vdW above.

A hexagonal unit cell comprised of 5 layers with 305 Au atoms in total was used with periodic boundary conditions. A $k$-grid of $2 \times 2 \times 1$ was employed. The geometry of two upper (three bottom) Au layers was relaxed (fixed to the bulk structure). The tight (light) default species settings were employed for the adsorbents' atoms (Au atoms).[379] All geometries were optimized until forces were smaller than 0.01 eV/Å (16 pN).

### Dissociation energies

The dissociation energies of reaction **I** (Tab. 9.1) were obtained in two steps: H+R–TOTA → H–R + TOTA→ H + R + TOTA. The first step was calculated with DFT+vdW. For the second step, experimental values of the dissociation energies of methane and ethyne measured at 298 K, 4.55 eV and 5.78 eV, were used.[370] The dissociations **II** (Tab. 9.1) were calculated in the same way but with R–TOTA and TOTA adsorbed on Au(111). All data for the reaction **III** (Tab. 9.1) were obtained with DFT+vdW calculations. Finally, the dissociation energies of reaction **IV** (see section 9.4.1) were determined in two steps: 2 R–TOTA/Au → 2 (R + TOTA/Au) → R–R + 2 TOTA/Au. The first step is reaction **II** for two isolated R–TOTA molecules on Au and was calculated as mentioned above. For the second step, experimental values of the bond formation energies of $H_3C–CH_3$ and $H_2C–CH_2$ measured at ambient temperature, –3.91 eV[370] and –6.51 eV,[371] were used.

### Adsorption energies

The adsorption energies of the bare platform **1** and functionalized platforms **3** and **4** (Tab. 9.2) were directly calculated with the PBE+vdW and PBE functionals. The adsorption energies of the radicals were extracted from Table 9.1 as difference of the dissociation energies of the reactions **II** and **III**.

## 9.9. Supporting information

### 9.9.1. Synthesis

**4,8,12-Trioxatriangulenium tetrafluoroborate (TOTA-$BF_4$)[232]:**

Tris-(2,6-dimethoxyphenyl)methanol (2 g, 4.54 mmol) and pyridine hydrochloride (10 g, 85.8 mmol) were stirred at 220 °C for 1.5 h. The melt was poured into water (600 ml) and the red precipitate was filtered off. The yellow solution was acidified with tetrafluoroboric acid and the resulting precipitate was filtered off. Recrystallization from dichloromethane gave 699 mg (1.88 mmol, 41 %, Ref. 232: N/A) of a yellow solid.

m.p.: 385°C (Ref. 232: N/A).
$^1$H NMR (500 MHz, $(CD_3)_2SO$): $\delta$ = 8.57 (t, $J$ = 8.5 Hz, 3H, $H$-5), 7.98 (d, $J$ = 8.5 Hz, 6H, $H$-4) ppm.
$^{13}$C NMR (125.8 MHz, $(CD_3)_2SO$): $\delta$ = 152.94 (q, $C$-3), 145.45 (q, $C$-1), 143.41 (t, $C$-5), 112.41 (t, $C$-4), 106.23 (q, $C$-2) ppm.
MS (EI): m/z (%) = 285 (100).

**12c-Hydro-4,8,12-trioxatriangulene (H-TOTA)[234]:**

4,8,12-Trioxatriangulenium tetrafluoroborate (300 mg, 806 $\mu$mol) was suspended in dimethoxyethane (150 ml) and sodium borohydride (150 mg, 3.98 mmol) was added. After stirring at room temperature for 2 h, diethyl ether (50 ml) was added and the reaction mixture was stirred for 30 min. Water (50 ml) was added and the solution was stirred further for 30 min. The mixture was extracted with diethyl ether (3 × 100 ml) and the combined organic extracts were dried ($MgSO_4$) and concentrated in vacuo. Recrystallization from ethyl acetate gave 167 mg (583 $\mu$mol, 72 %, Ref. 234: 61 %) of colorless crystals.

m.p.: 313 °C (Ref. 234: 313 °C).
$^1$H NMR (600 MHz, $CDCl_3$): $\delta$ = 7.22 (t, $J$ = 8.2 Hz, 3H, $H$-5), 6.91 (d, $J$ = 8.2 Hz, 6H, $H$-4), 4.89 (s, 1H, $H$-1) ppm.
$^{13}$C NMR (150.9 MHz, $CDCl_3$): $\delta$ = 152.94 (q, $C$-3), 128.43 (t, $C$-5), 111.36 (t, $C$-4), 109.09 (q, $C$-2), 20.69 (q, $C$-1) ppm.
MS (EI): m/z (%) = 286 (25), 285 (100).
MS (CI): m/z (%) = 287 (100), 285 (93).

**2c-Methyl-4,8,12-trioxatriangulen (methyl-TOTA)**

Under nitrogen, magnesium turnings (100 mg, 4.00 mmol) were suspended in dry diethyl ether (40 ml) and methyl iodide (250 $\mu$l, 4.02 mmol) was added dropwise. After the reactions had started, the mixture was stirred at room temperature for 1 h. A suspension of 4,8,12-trioxatriangulenium tetrafluoroborate (372 mg, 1.00 mmol) in dry THF (100 ml) was added and the mixture was stirred for 1 more h. The mixture was poured into an ammonium chloride solution (50 ml) and the organic layer was washed with water, dried ($Na_2SO_4$) and concentrated in vacuo. Recrystallization from benzene gave 98 mg (326 $\mu$mol, 33 %) of colorless crystals.

m.p.: 230 °C (Ref. 233: 230-231 °C).

$^1$H NMR (500 MHz, CDCl$_3$): $\delta$ = 7.22 (t, $J$ = 8.2 Hz, 3H, $H$-5), 6.93 (d, $J$ = 8.2 Hz, 6H, $H$-4), 1.54 (s, 3H, $H$-6) ppm.
$^{13}$C NMR (125.8 MHz, CDCl$_3$): $\delta$ = 152.34 (q, $C$-3), 128.07 (t, $C$-5), 114.72 (q, $C$-2), 111.34 (t, $C$-4), 31.58 (p, $C$-6), 24.17 (q, $C$-1) ppm.
MS (EI): m/z (%) = 300 (12), 285 (100).

**12c-Ethynyl-4,8,12-trioxatriangulen (ethynyl-TOTA):**

Under nitrogen, 4,8,12-trioxatriangulenium tetrafluoroborate (100 mg, 269 $\mu$mol) was suspended in dry THF (200 ml) and a 0.5 m solution of ethynyl magnesium bromide in THF (20 ml, 10 mmol) was added. After refluxing for 2 h, the mixture was cooled to room temperature, poured into water (100 ml) and extracted with diethyl ether. The combined organic extracts were dried (MgSO$_4$), concentrated in vacuo and the crude product was filtered over Florisil (cyclohexane / ethyl acetate 1:1) to give 47 mg (152 $\mu$mol, 57 %) of colorless crystals.

m.p.: 243 °C. $^1$H NMR (500 MHz, THF–d$_8$): $\delta$ = 7.33 (t, $J$ = 8.3 Hz, 3H, $H$-5), 6.99 (d, $J$ = 8.3 Hz, 6H, $H$-4), 2.96 (s, 1H, $H$-7) ppm.
$^{13}$C NMR (125.8 MHz, THF–d$_8$): $\delta$ = 153.04 (q, $C$-3), 129.97 (t, $C$-5), 112.29 (t, $C$-4), 111.54 (q, $C$-2), 84.84 (q, $C$-6), 74.59 (t, $C$-7), 22.55 (q, $C$-1) ppm.
MS (EI): m/z (%) = 310.1 (25), 285 (100).
MS (CI): m/z (%) = 311.1 (98), 285 (100).
IR (ATR): $\tilde{\nu}$ = 3640 (w), 3292 (w), 3278 (m), 2957 (w), 2923 (m), 2855 (w), 2111 (w), 1611 (s), 1479 (m), 1455 (s), 1258 (s), 1062 (m), 1009 (s), 927 (m), 783 (s), 756 (m), 724 (s) cm$^{-1}$.
HR-MS: (C$_{21}$H$_{10}$O$_3$, calc. 310.06299): 310, 06312 (0.41 ppm).
UV/Vis (toluene): $\lambda_{max}$ (lg $\epsilon$) = 286 (4.05) nm.

**12c-Ethyl-4,8,12-trioxatriangulen (ethyl-TOTA):**

Under nitrogen, magnesium turnings (500 mg, 20.6 mmol) were suspended in dry THF (100 ml) and ethyl bromide (200 $\mu$L, 2.67 mmol) were added dropwise. After the reaction had started, further ethyl bromide (1.60 ml, 21.4 mmol) was added and the mixture was stirred at 60 °C for 30 min. Meanwhile, a suspension of trioxatriangulenium tetrafluoroborate in dry THF was treated with ultrasound for 30 min. To this suspension ethyl magnesium bromide in THF (20 ml, 4.12 mmol) was added and the mixture was stirred at room temperature for 1 h. The mixture was poured into an ammonium chloride solution (100 ml) and the organic layer was washed with water, dried (MgSO$_4$) and concentrated in vacuo to give 222 mg (706 $\mu$mol, 88 %) of a colorless solid.
m.p.: 195 °C.

$^1$H NMR (500 MHz, THF–d$_8$): $\delta$ = 7.23 (t, $J$ = 8.2 Hz, 3H, $H$-5), 6.92 (d, $J$ = 8.2 Hz, 6H, $H$-4), 1.77 (q, $J$ = 7.5 Hz, 2H, $H$-6), 0.72 (t, $J$ = 7.5 Hz, 3H, $H$-7) ppm.
$^{13}$C NMR (125.8 MHz, THF–d$_8$): $\delta$ = 153.69 (q, $C$-3), 129.20 (t, $C$-5), 114.02 (q, $C$-2), 111.96 (t, $C$-4), 38.98 (s, $C$-6), 29.72 (q, $C$-1), 8.11 (p, $C$-7) ppm.
MS (EI): m/z (%) = 285 (100).
MS (CI): m/z (%) = 315 (100), 285 (23).
IR (ATR): $\tilde{\nu}$= 3065 (w), 2968 (w), 2915 (w), 2876 (w), 2849 (w), 1610 (s), 1482 (m), 1455 (s), 1256 (s), 1053 (m), 1009 (s), 931 (m), 782 (s), 755 (s) cm$^{-1}$.

Elemental analysis ($C_{21}H_{14}O_3$ calc.: C 80.24, H 4.49): C 76.03, H 4.46.
UV/Vis (DCM): $\lambda_{max}$ (lg $\epsilon$) = 283 (3.71) nm.

### 12c-Propynyl-4,8,12-trioxatriangulene (propynyl-TOTA)[140]:

4,8,12-Trioxatriangulenium tetrafluorborate (150 mg, 403 $\mu$mol) suspended in 200 ml anhydrous tetrahydrofuran (THF) were mixed with propynyl magnesium bromide (20 ml, 10 mmol, 0.5 M in THF) under nitrogen. The reaction mixture was heated under reflux for 7 h and the solvent was removed under reduced pressure. The residue was purified by chromatography over Florisil (cyclohexane/diethyl ether 1:1). The product was obtained as a colorless solid (31.2 mg, 96.2 $\mu$mol)

$^1$H NMR (500 MHz, THF−$d_8$): $\delta$ = 7.29 (t, J=8.2 Hz, 3H, $H$−5), 6.97 (d, J=8.2 Hz, 6H, $H$−4), 1.59 (s, 3H, $H$−8) ppm.
$^{13}$C NMR (125.8 MHz, THF−d8): $\delta$ = 153.03 (q, $C$−3), 129.56 (t, $C$−5), 112.18 (t, $C$−4), 111.78 (q, $C$−2), 81.62 (q, $C$−6), 80.86 (t, $C$−7), 22.23 (q, $C$−1), 3.05 (p, $C$−8) ppm.
MS (EI): m/z (%) = 324 (31), 285 (100).
MS (CI): m/z (%) = 325 (100), 285 (81).

## 9.9.2. Ethynyl-TOTA and TOTA on Ag(111)

Figures 9.7a and b present typical STM topographs recorded after sublimation of ethynyl-TOTA (**3**) and TOTA (**4**) molecules, respectively, onto Ag(111). On both samples the same triangular building block was found (yellow squares). It corresponds to the bare platform **4** on Ag(111). Like on Au(111), almost all ethynyl-TOTA molecules decompose on Ag(111).

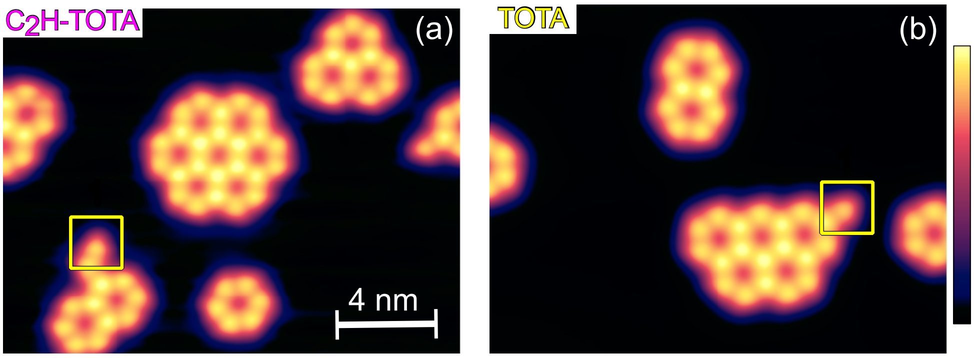

Figure 9.7.: (a–b) STM topographs after deposition of ethynyl-TOTA (left image) and bare TOTA (right image) molecules onto Ag(111). The color scale shown in (b) is used in both images and corresponds to a maximum apparent height of 0.2 nm. Both images were recorded at a sample voltage of 1 V.

The STM images in Figs. 9.7 reveal a further piece of information. Whereas bare platforms **4** do not aggregate on Au(111) (Fig. 9.1g in Sec. 9.3.1), they form clusters on Ag(111). The intermolecular interactions reflect the balance between attractive van der Waals and H bonding and Coulomb repulsion. The latter originates from charging of the adsorbed molecules. Consequently, the clustering on Ag(111) indicates a reduced molecular charge compared to the case of Au(111). Ag(111) being more reactive than Au(111), the platform is presumably more strongly coupled to the electron gas of Ag(111). In addition, the bare platform **4** is a cation. Therefore, increased coupling to a metal presumably reduces the positive partial charge on the molecule. Hence, a different coupling to the substrates is consistent with attractive/repulsive intermolecular interaction on Ag(111)/Au(111).

Next, we address the fragment **4b**. The properties of **4b** on Au(111) are similar to those of the bare platform **4** on Ag(111). Both form clusters, which is consistent with small partial charges, and do not exhibit a LUMO close to the Fermi energy. In contrast, the clustering, and hence the charge state of the bare platform **4** is different on Ag and Au as discussed above. Moreover, its LUMO is either far from or close to the Fermi energy on these surfaces, respectively. Taken together, these observations hint that the fragment **4b** may represent a differently charged state of the bare platform **4**.

### 9.9.3. Ethyl-TOTA and propynyl-TOTA on Au(111)

In addition to the molecules presented in the Section 9.3.1, we also deposited ethyl-TOTA and propynyl-TOTA on Au(111). Figures 9.8a and b present topographs of ethyl-TOTA. The shape of intact ethyl-TOTA molecules is similar to methyl-TOTA. However, it appears ≈ 0.05 nm higher (0.28 nm height) than methyl-TOTA. Almost all ethyl-TOTA molecules (99.7 % of more than 1000 molecules considered) are intact on Au(111), which is consistent with the interpretation of the fragmentation presented in the article.

Propynyl-TOTA was investigated by depositing a mixture of 60 % propynyl-TOTA

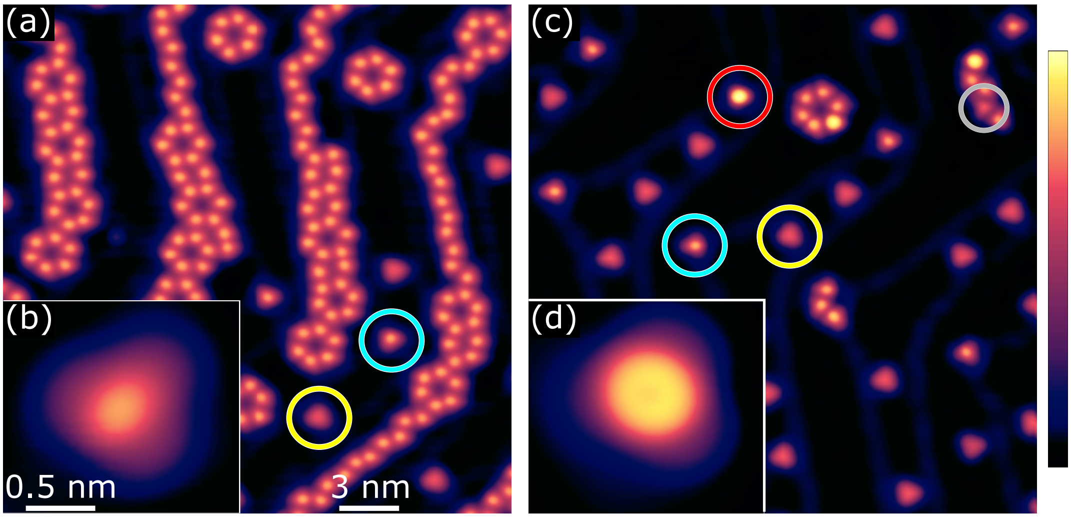

Figure 9.8.: STM topographs on Au(111) (100 mV; color scale: 0.32 nm). (a) Ethyl-TOTA. In (a) ethyl-TOTA and TOTA **4** are indicated by turquoise and yellow circles, respectively. A majority of molecules remain intact and display a correspondingly large height. (c) Mixture of 60% propynyl-TOTA and 40% ethyl-TOTA. Ethyl-TOTA, propynyl-TOTA, TOTA **4**, and TOTA **4b** are indicated by turquoise, red, yellow, and gray circles, respectively. The fraction of TOTA **4** and **4b** is much larger than in (a). Given that ethyl-TOTA is essentially stable, the fragments are due to the decomposition of propynyl-TOTA. (b) and (d) display detailed images of intact ethyl-TOTA and propynyl-TOTA.

and 40 % ethyl-TOTA onto Au(111) (Figs. 9.8c and d). A vast majority of molecules is fragmented.

## 9.9.4. Fragments of ethynyl-TOTA on Au(111)

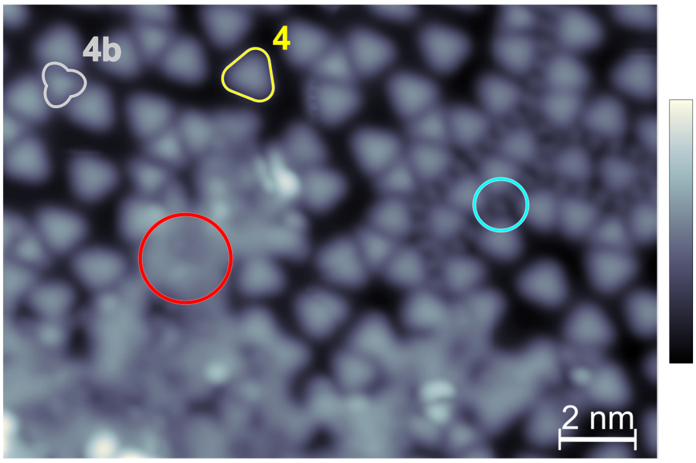

Figure 9.9.: STM topograph of typical fragments after deposition of ethynyl-TOTA (**3**) on Au(111) (100 mV; color scale: 0.37 nm). Besides fragments **4** (yellow) and **4b** (gray), *i. e.* TOTA platforms, fuzzy areas (red circle) occurred and also small dots were occasionally observed (turquoise circle). The fuzzy areas and small dots may originate from ethynyl moieties on Au(111).

## 9.9.5. Calculated MDOS

Figure 9.10 presents the calculated molecular orbital density of states (MODOS) of methyl–TOTA (**1**, green) and TOTA (**4**, yellow) adsorbed to Au(111). The MDOS is defined as the projection of all electronic states of the molecule-surface system into the states of the molecule in the gas phase. For molecule **1** ($CH_3$–TOTA) the calculated energy of the HOMO (LUMO) with respect of $E_F$ is ≈ −1.1 eV (2.9 eV). This is similar to the experimental data, where no LUMO was observed below 2 eV and an onset of an occupied state was detected at ≈ −1.5 eV (Fig. 9.3c). The HOMO in the theoretical data is closer to $E_F$ than in the experiment. This is actually expected, since DFT calculations tend to underestimates HOMO–LUMO gaps.[220] The MODOS of the bare platform **4** shows in contrast to that of molecule **1** a LUMO close to $E_F$. Consequently, the calculated platform corresponds to **4** and not **4b** on Au(111) (cf. Fig. 9.3d).

In our calculations, the platform relaxes to **4** (state close to $E_F$) rather than **4b** (no state), despite the fact that various starting geometries were used. This has so far prevented an unambiguous identification of **4b**. The fact that **4b** clusters and **4** does not, however, suggests that the charge state of **4b** is different from that of **4**. Such an electronically different, metastable state may be difficult to identify with DFT calculations.

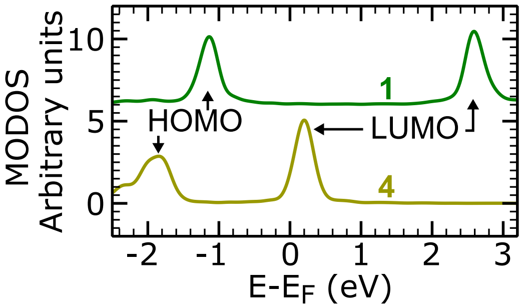

Figure 9.10.: Calculated molecular orbital density of states (MODOS) of methyl-TOTA (**1**) and TOTA (**4**) molecules adsorbed to Au(111). The MODOS is calculated via the projection of all gas-phase orbitals of the molecule onto the states of the molecule-surface system. The calculations have been done as implemented in the FHI-aims code (default settings). For clarity the MODOS of **1** is vertically shifted.

## 9.9.6. Adsorption geometry of TOTA and methyl-TOTA on Au(111)

The calculated adsorption geometries of TOTA (**4**) and methyl-TOTA (**1**) are very similar (Figs. 9.11a and b). Both molecule adsorb at the hcp-hollow site of the Au(111) surface. Moreover, the orientations of the molecules with respect to the substrate are almost identical. The calculated orientations are consistent with those found in STM topographs (see example in Fig. 9.12). The calculated distance of the planar TOTA platform and the surface atoms is 0.33 nm. Since the platform of methyl-TOTA is tilted, the central C atom is 0.1 nm higher than the outer C atoms. The distance between the outer C atoms and surface layer is 0.29 nm. The calculated adsorption geometry of ethynyl-TOTA (not shown) is essentially identical to that of methyl-TOTA because the same platform mediates the interaction with the surface.

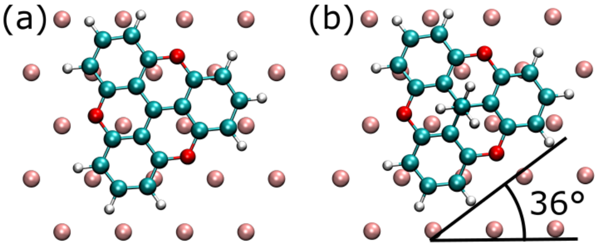

Figure 9.11.: Calculated adsorption geometry of TOTA and methyl-TOTA on Au(111). The center of both molecules is positioned at the hcp-hollow site of Au(111). As indicated in (b), the orientation on the molecules is characterized by an angle of 36° between the sides of the molecules and a close-packed direction of the Au(111) layer.

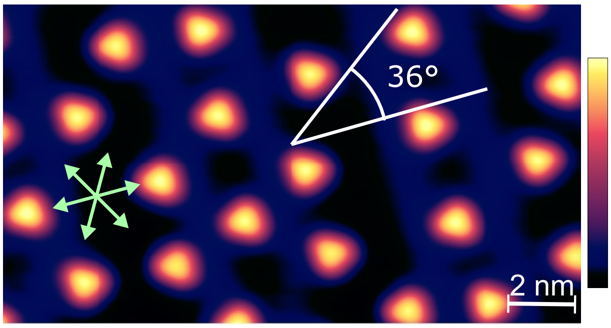

Figure 9.12.: STM topograph of TOTA on Au(111) (100 mV; color scale: 0.22 nm). The close-packed $\langle 1\bar{1}0 \rangle$ directions of Au(111) are shown by green arrows. The indicated angle between the sides of the molecules and a close-packed direction is close to the calculated value of 36°.

## 9.10. Acknowledgments

We thank the Deutsche Forschungsgemeinschaft for financial support via SFB 677 (Kiel) and by the FNR-CORE project QUANTION (Luxembourg).

## 9.11. Contributions

Sandra Ulrich, and Rainer Herges synthesized the molecules. I measured and analyzed the experimental data. Igor Poltavsky and Alexandre Tkatchenko performed the DFT calculations. I wrote the first draft of the manuscript.[284] Richard Berndt supervised the project. All authors discussed the results and improved and commented on the manuscript.

# Part IV.

# Deposition and Switching of a Fe(III) Spin-Crossover Complex

# 10

# Deposition of a Cationic Fe(III) Spin-Crossover Complex on Au(111): Impact of the Counter Ion

The results presented in this chapter were published in *The Journal of Physical Chemistry Letters*. The publication is reprinted (adapted) with permission from

Torben Jasper-Tönnies, Manuel Gruber, Sujoy Karan, Hanne Jacob, Felix Tuczek, and Richard Bernd, J. Phys. Chem. Lett. **8**, 1569 (2017). Copyright 2017 American Chemical Society.

## 10.1. Abstract

Spin-crossover molecules on metallic substrates have recently attracted considerable interest for their potential applications in molecular spintronics. Using scanning tunneling microscopy, we evidence the first successful deposition of a charged $Fe^{III}$ spin-crossover complex, $[Fe(pap)_2]^+$ (pap=N-2-pyridylmethylidene-2-hydroxyphenylaminato), on Au(111). Furthermore, the bulk form of the molecules is stabilized by a perchlorate counter ion, which depending on the deposition technique, may affect the quality of the deposition and the measurements. Finally, we evidence the switching of the molecules on Au(111).

## 10.2. Introduction

Molecular spintronics is a fertile research field that aims at exploiting molecules for spin transport.[21] Advantages over conventional spintronics can be found in new properties arising at molecule/metal interfaces[24–27,29–35] or the possibility to realize functions within the molecules themselves. Among functional molecules, spin-crossover (SCO) molecules are particularly interesting as their functionality is associated with a change of the spin. In that respect, SCO molecules on metal surfaces stimulated considerable efforts in recent years.[107,108,308,375,380–397] Yet, these studies are not only restricted to $Fe^{II}$ but also to uncharged complexes while the SCO family of molecules is much larger.[398] SCO compounds with different coordinations provide different sets of spin states, which is of interested for molecular spintronics. Here, using scanning tunneling microscopy (STM), we investigate a charged $Fe^{III}$ SCO complex, namely $[Fe(pap)_2]^+$ (pap=N-2-pyridylmethylidene-2-

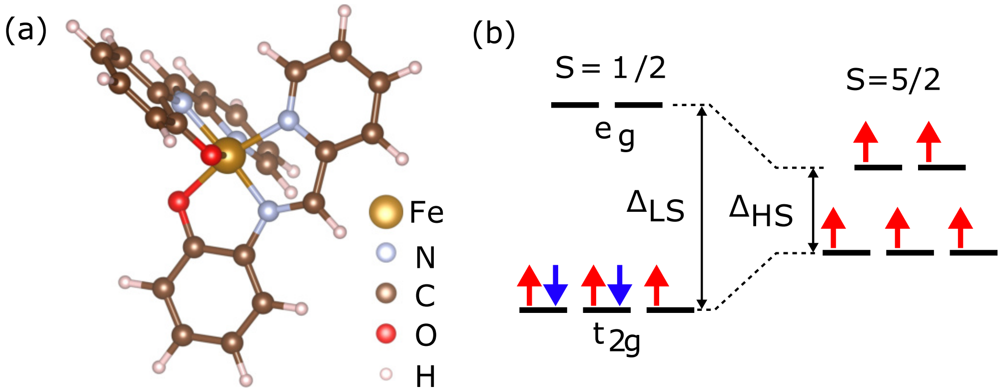

Figure 10.1.: (a) Model molecule of $[Fe(pap)_2]^+$, a spin-crossover complex composed of a central $Fe^{III}$ ion surrounded by two pap ligands. The angle between the two planes formed by the pap ligands is close to 90°. (b) Simplified electronic configuration of the five $d$ electrons of the $Fe^{III}$ ion. In the LS (HS) state, the electrons occupy the $t_{2g}$ ($t_{2g}$ and $e_g$) orbitals leading to a total spin S=1/2 (S=5/2). The molecular model was created with VESTA.[399]

hydroxyphenylaminato), deposited on Au(111) by sublimation and electrospray-ionization deposition (ESID). Intact $Fe(pap)_2$ molecules along with molecular fragments are observed on the surface. Furthermore, strong indications of the presence of perchlorate ions are shown for the samples prepared by sublimation in contrast to samples prepared by ESID. Finally, the switching of $Fe(pap)_2$ molecules is reported.

## 10.3. Results and discussion

$[Fe(pap)_2]^+$ molecules are composed of a central $Fe^{III}$ ion surrounded by two pap ligands (Fig. 10.1a). The two pap ligands are arranged orthogonally to each other, so that the central Fe ion is subject to an octahedral ligand field.[105] This field splits the initially degenerate $d$ orbitals of the Fe ion into $e_g$ and $t_{2g}$ sets of orbitals (Fig. 10.1b) which are differently populated depending on the spin state of the molecule.[400] In the low-spin (LS) state, the five $d$ electrons occupy the $t_{2g}$ orbitals leading to a total spin S=1/2, while in the high-spin (HS) state the electrons fill all $t_{2g}$ and $e_g$ orbitals leading to a total spin S=5/2 (Fig. 10.1b). In contrast to the precedent successful report of $Fe^{II}$-based SCO compound sublimation,[107,108,308,375,380–393] where the LS and HS have respectively S=0 and S=2, both spin electronic states of $[Fe(pap)_2]^+$ are paramagnetic. Since $[Fe(pap)_2]^+$ is positively charged, the crystallization of the compound requires a negative counter ion. Here we consider perchlorate ($ClO_4^-$) as counter ion. $[Fe(pap)_2]ClO_4$ exhibits a thermal spin transition with hysteresis around 180 K.[105,401–403] Furthermore, the spin transition can be induced by light. Actually $[Fe(pap)_2]ClO_4$ was the first $Fe^{III}$ compound reported to show light-induced excited spin state trapping,[105] an effect where light induces LS to HS transitions and the produced HS state remains metastable at low temperatures (typically below 80 K).[404,405] The main questions we address here are: (i) Does this $Fe^{III}$ compound withstands sublimation and deposition on metal surfaces? (ii) what is the impact of the counter ion, being present for charged SCO complexes, on the deposition?

We sublimed $[Fe(pap)_2]ClO_4$ on Au(111) (see Sec. 10.5) and investigated it using STM at low temperatures ($T$ = 4.6 K and 5.1 K). A typical large-scale STM topograph

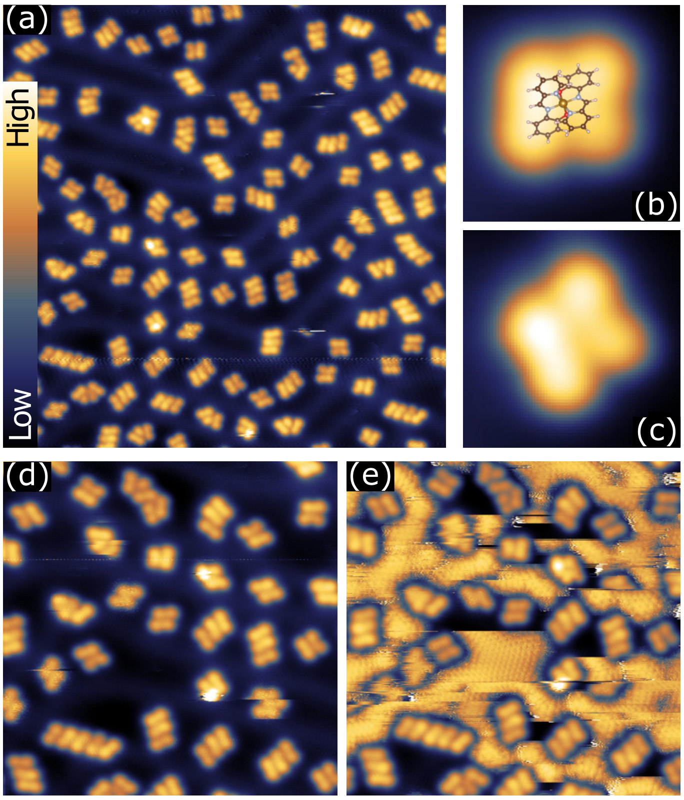

Figure 10.2.: STM topographs upon sublimation of $[Fe(pap)_2]ClO_4$ onto Au(111). (a) Large-scale topograph of $Fe(pap)_2$ on Au(111) exhibiting different molecular structures. The most common structure is composed of two elongated lobes such as the structure encircled by a solid red line. Different structures, notably composed by an odd number of elongated lobes can also be monitored (*e.g.* the structure encircled by a dashed red is composed of 3 elongated lobes). The inset of (a) describes the color scale used for all topographs throughout this chapter. (b) Topograph of the most frequent molecular structure together with a superimposed scaled molecular model of $[Fe(pap)_2]^+$. (c) Topograph of the molecule presented in (b) upon application of a −3 V voltage pulse that resulted in the rotation of the molecule. Consecutive topographs of the very same area imaged at (d) negative and (e) positive voltages. The image widths are (a) 35 nm ($V = -1.0$ V, $I = 370$ pA), (b), (c) 2.5 nm ($V = -1.0$ V, $I = 320$ pA), (d) 18 nm ($V = -1.0$ V, $I = 170$ pA) and (e) 18 nm ($V = 1.0$ V, $I = 170$ pA).

of the sample is shown in Fig. 10.2a. The Au(111) surface appears rather clean and the herring-bone reconstruction is discernible as blue lines on a darker background. Different molecular structures are observed, where the elementary unit is an elongated lobe. Fig. 10.2b shows the most common molecular structure, appearing as a pair of elongated lobes, with a superimposed scaled molecular model of the $[Fe(pap)_2]^+$ molecule. The symmetry of the topograph matches the molecular model. The topograph of the molecule has a width of 1.6 nm compared to the model's width of 0.8 nm. This apparent discrepancy is actually expected, as the topograph is related to the convolution of the molecule's orbitals with that of the tip. In contrast, the height of the model (0.77 nm) is larger than the apparent height of the topograph (0.15 nm). While the apparent height is strongly affected by electronic considerations and should not be expected to be similar to the height of the model molecule, the large difference may nevertheless reflect a flattening of the molecule upon adsorption on the surface. Based on the relatively good agreement between the topograph and the model molecule, we ascribe the double-lobe structures (Fig. 10.2b) to single Fe(pap)$_2$ molecules, where each of the lobes corresponds to a pap ligand. Further justifications for this assignment will be given below. Yet, other molecular structures are observed in Fig. 10.2a, notably structures composed of an odd number of lobes (*e.g.* structure encircled by a dashed red line in Fig. 10.2a). These structures may be composed of intact molecules together with fragments or composed only of fragments. Nevertheless, fragments of molecules are involved indicating a partial decomposition of the Fe(pap)$_2$ molecules. We estimate that the fragment proportion is larger than 40 % [LI]. In the following, we will focus on molecular structures resembling that of Fig. 10.2b, which are believed to be intact Fe(pap)$_2$ molecules.

Figs. 10.2b and c show topographs of a single Fe(pap)$_2$ molecule before and after the application of a $-3$ V voltage pulse over the center of the molecule with the feedback-loop open. The voltage pulse induces a rotation of the molecule. Furthermore, despite the relatively large applied sample voltage ($-3$ V), the overall shape of the molecules remains the same after the switching attempt. This supports our claim that the molecular structure observed in Fig. 10.2b is a single Fe(pap)$_2$ and not solely composed of two neighboring fragments. For completeness, we mention that the attempts to dissociate $2n+1$ lobe structures using voltages similar to that used for switching were unsuccessful.

The topographs presented in Figs. 10.2a–d, acquired with a negative sample voltage, reveal a relatively clean Au(111) surface. However, when imaging at positive sample voltages, the Au(111) surface appears fuzzy. For example, Figs. 10.2d and e show topographs of the very same area imaged at negative and positive voltage, respectively. Only the topograph imaged at positive voltage presents the fuzzy features (Fig. 10.2e). A modification of the STM tip, for instance by adsorption of a contaminant, is excluded here as the subsequent topograph acquired at negative sample voltage again (not shown) is similar to that presented in Fig. 10.2d. Therefore, the objects responsible for the fuzzy features resides on the Au(111) surface and seems to be displaced by the tip but blocked by the molecular structures. For instance, in the lower left area of the topograph presented in Fig. 10.2e, a part of the Au(111) surface does not show the fuzzy features as it is encircled by molecular structures. Interestingly, the fuzzy features appear with a small corrugation corresponding to the atomic arrangement of the underlying Au(111) as previously observed for different systems.[406,407] Yet, considering the nature of the object on the surface, we suggest that the object on the substrate is the small perchlorate counter ion. This hypothesis is checked in the following.

In order to prepare the Fe(pap)$_2$ molecules on Au(111) without the perchlorate counter ions, we employed a different deposition techniques, namely ESID. The general principle of the technique is to ionize the molecules dissolved in a solvent and to guide them towards the substrate located in an ultra-high vacuum chamber. In our setup, the molecules traverse a mass spectrometer, so that the mass-to-charge ratio of the molecules that will arrive at the substrate can be selected.[159] Fig. 10.3a shows the mass spectrum obtained for [Fe(pap)$_2$]ClO$_4$ in methanol (see Sec. 10.5) where three distinct peaks centered at $m/z$ = 440, 520 and 690 are resolved. The first peak is compatible with [Fe(pap)$_2$]$^+$ (ex-

---

[LI] To arrive at this lower-bound estimate, all molecular structures composed of $2n$ number of lobes are supposed to be $n$ intact molecules, while molecular structures composed of $2n + 1$ lobes are supposed to correspond to $n$ intact molecules and one fragment.

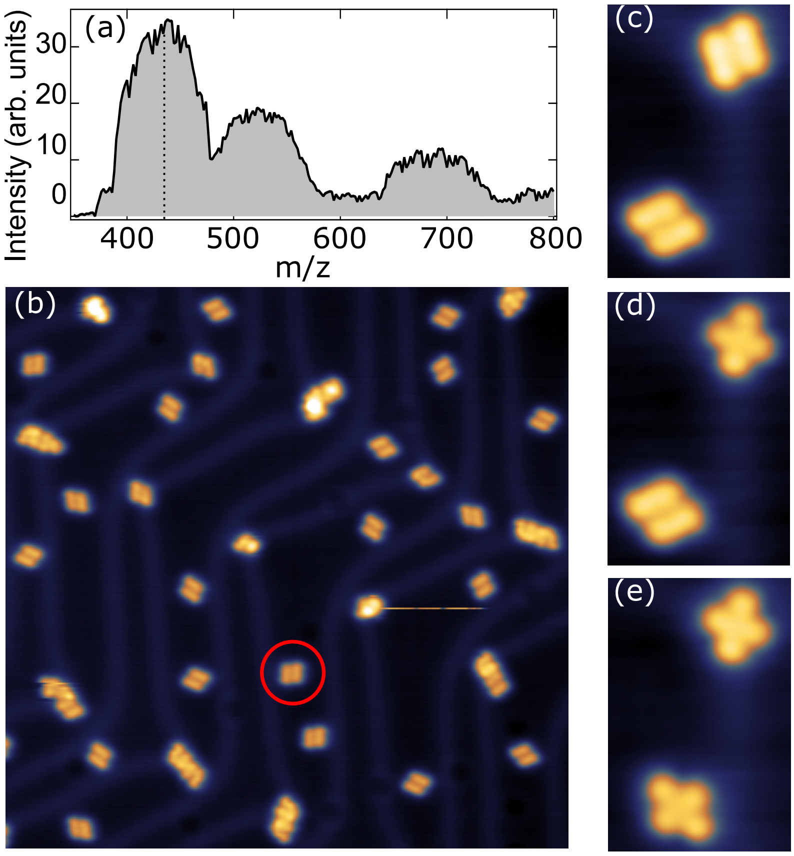

Figure 10.3.: (a) Electrospray-ionization mass spectrum of $[\mathrm{Fe(pap)_2}]\mathrm{ClO_4}$ dissolved in methanol. The dashed vertical line indicates $m/z$ setting of the mass spectrometer during deposition. (b) STM topograph upon ESID of $[\mathrm{Fe(pap)_2}]^+$ on Au(111). Mostly molecular structures composed of two elongated lobes, similar to that of Fig. 10.2b, are observed on the surface. Topographs (c) before and (d) after increasing the sample voltage to −2.5 V with the tip placed over the upper molecule. The appearance of the upper molecule changes from the usual double-lobe to a cross-shape appearance. Topographs (d) before and (e) after switching the lower molecule. The same procedure as between (c) and (d) was used. The image widths are (b) 35 nm ($V = 0.5$ V, $I = 50$ pA), (c)–(e) 6$x$4 nm$^2$ ($V = -0.5$ V, $I = 50$ pA).

pected $m/z = 450$), while the second and third peaks are indicative of $[\mathrm{Fe(pap)_2ClO_4H}]^+$ (expected $m/z = 550$) and $[(\mathrm{Fe(pap)_2})_2\mathrm{ClO_4}]^{2+}$ (expected $m/z = 725$), respectively[LII].

$[\mathrm{Fe(pap)_2}]^+$ molecules without their counter ion were deposited on the Au(111) surface by setting a $m/z$ value of 435 on the mass spectrometer (see Sec. 10.5). A typical large-scale post-deposition topograph is shown in Fig. 10.3b. A large number of molecular structures similar to those of Fig. 10.2b (*e.g.* molecule encircled by a solid red line in Fig. 10.3b), assigned to intact $\mathrm{Fe(pap)_2}$ molecules, are observed. An additional structure compatible with an $\mathrm{Fe(pap)_2}$ dimer (*e.g.* molecule encircled by a dashed red line in Fig. 10.3b) is present and further discussed in the supplementary information. In contrast to the samples prepared by sublimation, relatively few molecular fragments are found. Indeed, the lower bound of fragment proportion is about 5 % to compare to the

---

[LII] The center of all three peaks occurs below the expected $m/z$ value of the ions. This is because the data shown in Fig. 10.3a was acquired in constant-resolution mass mode with a low resolution to ensure a large ion transmission.

40 % found for the sample prepared by sublimation. This indicates that ESID is more suitable than evaporation for the present fragile SCO molecules. Furthermore, in the topograph presented in Fig. 10.3b, the Au(111) surface appears relatively clean in contrast to the topograph of Fig. 10.2e acquired with the same voltage polarity. Actually, the topographs are similar and independent of the sample voltage used for acquisition (not shown). Since the only difference between the two samples is the deposition method and considering the previous considerations, we suggest that the fuzzy features observed in Fig. 10.2e are indeed due to perchlorate counter ions. We conclude that sublimation of charged SCO molecules is possible with the counter ions being present on the surface. It should be noted that the data do not reveal whether the counter ions and the $[Fe(pap)_2]^+$ molecules remain charged on the surface. Consequently, no statement can be made on the oxidation state of the $Fe(pap)_2$ molecule adsorbed on the surface.

To switch the molecules, we positioned the tip on the top of the molecule and applied voltage pulses of up to about −3 V. This procedure was used as it led to tip-assisted switching of other spin crossover compounds on metallic substrates.[107,108,392] A large number of switching attempts were performed. The attempts resulted in the displacement or rotation of the molecule (as also seen for the samples prepared differently, Figs. 10.2b–c) expect for two successful attempt presented in Figs. 10.3c–e. Before the switching attempt, the molecule of interest appeared as two neighboring elongated lobes (Fig. 10.3c), while after switching, the molecule exhibits a cross-like shape (upper molecule in Fig. 10.3d). Next, Figs. 10.3d–e show topographs before and after switching the lower molecule. The switched molecules (Fig. 10.3e) both appear with a cross-like shape. The switching observed in Figs. 10.3c–e may be the expected spin crossover. However, since other processes may also be the origin of the conformational changes (*e.g.* change of oxidation state[408]) and since the differential conductance measurements (see SI) do not provide additional information, the origin of the conformational changes currently cannot be unambiguously identified. Nevertheless, the conformational switching from a parallel-lobe to a cross-like shape reflects a modification of the electronic structures in the entire molecule. Therefore, the switching independently demonstrates that the molecular structure ascribed to $Fe(pap)_2$ is not solely composed of two unconnected neighboring fragments. Unfortunately, this switching was observed only twice among hundreds of attempts. We infer that switching of $Fe(pap)_2$ molecules is possible but with a very low yield as the energy transferred to the molecule mostly led to a displacement or rotation of the molecule instead of a conformational change as reported for other complexes.[409] For completeness, we note that the two successful switching events were realized on a ESID sample.

## 10.4. Summary

The successful deposition of $[Fe(pap)_2]^+$ molecules, a charged $Fe^{III}$ SCO compound, on Au(111) was demonstrated. The ESID leads a much higher proportion of intact molecules on the Au(111) surface compared to the deposition by sublimation. Furthermore, we showed that evaporation of $[Fe(pap)_2]ClO_4$ on Au(111) result in not only having the $Fe(pap)_2$ molecules on the surface but also the $ClO_4$ counter ions visible at positive sample voltages. The $ClO_4$ counter ions were not observed on sample prepared with ESID, as the instrument was configured to only transmit $[Fe(pap)_2]^+$ ions. Finally, we observed a tip-assisted switching of a molecule, which may be ascribed to the expected spin transition.

We speculate that SCO transitions may be facilitated by intercalating a decoupling layer between the Fe(pap)$_2$ molecules and the metal substrates. This study paves the route of Fe$^{III}$ SCO complexes on single-crystal surfaces, which present promising molecular-spintronics perspectives.

## 10.5. Experimental details

### 10.5.1. Synthesis of the molecules

[Fe(pap)$_2$]ClO$_4$ molecules were synthesized following Ref. 401.

### 10.5.2. Sample preparation

Clean and flat Au(111) surfaces were prepared by several cycles of Ar sputtering (1.5 keV) and subsequent annealing to 550°C. Two techniques were used for the deposition of the molecules: (i) sublimation and (ii) ESID. For (i), the molecules were introduced into a Ta crucible, which was heated up until deposition could be monitored by a quartz balance. The temperature of the crucible could not be directly monitored. However, thanks to auxiliary measurements, the sublimation temperature is estimated to be between 80 and 100 °C. For (ii), the molecules were dissolved in methanol, then the molecules were injected with a syringe, guided towards the sample surface and characterized using a home-built instrument.[159] To get higher average ion current, we selected a $m/z$ of $435 \pm 20$ which encompass the expected $m/z$ of a charged [Fe(pap)$_2$]$^+$ at a relative kinetic energy of 5 eV. The molecule depositions were performed at pressures below $10^{-9}$ mbar onto a sample held at room temperature.

### 10.5.3. STM

STM tips were prepared by chemical etching of a tungsten wire and subsequent flashing in ultrahigh vacuum. The STM were operated at ~ 4 K. All the STM topographs were acquired using the constant-current mode.

## 10.6. Supporting information

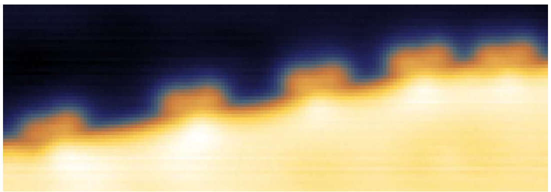

Figure 10.4.: STM topograph upon evaporation of $[Fe(pap)_2]ClO_4$ on Au(111). The topograph reveals a Au(111) step edge decorated with single pap ligands. The long axis of each pap ligand is oriented along the step edge. Image size is $12x4\,nm^2$ ($V = -0.1\,V$, $I = 300\,pA$).

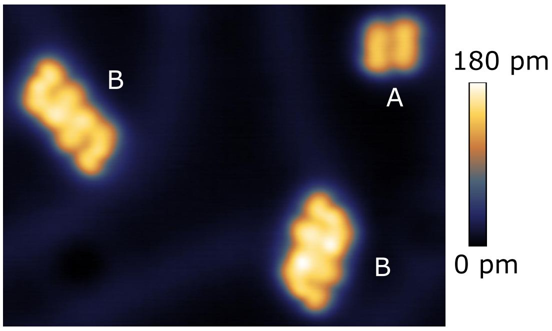

Figure 10.5.: Constant-current STM topograph on an ESID sample with molecular structures A and B. A is composed of a pair of parallel elongated lobes and compatible with a single $Fe(pap)_2$ molecule as discussed above. The overall size of B makes it consistent with a $Fe(pap)_2$ dimer. However, B appears as two neighboring $U$-shaped structures and not solely two times the A structure. Furthermore B has an apparent height about 60 pm larger than that of A. The origin of the B structure remains unclear, but we speculate that it may be $[(Fe(pap)_2)_2]ClO_4$, *i.e.* two $Fe(pap)_2$ molecules linked by a counter ion. This assumption is based on the fact that B is only observed on ESID samples and that the settings of the mass spectrometer were such that such a molecule could be transmitted. Image size is $11x8\,nm^2$ ($V = 0.5\,V$, $I = 50\,pA$).

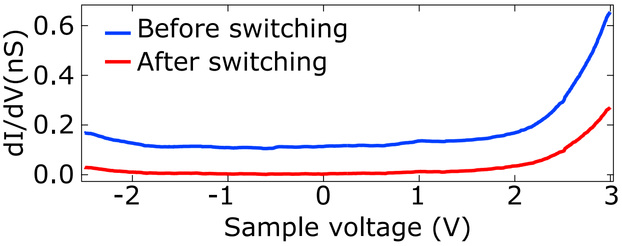

Figure 10.6.: Differential-conductance spectra of $Fe(pap)_2$ on Au(111). The measurements were performed pre and post switching of the very same molecule, *i.e.* the upper molecule in Figs. 10.3c and d. Both spectra have similar shapes and do not show strong molecular states over the entire sample voltage range. The blue spectrum is vertically shifted by 0.1 nS for clarity.

## 10.7. Acknowledgment

We thank Alexander Schlimm for auxiliary measurements. We acknowledge funding from the Deutsche Forschungsgemeinschaft (DFG) via Sonderforschungsbereich 677.

## 10.8. Contributions

Hanne Jacob and Felix Tuczek synthesized the compound. Sujoy Karan performed the measurements with electrospray deposition of the molecules. I carried out the measurements involving deposition via sublimation. Manuel Gruber (MG) joined the project and realized the impact of the work. I along with MG analyzed the data. MG wrote the first draft of the manuscript.[410] Richard Berndt supervised the project. All authors discussed the results and improved and commented on the manuscript.

# 11

# Robust and Selective Switching of a Fe(III) Spin-Crossover Compound on $Cu_2N/Cu(100)$ with Memristance Behavior

The results presented in this chapter were published in *Nano Letters*. The publication is reprinted (adapted) with permission from

Torben Jasper-Toennies, Manuel Gruber, Sujoy Karan, Hanne Jacob, Felix Tuczek, and Richard Berndt, Nano Lett. **17**, 6613 (2017). Copyright 2017 American Chemical Society.

## 11.1. Abstract

The switching between two spin states makes spin-crossover molecules on surfaces very attractive for potential applications in molecular spintronics. Using scanning tunneling microscopy, the successful deposition of $[Fe(pap)_2]^+$ (pap = N-2-pyridylmethylidene-2-hydroxyphenylaminato) molecules on $Cu_2N/Cu(100)$ surface is evidenced. The deposited $Fe^{III}$ spin-crossover compound is controllably switched between three different states, each of them exhibiting a characteristic tunneling conductance. The conductance is therefore employed to readily read the state of the molecules. A comparison of the experimental data with the results of density-functional-theory calculations suggests that all $Fe(pap)_2$ molecules are initially in their high-spin state. The two other states are compatible with the low-spin state of the molecule but differ with respect to their coupling to the substrate. As a proof of concept, the reversible and selective nature of the switching is used to build a two-molecule memory.

## 11.2. Introduction

Molecular spintronics aims at utilizing molecules for spin-based applications.[21] The main motivations to go beyond conventional spintronics are new properties emerging at the metal/molecule interfaces[24–27, 29–35, 411–414] and the possibility to incorporate functions (*e.g.*, switching) within the molecules themselves. In this context, spin-crossover

(SCO) molecules are particularly interesting since they provide a spin-switching functionality. Consequently, SCO molecules on surfaces attracted considerable interest in recent years.[107,108,308,375,380–397,410]

Two main difficulties were identified for SCO molecules on surfaces. First, the deposition of delicate SCO compounds on surfaces is challenging as it can lead to their dissociation.[33,375,385] Furthermore, strong molecule-substrate interaction often prevents switching of the adsorbed molecule.[108,392] In that respect, so far, all successful studies were limited to $Fe^{II}$ SCO molecules, although compounds with different oxidation states or different central ions are available[398] and actually desirable as they exhibit different sets of spin states. Very recently, an $Fe^{III}$ SCO molecule, $[Fe(pap)_2]^+$ (pap = N-2-pyridylmethylidene-2-hydroxyphenylaminato), was successfully deposited on Au(111).[410] However, although switching events were observed, they occurred with an extremely low yield, and thus the nature of the switching could not be determined.

Here, we employ the same molecule, namely $[Fe(pap)_2]^+$, and deposit it on a $Cu_2N/Cu(100)$ substrate. Using scanning tunneling microscopy (STM), we show that the molecules are intact on the surface, although the charge state cannot be unambiguously identified. Furthermore, thanks to a reduced molecule-substrate coupling, the molecule can be selectively and reversibly switched into three distinct states, characterized by different tunneling conductances, with a relatively high yield. With the help of gas-phase density-functional-theory (DFT) calculations, the spin states of the different molecular conformations are identified. Finally, the selective switching capability was used to build a two-molecule memory.

## 11.3. Results and discussions

$[Fe(pap)_2]^+$ molecules are composed of a central $Fe^{3+}$ ion surrounded by two pap ligands (Figure 11.1a). The pap ligands are orthogonal to each other, such that four nitrogen and two oxygen atoms form an octahedron around the Fe ion.[105,403] The Fe ion is therefore subject to an octahedral ligand field, which splits the initially degenerate $d$ orbitals of the Fe into $e_g$ and $t_{2g}$ sets of orbitals. Depending on the energy splitting between the $e_g$ and $t_{2g}$ orbitals, a total spin of $S = 1/2$ or of $S = 5/2$ may be realized (Figure 11.1b). This leads to a low-spin (LS) and high-spin (HS) state, respectively. The transition from one spin state to the other may be induced by external stimuli such as temperature and light.[105,401–403,415] Actually, the first observation of light-induced excited spin state trapping[404,405] on an $Fe^{III}$ compound was with $[Fe(pap)_2]^+$.[105] As stated above, $Fe(pap)_2$ was successfully deposited and switched on Au(111).[410] However, the switching yield is extremely low and the conformations of the molecule could not be related to a particular spin state of the molecule. As the low yield is probably caused by an overly strong molecule-substrate coupling, we use a $Cu_2N/Cu(100)$ substrate instead of Au(111) in the present study. This choice is motivated by a previous report of switching of single SCO molecules on $Cu_2N/Cu(100)$.[108]

We deposited $[Fe(pap)_2]^+$ molecules on a $Cu_2N/Cu(100)$ substrate by sublimation of $[Fe(pap)_2]ClO_4$ (see Section 11.5 and Ref. 410) and investigated it using STM at low temperature ($T = 4.6\,K$). The substrate surface is composed of $Cu_2N$ islands (about 5 nm wide) separated by trenches of bare copper.[154,156,416] Upon deposition of $[Fe(pap)_2]^+$

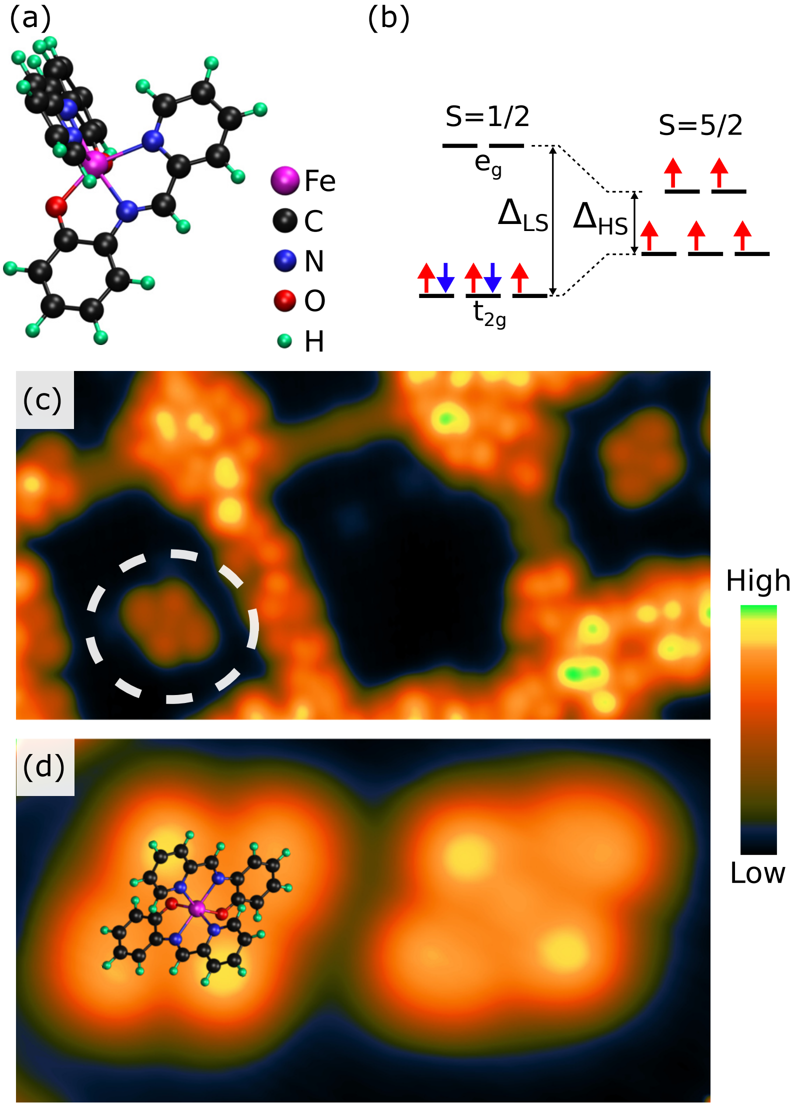

Figure 11.1.: (a) Model of $[Fe(pap)_2]^+$, a SCO complex composed of a central $Fe^{III}$ ion surrounded by two pap ligands. The angle between the planes of the pap ligands is close to 90°. (b) Simplified electronic configuration of the $Fe^{III}$ ions. In the HS (LS) state, the electrons occupy the $t_{2g}$ and $e_g$ ($t_{2g}$) orbitals leading to a total spin $S = 5/2$ ($S = 1/2$). (c) Large-scale STM topograph of $[Fe(pap)_2]^+$ deposited on $Cu_2N/Cu(100)$. The surface exhibits $Cu_2N$ islands (dark blue), some of which host a $Fe(pap)_2$ molecule (*e.g.*, dashed circle). Molecular adsorbates (reddish to yellowish) have aggregated at Cu(100) areas, which are located between the $Cu_2N$ islands. (d) STM topograph of two $Fe(pap)_2$ molecules on a $Cu_2N$ island. A calculated molecular structure of HS $[Fe(pap)_2]^+$ is overlaid over the left molecule. The color scale shown at the bottom was used through the entire chapter. Image sizes are (c) $14.1x7.1\,\mathrm{nm}^2$ and (d) $4.1x2.1\,\mathrm{nm}^2$. The color scales range over (c) 0.42 nm and (d) 0.23 nm.

molecules on the substrate at room temperature, the molecules preferentially adsorb at bare Cu trenches. Consequently, at low coverage, no Fe(pap)$_2$ molecules are observed on the $Cu_2N$ islands (see Supporting Information (SI), Sec. 11.6.1). However, when the molecular coverage is sufficiently increased to almost completely cover the Cu trenches, single Fe(pap)$_2$ molecules are found on $Cu_2N$ islands (*e.g.*, encircled molecule in Fig. 11.1c). Below, we focus on the molecules that are adsorbed on $Cu_2N$ islands. We would like to stress that, since the charge state of the adsorbed molecules cannot be unambiguously determined from our data (see below), they are henceforth referred to as Fe(pap)$_2$, *i.e.* without specifying their charge. In a previous report,[410] the sublimation of [Fe(pap)$_2$]$ClO_4$ led to the presence of the $ClO_4$ counter ions on the surface, observed as fuzzy features at positive sample voltage. In the present case, no such fuzzy features were observed. We speculate that the counter ions are still present at the surface, but are attached to the more reactive Cu trenches. They do not affect the measurements of single Fe(pap)$_2$ molecules on $Cu_2N$ islands.

Figure 11.1d shows two Fe(pap)$_2$ molecules on a $Cu_2N$ island. The topograph of Fe(pap)$_2$ on $Cu_2N$ is similar to that on Au(111) but exhibits different intramolecular features.[410] Differences in the topographs are expected as the molecule should be less coupled to a $Cu_2N$ substrate compared to a Au(111) substrate, hence leading to different hybridization of the molecular orbitals with that of the substrate. Indeed, the $Cu_2N$ acts as an insulating layer to electronically decouple the investigated object from the substrate.[417] The topograph of Fe(pap)$_2$ on $Cu_2N$ (Fig. 11.1d) displays a four-lobe structure. Two lobes, placed diagonally around the center, are laterally more extended and thus define the long axis of the molecule. The two other lobes are located almost perpendicularly to the long axis. These lobes are closer to each other and appear higher. As discussed below, long and short axes are expected for [Fe(pap)$_2$]$^+$ from DFT calculations. Furthermore, the length along the long axis depends on the molecular spin state, and thus may be used as a readout channel. Yet, anticipating the discussion below, we overlay the calculated molecular structure of HS [Fe(pap)$_2$]$^+$ on the topograph (left molecule in Fig. 11.1d). The agreement is relatively good. The calculated length of 1.0 nm is shorter than the 1.9 nm apparent length in the topograph. Such a difference between model and topograph is expected as the orbitals of the molecule extend into vacuum and the topograph is related to the overlap of the molecular orbitals with those of the tip (see Sec. 3.1.1). Interestingly, the apparent height of Fe(pap)$_2$ on $Cu_2N$ (0.24 nm) is much larger than that of Fe(pap)$_2$ on Au(111) (0.15 nm).[410] The different apparent height may reflect a reduced coupling to the substrate. In turn, a reduced molecule-substrate coupling facilitates switching of SCO molecules on surfaces.[108,375,387,392]

In order to switch the molecule, the tip was positioned over the center of the molecule followed by an increase of the sample voltage above 1.8 V until a change in the tunneling current was detected (feedback off). Switching of Fe(pap)$_2$ molecules is indeed possible with a much larger yield (discussed below) compared to that of Fe(pap)$_2$ on Au(111) (Ref. 410). Interestingly, and in contrast to previous reports of switching of SCO compounds in direct contact to surfaces,[108,308,390] not only two but three different states are found. Figures 11.2a–c show the three conformations (A, B, and C) of the same Fe(pap)$_2$ molecule upon switching. The first conformation (Fig. 11.2a), referred to as state A, has an elongated shape with an apparent length of 1.9 nm. All Fe(pap)$_2$ molecules on $Cu_2N$ are initially in state A, which presumably is the state of lowest energy. In conformations B and C, the Fe(pap)$_2$ molecule appears shorter by 11 % (1.7 nm), leading to an

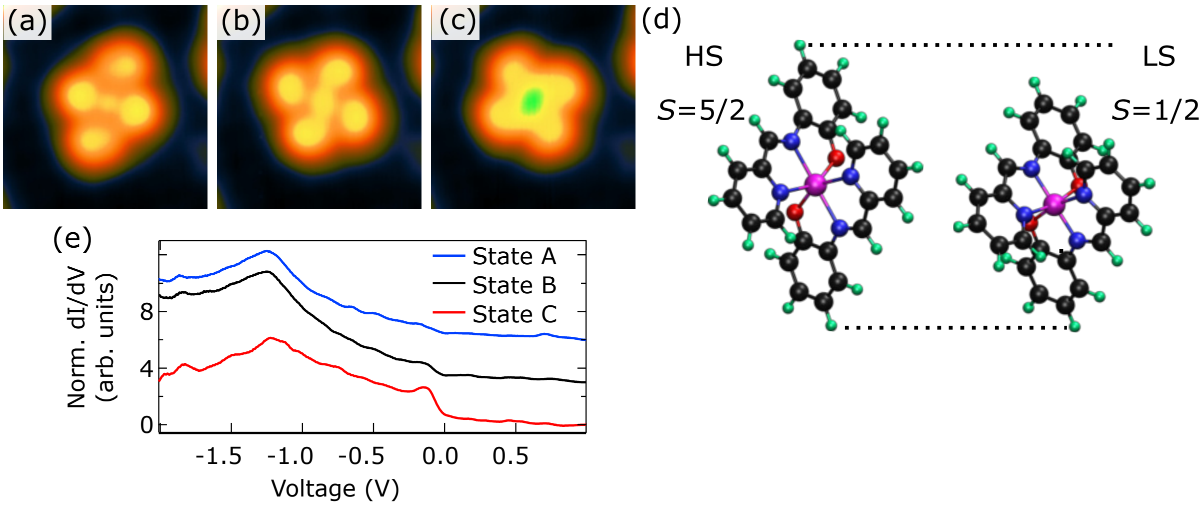

Figure 11.2.: STM topographs of the same Fe(pap)$_2$ molecule (a) in its initial state A; (b) and (c) in the switched states B and C, respectively. (d) Molecular structure resulting from gas-phase DFT calculations of HS and LS $[\mathrm{Fe(pap)_2}]^+$. The two molecular structures have different lengths as indicated by dotted lines. (e) Normalized differential-conductance spectra measured with the same tip over the center of the same molecule in states A, B, and C (see SI, Sec. 11.6.4, Fig. 11.9, for raw data). The normalized differential conductance $\sigma_{\mathrm{norm}}$ is obtained as follows: $\sigma_{\mathrm{norm}}(V) = \sigma_{\mathrm{raw}}(V) - C\sigma_{\mathrm{back.}}(V)$, where $C := \sigma_{\mathrm{raw}}(1\,\mathrm{V})/\sigma_{\mathrm{back.}}(1\,\mathrm{V})$. $\sigma_{\mathrm{raw}}(V)$ and $\sigma_{\mathrm{back.}}(V)$ are the differential conductances measured over the molecule's center and over the Cu$_2$N substrate, respectively. The normalization method is inspired from Ref. 418. The STM image in (a–c) share the same color scale covering 0.21 nm and have the same width (2.8 nm). They were acquired at a voltage $V = 0.1\,\mathrm{V}$ and a current $I = 700\,\mathrm{pA}$. In (e), the current feedback loop was opened at a set point of 1.2 nA and 1.0 V.

approximately square shape of the molecule. The main difference between B and C is the orientation of the molecule relative to the Cu$_2$N lattice (see SI, Sec. 11.6.2). C is rotated by approximately 45° compared to A and B. Furthermore, the center of the molecule appears higher in state C. Actually, the apparent height of the molecular center is unique for each conformation (Fig. 11.2a–c). Consequently, the molecular conformation can directly be inferred from the apparent height (or the conductance) of the molecule at its center. The three conformations of Fe(pap)$_2$ exhibit very distinct topographic features. The question arises whether the different conformations of the molecules are related to different spin states.

We performed gas-phase DFT calculations of $[\mathrm{Fe(pap)_2}]^+$ in the HS ($S = 5/2$) and low spin ($S = 1/2$) states. The calculated molecular structures are presented in Fig. 11.2d. In the HS (LS) state, the average Fe-O and Fe-N distances are 0.195 nm and 0.221 nm (0.189 nm and 0.194 nm), respectively. These calculated distances are very close (relative difference of 3 % or less) to 0.193 nm and 0.214 nm (0.188 nm and 0.195 nm) found by X-ray diffraction for the HS (LS) state.[105,403] The $[\mathrm{Fe(pap)_2}]^+$ molecule in the HS state is longer (1.0 nm) than in the LS state (0.9 nm). This corresponds to a length reduction of 10 % upon switching from HS to LS. Considering that a similar relative length reduction of 11 % was observed for the transitions from conformation A to conformations B and C, we ascribe conformation A as the HS state. From topographic considerations, molecular conformations B and C are both compatible with the LS state. As the charge state of the adsorbed molecule is unknown, the topographs are also compared to the calculated geometries of the neutral $Fe(pap)_2$ molecule (see SI, Sec. 11.6.3). This comparison leads to the same HS- and LS-state assignments, *i.e.* conformation A (B–C) corresponds to the molecule in the HS (LS) state.

To gain further insight into conformations A, B and C, differential-conductance spectra were measured over a $Fe(pap)_2$ molecule that was successively switched into the different conformations. The normalized $dI/dV$ spectrum taken atop the molecular center in state A shows a dominant feature around −1.24 V (blue curve in Fig. 11.2e). There is indication of a second peak at 0.71 V, whose amplitude, however, is close to the noise level. The corresponding spectra of the B and C states exhibit both an additional peak at −0.14 V (black and red curves in Fig. 11.2e). However, the amplitude of the peak is much more pronounced for state C. A second peak is observed at −1.25 V and −1.21 V in states B and C, respectively. These measurements reveal that A, B, and C have different but similar electronic structures. In particular, states B and C display additional states right below the Fermi level. While the HS state of other SCO molecules on surfaces could be inferred from the presence of a Kondo resonance,[107,108,392] in the present study no Kondo resonance was found for any of the states (like in Ref. 308). This is most probably due to a non-sufficient molecule-substrate coupling.

Note that, while bulk molecules are expected to be in the LS state at 4 K, the $Fe(pap)_2$ molecules on $Cu_2N$ are initially in the HS state. Similar observations were made for other complexes[387,392,419,420] and tentatively explained by state-dependent surface-energy considerations.[421]

From the the topographic considerations we may ascribe the state B *and* C as the LS state. Thus, both states are compatible with the LS state, although they have distinct topographs and slightly different differential-conductance spectra. We suggest three possible explanations: (i) One of the states B and C may be an intermediate trapped state; (ii) one of the two states is due to a different charge state of the molecule and (iii) states B and C both correspond to the LS state, their difference being the electronic coupling to the $Cu_2N$ substrate. An unambiguous decision cannot be made based on the present experimental data alone. However, the electronic structure is expected to change from a LS $[Fe(pap)_2]^+$ molecule to a molecule with an intermediate spin. Charging of molecules may also modify the electronic structure. Gas-phase DFT calculations of the projected density of states (PDOS) at the Fe center support these expectations.[422] However, the addition (removal) of a charge to (from) an adsorbate by injecting electrons (holes) usually requires different polarity of the voltage between tip and sample.[423] Moreover, scenarios (i) and (ii) *a priori* do not require a rotation of the molecule. This is not in favor of scenarios (i) and (ii). Instead, we favor scenario (iii) on the basis of the following arguments. The switching between B and C is characterized by a rotation of the molecule relative to the substrate, as previously reported for other systems.[127,253,409] The rotation of the molecule requires a degree of decoupling between the molecule and the substrate in line with the observation of lateral displacement of molecules (see SI, Sec. 11.6.7). As shown by the topographs of $Fe(pap)_2$ on an atomically resolved $Cu_2N$ substrate (see SI, Sec. 11.6.2), the rotation of the molecule leads to O atoms of the molecules be positioned differently with respect to $Cu_2N$, most probably resulting in a different coupling with the substrate. Therefore states B and C would both correspond to the LS state, but couple differently to the substrate, which induces subtle topographic and spectroscopic differences. In that case, the switch between B and C is not an intrinsic but an extrinsic property enabled

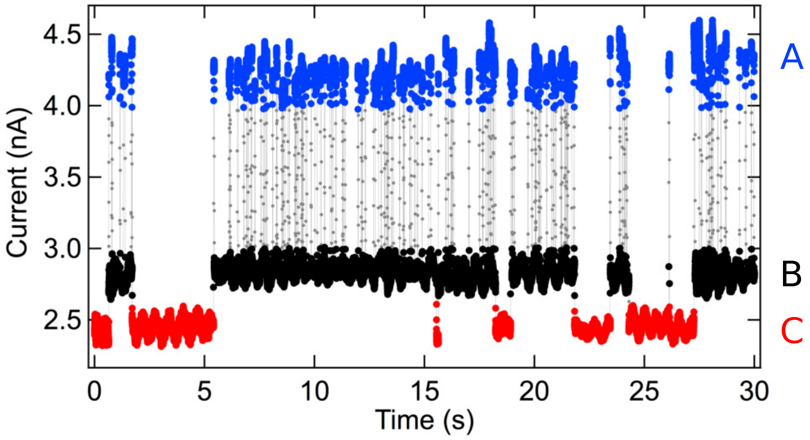

Figure 11.3.: Time series of the tunneling current measured with the tip positioned over the center of a Fe(pap)$_2$ molecule. A sample voltage of 2.5 V was applied. The current trace shows three current levels colored in blue, black and red from which the state of the molecule (A, B, and C) can be inferred. Intermediate tunneling currents (gray points) are visible as (i) the switches are faster than the I-V converter and (ii) the current is oversampled. Indeed, the sampling rate is about 7 kHz while the I-V converter has a cut-off frequency of 1 kHz. The current feedback was opened at a current of 2.4 nA and a voltage of 2.5 V.

by the substrate, as previously observed for other systems.[424,425] This interpretation is independently supported by differential conductance spectra with a voltage range larger than that presented in Figure 11.2e, *i.e.* from 1.0 to 2.1 V (see SI, Sec. 11.6.4).

As stated above, Fe(pap)$_2$ on Cu$_2$N can be switched into three different states, each of the state having a different apparent height at the center. These characteristic apparent heights suggest different tunneling conductances, which may be used to promptly and efficiently read the state of an investigated Fe(pap)$_2$ molecule. Figure 11.3 shows the tunneling current for the tip positioned over the center of a Fe(pap)$_2$ molecule with an applied sample voltage of 2.5 V. The current trace exhibits three distinct levels with an average current of 2.4 nA, 2.8 nA (+17 %) and 4.3 nA (+79 %) colored in red, black and blue, respectively. With the help of additional topographs and current-voltage curves (see SI, Sec. 11.6.5), they are identified to reflect states C, B, and A, respectively. In other words, Fe(pap)$_2$ on Cu$_2$N shows a memristive[108,426] behavior and the molecular state can be directly inferred from the tunneling current. Interestingly, the conductance level observed for the three states in Fig. 11.3 is different than what is expected from the apparent heights in the topographs acquired at low voltages (Figs. 11.2a–c). Actually, the HS state may be observed with the highest or lowest conductance, depending on the sample voltage (see SI, Sec. 11.6.5). Therefore, the assignment of spin states should not be solely based on conductance measurements.

The time series of the current in Fig. 11.3 provide some additional information. First, they show that the switching is fully reversible. Actually, the molecule can be put in any desired state (A, B, or C) by lowering the sample voltage once the target conductance, which is unique for each state at fixed tip-sample distance, is reached. Furthermore, the switching does not show any sign of fatigue, even after hundreds of events (SI, Sec. 11.6.6, Fig. 11.12a). No spontaneous switch of Fe(pap)$_2$ on Cu$_2$N was observed, even after hours of measurement with mild tunneling conditions ($V$ < 1.5 V and $I$ < 1 nA). In addition, the switching rate is found to be strongly voltage dependent. Indeed, the switching rate reduces from $7.3\,s^{-1}$ to $0.7\,s^{-1}$ when the voltage is decreased from 2.5 V ($I \approx 2.5$ nA) to 1.9 V ($I \approx 6$ nA). A detailed analysis of the switching can be found in Section 11.6.6 of the SI. Last but not least, the switching rate (and henceforth the switching yield) at $V = 2.5$ V is relatively high, exceeding by an order of magnitude that of previously reported switching of single SCO molecules on surfaces.[108]

For a potential integration of $Fe(pap)_2$ molecules into devices, *e.g.*, high-density memories, the selectivity of the switching process is demonstrated. Fig. 11.4a shows a topograph of two neighboring $Fe(pap)_2$ molecules in state A (HS) on $Cu_2N$. Placing the tip over the upper molecule and using a switching procedure similar to that of Fig. 11.3, the upper molecule is switched to state B, while the lower molecule remains in state A (Fig. 11.4b). This means that we can individually, selectively and actually deterministically switch a $Fe(pap)_2$ molecule without affecting its neighbors. Figs. 11.4a–e show a series of topographs that demonstrate selective and deterministic switching in a molecular dimer. Interestingly, the molecular dimer may assume $3^2 = 9$ configurations, out of which five are shown in the figure. Another sequence of switching is shown in Section 11.6.7 of the SI.

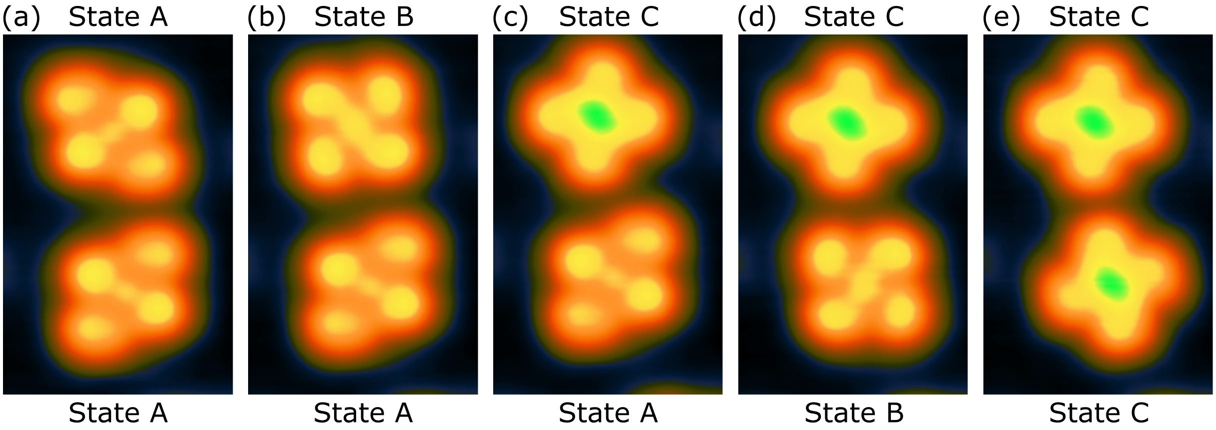

Figure 11.4.: (a–e) STM topographs recorded after selective and deterministic switching. In order to switch the molecules, the feedback loop was opened at 0.1 V and 100 pA, the sample voltage was then increased to 1.8 V, and kept until the targeted state was reached. Image sizes are $2.6x4\,nm^2$. The color scale covers 0.21 nm.

## 11.4. Summary

$[Fe(pap)_2]^+$ molecules have been successfully deposited on $Cu_2N$. The deposited $Fe^{III}$ SCO compound can be reversibly, selectively, and determistically switched into three states. Readout of the molecular state is possible through, *e.g.*, the conductance. With the help of DFT calculations it is inferred that the molecules are initially in a HS state. The two other states are compatible with the LS state, with most probably different electronic couplings to the substrate. This represents the first report of combined intrinsic (spin transition) and extrinsic (different coupling to the substrate) switching of a spin crossover compound on a surface. Furthermore, $Fe^{III}$ SCO provides different spin states than previously reported from $Fe^{II}$ compounds. The different set of spin states along with a "substrate-induced" additional state provides promising perspectives for molecular spintronics.

## 11.5. Experimental and theoretical details

*Synthesis of the molecules:* $[Fe(pap)_2]ClO_4$ molecules were synthesized following Ref. 401.

*Sample preparation:* Clean and flat Cu(100) surfaces were prepared by repeated cycles of Ar sputtering (1.0 keV) and subsequent annealing to 450 °C. Next, to obtain the $Cu_2N$ islands, $N_2$ was sputtered onto the clean Cu(100) substrate (500 V at an ion current of 3 µA for 70 s) and the sample was subsequently annealed to about 350 °C. Molecule deposition was performed by sublimation from a Ta crucible at pressures below $10^{-9}$ mbar onto a sample held at room temperature.

*STM:* STM tips were prepared by electrochemical etching of a tungsten wire and subsequent heating in ultrahigh vacuum. The STM was operated at ~ 4 K. All STM topographs were acquired using the constant-current mode. The differential conductance was measured using a lock-in amplifier with a voltage modulation of 10 mV at a frequency of 4780 Hz. The current feedback was turned off for spectroscopy while the sample-voltage was swept.

*DFT:* Gas-phase calculations shown in the main text were performed with Gaussian 09[427] using the PBE functional[428] with a def2svp basis set.[429]

To verify the robustness of the DFT results with respect to changes of the functional, we used four functionals, namely PBE,[428] B3LYP,[430,431] BP86,[432,433] and TPSS.[434,435] Furthermore, for a given functional, the calculations were performed using the following basis sets: def2svp,[429] def2svptzvp,[429] sto3G,[436,437] 6-311G**.[438–446] No significant differences were discernible between the various results.

## 11.6. Supporting information

### 11.6.1. Low coverage of $Fe(pap)_2$ on $Cu_2N$

Figure 11.5 shows an overview STM topograph of $Fe(pap)_2$ on $Cu_2N$ at low molecular coverage. The squarish $Cu_2N$ islands (blue/black) are separated by Cu trenches (brown). At low molecular coverages, the $Cu_2N$ islands are devoid of $Fe(pap)_2$. However, numerous molecular adsorbates are observed on the Cu trenches.

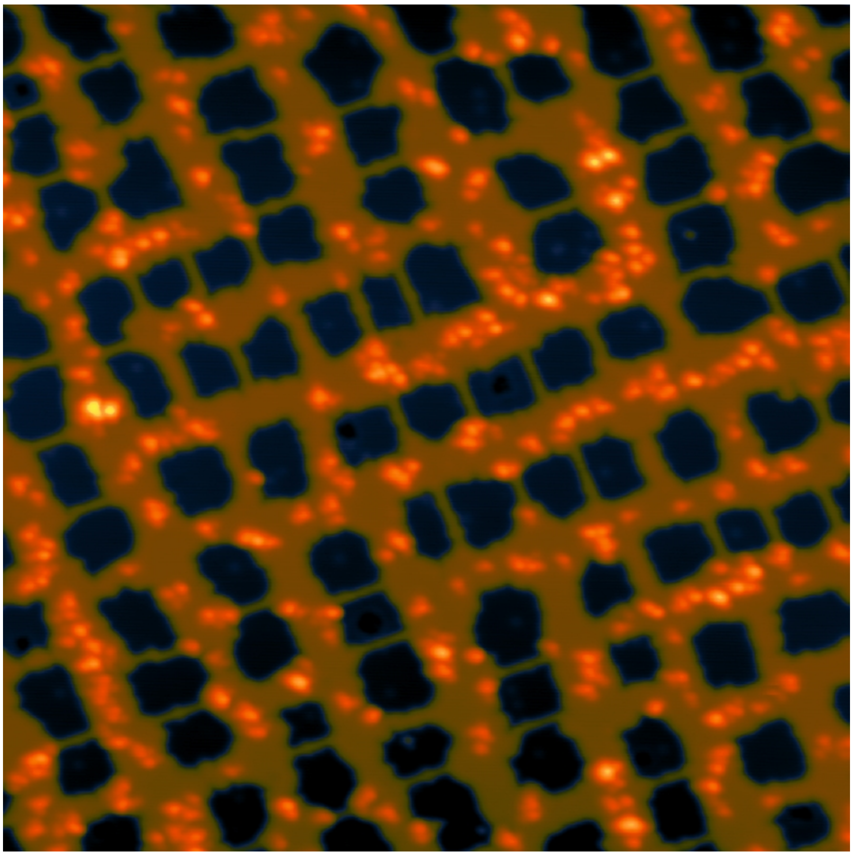

Figure 11.5.: Overview STM topograph of $Fe(pap)_2$ on $Cu_2N$ at low molecular coverage. The width of the topograph is 60 nm.

### 11.6.2. Adsorption sites of $Fe(pap)_2$ on $Cu_2N$

Figure 11.6 shows topographs of $Fe(pap)_2$ in states A, B, and C on an atomically resolved $Cu_2N$ substrate. Red dots indicate the positions of N atoms, which appear as depressions in the image. The N lattice was positioned using a larger topograph (12 nm width; not shown) and only the region of interest is displayed. In all observed molecular states, the Fe ion of the molecule lies on top of a N atom. From the model molecule positioned on the topograph, it is inferred that the O atoms are located on bridge sites (between two neighboring N atoms of the lattice) in states A and B. In state C, the O atoms are close to hollow sites. However, the limited distance between the two molecular O atoms (0.28 nm) may prevent the O atoms from resting precisely at the hollow positions, for which a O-O

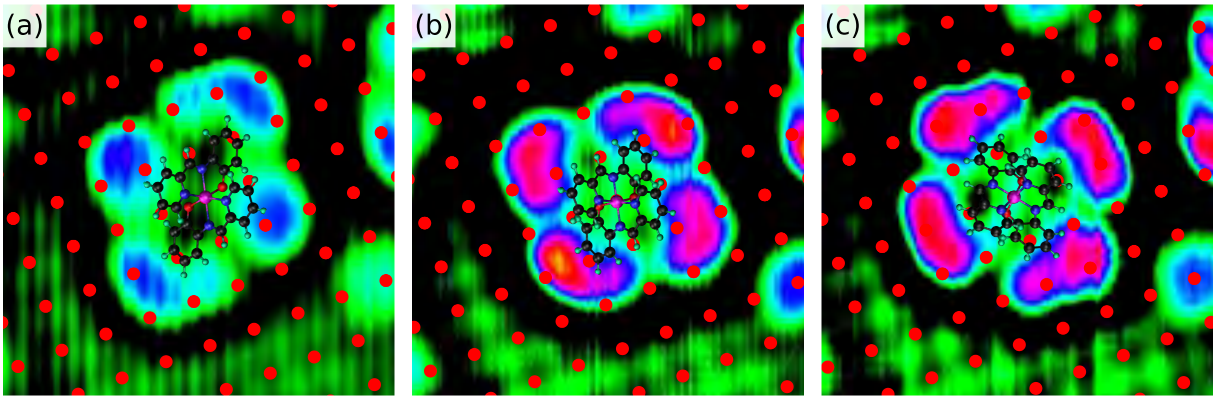

Figure 11.6.: STM topographs of the same molecule in the (a) A, (b) B and (c) C state with an atomically resolved $Cu_2N$ lattice. Scaled molecular models are superimposed on top of the topographs. Red dots indicate the positions of the N atoms, which appear as depression at a sample voltage of 1 V. The topographs have a width of 3 nm. Note that the topographs were processed to enhance the contrast. The images in (a–c) were obtained by merging the raw topograph with the inverted, smoothed, and Laplace-filtered image.

distance of 0.53 nm would be required. The different adsorption sites in states B and C may lead to different electronic coupling to the substrate.

### 11.6.3. Geometry of the neutral molecule

In the following, gas-phase calculations of the neutral $\mathrm{Fe(pap)_2}$ are considered. The neutral $\mathrm{Fe(pap)_2}$ complex has a HS and LS states with $S = 2$ and $S = 0$, respectively. The calculated geometries are presented in Figure 11.7. Interestingly, the calculations reveal identical lengths (within the precision given here) for the positively charged and neutral complex, *i.e.* 1.0 nm for the HS state and 0.9 nm for the LS state. This prevents a determination of the molecular charge solely based on topographic data.

Note that the above calculations were performed with the same functional (PBE) and same basis set (def2svp) as that presented in Section 11.3. These results are robust against a change of the functional or the basis set (see Paragraph *DFT* in Sec. 11.5).

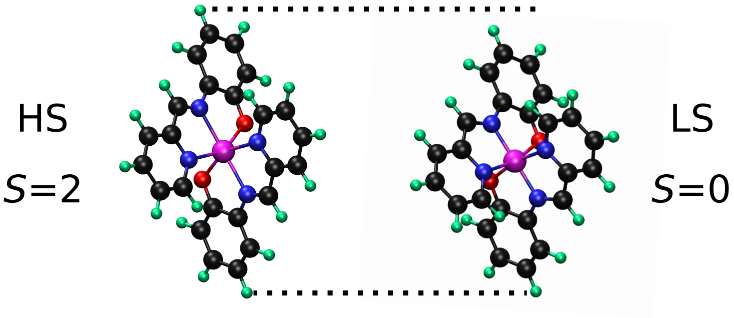

Figure 11.7.: Calculated geometry of the HS and LS state of the neutral $\mathrm{Fe(pap)_2}$ molecule.

### 11.6.4. Differential conductance spectra

Figure 11.8 shows differential conductance spectra with a voltage range larger than that presented in Section 11.3, *i.e.* from 1.0 to 2.1 V. Interestingly, for one measurement, the differential conductance exhibits a large jump at large sample voltage, and the differential conductance exhibits hysteresis. This is due to the switching of the investigated Fe(pap)$_2$ molecule from state A to C during data acquisition.

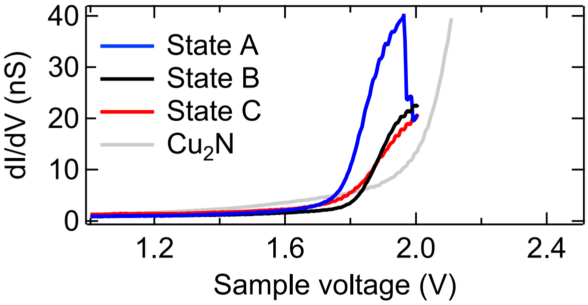

Figure 11.8.: Differential conductance spectra over the center of a Fe(pap)$_2$ in states A, B and C, along with a reference spectrum on Cu$_2$N. Spectra A and C were recorded during forward and backward voltage sweep, respectively. The feedback loop was opened at $V = 1.0$ V and $I = 0.7$ nA.

A peak-like feature is visible for the three different states (Figure 11.8), which suggest the presence of an unoccupied orbital. The onsets of the peaks in states B and C appear at approximately identical voltages, which are larger than in state A. Furthermore the differential conductance measured over A is significantly higher than that over B and C. This independently suggests that B and C correspond to the same spin state (LS) but differently coupled to the substrate, in agreement to the topographic comparison.

The switching of the molecule, observed as an abrupt jump in the differential conductance, occurs at a sample voltage at which the electrons are injected into an "unoccupied" orbital. We speculate that this orbital is involved in the detailed switching mechanism.

Normalized differential conductance spectra are presented in Section 11.3 in order to emphasize important features. For completeness, Figure 11.9 shows the raw $dI/dV$ spectra without normalization.

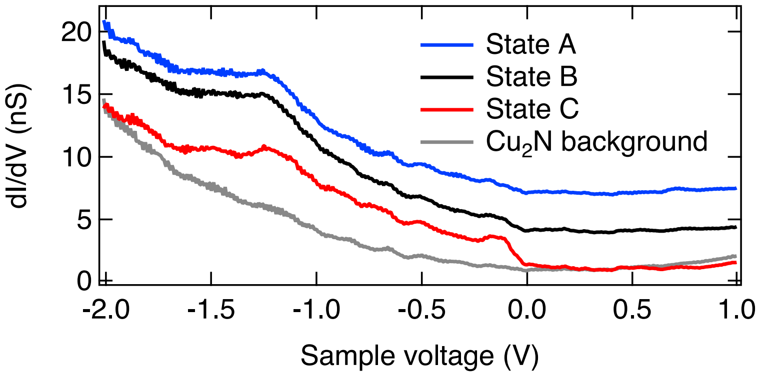

Figure 11.9.: Differential conductance spectra over Cu$_2$N and over the center of a Fe(pap)$_2$ molecule in states A, B, and C. The spectra of states A and B have been shifted by 3 nS and 6 nS, respectively, for clarity. The feedback loop was opened for at 1.2 nA and 1.0 V.

## 11.6.5. Assignment of the conductance states to molecular states

As discussed in Section 11.3, the different states of Fe(pap)$_2$ on Cu$_2$N are characterized by different conductances, which enables the direct observation of switching events in time-series. However, the assignment of the conductance states to the different states of the molecules is not trivial. Indeed, Figure 11.10a shows two current-voltage curves (corresponding to the forward and backward sweeps of the single spectroscopic measurement) acquired at the same tip-sample distance. The two curves cross at a sample voltage of 1.85 V. Below (above) this voltage the junction comprising a molecule in state C (A) has a higher conductance than that comprising a molecule in state A (C). Therefore, while a molecule in state C is observed with a higher conductance than a molecule in state A at low voltages, the sequence is reversed at voltage above 1.85 V.

A similar observation is made in Figure 11.10b where current-voltage data of states B and C are compared. However, the crossing of the two curves occurs at a voltage of 1.95 V. The main outcome of Figure 11.10 is that the highest conductance is not always observed for the same spin state. It depends on the sample voltage as summarized in Table 11.1. In that respect, no spin-state assignment should be solely based on conductance measurements.

In the Section 11.3 and in Figure 11.12, time-series acquired at voltages above 1.95 V are shown. The lowest conductance state is obtained when the investigated Fe(pap)$_2$ molecule is in the state C. In contrast, Figure 11.11 shows a time-series acquired at a

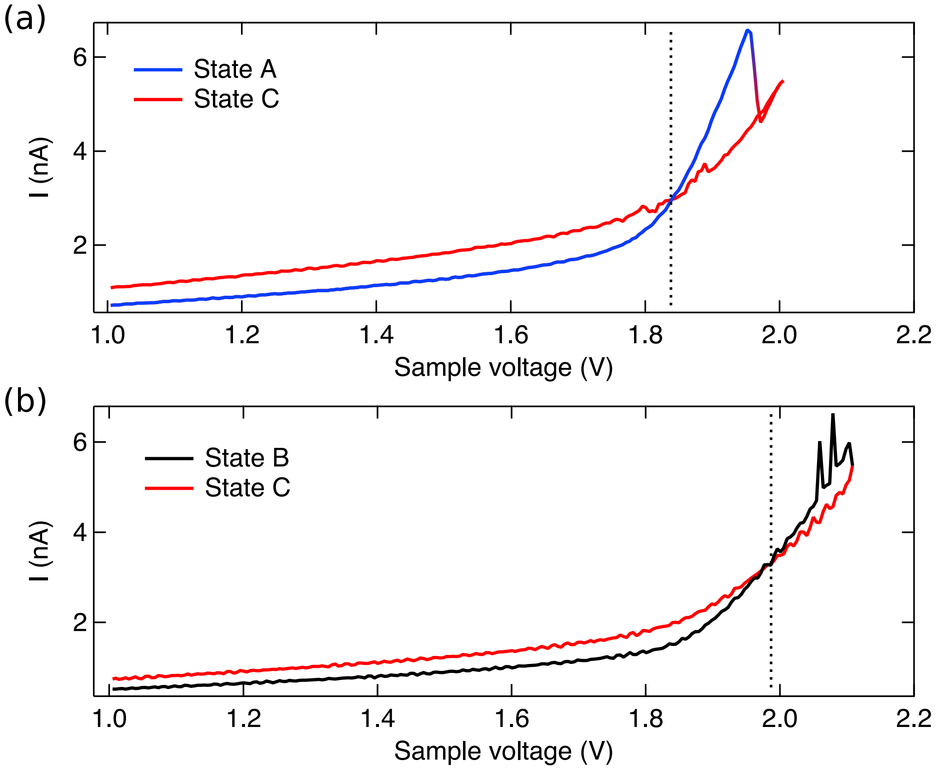

Figure 11.10.: Current-voltage curves monitoring the switching of the investigated molecule between the states a) A and C and (b) B and C. In each panel, the two curves correspond to the forward and backward sweeps of a single spectroscopic measurement.

| Conductance | $V < 1.85\,\mathrm{V}$ | $1.85\,\mathrm{V} < V < 1.95\,\mathrm{V}$ | $V > 1.95\,\mathrm{V}$ |
|---|---|---|---|
| Highest | State C | State A | State A |
| Intermediate | State B | State C | State B |
| Lowest | State A | State B | State C |

Table 11.1.: Correspondence between molecular and conductance states for different voltage ranges. Note that this correspondence could eventually change if substantially different tip-sample distances were used. In the present case, the distance is fixed by the tunnel parameters over the center of a molecule before opening the feedback loop ($V = 1\,\mathrm{V}$ and $I = 1\,\mathrm{nA}$ to $3\,\mathrm{nA}$).

sample voltage of 1.9 V. In that case, as indicated in Table 11.1, the molecule in the state B leads to the lowest conductance.

Figure 11.11 further illustrates the preparation of a Fe(pap)$_2$ molecule into a given state. At time zero, the feedback loop was opened at $I = 0.9\,\mathrm{nA}$ and $V = 1.0\,\mathrm{V}$. The tunneling current then increased in response to a progressive increase of the sample voltage from 1.0 to 1.9 V. While the sample voltage was 1.9 V, a certain number of switching events was monitored as abrupt changes in the tunneling current. Finally, when the desired state was reached (here C), the sample voltage was ramped down to 1.0 V. STM topographs were systematically acquired before (*e.g.*, Fig. 11.11b) and after (*e.g.* Figure 11.11c) switching, which allows to link a conductance state to a particular (topographic) state of the molecule. In the present example, the lower molecule is initially in state B (Figure 11.13b) corresponding to a given conductance (shown in black in Figure 11.13a). Upon switching, the conductance changes (shown in red in Figure 11.13a). With the help of an additional STM topograph, the red conductance state is associated to the molecule in state C. This correspondence between molecular and conductance states is in agreement with that inferred from Figure 11.10 and summarized in Table 11.1.

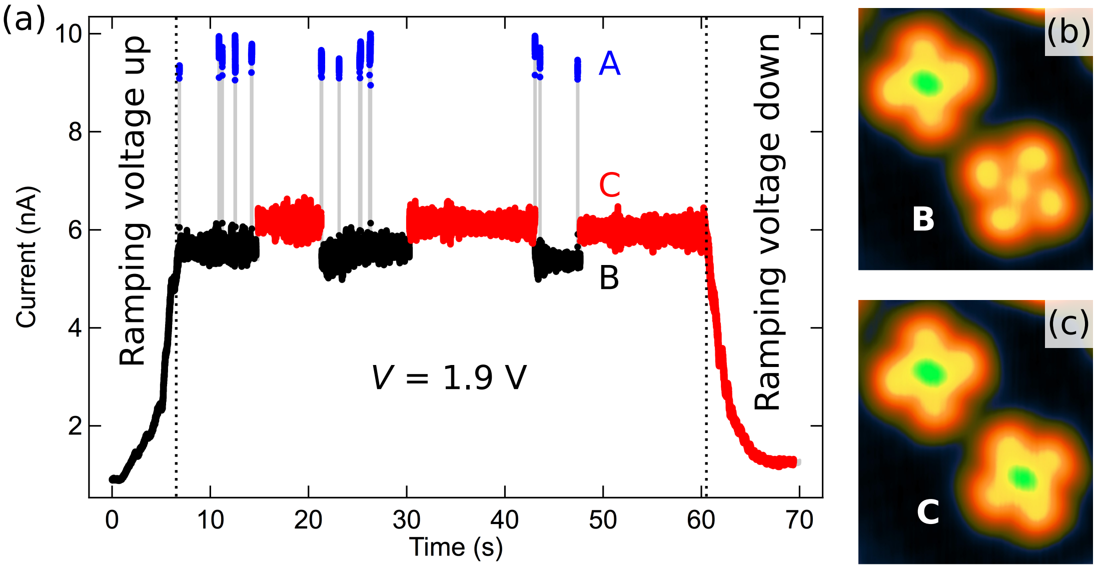

Figure 11.11.: (a) Current time series illustrating the preparation of a Fe(pap)$_2$ molecule from the B to C state. The feedback loop was opened at a current of 0.9 nA and a sample voltage of 1.0 V. STM topographs of two Fe(pap)$_2$ molecules (a) before and (b) after switching the lowest one from state B to C.

## 11.6.6. Analysis of current time-series

In the main manuscript, it is stated that the switching is robust, *i.e.*, it shows no sign of fatigue. Indeed, the current time-series shown in Figure 11.12a presents about 770 switching events. Nevertheless, the current levels of the different states at the end of the series do not significantly deviate from those at the beginning. In a histogram of current values (Figure 11.12b) this leads to three narrow peaks. To further characterize the peaks, they are fitted using Gaussians:

$$A \exp\left(-\left(\frac{x - x_0}{width}\right)^2\right), \tag{11.1}$$

where $x$ is the tunneling current. The parameters resulting from the the fits are summarized in Table 11.2. The positions of the peaks ($x_0$) represent the tunneling currents characteristic of the different molecular states, namely $2.416 + -0.002\,\mathrm{nA}$, $2.820 + -0.001\,\mathrm{nA}$ and $4.272 + -0.002\,\mathrm{nA}$ for states C, B, and A, respectively. Additionally, since the time interval between two points is constant ($\approx 145\,\mu\mathrm{s}$), the area of a given peak is directly related to the relative occupation of the corresponding state. As the peaks are Gaussians, the integral of each peak is the product $A \times width$. To obtain the relative occupation of a state this integral is normalized with the sum of all three integrals (Table 11.2). The highest relative occupation is found for state B (57 %).

To estimate individual transition probabilities, e.g., $r_{B\to C}$, the switching events from B to C were counted in Figure 11.12a and divided by the total duration of the time series. This leads to the average number of events per second. To arrive at the transition probability from B to C, one has to take into account the relative occupation of B, which describes the fact that the molecule is in state B only for a fraction of the entire time interval. The transition probability from B to C is then obtained by dividing the average number of B-to-C transitions by the relative occupation of B. Analogous operations performed for the other transitions lead to the following switching probabilities: $r_{A\to B} = 45.82\,\mathrm{s}^{-1}$; $r_{A\to C} = 1.00\,\mathrm{s}^{-1}$; $r_{B\to A} = 5.99\,\mathrm{s}^{-1}$; $r_{B\to C} = 0.27\,\mathrm{s}^{-1}$; $r_{C\to A} = 0.67\,\mathrm{s}^{-1}$ and $r_{C\to B} < 0.03\,\mathrm{s}^{-1}$.

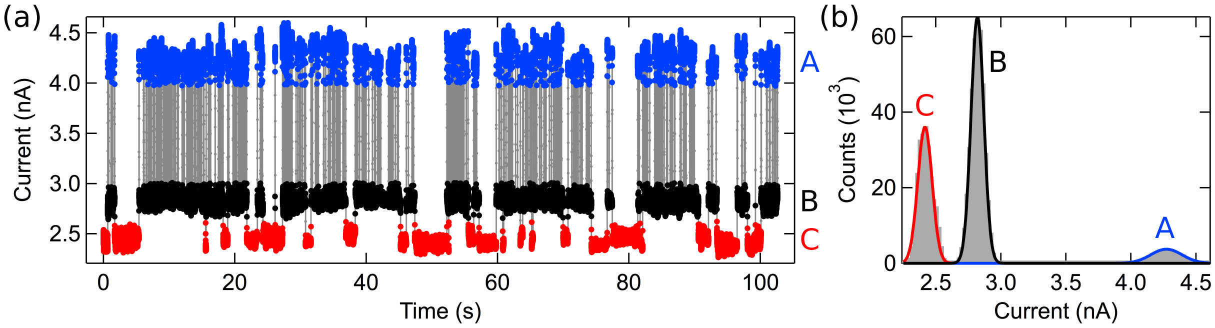

Figure 11.12.: (a) Tunneling current as a function of time at a sample voltage of 2.5 V with the tip over the center of a Fe(pap)$_2$ molecule. The colors of the points (red, black and blue) indicate the states of the molecules (C, B, and A, respectively). The feedback loop was opened at a current of 2.4 nA. (b) Histogram of the current data in (a) along with three fits according to Eq. 11.1. The fitted parameters are listed in Table 11.2.

| | State C | State B | State A |
|---|---|---|---|
| $A$ ($10^3$) | $36.1 + -1.3$ | $65.2 + -0.5$ | $3.7 + -0.1$ |
| $x_0$ (nA) | $2.416 + -0.002$ | $2.820 + -0.001$ | $4.272 + -0.002$ |
| *width* (nA) | $0.078 + -0.003$ | $0.070 + -0.001$ | $0.169 + -0.003$ |
| *relative occupation* (%) | 35 | 57 | 8 |

Table 11.2.: Result of the Gaussian fits shown in Figure 11.12b. The number in parenthesis indicate the uncertainty of the last digits given by the fitting procedure. The relative occupation is obtained as described in the text.

Only an upper limit is given for $r_{C\to B}$ as no direct C-to-B transition was observed. Note that these probabilities are valid for the tunneling conditions presented in Figure 11.12.

Similar analyses were made for time series as the one shown in Figure 11.11. These time series were acquired with a sample voltage of 1.9 V in contrast to the 2.5 V used in the previous series (Figure 11.12). The decrease of the sample voltage (while the tunneling current is larger) from 2.5 V (Figure 11.12) to 1.9 V (Figure 11.11) leads to a considerable reduction of the switching rate, from $7.32\,\mathrm{s}^{-1}$ to $0.70\,\mathrm{s}^{-1}$, *i.e.* by approximately one order of magnitude. The following switching probabilities are obtained: $r_{A\to B} = 36.31\,\mathrm{s}^{-1}$; $r_{A\to C} = 1.73\,\mathrm{s}^{-1}$; $r_{B\to A} = 0.55\,\mathrm{s}^{-1}$; $r_{B\to C} = 0.12\,\mathrm{s}^{-1}$; $r_{C\to A} = 0.09\,\mathrm{s}^{-1}$ and $r_{C\to B} < 0.03\,\mathrm{s}^{-1}$.

The switching probabilities from state B to A and from state C and A change considerably between the two experiments, suggesting that the mechanism at the origin of the corresponding switching is strongly voltage dependent.

### 11.6.7. Additional selective and deterministic switching of $Fe(pap)_2$

Figure 11.13 shows a time-lapse sequence of 11 STM topographs of two $Fe(pap)_2$ molecules on $Cu_2N/Cu(100)$. Between the acquisition of each topograph, the tip was placed over the center of one of the two molecule to switch it into the desired state. This sequence of topographs again exhibits the robust character of the switching. In addition, the tunneling parameters used in the present case to switch the molecule (about 2 V and 6 nA to 10 nA) lead to small lateral displacements of the molecules. Compare for instance Figure 11.13h to Figure 11.13j or Figure 11.13e to Figure 11.13k.

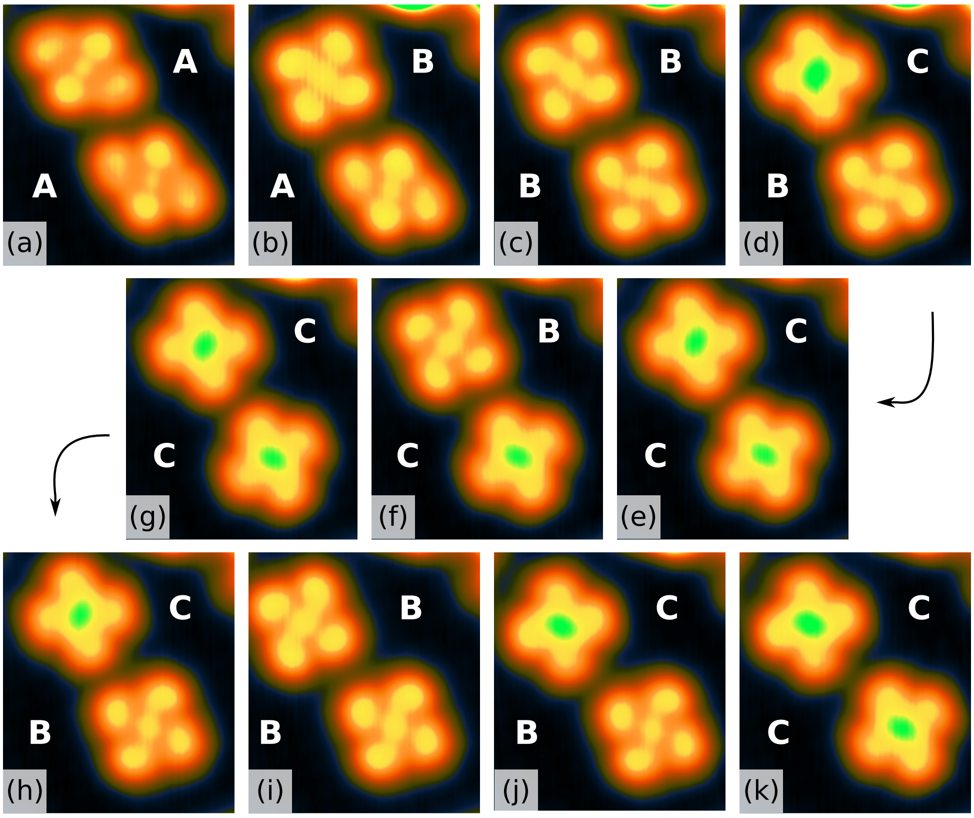

Figure 11.13.: STM topographs of two Fe(pap)$_2$ molecules selectively switched.

## 11.7. Acknowledgment

We acknowledge funding by the Deutsche Forschungsgemeinschaft via Sonderforschungsbereich 677.

## 11.8. Contributions

Hanne Jacob and Felix Tuczek synthesized the compound. I performed the measurements and enjoyed the support from Sujoy Karan. I along with Manuel Gruber (MG) analyzed the data and performed DFT calculations. MG wrote the first draft of the manuscript.[422] Richard Berndt supervised the project. All authors discussed the results and improved and commented on the manuscript.

# 12

# Concluding Remarks

Several aspects of molecules at metal electrodes are presented in this thesis exploring structural, electronic, and switching properties of molecules using a cryogenic STM in UHV. The results are summarized in the overview (Chap. 2) and in each chapter (Chaps. 5-11). I hope that they will contribute significantly to the understanding of molecular metal systems. Inspired by or based on the results of this thesis a few of my ideas for further research projects are presented in this final chapter. As ideas for projects with a platform molecule are most concrete, I will focus on them.

## Conductance of molecule-metal contacts

In this thesis the planar TOTA platform molecule is used as an anchor unit to place moieties in a vertical or inclined position on a metal substrate. Although this flat platform binds via physisorption, its $\pi$ system mediates an *extended* electrical contact to the metal. Moreover, the platform anchor group and pm-control of the electrode position lead to reproducible contacts and large conductance without requiring chemisorption. Hence, flat extended molecular units are an interesting alternative to the single-atom molecule-metal contacts that have been a focus of research so far.

Shot noise measurements along with DFT-NEGF calculations (not shown in this thesis, see Ref. 198) revealed that for a bare TOTA platform on Au(111) the electron transport is dominated by a fully open spin-degenerate channel (see Chap. 4.3.2 for a rudimentary introduction to transport channels). An eigenchannel usually gives a direct spatially resolved picture of the orbitals involved in the transport.[194] According to the calculations the dominant eigenchannel of the TOTA junction exhibits $\sigma$ symmetry. However, the available molecular orbitals of TOTA for electron transport exhibit $\pi$ symmetry and $\pi$-type channels contribute only a few percent to the conductance. This result indicates a filtering of the orbitals involved in the electron transport process. This orbital filtering may be caused by the predominant $s$ character of the Au apex atom.[198] In other words, the $s$ character of the current-carrying orbital of the tip and the $\pi$ character of the molecular orbitals may not match well for efficient electron transport.

I propose to measure with an STM the conductance of phenyl-TOTA or propynyl-TOTA on a metal such as Pt, which in contrast to Au has valence $d$ orbitals available for conductance.[228,LIII] Contacting the molecule with a tip of such a material may avoid orbital filtering, and may result in a much higher conductance. Break junction experiments at cryogenic temperature along with calculations of oligoacene molecules, *i. e.* flat extended $\pi$ systems, indeed suggest a drastically different conductance behavior for Pt and Ag electrodes.[228] In contrast to Ag-molecule contacts, the electron transmission through the Pt electrodes is reported to be band-like, *i. e.* molecular features in the transmission are smeared out, creating an energetically broad plateau of high transmission. Using an extended molecular anchor group that enables such band-like electric coupling at the molecule-metal interface may turn out to be less sensitive to geometric details of the interface. It may therefore help to create reproducible, stable, and reliable contacts to molecular circuits in future.

### Rotor molecules mounted on surfaces

This thesis presents two closely related molecular stepper motors that were designed to work on a metal substrate under excitation with tunneling electrons (Chap. 7). The motors are comprised of the TOTA platform as a stator and ethoxy and ethyl moieties as rotors. Although the resulting molecules exhibit no asymmetry, directional rotation was generated by interactions with the STM tip, which can be regarded as an external ligand. The natural continuation of these experiments would be to attach an asymmetric rotor on the TOTA platform. This asymmetry may lead to a build-in directionality of the rotation. Given the high scientific interest in molecular machines [LIV] and the only few examples of machines that are functioning on substrates, this project may contribute significantly to the understanding and future design of molecular machines.

### An alternative flat platform molecule

Although various interesting results of this thesis are obtained with TOTA derivatives, the TOTA platform is not an ideal anchor molecule, as different degrees of fragmentation were observed after deposition on Au(111), depending on the functional groups attached to the TOTA molecules.

The binding energies of the decomposition products to the Au surface essentially determine the molecular stability. This effect is undesirable and complicates the design of suitable platform derivatives that are stable upon adsorption.

An interesting alternative to TOTA is TOBTA (4,8,12-trioxa-12c-boratriangulen).[LV] The chemical structures of TOBTA and TOTA molecules differ only in the central atom. The central atom of TOBTA is a B atom. It is expected to be more reactive than the central C atom of TOTA. This expectation was confirmed by my preliminary STM results for the bare TOBTA on Au(111) (not shown). In contrast to TOTA molecules, TOBTA binds to step edges in an inclined position that probably enables the central B atom to form a chemical bond to the Au edge. Intriguingly, I was able to exploit the higher reactivity

---

[LIII] Preparation of *clean* Pt surfaces is challenging.

[LIV] The Nobel Prize in Chemistry 2016 was awarded jointly to Sauvage, Stoddart, and Feringa "for the design and synthesis of molecular machines."

[LV] The molecule was synthesized by Torben Jäkel und Rainer Herges.

to design a cluster most likely comprised of a TOBTA platform positioned parallel to the substrate and binds to a single Au atom on Au(111). This TOBTA/Au/Au(111) cluster was obtained after depositing a single Au atom from the tip and moving the atom with the tip first partly below a TOBTA molecule. After this step the TOBTA molecule was in an inclined position on the substrate. Further manipulation with the tip "pulls" the molecule in a parallel position. I suggest to continue such investigations of TOBTA. Especially, TOBTA clusters with different atoms such as Co, Ni, Ti etc. may exhibit interesting electronic structures. Moreover, it may be possible to attach a magnetic atom on top of TOBTA.

The higher reactivity may also enable an on-surface functionalization of TOBTA, *i. e.* an on-surface attachment of a desired moiety on the central B atom of TOBTA. According to chemical studies of Jäkel und Herges[LVI] the B atom of TOBTA is very reactive to nitrogen bases such as ammonia. I suggest to deposit pyrazine molecules on a TOBTA/Au(111) sample. This may lead to an on-surface functionalization of TOBTA with pyrazine. Pyrazine molecules are expected to desorb from the bare Au(111) at ambient temperature within hours.[447,448] This property may allow to prepare a sample of high quality, *i. e.* a sample that is free of all pyrazine molecules that did not form a bond to a TOBTA molecule. If successful, the project would be an important step to synthesize more advanced molecules on a substrate.

---

[LVI] Unpublished results.

# Acronyms

**AFM** atomic force microscopy

**DFT** density functional theory

**DOS** density of states

**ESID** electrospray-ionization deposition

**HOMO** highest-occupied molecular orbital

**HS** high spin

**IETS** inelastic electron tunneling spectroscopy

**LDOS** local density of states

**LUMO** lowest-unoccupied molecular orbital

**LS** low spin

**Me-TOTA** methyl-trioxatriangulenium

**ML** monolayer

**MODOS** molecular orbital density of states

**MPSH** molecular projected self-consistent Hamiltonian

**NEGF** nonequilibrium Green's function

**pap** N-2-pyridylmethylidene-2-hydroxyphenylaminato ligand

**P-TOTA** propynyl-trioxatriangulenium

**RTM** Rastertunnelmikroskopie oder Rastertunnelmikroskop

**SCO** spin crossover

**STS** scanning tunneling spectroscopy

**STM** scanning tunneling microscopy or scanning tunneling microscope

**TOTA** trioxatriangulenium

**UHV** ultra-high vacuum

**vDOS** vibrational density of states

# Bibliography

[1] United Nations. *Ending Poverty.* https://www.un.org/en/global-issues/ending-poverty, (2020).

[2] United Nations. *Children.* https://www.un.org/en/global-issues/children, (2020).

[3] United Nations. *Water.* https://www.un.org/en/global-issues/water, (2020).

[4] J. R. Rumble, editor. *CRC Handbook of Chemistry and Physics, 100th Edition.* Taylor & Francis Ltd. (2019).

[5] L. Sosa-Vargas, E. Kim, and A.-J. Attias. Beyond "decorative" 2D supramolecular self-assembly: strategies towards functional surfaces for nanotechnology. *Mater. Horiz.* **4**, 570 (2017).

[6] F. Ghilini, D. E. Pissinis, A. Miñán, P. L. Schilardi, and C. Diaz. How Functionalized Surfaces Can Inhibit Bacterial Adhesion and Viability. *ACS Biomater. Sci. Eng.* **5**, 4920 (2019).

[7] K.-Y. Chen, O. Ivashenko, G. T. Carroll, J. Robertus, J. C. M. Kistemaker, G. London, W. R. Browne, P. Rudolf, and B. L. Feringa. Control of Surface Wettability Using Tripodal Light-Activated Molecular Motors. *J. Am. Chem. Soc.* **136**, 3219 (2014).

[8] A. S. Goldmann, N. R. B. Boase, L. Michalek, J. P. Blinco, A. Welle, and C. Barner-Kowollik. Adaptable and reprogrammable surfaces. *Adv. Mater.* **31**, 1902665 (2019).

[9] D. Lensen and J. A. A. W. Elemans. Artificial molecular rotors and motors on surfaces: STM reveals and triggers. *Soft Matter* **8**, 9053 (2012).

[10] S. Kassem, T. van Leeuwen, A. S. Lubbe, M. R. Wilson, B. L. Feringa, and D. A. Leigh. Artificial molecular motors. *Chem. Soc. Rev.* **46**, 2592 (2017).

[11] C. Ni and J.-Z. Wang. STM sudies on molecular rotors and motors. *Surf. Rev. Lett.* **25**, 1841004 (2018).

[12] A. Aviram and M. A. Ratner. Molecular rectifiers. *Chem. Phys. Lett.* **29**, 277 (1974).

[13] A. Nitzan and M. A. Ratner. Electron transport in molecular wire junctions. *Science* **300**, 1385 (2003).

[14] N. J. Tao. Electron transport in molecular junctions. *Nat. Nanotechnol.* **1**, 173 (2006).

[15] F. Chen, J. Hihath, Z. Huang, X. Li, and N. Tao. Measurement of single-molecule conductance. *Annu. Rev. Phys. Chem.* **58**, 535 (2007).

[16] M. Kiguchi and S. Kaneko. Electron transport through single $\pi$-conjugated molecules bridging between metal electrodes. *ChemPhysChem* **13**, 1116 (2012).

[17] E. Leary, A. L. Rosa, M. T. González, G. Rubio-Bollinger, N. Agraït, and N. Martín. Incorporating single molecules into electrical circuits. the role of the chemical anchoring group. *Chem. Soc. Rev.* **44**, 920 (2015).

[18] T. Esat, N. Friedrich, F. S. Tautz, and R. Temirov. A standing molecule as a single-electron field emitter. *Nature* **558**, 573 (2018).

[19] B. Chen and K. Xu. Single Molecule-Based Electronic Devices: A Review. *Nano* **14**, 1930007 (2019).

[20] L. Bogani and W. Wernsdorfer. Molecular spintronics using single-molecule magnets. *Nature Mater.* **7**, 179 (2008).

[21] V. A. Dediu, L. E. Hueso, I. Bergenti, and C. Taliani. Spin Routes in Organic Semiconductors. *Nat. Mater.* **8**, 707 (2009).

[22] E. Moreno-Pineda, C. Godfrin, F. Balestro, W. Wernsdorfer, and M. Ruben. Molecular spin qudits for quantum algorithms. *Chem. Soc. Rev.* **47**, 501 (2018).

[23] K. S. Kumar and M. Ruben. Emerging trends in spin crossover (SCO) based functional materials and devices. *Coord. Chem. Rev.* **346**, 176 (2017).

[24] C. Barraud, P. Seneor, R. Mattana, S. Fusil, K. Bouzehouane, C. Deranlot, P. Graziosi, L. Hueso, I. Bergenti, V. Dediu, F. Petroff, and A. Fert. Unravelling the Role of the Interface for Spin Injection Into Organic Semiconductors. *Nat. Phys.* **6**, 615 (2010).

[25] K. V. Raman, A. M. Kamerbeek, A. Mukherjee, N. Atodiresei, T. K. Sen, P. Lazić, V. Caciuc, R. Michel, D. Stalke, S. K. Mandal, S. Blügel, M. Münzenberg, and J. S. Moodera. Interface-Engineered Templates for Molecular Spin Memory Devices. *Nature* **493**, 509 (2013).

[26] F. Djeghloul, F. Ibrahim, M. Cantoni, M. Bowen, L. Joly, S. Boukari, P. Ohresser, F. Bertran, P. Le Fèvre, P. Thakur, F. Scheurer, T. Miyamachi, R. Mattana, P. Seneor, A. Jaafar, C. Rinaldi, S. Javaid, J. Arabski, J.-P. Kappler, W. Wulfhekel, N. B. Brookes, R. Bertacco, A. Taleb-Ibrahimi, M. Alouani, E. Beaurepaire, and W. Weber. Direct Observation of a Highly Spin-Polarized Organic Spinterface at Room Temperature. *Sci. Rep.* **3**, 1272 (2013).

[27] S. Steil, N. Großmann, M. Laux, A. Ruffing, D. Steil, M. Wiesenmayer, S. Mathias, O. L. A. Monti, M. Cinchetti, and M. Aeschlimann. Spin-Dependent Trapping of Electrons at Spinterfaces. *Nat. Phys.* **9**, 242 (2013).

[28] K. V. Raman. Interface-assisted molecular spintronics. *Appl. Phys. Rev.* **1**, 031101 (2014).

[29] M. Gruber, F. Ibrahim, S. Boukari, H. Isshiki, L. Joly, M. Peter, M. Studniarek, V. Da Costa, H. Jabbar, V. Davesne, U. Halisdemir, J. Chen, J. Arabski, E. Otero, F. Choueikani, K. Chen, P. Ohresser, W. Wulfhekel, F. Scheurer, W. Weber, M. Alouani, E. Beaurepaire, and M. Bowen. Exchange Bias and Room-Temperature Magnetic Order in Molecular Layers. *Nat. Mater.* **14**, 981 (2015).

[30] S. Heutz. Molecular Spintronics: A Warm Exchange. *Nat. Mater.* **14**, 967 (2015).

[31] K. Bairagi, A. Bellec, V. Repain, C. Chacon, Y. Girard, Y. Garreau, J. Lagoute, S. Rousset, R. Breitwieser, Y.-C. Hu, Y. C. Chao, W. W. Pai, D. Li, A. Smogunov, and C. Barreteau. Tuning the Magnetic Anisotropy at a Molecule-Metal Interface. *Phys. Rev. Lett.* **114**, 247203 (2015).

[32] C. Barraud, K. Bouzehouane, C. Deranlot, S. Fusil, H. Jabbar, J. Arabski, R. Rakshit, D.-J. Kim, C. Kieber, S. Boukari, M. Bowen, E. Beaurepaire, P. Seneor, R. Mattana, and F. Petroff. Unidirectional Spin-Dependent Molecule-Ferromagnet Hybridized States Anisotropy in Cobalt Phthalocyanine Based Magnetic Tunnel Junctions. *Phys. Rev. Lett.* **114**, 206603 (2015).

[33] F. Djeghloul, M. Gruber, E. Urbain, D. Xenioti, L. Joly, S. Boukari, J. Arabski, H. Bulou, F. Scheurer, F. Bertran, P. Le Fèvre, A. Taleb-Ibrahimi, W. Wulfhekel, G. Garreau, S. Hajjar-Garreau, P. Wetzel, M. Alouani, E. Beaurepaire, M. Bowen, and W. Weber. High Spin Polarization at Ferromagnetic Metal-Organic Interfaces: A Generic Property. *J. Phys. Chem. Lett.* **7**, 2310 (2016).

[34] C. Barraud, K. Bouzehouane, C. Deranlot, D. J. Kim, R. Rakshit, S. Shi, J. Arabski, M. Bowen, E. Beaurepaire, S. Boukari, F. Petroff, P. Seneor, and R. Mattana. Phthalocyanine Based Molecular Spintronic Devices. *Dalton Trans.* **45**, 16694 (2016).

[35] S. Karan, N. Li, Y. Zhang, Y. He, I.-P. Hong, H. Song, J.-T. Lü, Y. Wang, L. Peng, K. Wu, G. S. Michelitsch, R. J. Maurer, K. Diller, K. Reuter, A. Weismann, and R. Berndt. Spin Manipulation by Creation of Single-Molecule Radical Cations. *Phys. Rev. Lett.* **116**, 027201 (2016).

[36] K. Moth-Poulsen and T. Bjørnholm. Molecular electronics with single molecules in solid-state devices. *Nat. Nanotechnol.* **4**, 551 (2009).

[37] F. von Wrochem, D. Gao, F. Scholz, H.-G. Nothofer, G. Nelles, and J. M. Wessels. Efficient electronic coupling and improved stability with dithiocarbamate-based molecular junctions. *Nat. Nanotechnol.* **5**, 618 (2010).

[38] L. Sun, Y. A. Diaz-Fernandez, T. A. Gschneidtner, F. Westerlund, S. Lara-Avila, and K. Moth-Poulsen. Single-molecule electronics: From chemical design to functional devices. *Chem. Soc. Rev.* **43**, 7378 (2014).

[39] V. Kaliginedi, A. V. Rudnev, P. Moreno-Garcia, M. Baghernejad, C. Huang, W. Hong, and T. Wandlowski. Promising anchoring groups for single-molecule conductance measurements. *Phys. Chem. Chem. Phys.* **16**, 23529 (2014).

[40] M. Valášek, M. Lindner, and M. Mayor. Rigid multipodal platforms for metal surfaces. *Beilstein J. Nanotechnol.* **7**, 374 (2016).

[41] M. Valášek and M. Mayor. Spatial and lateral control of functionality by rigid molecular platforms. *Chem. Eur. J.* **23**, 13538 (2017).

[42] B. Baisch, D. Raffa, U. Jung, O. M. Magnussen, C. Nicolas, J. Lacour, J. Kubitschke, and R. Herges. Mounting freestanding molecular functions onto surfaces: The platform approach. *J. Am. Chem. Soc.* **131**, 442 (2009).

[43] L. A. Zotti, T. Kirchner, J.-C. Cuevas, F. Pauly, T. Huhn, E. Scheer, and A. Erbe. Revealing the role of anchoring groups in the electrical conduction through single-molecule junctions. *Small* **6**, 1529 (2010).

[44] Z. Wei, X. Wang, A. Borges, M. Santella, T. Li, J. K. Sørensen, M. Vanin, W. Hu, Y. Liu, J. Ulstrup, G. C. Solomon, Q. Chi, T. Bjørnholm, K. Nørgaard, and B. W. Laursen. Triazatriangulene as binding group for molecular electronics. *Langmuir* **30**, 14868 (2014).

[45] N. Hauptmann, L. Groß, K. Buchmann, K. Scheil, C. Schütt, F. L. Otte, R. Herges, C. Herrmann, and R. Berndt. High-conductance surface-anchoring of a mechanically flexible platform-based porphyrin complex. *New J. Phys.* **17**, 013012 (2015).

[46] A. J. Heinrich. Single-Atom Spin-Flip Spectroscopy. *Science* **306**, 466 (2004).

[47] J. Repp, G. Meyer, S. M. Stojković, A. Gourdon, and C. Joachim. Molecules on Insulating Films: Scanning-Tunneling Microscopy Imaging of Individual Molecular Orbitals. *Phys. Rev. Lett.* **94**, 026803 (2005).

[48] J. Repp and G. Meyer. Scanning tunneling microscopy of adsorbates on insulating films. from the imaging of individual molecular orbitals to the manipulation of the charge state. *Appl. Phys. A* **85**, 399 (2006).

[49] C. F. Hirjibehedin, C.-Y. Lin, A. F. Otte, M. Ternes, C. P. Lutz, B. A. Jones, and A. J. Heinrich. Large Magnetic Anisotropy of a Single Atomic Spin Embedded in a Surface Molecular Network. *Science* **317**, 1199 (2007).

[50] T. L. Cocker, D. Peller, P. Yu, J. Repp, and R. Huber. Tracking the ultrafast motion of a single molecule by femtosecond orbital imaging. *Nature* **539**, 263 (2016).

[51] F. Schwarz and E. Lörtscher. Break-junctions for investigating transport at the molecular scale. *J. Phys.: Condens. Matter* **26**, 474201 (2014).

[52] R. Quan, C. S. Pitler, M. A. Ratner, and M. G. Reuter. Quantitative Interpretations of Break Junction Conductance Histograms in Molecular Electron Transport. *ACS Nano* **9**, 7704 (2015).

[53] J. M. Hamill, X. T. Zhao, G. Mészáros, M. R. Bryce, and M. Arenz. Fast Data Sorting with Modified Principal Component Analysis to Distinguish Unique Single Molecular Break Junction Trajectories. *Phys. Rev. Lett.* **120**, 016601 (2018).

[54] F. Evers, R. Korytár, S. Tewari, and J. M. van Ruitenbeek. Advances and challenges in single-molecule electron transport. *Rev. Mod. Phys.* **92**, 035001 (2020).

[55] M. Ruben and K. S. Kumar. Sublimable Spin Crossover Complexes: From Spin-State Switching to Molecular Devices. Angew. Chem. Int. Ed. 10.1002/anie.201911256, (2019).

[56] R. Schuhmann. Scanning probe microscopy: From sublime to ubiquitous. https://journals.aps.org/prl/scanning-probe-microscopy, (2016).

[57] T. Knaak. *Scanning tunneling microscopy of cobalt and iron complexes on metal surfaces.* PhD thesis, Christian-Albrechts-Universität zu Kiel, (2017).

[58] J. K. Gimzewski. Nanoscale science of single molecules using local probes. *Science* **283**, 1683 (1999).

[59] J. V. Barth. Molecular architectonic on metal surfaces. *Annu. Rev. Phys. Chem.* **58**, 375 (2007).

[60] D. P. Goronzy, M. Ebrahimi, F. Rosei, Arramel, Y. Fang, S. D. Feyter, S. L. Tait, C. Wang, P. H. Beton, A. T. S. Wee, P. S. Weiss, and D. F. Perepichka. Supramolecular assemblies on surfaces: Nanopatterning, functionality, and reactivity. *ACS Nano* **12**,

7445 (2018).

[61] G. Reecht, B. W. Heinrich, H. Bulou, F. Scheurer, L. Limot, and G. Schull. Imaging isodensity contours of molecular states with STM. *New J. Phys.* **19**, 113033 (2017).

[62] C. Joachim, J. K. Gimzewski, R. R. Schlittler, and C. Chavy. Electronic Transparence of a Single C 60 Molecule. *Phys. Rev. Lett.* **74**, 2102 (1995).

[63] N. Nèel, J. Kröger, L. Limot, T. Frederiksen, M. Brandbyge, and R. Berndt. Controlled Contact to a C 60 Molecule. *Phys. Rev. Lett.* **98**, 065502 (2007).

[64] J. Kröger, N. Néel, and L. Limot. Contact to single atoms and molecules with the tip of a scanning tunnelling microscope. *J. Phys.: Condens. Matter* **20**, 223001 (2008).

[65] R. Wiesendanger, H.-J. Güntherodt, G. Güntherodt, R. J. Gambino, and R. Ruf. Observation of vacuum tunneling of spin-polarized electrons with the scanning tunneling microscope. *Phys. Rev. Lett.* **65**, 247 (1990).

[66] J. Brede and R. Wiesendanger. Spin-resolved imaging and spectroscopy of individual molecules with sub-molecular spatial resolution. *MRS Bulletin* **39**, 608 (2014).

[67] Z. Huang, Y. Zhang, Y. He, H. Song, C. Yin, and K. Wu. A chemist's overview of surface electron spins. *Chem. Soc. Rev.* **46**, 1955 (2017).

[68] W. Meissner and B. Voigt. Messungen mit Hilfe von flüssigem Helium XI Widerstand der reinen Metalle in tiefen Temperaturen. *Ann. Phys.* **399**, 761 (1930).

[69] J. Kondo. Effect of ordinary scattering on exchange scattering from magnetic impurity in metals. *Phys. Rev.* **169**, 437 (1968).

[70] J. Li, W.-D. Schneider, R. Berndt, and B. Delley. Kondo Scattering Observed at a Single Magnetic Impurity. *Phys. Rev. Lett.* **80**, 2893 (1998).

[71] V. Madhavan, W. Chen, T. Jamneala, M. F. Crommie, and N. S. Wingreen. Tunneling into a single magnetic atom: Spectroscopic evidence of the Kondo resonance. *Science* **280**, 567 (1998).

[72] P. Wahl, L. Diekhöner, G. Wittich, L. Vitali, M. A. Schneider, and K. Kern. Kondo effect of molecular complexes at surfaces: Ligand control of the local spin coupling. *Phys. Rev. Lett.* 95 (2005).

[73] A. Zhao, Q. Li, L. Chen, H. Xiang, W. Wang, S. Pan, B. Wang, X. Xiao, J. Yang, J. G. Hou, and Q. Zhu. Controlling the Kondo effect of an adsorbed magnetic ion through its chemical bonding. *Science* **309**, 1542 (2005).

[74] M. Ternes. Spin excitations and correlations in scanning tunneling spectroscopy. *New J. Phys.* **17**, 063016 (2015).

[75] C. Iacovita, M. V. Rastei, B. W. Heinrich, T. Brumme, J. Kortus, L. Limot, and J. P. Bucher. Visualizing the spin of individual cobalt-phthalocyanine molecules. *Phys. Rev. Lett.* 101 (2008).

[76] J. A. Stroskio and D. M. Eigler. Atomic and molecular manipulation with the scanning tunneling microscope. *Science* **254**, 1319 (1991).

[77] S.-W. Hla. Scanning tunneling microscopy single atom/molecule manipulation and its application to nanoscience and technology. *Vac. Sci. Technol. B* **23**, 1351 (2005).

[78] J. L. Zhang, J. Q. Zhong, J. D. Lin, W. P. Hu, K. Wu, G. Q. Xu, A. T. S. Wee, and

W. Chen. Towards single molecule switches. *Chem. Soc. Rev.* **44**, 2998 (2015).

[79] S.-W. Hla and K.-H. Rieder. STM control of chemical reactions: Single-molecule synthesis. *Annu. Rev. Phys. Chem.* **54**, 307 (2003).

[80] C. Wang, L. Chi, A. Ciesielski, and P. Samorì. Chemical synthesis at surfaces with atomic precision: Taming complexity and perfection. *Angew. Chem. Int. Ed.* **58**, 18758 (2019).

[81] B. C. Stipe. Single-Molecule Vibrational Spectroscopy and Microscopy. *Science* **280**, 1732 (1998).

[82] S. You, J.-T. Lü, J. Guo, and Y. Jiang. Recent advances in inelastic electron tunneling spectroscopy. *Adv. Phys. X* **2**, 907 (2017).

[83] G. Binnig, C. F. Quate, and C. Gerber. Atomic force microscope. *Phys. Rev. Lett.* **56**, 930 (1986).

[84] F. J. Giessibl. Advances in atomic force microscopy. *Rev. Mod. Phys.* **75**, 949 (2003).

[85] T. L. Lemke, V. F. Roche, and S. W. Zito. *Review of Organic Functional Groups: Introduction to Medicinal Organic Chemistry.* Lippincott Williams & Wilkins, Baltimore (2012).

[86] S. Kuhn, B. Baisch, U. Jung, T. Johannsen, J. Kubitschke, R. Herges, and O. Magnussen. Self-assembly of triazatriangulenium-based functional adlayers on Au(111) surfaces. *Phys. Chem. Chem. Phys.* **12**, 4481 (2010).

[87] F. L. Otte, S. Lemke, C. Schütt, N. R. Krekiehn, U. Jung, O. M. Magnussen, and R. Herges. Ordered monolayers of free-standing porphyrins on gold. *J. Am. Chem. Soc.* **136**, 11248 (2014).

[88] M. Hammerich, T. Rusch, N. R. Krekiehn, A. Bloedorn, O. M. Magnussen, and R. Herges. Imine-Functionalized Triazatriangulenium Platforms: Towards an Artificial Ciliated Epithelium. *ChemPhysChem* **17**, 1870 (2016).

[89] R. Löw, T. Rusch, F. Röhricht, O. Magnussen, and R. Herges. Diazocine-functionalized TATA platforms. *Beilstein J. Org. Chem.* **15**, 1485 (2019).

[90] R. Löw, T. Rusch, T. Moje, F. Röhricht, O. M. Magnussen, and R. Herges. Norbornadiene-functionalized triazatriangulenium and trioxatriangulenium platforms. *Beilstein J. Org. Chem.* **15**, 1815 (2019).

[91] T. R. Rusch, A. Schlimm, N. R. Krekiehn, B. M. Flöser, F. Röhricht, M. Hammerich, I. Lautenschläger, T. Strunskus, R. Herges, F. Tuczek, and O. M. Magnussen. Ordered adlayers of a combined lateral switch and rotor. *J. Phys. Chem. C* **123**, 13720 (2019).

[92] A. Schlimm, R. Löw, T. Rusch, F. Röhricht, T. Strunskus, T. Tellkamp, F. Sönnichsen, U. Manthe, O. Magnussen, F. Tuczek, and R. Herges. Long-Distance Rate Acceleration by Bulk Gold. *Angew. Chem. Int. Ed.* **58**, 6574 (2019).

[93] U. Jung, O. Filinova, S. Kuhn, D. Zargarani, C. Bornholdt, R. Herges, and O. Magnussen. Photoswitching behavior of azobenzene-containing alkanethiol self-assembled monolayers on Au surfaces. *Langmuir* **26**, 13913 (2010).

[94] U. Jung, S. Kuhn, U. Cornelissen, F. Tuczek, T. Strunskus, V. Zaporojtchenko, J. Kubitschke, R. Herges, and O. Magnussen. Azobenzene-Containing Triazatriangulenium Adlayers on Au(111): Structural and Spectroscopic Characterization. *Langmuir* **27**,

5899 (2011).

[95] U. Jung, J. Kubitschke, R. Herges, and O. Magnussen. Studies of the molecular switching of azobenzene-functionalized platform adlayers on Au(111) by chronoamperometry. *Electrochim. Acta* **112**, 869 (2013).

[96] H. Jacob, S. Ulrich, U. Jung, S. Lemke, T. Rusch, C. Schütt, F. Petersen, T. Strunskus, O. Magnussen, R. Herges, and F. Tuczek. Monitoring the reversible photoisomerization of an azobenzene-functionalized molecular triazatriangulene platform on au(111) by IRRAS. *Phys. Chem. Chem. Phys.* **16**, 22643 (2014).

[97] S. Lemke, S. Ulrich, F. Claußen, A. Bloedorn, U. Jung, R. Herges, and O. M. Magnussen. Triazatriangulenium adlayers on Au(111): Superstructure as a function of alkyl side chain length. *Surf. Sci.* **632**, 71 (2015).

[98] M. Hammerich and R. Herges. Laterally mounted azobenzenes on platforms. *J. Org. Chem.* **80**, 11233 (2015).

[99] S. Lemke, C.-H. Chang, U. Jung, and O. M. Magnussen. Reversible potential-induced switching of alkyl chain aggregation in octyl-triazatriangulenium adlayers on Au(111). *Langmuir* **31**, 3115 (2015).

[100] N. R. Krekiehn, M. Müller, U. Jung, S. Ulrich, R. Herges, and O. M. Magnussen. UV/Vis spectroscopy studies of the photoisomerization kinetics in self-assembled azobenzene-containing adlayers. *Langmuir* **31**, 8362 (2015).

[101] S. Ulrich, U. Jung, T. Strunskus, C. Schütt, A. Bloedorn, S. Lemke, E. Ludwig, L. Kipp, F. Faupel, O. Magnussen, and R. Herges. X-ray spectroscopy characterization of azobenzene-functionalized triazatriangulenium adlayers on Au(111) surfaces. *Phys. Chem. Chem. Phys.* **17**, 17053 (2015).

[102] T. R. Rusch, M. Hammerich, R. Herges, and O. M. Magnussen. Molecular platforms as versatile building blocks for multifunctional photoswitchable surfaces. *Chem. Commun.* **55**, 9511 (2019).

[103] P. Gütlich and H. A. Goodwin. Spin crossover—an overall perspective. In *Topic in Current Chemistry*, pages 1–47. Springer Berlin Heidelberg, (2004).

[104] A. Bellec, J. Lagoute, and V. Repain. Molecular electronics: Scanning tunneling microscopy and single-molecule devices. *C. R. Chimie* **21**, 1287 (2018).

[105] S. Hayami, Z.-z. Gu, M. Shiro, Y. Einaga, A. Fujishima, and O. Sato. First Observation of Light-Induced Excited Spin State Trapping for an Iron(III) Complex. *J. Am. Chem. Soc.* **122**, 7126 (2000).

[106] E. Wiberg, N. Wiberg, and A. F. Holleman. *Holleman-Wiberg's Inorganic Chemistry.* Academic Press, San Diego (2001).

[107] T. G. Gopakumar, F. Matino, H. Naggert, A. Bannwarth, F. Tuczek, and R. Berndt. Electron-Induced Spin Crossover of Single Molecules in a Bilayer on Gold. *Angew. Chem., Int. Ed.* **51**, 6262–6266 (2012).

[108] T. Miyamachi, M. Gruber, V. Davesne, M. Bowen, S. Boukari, L. Joly, F. Scheurer, G. Rogez, T. K. Yamada, P. Ohresser, E. Beaurepaire, and W. Wulfhekel. Robust Spin Crossover and Memristance Across a Single Molecule. *Nat. Commun.* **3**, 938 (2012).

[109] G. Binnig, H. Rohrer, C. Gerber, and E. Weibel. Tunneling through a controllable

vacuum gap. *Appl. Phys. Lett.* **40**, 178 (1982).

[110] G. Binnig, H. Rohrer, C. Gerber, and E. Weibel. Surface Studies by Scanning Tunneling Microscopy. *Phys. Rev. Lett.* **49**, 57 (1982).

[111] C. J. Chen. *Introduction To Scanning Tunneling Microscopy.* Oxford University Press (1993).

[112] R. Wiesendanger. *Scanning Probe Microscopy. Methods and Applications.* Cambridge University Press (1994).

[113] J. Tersoff and D. R. Hamann. Theory and Application for the Scanning Tunneling Microscope. *Phys. Rev. Lett.* **50**, 1998 (1983).

[114] J. Tersoff and D. R. Hamann. Theory of the scanning tunneling microscope. *Phys. Rev. B* **31**, 805 (1985).

[115] J. Bardeen. Tunnelling from a Many-Particle Point of View. *Phys. Rev. Lett.* **6**, 57 (1961).

[116] C. J. Chen. Perturbation approach for quantum transmission. *Mod. Phys. Lett. B* **05**, 107 (1991).

[117] C. J. Chen. Origin of atomic resolution on metal surfaces in scanning tunneling microscopy. *Phys. Rev. Lett.* **65**, 448 (1990).

[118] C. J. Chen. Tunneling matrix elements in three-dimensional space: The derivative rule and the sum rule. *Phys. Rev. B* **42**, 8841 (1990).

[119] P. K. Hansma and J. Tersoff. Scanning tunneling microscopy. *J. Appl. Phys.* **61**, R1 (1987).

[120] R. Berndt, J. Gimzewski, and R. Schlittler. Bias-dependent STM images of oxygen-induced structures on Ti(0001) facets. *Surf. Sci.* **310**, 85 (1994).

[121] R. Wiesendanger. Spin mapping at the nanoscale and atomic scale. *Rev. Mod. Phys.* **81**, 1495 (2009).

[122] J. Klein, A. Léger, M. Belin, D. Défourneau, and M. J. L. Sangster. Inelastic-Electron-Tunneling Spectroscopy of Metal-Insulator-Metal Junctions. *Phys. Rev. B* **7**, 2336 (1973).

[123] M. Gruber, A. Weismann, and R. Berndt. The Kondo resonance line shape in scanning tunnelling spectroscopy: instrumental aspects. *J. Phys.: Condens. Matter* **30**, 424001 (2018).

[124] M. Ziegler, N. Néel, A. Sperl, J. Kröger, and R. Berndt. Local density of states from constant-current tunneling spectra. *Phys. Rev. B* **80**, 125402 (2009).

[125] H. Zheng, J. Kröger, and R. Berndt. Spectroscopy of Single Donors at ZnO(0001) Surfaces. *Phys. Rev. Lett.* 108 (2012).

[126] A. J. Mayne, G. Dujardin, G. Comtet, and D. Riedel. Electronic Control of Single-Molecule Dynamics. *Chem. Rev.* **106**, 4355 (2006).

[127] B. C. Stipe, M. A. Rezaei, and W. Ho. Coupling of vibrational excitation to the rotational motion of a single adsorbed molecule. *Phys. Rev. Lett.* **81**, 1263 (1998).

[128] W. Ho. Single-molecule chemistry. *J. Chem. Phys.* **117**, 11033 (2002).

[129] Y. Kim, K. Motobayashi, T. Frederiksen, H. Ueba, and M. Kawai. Action spectroscopy for single-molecule reactions – experiments and theory. *Prog. Surf. Sci.* **90**, 85 (2015).

[130] K. Motobayashi, Y. Kim, H. Ueba, and M. Kawai. Insight into action spectroscopy for single molecule motion and reactions through inelastic electron tunneling. *Phys. Rev. Lett.* **105**, 076101 (2010).

[131] T. Frederiksen, M. Paulsson, and H. Ueba. Theory of action spectroscopy for single-molecule reactions induced by vibrational excitations with STM. *Phys. Rev. B* **89**, 035427 (2014).

[132] M. Kawai, T. Komeda, Y. Kim, Y. Sainoo, and S. Katano. Single-molecule reactions and spectroscopy via vibrational excitation. *Phil. Trans. R. Soc. Lond. A* **362**, 1163 (2004).

[133] Y. S. Choi, T.-S. Kim, H. Petek, K. Yoshihara, and R. L. Christensen. Evidence for quantization of the transition state for cis-trans isomerization. *J. Chem. Phys.* **100**, 9269 (1994).

[134] M. Becker and R. Berndt. Influence of band structure on the apparent barrier height in scanning tunneling microscopy. *Phys. Rev. B* 81 (2010).

[135] J. G. Simmons. Electric Tunnel Effect between Dissimilar Electrodes Separated by a Thin Insulating Film. *J. Appl. Phys.* **34**, 2581 (1963).

[136] J. G. Simmons. Generalized Formula for the Electric Tunnel Effect between Similar Electrodes Separated by a Thin Insulating Film. *J. Appl. Phys.* **34**, 1793 (1963).

[137] M. Becker and R. Berndt. Contrast inversion of the apparent barrier height of Pb thin films in scanning tunneling microscopy. *Appl. Phys. Lett.* **96**, 033112 (2010).

[138] N. Noei, A. Weismann, and R. Berndt. Apparent tunneling barrier height and local work function of atomic arrays. *Beilstein J Nanotechnol.* **9**, 3048 (2018).

[139] J. Kröger, H. Jensen, and Berndt. Conductance of tip–surface and tip–atom junctions on Au(111) explored by a scanning tunnelling microscope. *New J. Phys.* **9**, 153 (2007).

[140] T. Jasper-Tönnies, A. Garcia-Lekue, T. Frederiksen, S. Ulrich, R. Herges, and R. Berndt. Conductance of a freestanding conjugated molecular wire. *Phys. Rev. Lett.* **119**, 066801 (2017).

[141] T. Jasper-Tönnies, A. Garcia-Lekue, T. Frederiksen, S. Ulrich, R. Herges, and R. Berndt. High-conductance contacts to functionalized molecular platforms physisorbed on Au(111). *J. Phys.: Condens. Matter* **31**, 18LT01 (2019).

[142] G. Schull, T. Frederiksen, M. Brandbyge, and R. Berndt. Passing Current through Touching Molecules. *Phys. Rev. Lett.* **103**, 206803 (2009).

[143] G. Schull, T. Frederiksen, A. Arnau, D. Sánchez-Portal, and R. Berndt. Atomic-scale engineering of electrodes for single-molecule contacts. *Nat. Nanotechnol.* **6**, 23 (2010).

[144] N. Hauptmann, F. Mohn, L. Gross, G. Meyer, T. Frederiksen, and R. Berndt. Force and conductance during contact formation to a C 60 molecule. *New J. Phys.* **14**, 073032 (2012).

[145] T. Frederiksen, G. Foti, F. Scheurer, V. Speisser, and G. Schull. Chemical control of electrical contact to $sp^2$ carbon atoms. *Nat. Commun.* **5**, 4659 (2014).

[146] M. Ratner. A brief history of molecular electronics. *Nat. Nanotech.* **8**, 378 (2013).

[147] M. S. Inkpen, M. Lemmer, N. Fitzpatrick, D. C. Milan, R. J. Nichols, N. J. Long, and T. Albrecht. New Insights into Single-Molecule Junctions Using a Robust, Unsupervised Approach to Data Collection and Analysis. *J. Am. Chem. Soc.* **137**, 9971 (2015).

[148] H. Jensen. *Scanning Tunneling Studies on Patterned Noble Metal (111) Substrates.* PhD thesis, Christian-Albrechts-Universität zu Kiel, (2017).

[149] A. Burtzlaff. *Shot Noise Measurements at Single Atom Contacts in a Low-Temperature Scanning Tunnelling Microscope.* PhD thesis, Christian-Albrechts-Universität zu Kiel, (2017).

[150] E. Soares, V. Nascimento, V. de Carvalho, C. de Castilho, A. de Carvalho, R. Toomes, and D. Woodruff. Structure determination of Ag(111) by low-energy electron diffraction. *Surf. Sci.* **419**, 89 (1999).

[151] C. Wöll, S. Chiang, R. J. Wilson, and P. H. Lippel. Determination of atom positions at stacking-fault dislocations on Au(111) by scanning tunneling microscopy. *Phys. Rev. B* **39**, 7988 (1989).

[152] S. Narasimhan and D. Vanderbilt. Elastic stress domains and the herringbone reconstruction on au(111). *Phys. Rev. Lett.* **69**, 1564 (1992).

[153] F. Hanke and J. Björk. Structure and local reactivity of the Au(111) surface reconstruction. *Phys. Rev. B* 87 (2013).

[154] T. Choi, C. D. Ruggiero, and J. A. Gupta. Incommensurability and Atomic Structure of c(2x2)N/Cu(100): A Scanning Tunneling Microscopy Study. *Phys.Rev. B* **78**, 035430 (2008).

[155] T. Choi. *STM studies of charge transfer and transport through metal-molecule complexes on ultrathin insulating films.* PhD thesis, The Ohio State University, (2011).

[156] C. D. Ruggiero, T. Choi, and J. A. Gupta. Tunneling Spectroscopy of Ultrathin Insulating Films: CuN on Cu(100). *Appl. Phys. Lett.* **91**, 253106 (2007).

[157] J. Fenn, M. Mann, C. Meng, S. Wong, and C. Whitehouse. Electrospray ionization for mass spectrometry of large biomolecules. *Science* **246**, 64 (1989).

[158] C. Hamann. *An Electrospray Ion Source for Ultra-High Vacuum Deposition of Organic Molecules.* PhD thesis, Christian-Albrechts-Universität zu Kiel, (2011).

[159] C. Hamann, R. Woltmann, I.-P. Hong, N. Hauptmann, S. Karan, and R. Berndt. Ultrahigh Vacuum Deposition of Organic Molecules by Electrospray Ionization. *Rev. Sci. Instrum.* **82**, 033903 (2011).

[160] M. González. Force fields and molecular dynamics simulations. *École thématique de la Société Française de la Neutronique* **12**, 169 (2011).

[161] S. Lifson and A. Warshel. Consistent Force Field for Calculations of Conformations, Vibrational Spectra, and Enthalpies of Cycloalkane and n-Alkane Molecules. *J. Chem. Phys.* **49**, 5116 (1968).

[162] J. B. Hendrickson. Molecular Geometry. I. Machine Computation of the Common Rings. *J. Am. Chem. Soc.* **83**, 4537 (1961).

[163] L.-P. Wang, T. J. Martinez, and V. S. Pande. Building Force Fields: An Automatic,

Systematic, and Reproducible Approach. *J. Phys. Chem. Lett.* **5**, 1885 (2014).

[164] R. Schulz, B. Lindner, L. Petridis, and J. C. Smith. Scaling of multimillion-atom biological molecular dynamics simulation on a petascale supercomputer. *J. Chem. Theory Comput.* **5**, 2798 (2009).

[165] A. K. Rappe, C. J. Casewit, K. S. Colwell, W. A. Goddard, and W. M. Skiff. UFF, a full periodic table force field for molecular mechanics and molecular dynamics simulations. *J. Am. Chem. Soc.* **114**, 10024 (1992).

[166] M. D. Hanwell, D. E. Curtis, D. C. Lonie, T. Vandermeersch, E. Zurek, and G. R. Hutchison. Avogadro: an advanced semantic chemical editor, visualization, and analysis platform. *J Cheminform* **4**, 17 (2012).

[167] J. Wang, R. M. Wolf, J. W. Caldwell, P. A. Kollman, and D. A. Case. Development and testing of a general amber force field. *J. Comput. Chem.* **25**, 1157 (2004).

[168] T. A. Halgren. Merck molecular force field. I. Basis, form, scope, parameterization, and performance of MMFF94. *J. Comput. Chem.* **17**, 490 (1996).

[169] P. Hohenberg and W. Kohn. Inhomogeneous Electron Gas. *Phys. Rev.* **136**, B864 (1964).

[170] W. Kohn, A. Savin, and C. A. Ullrich. Hohenberg-Kohn theory including spin magnetism and magnetic fields. *Int. J. Quantum Chem.* **100**, 20 (2004).

[171] P. W. Ayers and W. Yang. Legendre-transform functionals for spin-density-functional theory. *J. Chem. Phys.* **124**, 224108 (2006).

[172] D. S. Sholl and J. A. Steckel. *Density Functional Theory: A Practical Introduction.* Wiley, Hoboken, New Jersey (2009).

[173] M. Born and R. Oppenheimer. Zur Quantentheorie der Molekeln. *Ann. Phys.* **389**, 457 (1927).

[174] W. Kohn and L. J. Sham. Self-Consistent Equations Including Exchange and Correlation Effects. *Phys. Rev.* **140**, A1133 (1965).

[175] R. Stowasser and R. Hoffmann. What Do the Kohn-Sham Orbitals and Eigenvalues Mean? *J. Am. Chem. Soc.* **121**, 3414 (1999).

[176] E. J. Baerends, O. V. Gritsenko, and R. van Meer. The Kohn-Sham gap, the fundamental gap and the optical gap: the physical meaning of occupied and virtual Kohn-Sham orbital energies. *Phys. Chem. Chem. Phys.* **15**, 16408 (2013).

[177] J. P. Perdew, W. Yang, K. Burke, Z. Yang, E. K. U. Gross, M. Scheffler, G. E. Scuseria, T. M. Henderson, I. Y. Zhang, A. Ruzsinszky, H. Peng, J. Sun, E. Trushin, and A. Görling. Understanding band gaps of solids in generalized Kohn-Sham theory. *Proc. Natl. Acad. Sci. U.S.A.* **114**, 2801 (2017).

[178] M. Stöhr, T. V. Voorhis, and A. Tkatchenko. Theory and practice of modeling van der Waals interactions in electronic-structure calculations. *Chem. Soc. Rev.* **48**, 4118 (2019).

[179] V. G. Ruiz, W. Liu, E. Zojer, M. Scheffler, and A. Tkatchenko. Density-functional theory with screened van der waals interactions for the modeling of hybrid inorganic-organic systems. *Phys. Rev. Lett.* **108**, 146103 (2012).

[180] R. J. Maurer, V. G. Ruiz, and A. Tkatchenko. Many-body dispersion effects in the binding of adsorbates on metal surfaces. *J. Chem. Phys.* **143**, 102808 (2015).

[181] V. G. Ruiz, W. Liu, and A. Tkatchenko. Density-functional theory with screened van der waals interactions applied to atomic and molecular adsorbates on close-packed and non-close-packed surfaces. *Phys. Rev. B* **93**, 035118 (2016).

[182] J. Klimeš, D. R. Bowler, and A. Michaelides. Chemical accuracy for the van der Waals density functional. *J. Phys. Condens. Matter* **22**, 022201 (2010).

[183] T. Ichibha, Z. Hou, K. Hongo, and R. Maezono. New Insight into the Ground State of FePc: A Diffusion Monte Carlo Study. *Sci. Rep.* **7**, 2011 (2017).

[184] D. Nachtigallová, A. Antalík, R. Lo, R. Sedlák, D. Manna, J. Tuček, J. Ugolotti, L. Veis, Örs Legeza, J. Pittner, R. Zbořil, and P. Hobza. An Isolated Molecule of Iron(II) Phthalocyanin Exhibits Quintet Ground-State: A Nexus between Theory and Experiment. *Chem. Eur. J* **24**, 13413 (2018).

[185] Y. Imry. *Introduction To Mesoscopic Physics.* Oxford University Press (1997).

[186] N. Agraït, A. L. Yeyati, and J. M. van Ruitenbeek. Quantum properties of atomic-sized conductors. *Phys. Rep.* **377**, 81 (2003).

[187] R. Landauer. Spatial Variation of Currents and Fields Due to Localized Scatterers in Metallic Conduction. *IBM J. Res. Dev.* **1**, 223 (1957).

[188] R. Landauer. Spatial variation of currents and fields due to localized scatterers in metallic conduction (and comment). *J. Math. Phys.* **37**, 5259 (1996).

[189] J. Kröger, N. Néel, A. Sperl, Y. F. Wang, and R. Berndt. Single-atom contacts with a scanning tunnelling microscope. *New J. Phys.* **11**, 125006 (2009).

[190] S. Datta. *Electronic Transport in Mesoscopic Systems.* Cambridge University Press, Cambridge (1995).

[191] S. Datta. *Quantum Transport: Atom to Transistor.* Cambridge University Press, Cambridge (2005).

[192] M. Brandbyge, J.-L. Mozos, P. Ordejón, J. Taylor, and K. Stokbro. Density-functional method for nonequilibrium electron transport. *Phys. Rev. B* **65**, 165401 (2002).

[193] N. Papior, N. Lorente, T. Frederiksen, A. García, and M. Brandbyge. Improvements on non-equilibrium and transport green function techniques: The next-generation TRANSIESTA. *Comp. Phys. Comm.* **212**, 8 (2017).

[194] M. Paulsson and M. Brandbyge. Transmission eigenchannels from nonequilibrium green's functions. *Phys. Rev. B* **76**, 115117 (2007).

[195] K. Stokbro, J. Taylor, M. Brandbyge, J.-L. Mozos, and P. Ordejon. Theoretical study of the nonlinear conductance of di-thiol benzene coupled to Au(111) surfaces via thiol and thiolate bonds. *Comput. Mater. Sci.* **27**, 151 (2003).

[196] N. L. Schneider, G. Schull, and R. Berndt. Optical Probe of Quantum Shot-Noise Reduction at a Single-Atom Contact. *Phys. Rev. Lett.* 105 (2010).

[197] A. Burtzlaff, A. Weismann, M. Brandbyge, and R. Berndt. Shot noise as a probe of spin-polarized transport through single atoms. *Phys. Rev. Lett.* **114**, 016602 (2015).

[198] M. Mohr, T. Jasper-Toennies, A. Weismann, T. Frederiksen, A. Garcia-Lekue, S. Ul-

rich, R. Herges, and R. Berndt. Conductance channels of a platform molecule on Au(111) probed with shot noise. *Phys. Rev. B* **99**, 245417 (2019).

[199] L. Lafferentz, F. Ample, H. Yu, S. Hecht, C. Joachim, and L. Grill. Conductance of a single conjugated polymer as a continuous function of its length. *Science* **323**, 1193 (2009).

[200] M. Koch, F. Ample, C. Joachim, and L. Grill. Voltage-dependent conductance of a single graphene nanoribbon. *Nat. Nanotechnol.* **7**, 713 (2012).

[201] G. Reecht, F. Scheurer, V. Speisser, Y. J. Dappe, F. Mathevet, and G. Schull. Electroluminescence of a polythiophene molecular wire suspended between a metallic surface and the tip of a scanning tunneling microscope. *Phys. Rev. Lett.* **112**, 047403 (2014).

[202] C. Nacci, F. Ample, D. Bleger, S. Hecht, C. Joachim, and L. Grill. Conductance of a single flexible molecular wire composed of alternating donor and acceptor units. *Nat. Commun.* **6**, 7397 (2015).

[203] C. Thiele, L. Gerhard, T. R. Eaton, D. M. Torres, M. Mayor, W. Wulfhekel, H. v Löhneysen, and M. Lukas. STM study of oligo(phenylene-ethynylene)s. *New J. Phys.* **17**, 053043 (2015).

[204] G. Reecht, H. Bulou, F. Scheurer, V. Speisser, F. Mathevet, C. González, Y. J. Dappe, and G. Schull. Pulling and stretching a molecular wire to tune its conductance. *J. Phys. Chem. Lett.* **6**, 2987 (2015).

[205] M. C. Chong, G. Reecht, H. Bulou, A. Boeglin, F. Scheurer, F. Mathevet, and G. Schull. Narrow-line single-molecule transducer between electronic circuits and surface plasmons. *Phys. Rev. Lett.* **116**, 036802 (2016).

[206] R. Temirov, A. Lassise, F. B. Anders, and F. S. Tautz. Kondo effect by controlled cleavage of a single-molecule contact. *Nanotechnology* **19**, 065401 (2008).

[207] N. Fournier, C. Wagner, C. Weiss, R. Temirov, and F. S. Tautz. Force-controlled lifting of molecular wires. *Phys. Rev. B* **84**, 035435 (2011).

[208] G. Reecht, C. Lotze, D. Sysoiev, T. Huhn, and K. J. Franke. Visualizing the role of molecular orbitals in charge transport through individual diarylethene isomers. *ACS Nano* **10**, 10555 (2016).

[209] N. L. Schneider, F. Matino, G. Schull, S. Gabutti, M. Mayor, and R. Berndt. Light emission from a double-decker molecule on a metal surface. *Phys. Rev. B* **84**, 153403 (2011).

[210] L. Gerhard, K. Edelmann, J. Homberg, M. Valášek, S. G. Bahoosh, M. Lukas, F. Pauly, M. Mayor, and W. Wulfhekel. An electrically actuated molecular toggle switch. *Nat. Commun.* **8**, 14672 (2017).

[211] J. M. Soler, E. Artacho, J. D. Gale, A. Garía, J. Junquera, P. Ordejón, and D. Sánchez-Portal. The SIESTA method for ab initio orden-N materials simulation. *J. Phys. Condens. Matter* **11**, 2745 (2002).

[212] T. Frederiksen, M. Paulsson, M. Brandbyge, and A.-P. Jauho. Inelastic transport theory from first principles: Methodology and application to nanoscale devices. *Phys. Rev. B* **75**, 205413 (2007).

[213] The Inelastica software suite is freely available at

`https://github.com/tfrederiksen/inelastica/.`, (2019).

[214] M. Corso, M. Ondráček, C. Lotze, P. Hapala, K. J. Franke, P. Jelínek, and J. I. Pascual. Charge redistribution and transport in molecular contacts. *Phys. Rev. Lett.* **115**, 136101 (2015).

[215] Y. Wang, M. Zhu, L. Kang, and B. Dai. Neutral $\mathrm{Au}_n(n = 3 - 10)$ clusters catalyze acetylene hydrochlorination: a density functional theory study. *RSC Adv.* **4**, 38466 (2014).

[216] F. Ferraro, J. F. Pérez-Torres, and C. Hadad. Selective catalytic activation of acetylene by a neutral gold cluster of experimentally known gas-phase geometry. *J. Phys. Chem. C* **119**, 7755 (2015).

[217] G. Bistoni, P. Belanzoni, L. Belpassi, and F. Tarantelli. $\pi$ activation of alkynes in homogeneous and heterogeneous gold catalysis. *J. Phys. Chem. A* **120**, 5239 (2016).

[218] A. C. Tsipis. Unveiling the nature of binding interactions of acetylene and ethylene with triangular coinage metal clusters: A DFT computational study. *Organometallics* **29**, 354 (2010).

[219] U. Landman, W. D. Luedtke, N. A. Burnham, and R. J. Colton. Atomistic mechanisms and dynamics of adhesion, nanoindentation, and fracture. *Science* **248**, 454 (1990).

[220] R. W. Godby, M. Schlüter, and L. J. Sham. Accurate exchange-correlation potential for silicon and its discontinuity on addition of an electron. *Phys. Rev. Lett.* **56**, 2415 (1986).

[221] S. Y. Quek, L. Venkataraman, H. J. Choi, S. G. Louie, M. S. Hybertsen, and J. B. Neaton. Amine-gold linked single-molecule circuits: experiment and theory. *Nano Lett.* **7**, 3477 (2007).

[222] M. G. Reuter, T. Seideman, and M. A. Ratner. Guidelines for choosing molecular 'alligator clip' binding motifs in electron transport devices. *J. Chem. Phys.* **134**, 154708 (2011).

[223] Y. F. Wang, J. Kröger, R. Berndt, H. Vázquez, M. Brandbyge, and M. Paulsson. Atomic-scale control of electron transport through single molecules. *Phys. Rev. Lett.* **104**, 176802 (2010).

[224] S. J. Altenburg, J. Kröger, B. Wang, M.-L. Bocquet, N. Lorente, and R. Berndt. Graphene on Ru(0001): Contact Formation and Chemical Reactivity on the Atomic Scale. *Phys. Rev. Lett.* **105**, 236101 (2010).

[225] M. Kiguchi and S. Kaneko. Single molecule bridging between metal electrodes. *Phys. Chem. Chem. Phys.* **15**, 2253 (2013).

[226] Y. Zhang, Y. Wang, J.-T. Lü, M. Brandbyge, and R. Berndt. Mechanochemistry induced using force exerted by a functionalized microscope tip. *Angew. Chem.* **129**, 11931 (2017).

[227] S. Karan, C. García, M. Karolak, D. Jacob, N. Lorente, and R. Berndt. Spin control induced by molecular charging in a transport junction. *Nano Lett.* **18**, 88 (2017).

[228] T. Yelin, R. Korytár, N. Sukenik, R. Vardimon, B. Kumar, C. Nuckolls, F. Evers, and O. Tal. Conductance saturation in a series of highly transmitting molecular junctions. *Nat. Mater.* **15**, 444 (2016).

[229] C. A. Martin, D. Ding, J. K. Sørensen, T. Bjørnholm, J. M. van Ruitenbeek, and H. S. J. van der Zant. Fullerene-based anchoring groups for molecular electronics. *J. Am. Chem. Soc.* **130**, 13198 (2008).

[230] E. Leary, M. T. González, C. van der Pol, M. R. Bryce, S. Filippone, N. Martín, G. Rubio-Bollinger, and N. Agraït. Unambiguous One-molecule conductance measurements under ambient conditions. *Nano Lett.* **11**, 2236 (2011).

[231] R. F. W. Bader. *Atoms in Molecules, Handbook of Molecular Physics and Quantum Chemistry*, volume 2. Chicester: Wiley (2003).

[232] J. C. Martin and R. G. Smith. Factors influencing the basicities of triarylcarbinols. the synthesis of sesquixanthydrol. *J. Am. Chem. Soc.* **86**, 2252 (1964).

[233] M. Lofthagen, R. VernonClark, K. K. Baldridge, and J. S. Siegel. Synthesis of trioxatricornan and derivatives. useful keystones for the construction of rigid molecular cavities. *J. Org. Chem.* **57**, 61 (1992).

[234] A. Faldt, F. C. Krebs, and N. Thorup. Synthesis, structure and properties of various molecules based on the 4,8,12-trioxa-4,8,12,12c-tetrahydrodibenzo[*cd*,*mn*]pyrene system with an evaluation of the effect differing molecular substituti on patterns has on the space group symmetry. *J. Chem. Soc., Perkin Trans. 2* pages 2219–2228 (1997).

[235] P. Liljeroth, J. Repp, and G. Meyer. Current-induced hydrogen tautomerization and conductance switching of naphthalocyanine molecules. *Science* **317**, 1203 (2007).

[236] S. Pan, Q. Fu, T. Huang, A. Zhao, B. Wang, Y. Luo, J. Yang, and J. Hou. Design and control of electron transport properties of single molecules. *Proc. Natl. Acad. Sci. USA* **106**, 15259 (2009).

[237] L. Olesen, M. Brandbyge, M. R. Sørensen, K. W. Jacobsen, E. Lægsgaard, I. Stensgaard, and F. Besenbacher. Apparent barrier height in scanning tunneling microscopy revisited. *Phys. Rev. Lett.* **76**, 1485 (1996).

[238] Y. Komoto, S. Fujii, M. Iwane, and M. Kiguchi. Single-molecule junctions for molecular electronics. *J. Mater. Chem. C* **4**, 8842 (2016).

[239] Y. Zang, A. Pinkard, Z.-F. Liu, J. B. Neaton, M. L. Steigerwald, X. Roy, and L. Venkataraman. Electronically transparent Au–N bonds for molecular junctions. *J. Am. Chem. Soc.* **139**, 14845 (2017).

[240] M. Carini, M. P. Ruiz, I. Usabiaga, J. A. Fernández, E. J. Cocinero, M. Melle-Franco, I. Diez-Perez, and A. Mateo-Alonso. High conductance values in $\pi$-folded molecular junctions. *Nat. Commun.* **8**, 15195 (2017).

[241] A. Yazdani, D. M. Eigler, and N. D. Lang. Off-resonance conduction through atomic wires. *Science* **272**, 1921 (1996).

[242] J. A. Stroscio and R. J. Celotta. Controlling the dynamics of a single atom in lateral atom manipulation. *Science* **306**, 242 (2004).

[243] A. Sperl, J. Kröger, and R. Berndt. Direct observation of conductance fluctuations of a single-atom tunneling contact. *Phys. Rev. B* **81**, 035406 (2010).

[244] H. Sellers, A. Ulman, Y. Shnidman, and J. E. Eilers. Structure and binding of alkanethiolates on gold and silver surfaces: implications for self-assembled monolayers. *J. Am. Chem. Soc.* **115**, 9389 (1993).

[245] I. S. Butler, A. Neppel, K. R. Plowman, and C. F. Shaw. Vibrational spectra and normal coordinate calculations for some dimethyl sulfide complexes of gold(I) and gold(III). *J. Raman Spectrosc.* **15**, 310 (1984).

[246] H. Park, J. Park, A. K. L. Lim, E. H. Anderson, A. P. Alivisatos, and P. L. McEuen. Nanomechanical oscillations in a single-$C_{60}$ transistor. *Nature* **407**, 57 (2000).

[247] A. Franke and E. Pehlke. Adsorption and diffusion of $SCH_3$ radicals and $Au(SCH_3)_2$ complexes on the unreconstructed Au(111) surface in the submonolayer coverage regime. *Phys. Rev. B* **79**, 235441 (2009).

[248] C. M. Guédon, H. Valkenier, T. Markussen, K. S. Thygesen, J. C. Hummelen, and S. J. van der Molen. Observation of quantum interference in molecular charge transport. *Nat. Nanotechnol.* **7**, 305 (2012).

[249] M. Brandbyge, J. L. Mozos, P. Ordejón, J. Taylor, and K. Stokbro. Density-functional method for nonequilibrium electron transport. *PRB* **65**, 165401 (2002).

[250] M. Schliwa and G. Woehlke. Molecular motors. *Nature* **422**, 759 (2003).

[251] K. Kinbara and T. Aida. Toward intelligent molecular machines: directed motions of biological and artificial molecules and assemblies. *Chem. Rev.* **105**, 1377 (2005).

[252] J. K. Gimzewski, C. Joachim, R. R. Schlittler, V. Langlais, and I. J. H. Tang. Rotation of a single molecule within a supramolecular bearing. *Science* **281**, 531 (1998).

[253] B. C. Stipe, M. A. Rezaei, and W. Ho. Inducing and viewing the rotational motion of a single molecule. *Science* **279**, 1907 (1998).

[254] A. E. Baber, H. L. Tierney, and E. C. H. Sykes. A quantitative single-molecule study of thioether molecular rotors. *ACS Nano* **2**, 2385 (2008).

[255] L. Gao, Q. Liu, Y. Y. Zhang, N. Jiang, H. G. Zhang, Z. H. Cheng, W. F. Qiu, S. X. Du, Y. Q. Liu, W. A. Hofer, and H.-J. Gao. Constructing an array of anchored single-molecule rotors on gold surfaces. *Phys Rev Lett* **101**, 197209 (2008).

[256] C. Manzano, W.-H. Soe, H. S. Wong, F. Ample, A. Gourdon, N. Chandrasekhar, and C. Joachim. Step-by-step rotation of a molecule-gear mounted on an atomic-scale axis. *Nat. Mater.* **8**, 576 (2009).

[257] D. Zhong, T. Blömker, K. Wedeking, L. Chi, G. Erker, and H. Fuchs. Surface-mounted molecular rotors with variable functional groups and rotation radii. *Nano Lett.* **9**, 4387 (2009).

[258] H. L. Tierney, C. J. Murphy, A. D. Jewell, A. E. Baber, E. V. Iski, H. Y. Khodaverdian, A. F. McGuire, N. Klebanov, and E. C. H. Sykes. Experimental demonstration of a single-molecule electric motor. *Nat. Nanotechnol.* **6**, 625 (2011).

[259] H. L. Tierney, C. J. Murphy, and E. C. H. Sykes. Regular scanning tunneling microscope tips can be intrinsically chiral. *Phys. Rev. Lett.* **106**, 010801 (2011).

[260] C.-A. Palma, J. Björk, F. Rao, D. Kühne, F. Klappenberger, and J. V. Barth. Topological dynamics in supramolecular rotors. *Nano Lett.* **14**, 4461 (2014).

[261] R. Ohmann, J. Meyer, A. Nickel, J. Echeverria, M. Grisolia, C. Joachim, F. Moresco, and G. Cuniberti. Supramolecular rotor and translator at work: On-surface movement of single atoms. *ACS Nano* **9**, 8394 (2015).

[262] A. Krönlein, J. Kügel, K. A. Kokh, O. E. Tereshchenko, and M. Bode. Energetic and spatial mapping of resonant electronic excitations. *J. Phys. Chem. C* **120**, 13843 (2016).

[263] K. Sun, J.-Y. Luo, X. Zhang, Z.-J. Wu, Y. Wang, H.-K. Yuan, Z.-H. Xiong, S.-C. Li, Q.-K. Xue, and J.-Z. Wang. Supramolecular motors on graphite surface stabilized by charge states and hydrogen bonds. *ACS Nano* **11**, 10236 (2017).

[264] J. C. Gehrig, M. Penedo, M. Parschau, J. Schwenk, M. A. Marioni, E. W. Hudson, and H. J. Hug. Surface single-molecule dynamics controlled by entropy at low temperatures. *Nat. Commun.* **8**, 14404 (2017).

[265] F. Eisenhut, J. Meyer, J. Krüger, R. Ohmann, G. Cuniberti, and F. Moresco. Inducing the controlled rotation of single o-MeO-DMBI molecules anchored on Au(111). *Surf. Sci.* **678**, 177 (2018).

[266] H.-L. Lu, Y. Cao, J. Qi, A. Bakker, C. A. Strassert, X. Lin, K.-H. Ernst, S. Du, H. Fuchs, and H.-J. Gao. Modification of the potential landscape of molecular rotors on Au(111) by the presence of an STM tip. *Nano Lett.* **18**, 4704 (2018).

[267] G. J. Simpson, V. García-López, A. D. Boese, J. M. Tour, and L. Grill. How to control single-molecule rotation. *Nat. Commun.* **10**, 4631 (2019).

[268] W. Wang, X. Shi, M. Jin, C. Minot, M. A. V. Hove, J.-P. Collin, and N. Lin. Electron stimulation of internal torsion of a surface-mounted molecular rotor. *ACS Nano* **4**, 4929 (2010).

[269] U. G. E. Perera, F. Ample, H. Kersell, Y. Zhang, G. Vives, J. Echeverria, M. Grisolia, G. Rapenne, C. Joachim, and S.-W. Hla. Controlled clockwise and anticlockwise rotational switching of a molecular motor. *Nat. Nanotechnol.* **8**, 46 (2012).

[270] Y. Zhang, H. Kersell, R. Stefak, J. Echeverria, V. Iancu, U. G. E. Perera, Y. Li, A. Deshpande, K.-F. Braun, C. Joachim, G. Rapenne, and S.-W. Hla. Simultaneous and coordinated rotational switching of all molecular rotors in a network. *Nat. Nanotechnol.* **11**, 706 (2016).

[271] J. Homberg, M. Lindner, L. Gerhard, K. Edelmann, T. Frauhammer, Y. Nahas, M. Valášek, M. Mayor, and W. Wulfhekel. Six state molecular revolver mounted on a rigid platform. *Nanoscale* **11**, 9015 (2019).

[272] Y. Zhang, J. P. Calupitan, T. Rojas, R. Tumbleson, G. Erbland, C. Kammerer, T. M. Ajayi, S. Wang, L. A. Curtiss, A. T. Ngo, S. E. Ulloa, G. Rapenne, and S. W. Hla. A chiral molecular propeller designed for unidirectional rotations on a surface. *Nat. Commun.* **10**, 3742 (2019).

[273] N. A. Wasio, D. P. Slough, Z. C. Smith, C. J. Ivimey, S. W. T. III, Y.-S. Lin, and E. C. H. Sykes. Correlated rotational switching in two-dimensional self-assembled molecular rotor arrays. *Nat. Commun.* **8**, 16057 (2017).

[274] T. A. Balema, N. Ulumuddin, C. J. Murphy, D. P. Slough, Z. C. Smith, R. T. Hannagan, N. A. Wasio, A. M. Larson, D. A. Patel, K. Groden, J.-S. McEwen, Y.-S. Lin, and E. C. H. Sykes. Controlling molecular switching via chemical functionality: Ethyl vs methoxy rotors. *J. Phys. Chem. C* **123**, 23738 (2019).

[275] K.-H. Ernst. Molecular chirality at surfaces. *Phys. Status Solidi B* **249**, 2057 (2012).

[276] P. Mishra, J. P. Hill, S. Vijayaraghavan, W. V. Rossom, S. Yoshizawa, M. Grisolia,

J. Echeverria, T. Ono, K. Ariga, T. Nakayama, C. Joachim, and T. Uchihashi. Current-driven supramolecular motor with in situ surface chiral directionality switching. *Nano Lett.* **15**, 4793 (2015).

[277] A. M. Larson, K. Groden, R. T. Hannagan, J.-S. McEwen, and E. C. H. Sykes. Understanding enantioselective interactions by pulling apart molecular rotor complexes. *ACS Nano* **13**, 5939 (2019).

[278] U. Jung, C. Schütt, O. Filinova, J. Kubitschke, R. Herges, and O. Magnussen. Photoswitching of azobenzene-functionalized molecular platforms on au surfaces. *J. Phys. Chem. C* **116**, 25943 (2012).

[279] N. Koumura, R. W. J. Zijlstra, R. A. van Delden, N. Harada, and B. L. Feringa. Light-driven monodirectional molecular rotor. *Nature* **401**, 152 (1999).

[280] G. T. Carroll, M. M. Pollard, R. van Delden, and B. L. Feringa. Controlled rotary motion of light-driven molecular motors assembled on a gold film. *Chem. Sci.* **1**, 97 (2010).

[281] B. N. J. Persson and A. Baratoff. Inelastic electron tunneling from a metal tip: The contribution from resonant processes. *Phys. Rev. Lett.* **59**, 339 (1987).

[282] N. Lorente and M. Persson. Theory of single molecule vibrational spectroscopy and microscopy. *Phys. Rev. Lett.* **85**, 2997 (2000).

[283] S. Monturet and N. Lorente. Inelastic effects in electron transport studied with wave packet propagation. *Phys. Rev. B* **78**, 035445 (2008).

[284] T. Jasper-Tönnies, I. Poltavsky, S. Ulrich, T. Moje, A. Tkatchenko, R. Herges, and R. Berndt. Stability of functionalized platform molecules on Au(111). *J. Chem. Phys.* **149**, 244705 (2018).

[285] H. Arnolds. Vibrational dynamics of adsorbates – quo vadis? *Prog. Surf. Sci.* **86**, 1 (2011).

[286] Y. E. Shchadilova, S. G. Tikhodeev, M. Paulsson, and H. Ueba. Rotation of a single acetylene molecule on Cu(001) by tunneling electrons in STM. *Phys. Rev. Lett.* **111**, 186102 (2013).

[287] H. W. Kim, M. Han, H.-J. Shin, S. Lim, Y. Oh, K. Tamada, M. Hara, Y. Kim, M. Kawai, and Y. Kuk. Control of molecular rotors by selection of anchoring sites. *Phys. Rev. Lett.* **106**, 146101 (2011).

[288] Y. Kim, T. Komeda, and M. Kawai. Single-molecule reaction and characterization by vibrational excitation. *Phys. Rev. Lett.* **89**, 126104 (2002).

[289] A. Laubereau and W. Kaiser. Vibrational dynamics of liquids and solids investigated by picosecond light pulses. *Rev. Mod. Phys.* **50**, 607 (1978).

[290] T. Kumagai, F. Hanke, S. Gawinkowski, J. Sharp, K. Kotsis, J. Waluk, M. Persson, and L. Grill. Controlling intramolecular hydrogen transfer in a porphycene molecule with single atoms or molecules located nearby. *Nat. Chem.* **6**, 41 (2013).

[291] J. Kügel, L. Klein, M. Leisegang, and M. Bode. Analyzing and tuning the energetic landscape of $H_2$Pc tautomerization. *J. Phys. Chem. C* **121**, 28204 (2017).

[292] G. Kresse and J. Furthmüller. Efficient iterative schemes for ab initio total-energy calculations using a plane-wave basis set. *Phys. Rev. B* **54**, 11169 (1996).

[293] G. Mills, H. Jónsson, and G. K. Schenter. Reversible work transition state theory: application to dissociative adsorption of hydrogen. *Surf. Sci.* **324**, 305 (1995).

[294] J. Lambe and S. L. McCarthy. Light emission from inelastic electron tunneling. *Phys. Rev. Lett.* **37**, 923 (1976).

[295] T. Jasper-Toennies, M. Gruber, S. Johannsen, T. Frederiksen, A. Garcia-Lekue, T. Jäkel, F. Roehricht, R. Herges, and R. Berndt. Rotation of Ethoxy and Ethyl Moieties on a Molecular Platform on Au(111). *ACS Nano* **14**, 3907 (2020).

[296] B. Xu, C. Tao, E. D. Williams, and J. E. Reutt-Robey. Coverage Dependent Supramolecular Structures: C60:ACA Monolayers on Ag(111). *J. Am. Chem. Soc.* **128**, 8493 (2006).

[297] H. Liang, W. Sun, X. Jin, H. Li, J. Li, X. Hu, B. K. Teo, and K. Wu. Two-Dimensional Molecular Porous Networks Formed by Trimesic Acid and 4,4'-Bis(4-pyridyl)biphenyl on Au(111) through Hierarchical Hydrogen Bonds: Structural Systematics and Control of Nanopore Size and Shape. *Angew. Chem. Int. Ed.* **50**, 7562 (2011).

[298] R. Otero, J. M. Gallego, A. L. V. de Parga, N. Martín, and R. Miranda. Molecular Self-Assembly at Solid Surfaces. *Adv. Mater.* **23**, 5148 (2011).

[299] L. Dong, Z. Gao, and N. Lin. Self-assembly of metal–organic coordination structures on surfaces. *Prog. Surf. Sci.* **91**, 101 (2016).

[300] J. Shang, Y. Wang, M. Chen, J. Dai, X. Zhou, J. Kuttner, G. Hilt, X. Shao, J. M. Gottfried, and K. Wu. Assembling molecular Sierpiński triangle fractals. *Nat. Chem.* **7**, 389 (2015).

[301] M. E. Cañas-Ventura, F. Klappenberger, S. Clair, S. Pons, K. Kern, H. Brune, T. Strunskus, C. Wöll, R. Fasel, and J. V. Barth. Coexistence of one- and two-dimensional supramolecular assemblies of terephthalic acid on Pd(111) due to self-limiting deprotonation. *J. Chem. Phys.* **125**, 184710 (2006).

[302] F. Klappenberger, M. E. Cañas-Ventura, S. Clair, S. Pons, U. Schlickum, Z.-R. Qu, H. Brune, K. Kern, T. Strunskus, C. Wöll, A. Comisso, A. De Vita, M. Ruben, and J. V. Barth. Conformational Adaptation in Supramolecular Assembly on Surfaces. *ChemPhysChem* **8**, 1782 (2007).

[303] U. Schlickum, R. Decker, F. Klappenberger, G. Zoppellaro, S. Klyatskaya, M. Ruben, I. Silanes, A. Arnau, K. Kern, H. Brune, and J. V. Barth. Metal-organic Honeycomb Nanomeshes with Tunable Cavity Size. *Nano Lett.* **7**, 3813 (2007).

[304] S. Stepanow, N. Lin, D. Payer, U. Schlickum, F. Klappenberger, G. Zoppellaro, M. Ruben, H. Brune, J. V. Barth, and K. Kern. Surface-Assisted Assembly of 2D Metal–organic Networks That Exhibit Unusual Threefold Coordination Symmetry. *Angew. Chem. Int. Ed.* **46**, 710 (2007).

[305] U. Schlickum, R. Decker, F. Klappenberger, G. Zoppellaro, S. Klyatskaya, W. Auwärter, S. Neppl, K. Kern, H. Brune, M. Ruben, and J. V. Barth. Chiral Kagomé Lattice from Simple Ditopic Molecular Bricks. *J. Am. Chem. Soc.* **130**, 11778 (2008).

[306] S. Clair, M. Abel, and L. Porte. Mesoscopic arrays from supramolecular self-assembly. *Angew. Chem.* **122**, 8413 (2010).

[307] S. Gottardi, K. Müller, J. C. Moreno-López, H. Yildirim, U. Meinhardt, M. Kivala,

A. Kara, and M. Stöhr. Cyano-Functionalized Triarylamines on Au(111): Competing Intermolecular versus Molecule/Substrate Interactions. *Adv. Mater. Interfaces* **1**, 1300025 (2013).

[308] K. Bairagi, O. Iasco, A. Bellec, A. Kartsev, D. Li, J. Lagoute, C. Chacon, Y. Girard, S. Rousset, F. Miserque, Y. J. Dappe, A. Smogunov, C. Barreteau, M. L. Boillot, T. Mallah, and V. Repain. Molecular-Scale Dynamics of Light-Induced Spin Cross-Over in a Two-Dimensional Layer. *Nat. Commun.* **7**, 12212 (2016).

[309] L. Yan, G. Kuang, Q. Zhang, X. Shang, P. N. Liu, and N. Lin. Self-assembly of a binodal metal–organic framework exhibiting a demi-regular lattice. *Faraday Discuss.* **204**, 111 (2017).

[310] J. A. Theobald, N. S. Oxtoby, M. A. Phillips, N. R. Champness, and P. H. Beton. Controlling molecular deposition and layer structure with supramolecular surface assemblies. *Nature* **424**, 1029 (2003).

[311] H. Liang, Y. He, Y. Ye, X. Xu, F. Cheng, W. Sun, X. Shao, Y. Wang, J. Li, and K. Wu. Two-dimensional molecular porous networks constructed by surface assembling. *Coord. Chem. Rev.* **253**, 2959 (2009).

[312] Q. Zhou, Y. Li, Q. Li, Y. Wang, Y. Yang, Y. Fang, and C. Wang. Switchable supramolecular assemblies on graphene. *Nanoscale* **6**, 8387 (2014).

[313] J. Teyssandier, S. D. Feyter, and K. S. Mali. Host–guest chemistry in two-dimensional supramolecular networks. *Chem. Commun.* **52**, 11465 (2016).

[314] J. D. C. González, M. Iyoda, and J. P. Rabe. Templated bilayer self-assembly of fully conjugated $\pi$-expanded macrocyclic oligothiophenes complexed with fullerenes. *Nat. Commun.* **8**, 14717 (2017).

[315] X. Lin, J. C. Lu, Y. Shao, Y. Y. Zhang, X. Wu, J. B. Pan, L. Gao, S. Y. Zhu, K. Qian, Y. F. Zhang, D. L. Bao, L. F. Li, Y. Q. Wang, Z. L. Liu, J. T. Sun, T. Lei, C. Liu, J. O. Wang, K. Ibrahim, D. N. Leonard, W. Zhou, H. M. Guo, Y. L. Wang, S. X. Du, S. T. Pantelides, and H.-J. Gao. Intrinsically patterned two-dimensional materials for selective adsorption of molecules and nanoclusters. *Nat. Mater.* **16**, 717 (2017).

[316] X. Cui, C. Troadec, A. T. S. Wee, and Y. L. Huang. Surface nanostructure formation and atomic-scale templates for nanodevices. *ACS Omega* **3**, 3285 (2018).

[317] S. Griessl, M. Lackinger, M. Edelwirth, M. Hietschold, and W. M. Heckl. Self-assembled two-dimensional molecular host-guest architectures from trimesic acid. *Single Mol.* **3**, 25 (2002).

[318] M. Lackinger, S. Griessl, W. M. Heckl, M. Hietschold, and G. W. Flynn. Self-assembly of trimesic acid at the liquid-solid interfacea study of solvent-induced polymorphism. *Langmuir* **21**, 4984 (2005).

[319] K. Kannappan, T. L. Werblowsky, K. T. Rim, B. J. Berne, and G. W. Flynn. An experimental and theoretical study of the formation of nanostructures of self-assembled cyanuric acid through hydrogen bond networks on graphite†. *J. Phys. Chem. B* **111**, 6634 (2007).

[320] Y. Ye, W. Sun, Y. Wang, X. Shao, X. Xu, F. Cheng, J. Li, and K. Wu. A unified model: self-assembly of trimesic acid on gold. *J. Phys. Chem. C* **111**, 10138 (2007).

[321] W. Xiao, X. Feng, P. Ruffieux, O. Gröning, K. Müllen, and R. Fasel. Self-Assembly of Chiral Molecular Honeycomb Networks on Au(111). *J. Am. Chem. Soc.* **130**, 8910 (2008).

[322] J. Zhang, B. Li, X. Cui, B. Wang, J. Yang, and J. G. Hou. Spontaneous Chiral Resolution in Supramolecular Assembly of 2,4,6-Tris(2-pyridyl)-1,3,5-triazine on Au(111). *J. Am. Chem. Soc.* **131**, 5885 (2009).

[323] J. Eichhorn, S. Schlögl, B. V. Lotsch, W. Schnick, W. M. Heckl, and M. Lackinger. Self-assembly of melem on Ag(111)—emergence of porous structures based on aminoheptazine hydrogen bonds. *CrystEngComm* **13**, 5559 (2011).

[324] S.-S. Jester, E. Sigmund, L. M. Röck, and S. Höger. Hierarchical self-assembly of polycyclic heteroaromatic stars into snowflake patterns. *Angew. Chem. Int. Ed.* **51**, 8555 (2012).

[325] H.-Y. Gao, H. Wagner, P. A. Held, S. Du, H.-J. Gao, A. Studer, and H. Fuchs. In-plane Van der Waals interactions of molecular self-assembly monolayer. *Appl. Phys. Lett.* **106**, 081606 (2015).

[326] M. Lindner, M. Valášek, J. Homberg, K. Edelmann, L. Gerhard, W. Wulfhekel, O. Fuhr, T. Wächter, M. Zharnikov, V. Kolivoška, L. Pospíšil, G. Mészáros, M. Hromadová, and M. Mayor. Importance of the Anchor Group Position (*Para* versus *Meta*) in Tetraphenylmethane Tripods: Synthesis and Self-Assembly Features. *Chem. Eur. J.* **22**, 13218 (2016).

[327] M. Lindner, M. Valášek, M. Mayor, T. Frauhammer, W. Wulfhekel, and L. Gerhard. Molecular Graph Paper. *Angew. Chem. Int. Ed.* **56**, 8290 (2017).

[328] J. Homberg, M. Lindner, L. Gerhard, K. Edelmann, T. Frauhammer, Y. Nahas, M. Valášek, M. Mayor, and W. Wulfhekel. Six state molecular revolver mounted on a rigid platform. *Nanoscale* **11**, 9015 (2019).

[329] A. Ibenskas and E. E. Tornau. Statistical model for self-assembly of trimesic acid molecules into homologous series of flower phases. *Phys. Rev. E* **86**, 051118 (2012).

[330] L.-M. Wang, J.-Y. Yue, Q.-Y. Zheng, and D. Wang. Temperature-directed hierarchical surface supramolecular assembly. *J. Phys. Chem. C* **123**, 13775 (2019).

[331] N. Kepčija, Y.-Q. Zhang, M. Kleinschrodt, J. Björk, S. Klyatskaya, F. Klappenberger, M. Ruben, and J. V. Barth. Steering on-surface self-assembly of high-quality hydrocarbon networks with terminal alkynes. *J. Phys. Chem. C* **117**, 3987 (2013).

[332] A. Ibenskas, M. Šimėnas, and E. E. Tornau. Numerical engineering of molecular self-assemblies in a binary system of trimesic and benzenetribenzoic acids. *J. Phys. Chem. C* **120**, 6669 (2016).

[333] T. Jasper-Tönnies, M. Gruber, S. Ulrich, R. Herges, and R. Berndt. Coverage-Controlled Superstructures of C3-Symmetric Molecules: Honeycomb versus Hexagonal Tiling. *Angew. Chem. Int. Ed.* **59**, 7008 (2020).

[334] K. Ichimura, S. K. Oh, and M. Nakagawa. Light-driven motion of liquids on a photoresponsive surface. *Science* **288**, 1624 (2000).

[335] E. Galoppini, W. Guo, W. Zhang, P. G. Hoertz, P. Qu, and G. J. Meyer. Long-range electron transfer across molecule-nanocrystalline semiconductor interfaces using tripodal

sensitizers. *J. Am. Chem. Soc.* **124**, 7801 (2002).

[336] H. Jian and J. M. Tour. En route to surface-bound electric field-driven molecular motors. *J. Org. Chem.* **68**, 5091 (2003).

[337] Q. Li, A. V. Rukavishnikov, P. A. Petukhov, T. O. Zaikova, C. Jin, and J. F. W. Keana. Nanoscale tripodal 1,3,5,7-tetrasubstituted adamantanes for AFM applications. *J. Org. Chem.* **68**, 4862 (2003).

[338] T. Kitagawa, Y. Idomoto, H. Matsubara, D. Hobara, T. Kakiuchi, T. Okazaki, and K. Komatsu. Rigid molecular tripod with an adamantane framework and thiol legs. Synthesis and observation of an ordered monolayer on Au(111). *J. Org. Chem.* **71**, 1362 (2006).

[339] S. Wagner, F. Leyssner, C. Kördel, S. Zarwell, R. Schmidt, M. Weinelt, K. Rück-Braun, M. Wolfad, and P. Tegeder. Reversible photoisomerization of an azobenzene-functionalized self-assembled monolayer probed by sum-frequency generation vibrational spectroscopy. *Phys. Chem. Chem. Phys.* **11**, 6242 (2009).

[340] U. Siemeling, C. Bruhn, F. Bretthauer, M. Borg, F. Träger, F. Vogel, W. Azzam, M. Badin, T. Strunskus, and C. Wöll. Photoresponsive SAMs on gold fabricated from azobenzene-functionalised asparagusic acid derivatives. *Dalton Trans.* **2009**, 8593 (2009).

[341] A. Schramm, C. Stroh, K. Dössel, M. Lukas, M. Fischer, F. Schramm, O. Fuhr, H. v. Löhneysen, and M. Mayor. Tripodal $M^{III}$ complexes on Au(111) surfaces: Towards molecular "lunar modules". *Eur. J. Inorg. Chem.* **2013**, 70 (2013).

[342] W. Li, L. G. C. Rego, F.-Q. Bai, J. Wang, R. Jia, L.-M. Xie, and H.-X. Zhang. What Makes Hydroxamate a Promising Anchoring Group in Dye-Sensitized Solar Cells? Insights from Theoretical Investigation. *J. Phys. Chem. Lett.* **5**, 3992 (2014).

[343] R. Frisenda, S. Tarkuç, E. Galán, M. L. Perrin, R. Eelkema, F. C. Grozema, and H. S. J. van der Zant. Electrical properties and mechanical stability of anchoring groups for single-molecule electronics. *Beilstein J. Nanotechnol.* **6**, 1558 (2015).

[344] Y. Ie, K. Tanaka, A. Tashiro, S. K. Lee, H. R. Testai, R. Yamada, H. Tada, and Y. Aso. Thiophene-based tripodal anchor units for hole transport in single-molecule junctions with gold electrodes. *J. Phys. Chem. Lett.* **6**, 3754 (2015).

[345] C. Schuschke, M. Schwarz, C. Hohner, T. N. Silva, L. Fromm, T. Döpper, A. Görling, and J. Libuda. Phosphonic Acids on an Atomically Defined Oxide Surface: The Binding Motif Changes with Surface Coverage. *J. Phys. Chem. Lett.* **9**, 1937 (2018).

[346] P. Du, M. Jaouen, A. Bocheux, C. Bourgogne, Z. Han, V. Bouchiat, D. Kreher, F. Mathevet, C. Fiorini-Debuisschert, F. Charra, and A.-J. Attias. Surface-confined self-assembled janus tectons: A versatile platform towards the noncovalent functionalization of graphene. *Angew. Chem. Int. Ed.* **53**, 10060 (2014).

[347] F. Matino, G. Schull, F. Köhler, S. Gabutti, M. Mayor, and R. Berndt. Electronic decoupling of a cyclophane from a metal surface. *Proc. Natl. Acad. Sci. USA* **108**, 961 (2010).

[348] S.-E. Zhu, Y.-M. Kuang, F. Geng, J.-Z. Zhu, C.-Z. Wang, Y.-J. Yu, Y. Luo, Y. Xiao, K.-Q. Liu, Q.-S. Meng, L. Zhang, S. Jiang, Y. Zhang, G.-W. Wang, Z.-C. Dong, and J. G. Hou. Self-decoupled porphyrin with a tripodal anchor for molecular-scale electro-

luminescence. *J. Am. Chem. Soc.* **135**, 15794 (2013).

[349] S. Yokoyama, T. Hirose, and K. Matsuda. Photochemical cleavage of axial group attached to the central carbon atom of triangulene leuco derivatives at the ethanol/Au(111) substrate. *Chem. Lett.* **44**, 1616 (2015).

[350] B. Hammer and J. K. Norskov. Why gold is the noblest of all the metals. *Nature* **376**, 238 (1995).

[351] A. Sanchez, S. Abbet, U. Heiz, W.-D. Schneider, H. Häkkinen, R. N. Barnett, and U. Landman. When gold is not noble: nanoscale gold catalysts. *J. Phys. Chem. A* **103**, 9573 (1999).

[352] M. Haruta. When gold is not noble: Catalysis by nanoparticles. *Chem. Rec.* **3**, 75 (2003).

[353] M. Chen and D. Goodman. The structure of catalytically active gold on titania. *Science* **306**, 252 (2004).

[354] Chen, Y. Cai, Z. Yan, and D. W. Goodman. On the origin of the unique properties of supported au nanoparticles. *J. Am. Chem. Soc.* **128**, 6341 (2006).

[355] A. S. K. Hashmi and G. J. Hutchings. Gold catalysis. *Angew. Chem. Int. Ed.* **45**, 7896 (2006).

[356] B. Hvolbæk, T. V. Janssens, B. S. Clausen, H. Falsig, C. H. Christensen, and J. K. Nørskov. Catalytic activity of Au nanoparticles. *Nano Today* **2**, 14 (2007).

[357] H.-T. Chen, J.-G. Chang, S.-P. Ju, and H.-L. Chen. Ethylene Epoxidation on a Au Nanoparticle versus a Au(111) Surface: A DFT Study. *J. Phys. Chem. Lett.* **1**, 739 (2010).

[358] J. Gong. Structure and surface chemistry of gold-based model catalysts. *Chem. Rev.* **112**, 2987 (2011).

[359] N. Hauptmann, R. Robles, P. Abufager, N. Lorente, and R. Berndt. AFM Imaging of Mercaptobenzoic Acid on Au(110): Submolecular Contrast with Metal Tips. *J. Phys. Chem. Lett.* **7**, 1984 (2016).

[360] J. Repp, F. Moresco, G. Meyer, K.-H. Rieder, P. Hyldgaard, and M. Persson. Substrate Mediated Long-Range Oscillatory Interaction between Adatoms: Cu/Cu(111). *Phys. Rev. Lett.* **85**, 2981 (2000).

[361] S. Lukas, G. Witte, and C. Wöll. Novel Mechanism for Molecular Self-Assembly on Metal Substrates: Unidirectional Rows of Pentacene on Cu(110) Produced by a Substrate-Mediated Repulsion. *Phys. Rev. Lett.* **88**, 028301 (2001).

[362] N. Knorr, H. Brune, M. Epple, A. Hirstein, M. A. Schneider, and K. Kern. Long-range adsorbate interactions mediated by a two-dimensional electron gas. *Phys. Rev. B* **65**, 115420 (2002).

[363] K. Lau and W. Kohn. Indirect long-range oscillatory interaction between adsorbed atoms. *Surf. Sci.* **75**, 69 (1978).

[364] H. Brune, M. Giovannini, K. Bromann, and K. Kern. Self-organized growth of nanostructure arrays on strain-relief patterns. *Nature* **394**, 451 (1998).

[365] K. Pohl, M. C. Bartelt, J. de la Figuera, N. C. Bartelt, J. Hrbek, and R. Q. Hwang.

Identifying the forces responsible for self-organization of nanostructures at crystal surfaces. *Nature* **397**, 238 (1999).

[366] I. Fernandez-Torrente, S. Monturet, K. J. Franke, J. Fraxedas, N. Lorente, and J. I. Pascual. Long-range repulsive interaction between molecules on a metal surface induced by charge transfer. *Phys. Rev. Lett.* **99**, 176103 (2007).

[367] T. Knaak, T. G. Gopakumar, B. Schwager, F. Tuczek, R. Robles, N. Lorente, and R. Berndt. Surface cis effect: Influence of an axial ligand on molecular self-assembly. *J. Am. Chem. Soc.* **138**, 7544 (2016).

[368] J. Kröger, H. Jensen, R. Berndt, R. Rurali, and N. Lorente. Molecular orbital shift of perylenetetracarboxylic-dianhydride on gold. *Chem. Phys. Lett.* **438**, 249 (2007).

[369] S. Soubatch, C. Weiss, R. Temirov, and F. S. Tautz. Site-specific polarization screening in organic thin films. *Phys. Rev. Lett.* **102**, 177405 (2009).

[370] S. J. Blanksby and G. B. Ellison. Bond dissociation energies of organic molecules. *Acc. Chem. Res.* **36**, 255 (2003).

[371] S. W. Benson. III - Bond energies. *J. Chem. Educ.* **42**, 502 (1965).

[372] M. Pan, D. W. Flaherty, and C. B. Mullins. Low-Temperature Hydrogenation of Acetaldehyde to Ethanol on H-Precovered Au(111). *J. Phys. Chem. Lett.* **2**, 1363 (2011).

[373] J. C. F. Rodriguez-Reyes, C. G. F. Siler, W. Liu, A. Tkatchenko, C. M. Friend, and R. J. Madix. van der Waals Interactions Determine Selectivity in Catalysis by Metallic Gold. *J. Am. Chem. Soc.* **136**, 13333 (2014).

[374] S. Karakalos, Y. Xu, F. C. Kabeer, W. Chen, J. C. F. Rodríguez-Reyes, A. Tkatchenko, E. Kaxiras, R. J. Madix, and C. M. Friend. Noncovalent bonding controls selectivity in heterogeneous catalysis: Coupling reactions on gold. *J. Am. Chem. Soc.* **138**, 15243 (2016).

[375] S. Ossinger, H. Naggert, L. Kipgen, T. Jasper-Toennies, A. Rai, J. Rudnik, F. Nickel, L. M. Arruda, M. Bernien, W. Kuch, R. Berndt, and F. Tuczek. Vacuum-evaporable spin-crossover complexes in direct contact with a solid surface: Bismuth versus gold. *J. Phys. Chem. C* **121**, 1210 (2017).

[376] Y. Xu, W. Chen, E. Kaxiras, C. M. Friend, and R. J. Madix. General Effect of van der Waals Interactions on the Stability of Alkoxy Intermediates on Metal Surfaces. *J. Phys. Chem. B* **122**, 555 (2017).

[377] F. C. Kabeer, W. Chen, R. J. Madix, C. M. Friend, and A. Tkatchenko. First-Principles Study of Alkoxides Adsorbed on Au(111) and Au(110) Surfaces: Assessing the Roles of Noncovalent Interactions and Molecular Structures in Catalysis. *J. Phys. Chem. C* **121**, 27905 (2017).

[378] J. P. Perdew, K. Burke, and M. Ernzerhof. Generalized gradient approximation made simple. *Phys. Rev. Lett.* **77**, 3865 (1996).

[379] V. Blum, R. Gehrke, F. Hanke, P. Havu, V. Havu, X. Ren, K. Reuter, and M. Scheffler. Ab initio molecular simulations with numeric atom-centered orbitals. *Comput. Phys. Commun.* **180**, 2175 (2009).

[380] S. Shi, G. Schmerber, J. Arabski, J.-B. Beaufrand, D. J. Kim, S. Boukari, M. Bowen, N. T. Kemp, N. Viart, G. Rogez, E. Beaurepaire, H. Aubriet, J. Petersen, C. Becker,

and D. Ruch. Study of Molecular Spin-Crossover Complex Fe(phen)$_2$(NCS)$_2$ Thin Films. *Appl. Phys. Lett.* **95**, 043303 (2009).

[381] H. Naggert, A. Bannwarth, S. Chemnitz, T. von Hofe, E. Quandt, and F. Tuczek. First Observation of Light-Induced Spin Change in Vacuum Deposited Thin Films of Iron Spin Crossover Complexes. *Dalton Trans.* **40**, 6364–6366 (2011).

[382] T. Mahfoud, G. Molnár, S. Cobo, L. Salmon, C. Thibault, C. Vieu, P. Demont, and A. Bousseksou. Electrical Properties and Non-Volatile Memory Effect of the [Fe(HB(pz)$_3$)$_2$] Spin Crossover Complex Integrated in a Microelectrode Device. *Appl. Phys. Lett.* **99**, 053307 (2011).

[383] M. Bernien, D. Wiedemann, C. F. Hermanns, A. Krüger, D. Rolf, W. Kroener, P. Müller, A. Grohmann, and W. Kuch. Spin Crossover in a Vacuum-Deposited Submonolayer of a Molecular Iron(II) Complex. *J. Phys. Chem. Lett.* **3**, 3431 (2012).

[384] T. Palamarciuc, J. C. Oberg, F. El Hallak, C. F. Hirjibehedin, M. Serri, S. Heutz, J. F. Létard, and P. Rosa. Spin Crossover Materials Evaporated Under Clean High Vacuum and Ultra-High Vacuum Conditions: From Thin Films to Single Molecules. *J. Mater. Chem.* **22**, 9690–9695 (2012).

[385] T. G. Gopakumar, M. Bernien, H. Naggert, F. Matino, C. F. Hermanns, A. Bannwarth, S. Mühlenberend, A. Krüger, D. Krüger, F. Nickel, W. Walter, R. Berndt, W. Kuch, and F. Tuczek. Spin-Crossover Complex on Au(111): Structural and Electronic Differences Between Mono- And Multilayers. *Chem. Eur. J.* **19**, 15702 (2013).

[386] B. Warner, J. C. Oberg, T. G. Gill, F. El Hallak, C. F. Hirjibehedin, M. Serri, S. Heutz, M.-A. Arrio, P. Sainctavit, M. Mannini, G. Poneti, R. Sessoli, and P. Rosa. Temperature-And Light-Induced Spin Crossover Observed by X-Ray Spectroscopy on Isolated Fe(II) Complexes on Gold. *J. Phys. Chem. Lett.* **4**, 1546 (2013).

[387] M. Gruber, V. Davesne, M. Bowen, S. Boukari, E. Beaurepaire, W. Wulfhekel, and T. Miyamachi. Spin State of Spin-Crossover Complexes: From Single Molecules to Ultrathin Films. *Phys. Rev. B* **89**, 195415 (2014).

[388] G. Molnár, L. Salmon, W. Nicolazzi, F. Terki, and A. Bousseksou. Emerging Properties and Applications of Spin Crossover Nanomaterials. *J. Mater. Chem. C* **2**, 1360 (2014).

[389] V. Davesne, M. Gruber, M. Studniarek, W. H. Doh, S. Zafeiratos, F. Joly, L. Sirotti, M. G. Silly, A. B. Gaspar, J. A. Real, G. Schmerber, M. Bowen, W. Weber, S. Boukari, V. Da Costa, J. Arabski, W. Wulfhekel, and E. Beaurepaire. Hysteresis and Change of Transition Temperature in Thin Films of Fe[Me$_2$Pyrz]$_3$BH$_2$, a New Sublimable Spin-Crossover Molecule. *J. Chem. Phys.* **142**, 194702 (2015).

[390] M. Bernien, H. Naggert, L. M. Arruda, L. Kipgen, F. Nickel, J. Miguel, C. F. Hermanns, A. Krüger, D. Krüger, E. Schierle, E. Weschke, F. Tuczek, and W. Kuch. Highly Efficient Thermal and Light-Induced Spin-State Switching of an Fe(II) Complex in Direct Contact With a Solid Surface. *ACS Nano* **9**, 8960 (2015).

[391] S. Gueddida, M. Gruber, T. Miyamachi, E. Beaurepaire, W. Wulfhekel, and M. Alouani. Exchange Coupling of Spin-Crossover Molecules to Ferromagnetic Co Islands. *J. Phys. Chem. Lett.* **7**, 900 (2016).

[392] M. Gruber, T. Miyamachi, V. Davesne, M. Bowen, S. Boukari, W. Wulfhekel, M. Alouani, and E. Beaurepaire. Spin Crossover in Fe(phen)$_2$(NCS)$_2$ Complexes on

Metallic Surfaces. *J. Chem. Phys.* **146**, 092312 (2017).

[393] W. Kuch and M. Bernien. Controlling the Magnetism of Adsorbed Metalextendashorganic Molecules. *J. Phys.: Condens. Matter* **29**, 023001 (2017).

[394] H. J. Shepherd, G. Molnár, W. Nicolazzi, L. Salmon, and A. Bousseksou. Spin Crossover at the Nanometre Scale. *Eur. J. Inorg. Chem.* **2013**, 653–661 (2012).

[395] C. Lefter, V. Davesne, L. Salmon, G. Molnár, P. Demont, A. Rotaru, and A. Bousseksou. Charge Transport and Electrical Properties of Spin Crossover Materials: Towards Nanoelectronic and Spintronic Devices. *Magnetochemistry* **2**, 18 (2016).

[396] S. Gueddida and M. Alouani. Spin Crossover in a Single $\mathrm{Fe(phen)_2(NCS)_2}$ Molecule Adsorbed Onto Metallic Substrates: An Ab Initio Calculation. *Phys. Rev. B* **87**, 144413 (2013).

[397] S. Gueddida and M. Alouani. Calculated Impact of Ferromagnetic Substrate on the Spin Crossover in a $\mathrm{Fe(1,10-phenanthroline)_2}(NCS)_2$ Molecule. *Phys. Rev. B* **93**, 184433 (2016).

[398] M. A. Halcrow. *Spin-Crossover Materials: Properties and Applications.* Wiley, Chichester, West Sussex, United Kingdom, 1 edition (2013).

[399] K. Momma and F. Izumi. VESTA 3 for Three-Dimensional Visualization of Crystal, Volumetric and Morphology Data. *J. Appl. Crystallogr.* **44**, 1272 (2011).

[400] P. Gütlich, Y. Garcia, and H. A. Goodwin. Spin Crossover Phenomena in Fe (II) Complexes. *Chem. Soc. Rev.* **29**, 419–427 (2000).

[401] H. Oshio, K. Kitazaki, J. Mishiro, N. Kato, Y. Maeda, and Y. Takashima. New Spin-Crossover Iron(III) Complexes With Large Hysteresis Effects and Time Dependence of Their Magnetism. *J. Chem. Soc. Dalton Trans.* **1987**, 1341 (1987).

[402] S. Hayami and Y. Maeda. Time-dependence of the magnetism of $\mathrm{[fe(pap)_2]ClO_4}$ and its solvent adducts; Unexpected solid state effect in high-spin<->low-spin state transition. *Inorg. Chim. Acta* **255**, 181 (1997).

[403] S. Hayami, K. Hiki, T. Kawahara, Y. Maeda, D. Urakami, K. Inoue, M. Ohama, S. Kawata, and O. Sato. Photo-Induced Spin Transition of Iron(III) Compounds With $\pi$–$\pi$ Intermolecular Interactions. *Chem. Eur. J.* **15**, 3497 (2009).

[404] A. Hauser. Light-Induced Spin Crossover and the High-SpinextrightarrowLow-Spin Relaxation. In *Spin Crossover in Transition Metal Compounds II*, number 234 in Topics in Current Chemistry, pages 155–198. Springer Berlin Heidelberg, (2004).

[405] J.-F. Létard, L. Capes, G. Chastanet, N. Moliner, S. Létard, J.-A. Real, and O. Kahn. Critical Temperature of the LIESST Effect in Iron(II) Spin Crossover Compounds. *Chem. Phys. Lett.* **313**, 115 (1999).

[406] M. Böhringer, W.-D. Schneider, R. Berndt, K. Glöckler, M. Sokolowski, and E. Umbach. Corrugation Reversal in Scanning Tunneling Microscope Images of Organic Molecules. *Phys. Rev. B* **57**, 4081 (1998).

[407] M. Böhringer, K. Morgenstern, W.-D. Schneider, and R. Berndt. Reversed Surface Corrugation in STM Images on Au (111) by Field-Induced Lateral Motion of Adsorbed Molecules. *Surf. Sci.* **457**, 37–50 (2000).

[408] T. Leoni, O. Guillermet, H. Walch, V. Langlais, A. Scheuermann, J. Bonvoisin, and

S. Gauthier. Controlling the Charge State of a Single Redox Molecular Switch. *Phys. Rev. Lett.* **106**, 216103 (2011).

[409] M. Gruber and R. Berndt. Manipulation of Cyclohexene-Based Organic Molecules on Various Metallic Substrates. *J. Phys. Chem. C* **120**, 18642 (2016).

[410] T. Jasper-Tönnies, M. Gruber, S. Karan, H. Jacob, F. Tuczek, and R. Berndt. Deposition of a Cationic $Fe^{III}$ Spin-Crossover Complex on Au(111): Impact of the Counter Ion. *J. Phys. Chem. Lett.* **8**, 1569 (2017).

[411] M. Gruber, F. Ibrahim, S. Boukari, L. Joly, V. Da Costa, M. Studniarek, M. Peter, H. Isshiki, H. Jabbar, V. Davesne, J. Arabski, E. Otero, F. Choueikani, K. Chen, P. Ohresser, W. Wulfhekel, F. Scheurer, E. Beaurepaire, M. Alouani, W. Weber, and M. Bowen. Spin-Dependent Hybridization between Molecule and Metal at Room Temperature through Interlayer Exchange Coupling. *Nano Lett.* **15**, 7921 (2015).

[412] F. A. Ma'Mari, T. Moorsom, G. Teobaldi, W. Deacon, T. Prokscha, H. Luetkens, S. Lee, G. E. Sterbinsky, D. A. Arena, D. A. MacLaren, M. Flokstra, M. Ali, M. C. Wheeler, G. Burnell, B. J. Hickey, and O. Cespedes. Beating the Stoner Criterion Using Molecular Interfaces. *Nature* **524**, 69 (2015).

[413] F. A. Ma'Mari, M. Rogers, S. Alghamdi, T. Moorsom, S. Lee, T. Prokscha, H. Luetkens, M. Valvidares, G. Teobaldi, M. Flokstra, R. Stewart, P. Gargiani, M. Ali, G. Burnell, B. J. Hickey, and O. Cespedes. Emergent Magnetism at Transition-Metal–Nanocarbon Interfaces. *Proc. Natl. Acad. Sci.* **114**, 5583 (2017).

[414] M. Cinchetti, V. A. Dediu, and L. E. Hueso. Activating the Molecular Spinterface. *Nat. Mater.* **16**, 507 (2017).

[415] H. Ando, Y. Nakao, H. Sato, and S. Sakaki. Theoretical Study of Low-Spin, High-Spin, and Intermediate-Spin States of [FeIII(pap)2]+ (Pap = N-2-Pyridylmethylidene-2-Hydroxyphenylaminato). Mechanism of Light-Induced Excited Spin State Trapping. *J. Phys. Chem. A* **111**, 5515 (2007).

[416] M. Gruber. *Electronic and Magnetic Properties of Hybrid Interfaces. From Single Molecules to Ultra-thin Molecular Films on Metallic Substrates.* PhD thesis, University of Strasbourg and Karlsruhe Institute of Technology, (2014).

[417] C. F. Hirjibehedin, C. P. Lutz, and A. J. Heinrich. Spin Coupling in Engineered Atomic Structures. *Science* **312**, 1021 (2006).

[418] P. Wahl, L. Diekhöner, M. A. Schneider, and K. Kern. Background Removal in Scanning Tunneling Spectroscopy of Single Atoms and Molecules on Metal Surfaces. *Rev. Sci. Instrum.* **79**, 043104 (2008).

[419] A. Pronschinske, R. C. Bruce, G. Lewis, Y. Chen, A. Calzolari, M. Buongiorno-Nardelli, D. A. Shultz, W. You, and D. B. Dougherty. Iron(II) spin crossover films on Au(111): scanning probe microscopy and photoelectron spectroscopy. *Chem. Commun.* **49**, 10446 (2013).

[420] A. Pronschinske, Y. Chen, G. F. Lewis, D. A. Shultz, A. Calzolari, M. Buongiorno Nardelli, and D. B. Dougherty. Modification of Molecular Spin Crossover in Ultrathin Films. *Nano Lett.* **13**, 1429 (2013).

[421] G. Félix, W. Nicolazzi, L. Salmon, G. Molnár, M. Perrier, G. Maurin, J. Larionova, J. Long, Y. Guari, and A. Bousseksou. Enhanced Cooperative Interactions at the

Nanoscale in Spin-Crossover Materials with a First-Order Phase Transition. *Phys. Rev. Lett.* **110**, 235701 (2013).

[422] T. Jasper-Toennies, M. Gruber, S. Karan, H. Jacob, F. Tuczek, and R. Berndt. Robust and Selective Switching of an $Fe^{III}$ Spin- Crossover compound on $Cu_2N$/Cu(100) with Memristance Behavior. *Nano Letters* **17**, 6613 (2017).

[423] J. Repp, G. Meyer, F. E. Olsson, and M. Persson. Controlling the Charge State of Individual Gold Adatoms. *Science* **305**, 493 (2004).

[424] Y. Wang, X. Ge, G. Schull, R. Berndt, C. Bornholdt, F. Koehler, and R. Herges. Azo Supramolecules on Au(111) with Controlled Size and Shape. *J. Am. Chem. Soc.* **130**, 4218 (2008).

[425] K. Scheil, T. G. Gopakumar, J. Bahrenburg, F. Temps, R. J. Maurer, K. Reuter, and R. Berndt. Switching of an Azobenzene-Tripod Molecule on Ag(111). *J. Phys. Chem. Lett.* **7**, 2080 (2016).

[426] D. B. Strukov, G. S. Snider, D. R. Stewart, and R. S. Williams. The Missing Memristor Found. *Nature* **453**, 80 (2008).

[427] M. J. Frisch, G. W. Trucks, H. B. Schlegel, G. E. Scuseria, M. A. Robb, J. R. Cheeseman, G. Scalmani, V. Barone, B. Mennucci, and G. A. e. a. Petersson. Gaussian 09 Revision D.01, (2013). Gaussian Inc. Wallingford CT.

[428] J. P. Perdew, K. Burke, and M. Ernzerhof. Generalized Gradient Approximation Made Simple. *Phys. Rev. Lett.* **77**, 3865 (1996).

[429] F. Weigend and R. Ahlrichs. Balanced basis sets of split valence, triple zeta valence and quadruple zeta valence quality for H to Rn: Design and assessment of accuracy. *Phys. Chem. Chem. Phys.* **7**, 3297 (2005).

[430] A. D. Becke. Density-functional thermochemistry. III. The role of exact exchange. *J. Chem. Phys.* **98**, 5648 (1993).

[431] C. Lee, W. Yang, and R. G. Parr. Development of the Colle-Salvetti correlation-energy formula into a functional of the electron density. *Phys. Rev. B* **37**, 785 (1988).

[432] J. P. Perdew. Density-functional approximation for the correlation energy of the inhomogeneous electron gas. *Phys. Rev. B* **33**, 8822 (1986).

[433] A. D. Becke. Density-functional exchange-energy approximation with correct asymptotic behavior. *Phys. Rev. A* **38**, 3098 (1988).

[434] J. Tao, J. P. Perdew, V. N. Staroverov, and G. E. Scuseria. Climbing the Density Functional Ladder: Nonempirical Meta-generalized Gradient Approximation Designed for Molecules and Solids. *Phys. Rev. Lett.* **91**, 146401 (2003).

[435] V. N. Staroverov, G. E. Scuseria, J. Tao, and J. P. Perdew. Comparative assessment of a new nonempirical density functional: Molecules and hydrogen-bonded complexes. *J. Chem. Phys.* **119**, 12129 (2003).

[436] W. J. Hehre, R. F. Stewart, and J. A. Pople. Self-consistent Molecular-orbital Methods. I. Use of Gaussian Expansions of Slater-type Atomic Orbitals. *J. Chem. Phys.* **51**, 2657 (1969).

[437] J. B. Collins, P. von R. Schleyer, J. S. Binkley, and J. A. Pople. Self-consistent molecular orbital methods. XVII. Geometries and binding energies of second-row molecules.

A comparison of three basis sets. *J. Chem. Phys.* **64**, 5142 (1976).

[438] A. D. McLean and G. S. Chandler. Contracted Gaussian basis sets for molecular calculations. I. Second row atoms, Z=11–18. *J. Chem. Phys.* **72**, 5639 (1980).

[439] R. Krishnan, J. S. Binkley, R. Seeger, and J. A. Pople. Self-consistent molecular orbital methods. XX. A basis set for correlated wave functions. *J. Chem. Phys.* **72**, 650 (1980).

[440] J.-P. Blaudeau, M. P. McGrath, L. A. Curtiss, and L. Radom. Extension of Gaussian-2 (g2) theory to molecules containing third-row atoms K and Ca. *J. Chem. Phys.* **107**, 5016 (1997).

[441] A. J. H. Wachters. Gaussian Basis Set for Molecular Wavefunctions Containing Third-row Atoms. *J. Chem. Phys.* **52**, 1033 (1970).

[442] P. J. Hay. Gaussian basis sets for molecular calculations. The representation of 3d orbitals in transition-metal atoms. *J. Chem. Phys.* **66**, 4377 (1977).

[443] K. Raghavachari and G. W. Trucks. Highly correlated systems. Excitation energies of first row transition metals Sc–Cu. *J. Chem. Phys.* **91**, 1062 (1989).

[444] R. C. Binning and L. A. Curtiss. Compact contracted basis sets for third-row atoms: Ga–kr. *J. Comput. Chem.* **11**, 1206 (1990).

[445] M. P. McGrath and L. Radom. Extension of Gaussian-1 (g1) theory to bromine-containing molecules. *J. Chem. Phys.* **94**, 511 (1991).

[446] L. A. Curtiss, M. P. McGrath, J. Blaudeau, N. E. Davis, R. C. Binning, and L. Radom. Extension of Gaussian-2 theory to molecules containing third-row atoms Ga–Kr. *J. Chem. Phys.* **103**, 6104 (1995).

[447] P. Avouris and J. E. Demuth. Electronic excitations of benzene, pyridine, and pyrazine adsorbed on Ag(111). *J. Chem. Phys.* **75**, 4783 (1981).

[448] D. B. Dougherty, J. Lee, and J. T. Yates. Role of Conformation in the Electronic Properties of Chemisorbed Pyridine on Cu(110): An STM/STS Study. *J. Phys. Chem. B* **110**, 11991 (2006).